TWO- AND THREE-BODY CORRELATIONS IN SIMPLE GASES

By

LYNN JAMES GROOME

A DISSERTATION PRESENTED TO THE GRADUATE COUNCIL
OF THE UNIVERSITY OF FLORIDA IN PARTIAL FULFILLMENT OF THE REQUIREMENTS
FOR THE DEGREE OF DOCTOR OF PHILOSOPHY

UNIVERSITY OF FLORIDA

1977

ACKNOWLEDGEMENTS

The author wishes to express his appreciation to Dr. K. E. Gubbins, chairman of his supervisory committee, and Dr. J. W. Dufty, co-chairman of his supervisory committee, for their interest and many valuable suggestions throughout this study. The author also wishes to express his appreciation to Professor P. A. Egelstaff, whose continuous energy and enthusiasm pervaded the experimental effort.

The hospitality of the Physics Department, University of Guelph, is gratefully acknowledged, and thanks is extended to members of the mechanical shop for constructing the high pressure sample vessel used in this study.

The Solid State Division at Oak Ridge National Laboratory deserves special recognition for the unrestricted use of their facilities, and especially Dr. H. A. Mook, who volunteered the use of his time-of-flight spectrometer. Without their support, this experiment would have been impossible.

The author would also like to thank R. K. Hawkins for his timely help and good-natured criticism.

Financial support from the National Science Foundation and the Southern Regional Education Board is gratefully acknowledged.

Most especially, the author wishes to thank Dr. J. P. O'Connell, whose office was always open.

TABLE OF CONTENTS

	Page
ACKNOWLEDGEMENTS	ii
LIST OF TABLES	vi
LIST OF FIGURES	viii
ABSTRACT	xvi
CHAPTER	
1. DENSITY CORRELATIONS IN EQUILIBRIUM FLUIDS: DEFINITIONS AND CONCEPTS	1
1.1 Introduction	1
1.2 Local Properties and Fluid Structure	6
1.3 Connection with Experiment	9
2. STATIC CORRELATIONS IN SIMPLE, DILUTE GASES	20
2.1 Introduction	20
2.2 Two-Body Correlations	24
2.3 The Triplet Correlation Function	37
3. THE FORMAL KINETIC THEORY FOR TIME-DEPENDENT CORRELATION FUNCTIONS	46
3.1 Introduction	46
3.2 Properties of $S(Q,\omega)$	47
3.2.1 Relationship to Linear Response and Sum Rules	47
3.2.2 Free-Particle and Hydrodynamic Limits	51
3.2.3 Formal Models for Liquids	56
3.3 Formal Kinetic Theory	58
3.3.1 Outline of the Method and Results	59
3.3.2 Derivation of the Formal Kinetic Equation	62
3.3.3 Generalized Enskog Models	70
3.3.4 Connection with Liquid Models	73
3.4 Triplet Correlations and the Isothermal Pressure Derivative of $S(Q,\omega)$	76
3.5 Model Calculations	82
3.6 Concluding Remarks	90

TABLE OF CONTENTS (continued)

CHAPTER		Page
4.	KINETIC MODELING OF THE DYNAMIC STRUCTURE FACTOR. .	91
	4.1 Introduction.	91
	4.2 Gross-Jackson Kinetic Modeling.	93
	4.3 Optimization of the Gross-Jackson Kinetic Model	100
	4.3.1 Formal Expression for $\lambda(Q,\omega)$	102
	4.4 Model Calculations.	108
	4.4.1 The Fokker-Planck Kinetic Equation .	109
	4.4.2 The Boltzmann-Lorentz Kinetic Equation	114
	4.5 Model Calculations.	117
5.	NEUTRON SCATTERING TIME-OF-FLIGHT SPECTROMETRY. . .	123
	5.1 Introduction.	123
	5.2 The Correlation Method in Time-of-Flight Experiments	128
	5.3 The Magnetically-Pulsed Time-of-Flight Spectrometer.	133
	5.4 Vessel Design	141
	5.5 Filling Procedure	149
6.	DATA REDUCTION.	157
	6.1 Introduction.	157
	6.2 Correction for Multiple Scattering.	162
	6.3 Correction for Absorption	166
	6.4 Normalization of Data	175
	6.5 Instrument Resolution and Stability	179
	6.5.1 Instrument Resolution.	179
	6.5.2 Instrument Stability	182
7.	COMPARISON OF THEORY WITH EXPERIMENT.	187
	7.1 Introduction.	187
	7.2 Treatment of Data	188
	7.3 The Static Structure Factor	193
	7.4 The Isothermal Pressure Derivative of $S(Q)$.	209
	7.5 The Dynamic Structure Factor.	213
	7.5.1 Relationship of $\tilde{S}(Q,\omega)$, $S(Q,\omega)$, and $S_s(Q,\omega)$ to Experiment.	215
	7.5.2 Comparison with Free-Particle and Collisionless Theories	220
	7.5.3 Comparison with Generalized Enskog Hard Sphere Fluid.	227
	7.5.4 Comparison with a Hard Core Fluid with Attractive Forces	230

TABLE OF CONTENTS (continued)

CHAPTER		Page
	7.6 The Isothermal Pressure Derivative of $S(Q,\omega)$	234
	7.7 Concluding Remarks	243
	7.7.1 Summary of the Results for the Static Structure Factor	243
	7.7.2 Summary of the Results for the Dynamic Structure Factor	244
APPENDICES		247
A.	Properties of the Complex Susceptibility	247
	A.1 Derivation of Equation (3-7)	247
	A.2 Sum Rule Relations	249
B.	Determination of $\Psi^{(2)}(x_1,x_2;t=o\|\cdot)$ and B[ ]	251
C.	Determination of $G_2^{-1}(\vec{r}',o;\vec{r}'',o)$	255
D.	Details of Model Calculations (Section 3.5)	257
	D.1 Expression for $A(Q)$	257
	D.2 Expression for $\tau(Q)$	260
E.	The N=6 Gross-Jackson Kinetic Model	263
F.	The Optimized Kinetic Model for the Fokker-Planck Collision Operator	271
G.	The Optimized Kinetic Model for the Boltzmann-Lorentz Collision Operator	274
	G.1 Evaluation of $(1, R_{oo} M_s R_{oo} 1)$	274
	G.2 Large Z Expansion of $\lambda(Q,\omega)$	280
H.	Detailed Drawings of the High Pressure Xenon Sample Vessel	284
I.	Sample Homogenization	292
J.	Data Tables	296
BIBLIOGRAPHY		328
BIOGRAPHICAL SKETCH		333

LIST OF TABLES

Table		Page
1-1	SCATTERING PROPERTIES OF VARIOUS TYPES OF RADIATION (17)	14
1-2	WAVELENGTH AND ENERGY OF VARIOUS TYPES OF RADIATION (17)	15
2-1	BARKER PAIR POTENTIAL (EQUATION (2-10)) PARAMETERS FOR KRYPTON AND XENON (12)	27
5-1	PULSING SEQUENCES USED IN THE TIME-OF-FLIGHT EXPERIMENT	133
5-2	DETECTOR ANGLES	141
5-3	EQUATION OF STATE (EQUATION (5-16)) PARAMETERS FOR ARGON AND XENON	147
5-4	CRITICAL PARAMETERS FOR ARGON AND XENON	148
6-1	RATIO OF TWICE-SCATTERED TO SINGLY-SCATTERED NEUTRONS (δ)	164
6-2	ABSORPTION (λ=1.8 Å) AND SCATTERING CROSS-SECTIONS FOR ALUMINUM, XENON AND VANADIUM	172
6-3	EXPERIMENTAL TRANSMISSIONS	174
6-4	TYPICAL PEAK (N_p) AND BACKGROUND (N_B) COUNTS FOR XENON, THE SAMPLE VESSEL, VANADIUM, AND AIR	185
7-1	SUMMARY OF EXPERIMENTAL STATE CONDITIONS. ALL RUNS AT T = 303 K	199
7-2	SUMMARY OF F(Q) APPEARING IN EQUATION (7-7)	214
I-1	EFFECTIVE XENON NUMBER DENSITIES. ALL RUNS AT T = 303 K	294
J-1	THE STATIC STRUCTURE FACTOR, S(Q)	297

LIST OF TABLES (continued)

Table		Page
J-2	$\tilde{S}(Q,\omega)$: P = 51.7 atm, ρ = 3.08 mole/liter, T = 303 K (Run 1)	298
J-3	$\tilde{S}(Q,\omega)$: P = 51.7 atm, ρ = 3.08 mole/liter, T = 303 K (Run 2)	303
J-4	$\tilde{S}(Q,\omega)$: P = 57.1 atm, ρ = 3.80 mole/liter, T = 303 K	308
J-5	$\tilde{S}(Q,\omega)$: P = 62.9 atm, ρ = 4.67 mole/liter, T = 303 K	313
J-6	$\tilde{S}(Q,\omega)$: P = 66.5 atm, ρ = 5.51 mole/liter, T = 303 K	318
J-7	$\tilde{S}(Q,\omega)$: P = 72.7 atm, ρ = 7.60 mole/liter, T = 303 K	323

LIST OF FIGURES

Figure		Page
1-1	The relationship between the pair potential, $\phi(r)$, and $g(r)$ for a dilute gas; r is the distance of separation between two atoms.	10
1-2	Qualitative behavior of the self (G_s) and distinct (G_d) time correlation functions for various times; τ_o is a relaxation time for the fluid structure (17). .	11
1-3	Incident and scattered radiation.	12
1-4	Schematic diagram of the scattering process. The incident (A) and scattered (B) beams are shown as viewed at large distances from the scattering center.	16
2-1	Term-by-term comparison of $g(r)$ for xenon assuming pairwise additivity of the potential. The curves labeled 1, 2 and 3 are for terms up to and including g_o, g_1 and g_2 in equation (2-6), respectively; $\rho^* = \rho r_m^3 = 1.0$. . . .	28
2-2	Comparison of the Monte Carlo (g_{MC}) calculation of $g(r)$ with equation (2-6) (g_e) for krypton. Pairwise additivity of the potential was assumed, and terms up to and including g_2 were used in calculating g_e. For $\rho^* \leq 0.4$, three terms are sufficient for agreement (estimated error: $\pm 2\%$) with the MC calculations at $r^* = r/r_m = 1$; $T^* = kT/\varepsilon$	30
2-3	Spatial configuration of molecules i, j, and k.	31
2-4	Influence of the Axilrod-Teller three-body potential on $g_1(r)$ for xenon; g_1^A, g_1^{NA}, are the values of $g_1(r)$ assuming pairwise additivity and non-additivity (equation (2-11)), respectively; $r^* = r/r_m$, $T^* = kT/\varepsilon$. . . .	32
2-5	Term-by-term comparison of $S(Q)$ for xenon assuming pairwise additivity of the potential. The curves labeled 1, 2, and 3 are for terms up to and including S_1, S_2, and S_3 in equation (2-13), respectively. Here, $\rho^* = \rho r_m^3 = 1.0$	34

2-6 Term-by-term comparison of S(Q) for xenon assuming pairwise additivity of the potential. The curves labeled 1, 2, and 3 are for terms up to and including S_1, S_2, and S_3 in equation (2-13), respectively; $\rho^* = \rho r_m^3 = 0.188$. 35

2-7 Influence of the Axilrod-Teller three-body potential on $S_1(Q)$ for xenon; S_1^A, S_1^{NA}, are the values of $S_1(Q)$ assuming pairwise additivity and non-additivity (equation (2-11)), respectively. 36

2-8 Plot of $(S(Q)-1)/\rho^*$ for xenon as a function of Q for the higher (——, $\rho^* = 0.38$) and lower (---, $\rho^* = 0.156$) densities covered experimentally; $\rho^*=\rho r_m^3$, $T^*=kT/\varepsilon$ . . 38

2-9 Test of the convergence of $g_1^{(3)}$ for krypton; N is the number of configurations generated by the Monte Carlo procedure. 40

2-10 Comparison of the superposition approximation for $g^{(3)}$ (---, equation 2-20) with that predicted by equation (2-17) (——) for terms up to and including $g_1^{(3)}$; $\rho^* = \rho r_m^3 = 1.0$. 42

2-11 Monte Carlo results for $\partial g(r)/\partial P$ for a dense ($\rho^* = 0.83$) system of Lennard-Jones atoms, obtained by differentiating Verlet's (28) Monte Carlo calculations 44

2-12 Monte Carlo results for $\partial S(Q)/\partial P$ for a dense ($\rho^* = 0.83$) system of Lennard-Jones atoms (——), obtained by Fourier transforming $\partial g(r)/\partial P$ given in Figure 2-11. Also included is $\partial S(Q)/\partial P$ predicted by equation (2-22) (---). 45

3-1 Qualitative behavior of the dynamic structure factor, $S(Q,\omega)$, in the hydrodynamic limit. 54

3-2 The static structure factor, S(Q), and $\partial S(Q)/\partial P$, for liquid argon near its triple point (T = 86.56 K, $\rho = 1.402$ gram/cm^3). 85

3-3 The dynamic structure factor, $S(Q,\omega)$, and $\partial S(Q,\omega)/\partial P$ for liquid argon near its triple point (T = 86.56 K, $\rho = 1.402$ gram/cm^3) at Q = 1.1 Å^{-1} 86

3-4 Same as Figure 3-3 except that Q = 2.0 Å^{-1}. 87

3-5 Same as Figure 3-3 except that Q = 3.6 Å^{-1}. 88

Figure LIST OF FIGURES (continued) Page

3-6 Comparison of $\partial \ln S(Q)/\partial P$ (---) and $\partial \ln S(Q,\omega)/\partial P$ (——) for liquid argon near its triple point (T = 86.56 K, ρ = 1.402 gram/cm^3) at Q = 2.0 Å^{-1}. 89

4-1 The dynamic structure factor, $S(Q,\omega)$, for the N = 6 Gross-Jackson kinetic model (·). Included is the fully converged, N = 30, solution (——) 101

4-2 The self structure factor, $S_s(Q,\omega)$, for the Fokker-Planck model; exact solution (——), N = 1 Gross-Jackson (∘) and optimized (·) kinetic models. 113

4-3 Half-width at half-maximum ($x_{\frac{1}{2}}$) for the Fokker-Planck model; exact solution (——), N = 1 Gross-Jackson (---), and optimized (·) kinetic models. 115

4-4 Percent deviation of the N = 1 (-·-·-), the N = 6 (-∘-∘-) and the optimized (——) kinetic models from the fully converged, N = 30, solution, $R_S(x,y)$. 118

4-5 Same as Figure 4-4 except that y = 2.62. 119

4-6 Half-width at half-maximum ($x_{\frac{1}{2}}$) for a dilute gas of hard spheres; exact solution (——), the N = 1 (---), N = 6 (▲) and the optimized (·) kinetic models. 120

4-7 Behavior of the real (λ_R) and imaginary (λ_I) parts of the optimized kinetic model eigenvalue (equation (4-56)) for a dilute, hard sphere gas; y = 0.247 (——), y = 1.00 (-·-·-) 121

5-1 Schematic layout for the measurement of $d^2\sigma/d\Omega d\omega$. . . . 125

5-2 Illustration of the time-of-flight measurement; N is the neutron intensity and v_0 is the known incident neutron velocity 127

5-3 The mechanical chopper. 129

5-4 The forcing function, M(t), for various pulse shapes; θ is the pulse width and N is the number of intervals per period. 131

5-5 Qualitative behavior of the forcing function (M), the time-of-flight distribution (Z), and the correlated time-of-flight spectrum (U); θ is the pulse width and c_w is the channel width 135

5-6 Qualitative behavior of the correlated spectrum (U). The background oscillations are attributed to the pseudo-random correlation technique. 136

5-7 Schematic layout of the HFIR magnetically pulsed time-of-flight spectrometer at ORNL. 137

5-8 Qualitative behavior of the static structure factor, S(Q); Region I: $11.8° \leq 2\theta \leq 36.5°$, Region II: $39.1° \leq 2\theta \leq 63.4°$ 140

5-9 Phase diagram for xenon; T = 303 K is the experimental run temperature. 144

5-10 Xenon density as a function of pressure at T = 303 K. The solid line is the equation of state, equation (5-13), and the dashed line is the virial equation, equation (5-11). 145

5-11 Comparison of the equation of state (equation (5-13)) with the experimental data of Beattie et al. (72) for xenon at 298 K; the solid line is equation (5-13), and (°) is data. 149

5-12 Xenon sample vessel. 153

5-13 Schematic layout of the gas transfer lines and the xenon sample vessel (A). 154

5-14 Schematic layout of the xenon sample vessel (A) during operation. 156

6-1 Raw time-of-flight data for xenon plus the sample vessel (·) and the sample vessel alone (°), normalized to the total incident flux 158

6-2 Data from Figure 6-1 corrected for neutron absorption; xenon plus sample vessel (·), sample vessel alone (°). 160

6-3 The ratio, δ, of twice-scattered neutrons (I_2) to singly scattered neutrons (I_1) as a function of the xenon density; $\rho = 0$ corresponds to the aluminum sample vessel 165

6-4 Procedure used for estimating τ_f in equation (6-9). The xenon time-of-flight spectrum (——) is shown for low angles, and (---) is the multiple scattering correction of equation (6-9). Note that this figure is not drawn to scale. 167

6-5 Behavior of the absorption correction, $A(\theta,\tau)$, as a function of the time-of-flight; $\theta = 0°$, $\rho = 7.6$ mole/liter 171

6-6 Comparison of the experimental transmissions (·), equation (6-24) with the calculated transmissions (——, equation (6-14) for $\theta = 0°$). The effective xenon number density is obtained by homogenization of xenon plus the sample vessel 173

6-7 An (ω,Q) diagram for various scattering angles, 2θ. . . 177

6-8 The spectrometer resolution function $R(\omega)$. The closed circles are the data and the solid line is drawn as a visual aid. 180

6-9 Comparison of the spectrometer energy resolution function (---) with a typical xenon spectrum (——). Both are normalized to a peak value of unity for comparison 181

6-10 Areas used in estimating errors due to counting statistics. The shaded area (A) is the area under the central peak and the two background areas (B/2) are separated from (A) by vertical lines. 183

6-11 Integrated vanadium spectrum (air subtracted) as a function of the scattering angle. The solid line is a least squares fit of the data (·) and the dashed lines denote a $\pm 2\%$ error bar due to counting statistics . . . 186

7-1 Qualitative behavior of the static structure factor observed experimentally (·) and predicted from the density expansion (equation (2-13)) of $S(Q)$ (——). The arrows ($Q = 2.13$ Å^{-1}, $Q = 2.19$ Å^{-1}) denote the pathological data points. 190

7-2 Qualitative behavior of $S(Q,\omega)$ for $Q = 2.13$ Å^{-1} and $Q = 2.19$ Å^{-1}. The large oscillations in the background are due to second-order Bragg scattering 191

7-3 Data of Figure 7-1 with S(Q = 2.13 Å^{-1}) and S(Q = 2.19 Å^{-1}) discarded. The remaining S(Q) values are normalized to the second node in S(Q) (arrow). 192

7-4 Comparison of the density expansion (equation (2-13)) of S(Q) (——) with experiment (·). Pairwise additivity and Barker's pair potential for xenon were assumed for terms up to and including $S_3(Q)$. State conditions: P = 51.7 atm, ρ = 3.08 mole/liter, T = 303 K 194

7-5 Same as Figure 7-4 except: P = 57.1 atm, ρ = 3.80 mole/liter, T = 303 K 195

7-6 Same as Figure 7-4 except: P = 62.9 atm, ρ = 4.67 mole/liter, T = 303 K 196

7-7 Same as Figure 7-4 except: P = 66.5 atm, ρ = 5.51 mole/liter, T = 303 K 197

7-8 Same as Figure 7-4 except: P = 72.7 atm, ρ = 7.60 mole/liter, T = 303 K 198

7-9 Term-by-term comparison of S(Q) for xenon. The curves labeled 1, 2, and 3 are for terms up to and including S_1, S_2, and S_3 in equation (2-13), respectively. Pairwise additivity and Barker's pair potential for xenon were assumed. Full circles are experimental values. . 201

7-10 Same as Figure 7-9 except: P = 72.7 atm, ρ = 7.60 mole/liter, T = 303 K 202

7-11 Plot of (S(Q)-1)/ρ* versus Q. Included are the results from equation (2-13) for ρ = 7.60 mole/liter (——) and ρ = 3.08 mole/liter (---). Pairwise additivity and Barker's pair potential for xenon were assumed for terms up to and including $S_3(Q)$. 204

7-12 Results of averaging the data from Figure 7-11. Open circles (°) are averages for $P < P_c$, crosses (+) are averages for $P > P_c$, and full circles (·) are averages for all P at fixed Q; P_c is the critical pressure for xenon. Included is the first term in the density expansion, $S_1(Q)$ (---). The solid lines are drawn as a visual aid 206

7-13 The effect of non-additivity of the intermolecular potential on S(Q). Non-additivity in $S_2(Q)$ (——) was modeled using the Axilrod-Teller dispersion potential; the dashed line was calculated assuming pairwise additivity and Barker's potential for xenon for terms up to and including $S_3(Q)$. 207

7-14 Same as Figure 7-13 except: $P = 72.7$ atm, $\rho = 7.60$ mole/liter, $T = 303$ K. 208

7-15 Comparison of theory (——) with experiment (·) for $\partial S(Q)/\partial P$. Pairwise additivity and Barker's pair potential for xenon was assumed for terms up to and including $S_3(Q)$; $P_2 = 62.9$ atm, $P_1 = 51.7$ atm. 211

7-16 Same as Figure 7-15 except: $P_2 = 72.7$ atm, $P_1 = 62.9$ atm. 212

7-17 The dynamic structure factor, $\tilde{S}(Q,\omega)$, as a function of ω for various Q_o values. Here, $\tilde{S}(Q,\omega)$ is defined in equation (6-30), (·) are experimental points, and (——) is drawn as a visual aid. Also included is the static structure factor, $S(Q)$ 216

7-18 Same as Figure 7-17 except: $P = 72.7$ atm, $\rho = 7.60$ mole/liter, $T = 303$ K. 217

7-19 Relative magnitudes of $S(Q,\omega)$ (---) and $S_s(Q,\omega)$ (-·-·-) as calculated from kinetic theory. Also included is $\tilde{S}(Q,\omega)$ (——) defined in equation (6-30). 218

7-20 Contribution of $b^2_{coh}\, S(Q,\omega)$ (---) and $b^2_{incoh}\, S_s(Q,\omega)$ (-·-·-) to $\tilde{S}(Q,\omega)$ (——). 219

7-21 The convolution of $\tilde{S}(Q,\omega)$ as calculated from kinetic theory (---) with the spectrometer resolution function, $R(\omega)$ (- - -); Here, (——) is the convoluted function, $\tilde{S}_c(Q,\omega)$, defined in equation (7-9) 221

7-22 Comparison of free-particle (-·-·-) and collisionless theories (---, hard sphere; ——, continuous) with experimental data (·) for $\tilde{S}_c(Q,\omega)$. The error bars are estimated by averaging two experimental runs at $\rho = 3.08$ mole/liter. 223

7-23 Comparison of free-particle (-·-·-) and Sutherland fluid (---) with experiment (·). 226

7-24 Calculation of $\tilde{S}_c(Q,\omega)$ using Enskog's theory for hard spheres. Here, (---) is for $r_o = 2.75$ Å, (——) for $r_o = 6.0$ Å, and (·) denotes experimental data. 229

7-25 Comparison of $g(r)$ as predicted from Percus-Yevick hard spheres (-·-·-, $r_o = 6.0$ Å) and $g(r)$ from the Sutherland potential (---; $\varepsilon/k = 277.5$ K, $r_o = r_{min}$) with the virial calculation (——) of $g(r)$ for Barker's pair potential assuming pairwise additivity and for terms up to and including $g_2(r)$ in equation (2-6). . . 233

7-26 The structure factor $\tilde{S}_c(Q,\omega)$ as calculated from the Enskog kinetic equation (---, $r_o = r_m$) for a hard core fluid having attractive forces. Also included is the Enskog calculation for hard spheres (---, $r_o = r_m$), and the experimental results (·). 235

7-27 Behavior of $g(r_o)$ determined by fitting the attractive hard core $\tilde{S}_c(Q,\omega)$ to experiment 236

7-28 The isothermal pressure derivative of $S(Q,\omega)$ at a fixed $Q = 0.58$ Å^{-1}. The solid line is drawn as a visual aid 238

7-29 Same as Figure 7-28 except: $Q = 1.10$ Å^{-1}. 239

7-30 The isothermal pressure derivative of $\ln S(Q,\omega)$ at a fixed $Q = 0.58$ Å^{-1}. The solid line is drawn as a visual aid, and (---) denotes the quantity $\partial \ln S(Q)/\partial P$ . . 241

7-31 Same as Figure 7-30 except: $Q = 1.10$ Å^{-1}. 242

G-1 Binary collision geometry 279

H-1 Front view of sample vessel 285

H-2 Top view of sample vessel 286

H-3 Side view of end cap. 287

H-4 Top view of end cap 288

H-5 Top view of 1/8 tool steel washer 289

H-6 Top view of Teflon O-ring seal. 290

H-7 Plastic end cover 291

I-1 Xenon effective number density, ρ_{eff}, as a function of the xenon number density, ρ. The extrapolation (---) to ρ=o yields ρ_{eff}^{al}, the aluminum effective number density 295

Abstract of Dissertation Presented to the Graduate Council
of the University of Florida in Partial Fulfillment of the Requirements
for the Degree of Doctor of Philosophy

TWO- AND THREE-BODY CORRELATIONS IN SIMPLE GASES

By

Lynn James Groome

August 1977

Chairman: K. E. Gubbins
Co-chairman: J. W. Dufty
Major Department: Chemical Engineering

The static and dynamic behavior of a simple gas is studied both experimentally (via inelastic neutron scattering) and theoretically. Measurement of the static structure factor, S(Q), at low densities is discussed as a means for providing details concerning three-body forces. An analysis of the density expansion of the static structure factor reveals S(Q) to be insensitive to higher-order terms, i.e., $S_2(Q)$ and $S_3(Q)$, beyond the first peak in S(Q) ($Q > 1.5$ Å^{-1} for xenon). Also, $S_2(Q)$ is found to be most sensitive to three-body forces in the region $Q \sim 1.0$ Å^{-1}. The comparison of the virial expansion (assuming pairwise additivity and the Barker pair potential for xenon) with experimental measurements of S(Q) for low density xenon gas tentatively suggests that Barker's pair potential for xenon may be somewhat erroneous. The inclusion of three-body forces (e.g., the Axilrod-Teller dispersion potential) reduces the discrepancy between theory and experiment, particularly at the lower densities. These results suggest that a combination of uncertainty

in both the pair and three-body potentials contributes to the difference between the theoretical calculations and what is observed experimentally.

A similar study of the dynamic structure factor is proposed as a test of linear kinetic theory. The analysis of the time-of-flight data is performed using the N = 6 Gross-Jackson kinetic model for a hard core fluid. A comparison of this model (assuming (i) hard spheres, and (ii) hard cores having attractive forces) with experiment indicates clearly that hard spheres are not an adequate model for xenon at the state conditions studied. The agreement between experiment and the theory for attractive spheres is quite good, and we therefore conclude that the effect of the attractive part of the xenon potential is significant in representing the collisional narrowing of $\tilde{S}(Q,\omega)$.

The spectrometer is demonstrated to be unstable, and it is for this reason that no definite conclusions concerning the isothermal pressure derivatives, $\frac{\partial S(Q)}{\partial P}$ and $\frac{\partial S(Q,\omega)}{\partial P}$, can be made. However, a considerable amount of structure is observed for these quantities, indicating that neutron scattering provides a sensitive probe into the structure and dynamics of dilute, simple gases.

CHAPTER 1

DENSITY CORRELATIONS IN EQUILIBRIUM FLUIDS: DEFINITIONS AND CONCEPTS

1.1 Introduction

The design engineer is continually faced with situations in which the data he needs are not available, particularly at the system state conditions of interest. He must then resort to techniques for estimating their value. Many of these techniques are empirical or semi-empirical in nature. Considerable progress has been made towards replacing existing empirical and semi-empirical techniques with a unified statistical mechanical theory in which all the physical properties of a given substance or mixture are related to a single intermolecular pair potential (and perhaps a three-body potential). Advances made in the last 40-50 years include the following: the detailed understanding of ideal gases leading to the JANAF (1) and Rossini (2) property tabulations, which are useful for computing heat capacities, equilibrium constants, and the like; the development of the virial equation of state (3), now widely used in vapor-liquid equilibrium calculations; the corresponding states theory and the extensions by Pitzer and others (4); and the more recent theories of liquid solutions, including conformal solution theory (5) and perturbation theories (6), which are now finding applications in chemical engineering.

Two-point correlation functions are fundamental to the development of sound theories for the prediction of physical property data:

by knowing the pair correlation function, g(r), and specifying the intermolecular potential, all the thermodynamic properties can be readily calculated from first principles. Moreover, Green (7) has shown that two-time correlation functions are fundamental to the theory of transport processes. Two-point correlation functions present an immensely detailed picture of fluids, in addition to providing information on bulk thermodynamic and transport properties. For example, the pair correlation function of a fluid yields not only the thermodynamic properties, but also a semimicroscopic view of the pairwise distribution of molecules in space. More generally, the time-dependent density-density correlation function provides the transport properties and dynamical modes of the system in addition to the information contained in the static pair correlation function. Furthermore, there is direct and precise experimental accessibility to these functions through radiation scattering. This combination of theoretical information and ease of measurement has given these two-point functions a prominent role in the study of fluids.

For similar reasons the corresponding multipoint correlation functions present an even more penetrating view into the behavior of macroscopic systems. Higher-order correlation functions, while important in the modeling of two-point correlation functions, also appear explicitly in the description of a variety of problems including nonlinear response theory (8), perturbation theory for two-time correlation functions (9), multiple scattering of light and neutrons, and in radiation scattering from nonequilibrium systems.

Neutron scattering experiments provide a particularly useful method for the investigation of correlations in fluids. Previous

neutron scattering experiments have been concerned primarily with the analysis of liquids, for which the scattering cross section is relatively large. With the recent development of high flux neutron sources it is now possible to obtain precise neutron scattering data for dilute and moderately dense gases. This thesis will be concerned with experimental neutron scattering studies on gaseous xenon and a theoretical analysis of the associated static and dynamic correlation functions in simple gases. Measurement of the static pair correlation function at low densities is discussed as a means to detect the presence and form of three-body forces. Similar studies of the time-dependent pair correlation function are proposed as a test of linear kinetic theory. Few studies of higher-order correlation functions (static or time-dependent) have been made, partly because of the difficulty of their direct experimental measurement. However, it is known (10) that the pressure derivative of the static pair correlation function is related to the three-point correlation function, so that careful isothermal measurements of the pair function over a pressure interval would provide indirect information regarding the triplet function. Recently, Egelstaff, Gray, and Gubbins (11) have pointed out a similar relationship between the isothermal pressure derivative of the time-dependent pair correlation function and the corresponding triplet function. In this context, the low density forms of the static and time-dependent three-point functions are discussed.

In Chapter 2 the problem of obtaining information on the intermolecular forces from experimental data on the static structure factor, $S(Q)$, for a low density gas is considered. The structure factor is related to the static pair correlation function through

$$S(Q) = 1 + \rho \int d\vec{r}\, e^{-i\vec{Q}\cdot\vec{r}} \, [g(r) - 1] \, , \tag{1-1}$$

where ρ is the macroscopic number density (N/V). The density expansion for S(Q),

$$S(Q) = 1 + \rho S_1(Q) + \rho^2 S_2(Q) + \ldots \, , \tag{1-2}$$

is obtained from the corresponding expansion of g(r), and the explicit dependence of $S_2(Q)$ on the two- and three-body potentials is given. Calculations of g(r) and S(Q) are performed using the Barker pair potential (12) for krypton and xenon, and the three-body contribution is modeled using the Axilrod-Teller (13) dispersion potential. Comparison of S(Q) with and without the three-body forces is used to indicate the accuracy required to measure such effects. Also given in this chapter is the relationship of $\frac{\partial S(Q)}{\partial P}$ to the static three-point correlation function. The failure of simple models for the three-point correlation function in describing the experimental pressure derivative has been shown by Egelstaff <u>et al</u>. (14). To emphasize the difficulty of modeling the three-point function, its low density form is calculated and compared with the associated Kirkwood superposition approximation.

The relationship of the dynamic structure factor, $S(Q,\omega)$, to linear kinetic theory is given in Chapter 3. The dynamic structure factor is the Fourier transformed time-dependent pair correlation function, $G(\vec{r};t)$,

$$S(Q,\omega) = \int_{-\infty}^{+\infty} dt\, e^{i\omega t} \int d\vec{r}\, e^{-i\vec{Q}\cdot\vec{r}}\, G(\vec{r};t). \tag{1-3}$$

It is shown that $G(\vec{r};t)$ may be expressed as

$$G(\vec{r};t) = \int d\vec{p} \quad \psi(\vec{p};\vec{r},t) \ , \tag{1-4}$$

where $\vec{p}$ is a momentum vector and $\psi(\vec{p};\vec{r},t)$ is the solution to a linear kinetic equation

$$[\frac{\partial}{\partial t} + \frac{\vec{p}}{m} \cdot \vec{\nabla}]\psi = C[\psi] \ . \tag{1-5}$$

A formal expression for the collision operator, $C[\cdot]$, is obtained and evaluated at low density. The relationship of the kinetic formulation to several phenomenological models used to analyze liquids is established. Also discussed in this chapter is the pressure derivative, $\frac{\partial S(Q,\omega)}{\partial P}$, and the associated time-dependent three-point correlation function. Such functions may also be determined from the linear kinetic theory of two-point correlation functions, and the low density form of the time-dependent triplet function is obtained. A simple phenomenological model of equation (1-5) is used to calculate $S(Q,\omega)$, and from it $\frac{\partial S(Q,\omega)}{\partial P}$, thus illustrating their behavior in the liquid state where such models are applicable.

Chapter 4 is concerned with the problem of solving kinetic equations such as equation (1-5) once the collision operator, $C[\cdot]$, is obtained. This is crucial for a comparison between theory and experiment, as errors involved in the theory of the collision operator become entangled with errors associated with solving the kinetic equation. Present kinetic modeling techniques are reviewed along with their limitations. A principal objective of Chapter 4 is the presentation of an optimization of kinetic models that is more economical in terms of algebraic complexity and computer time. The procedure is tested on the Fokker-Planck and Boltzmann-Enskog kinetic equations where favorable agreement with known results is obtained.

Finally, Chapters 5 and 6 discuss details of the neutron scattering experiment performed on low density xenon gas at the Oak Ridge National Laboratory. Chapter 5 discusses features of the experiment peculiar to the High Flux Isotope Reactor (HFIR), whereas Chapter 6 contains details of the data analysis. In Chapter 7 the theories developed in Chapters 2, 3, and 4 are compared with the experimental results.

The remainder of this chapter is devoted to the introduction of basic concepts and definitions arising in the study of the microscopic behavior of equilibrium systems. In particular, local microscopic properties are defined and the density-density time correlation function, $G(\vec{r};t)$, is discussed on a physical basis. The connection between density correlations and radiation scattering experiments is then made in Section 1.3.

1.2 Local Properties and Fluid Structure

If we consider a volume element, $d\vec{r}$, where $d\vec{r}$ is macroscopically small but contains many molecules, it is then possible to define local microscopic variables associated with this volume element. Consider a local variable $H(\vec{r};t)$, where $H(\vec{r};t)$ is a sum of arbitrary single-particle functions, $h(x_i;t)$,

$$H(\vec{r};t) = \sum_{i=1}^{N} h(x_i;t) \ . \tag{1-6}$$

Here, x_i denotes the position $\vec{q}_i$ and momentum $\vec{p}_i$ of the ith particle. Of special interest is the conditon where $H(\vec{r};t)$ is the local number density, $\rho(\vec{r};t)$, obtained by setting $h(x_i;t) = \delta(\vec{r}-\vec{q}_i(t))$:

$$\rho(\vec{r};t) = \sum_{i=1}^{N} \delta(\vec{r}-\vec{q}_i(t)) \ . \tag{1-7}$$

The connection between the local microscopic properties and the corresponding macroscopic quantities is

$$H_0 = \frac{1}{V} \int_V d\vec{r} < H(\vec{r};t=o)> \quad , \tag{1-8}$$

where H_0 is the macroscopic property and, for a grand-canonical ensemble, $<\ldots>$ is

$$<\ldots> = \sum_{N\geq 0}^{\infty} \frac{z^N}{h^{3N}N!} \frac{1}{\mathcal{Z}} \int dx_1(o) \ldots dx_N \, e^{-\beta H_N} \ldots \quad . \tag{1-9}$$

In equation (1-9), $z(\equiv \exp(\beta\mu))$ is the activity, μ is the chemical potential, $\mathcal{Z}$ is the grand partition function, H_N is the system total energy, and $\beta = 1/kT$.

Information on fluid structure can be obtained by considering the correlation between local number densities. A convenient measure of this correlation is the density-density time-correlation function, also referred to as the van Hove (15) function, $G(\vec{r};t)$,

$$G(\vec{r};t) = \frac{1}{\rho} \quad <\rho(\vec{o};o) \; \rho(\vec{r};t)> \quad , \tag{1-10}$$

where ρ is the macroscopic number density. The quantity $G(\vec{r};t)$ measures the extent to which $\rho(\vec{r};t)$ is affected by the local number density at the origin, $\rho(\vec{o};o)$. To understand the concept of density correlations, consider a molecule at the origin initially and pose the question "Given a molecule at the origin, how can this molecule affect the number density at a position $\vec{r}$ from the origin a time t later?" The influence this molecule has on the local number density at $(\vec{r};t)$ is achieved in one of two ways: (1) by direct diffusion from $(\vec{o};o)$ to $(\vec{r};t)$, and (2) by perturbing neighboring molecules about $(\vec{o};o)$ through the intermolecular potential, with this perturbation spreading to $(\vec{r};t)$. These two effects

can be separated mathematically with the substitution of equation (1-7) for the local number densities into equation (1-10) for $G(\vec{r};t)$, with the result

$$G(\vec{r};t) = G_s(\vec{r};t) + G_d(\vec{r};t) \ , \tag{1-11}$$

where

$$G_s(\vec{r};t) \equiv \frac{1}{\rho} \cdot \langle \sum_{i=j} \sum \delta(\vec{o}-\vec{q}_i(o)) \ \delta(\vec{r}-\vec{q}_j(t)) \rangle$$

and (1-12)

$$G_d(\vec{r};t) \equiv \frac{1}{\rho} \cdot \langle \sum_{i\neq j} \sum \delta(\vec{o}-\vec{q}_i(o)) \ \delta(\vec{r}-\vec{q}_j(t)) \rangle \ .$$

Here, $G_s(\vec{r};t)$ represents the contribution of self diffusion to $G(\vec{r};t)$ and is referred to as the self correlation function; $G_d(\vec{r};t)$, called the distinct correlation function, is that part of $G(\vec{r};t)$ due to perturbation effects.

Equation (1-11) is related to the static pair correlation function by

$$G(\vec{r};t=o) = \delta(\vec{r}) + \rho g(r) \tag{1-13}$$

for the special case t=o, where

$$g(r) = \frac{1}{\rho^2} \ \langle \sum_{i\neq j} \sum \delta(\vec{r}-\vec{q}_{ij}(o)) \rangle \ . \tag{1-14}$$

Here, $\vec{q}_{ij}(o)$ is the separation between molecules i and j,

$$\vec{q}_{ij}(o) = \vec{q}_i(o) - \vec{q}_j(o).$$

From the previous discussion of the local number density, it is apparent that g(r) is the ratio of the local number density at a distance r from

a central molecule to the macroscopic number density ρ, and is a measure of the time-average, or static, microstructure of the system.

The mean number of molecules observed in a volume $d\vec{r}$ at a distance r from a central molecule will not be, in general, simply $\rho\, d\vec{r}$, because the presence of this central molecule itself perturbs its immediate environment. For example (16), if the molecules of a fluid are hard spheres of diameter r_o, then no other molecules would be found at distances $r<r_o$. Or, if the intermolecular potential is of the Lennard-Jones type, there would be a tendency for other molecules to accumulate at a distance near the minimum in the potential well. In any case, at large separations, where the influence of the central molecule is negligible, the mean number of molecules, $\rho\, d\vec{r}$, would be approached. Figure 1-1 illustrates these qualitative features for a dilute gas at some fixed T and ρ. The general time-dependent case is shown in Figure 1-2. In Figure 1-2, the time τ_o is a relaxation time for the fluid structure (17).

1.3 Connection with Experiment

Since $G(\vec{r};t)$ is a microscopic property, this function cannot be obtained by direct thermodynamic measurements. Fortunately, $G(\vec{r};t)$ can be deduced from radiation scattering experiments.

Consider an incident beam of radiation on an atom, as shown in Figure 1-3. Quantum mechanics states that wave properties, as well as particle properties, can be assigned to the radiation. Specifically, there is a wavelength, λ, and a wave vector, $\vec{k}$,

$$\lambda = \frac{h}{|\vec{p}|}\ , \qquad \vec{k} = \frac{\vec{p}}{h}\ , \tag{1-15}$$

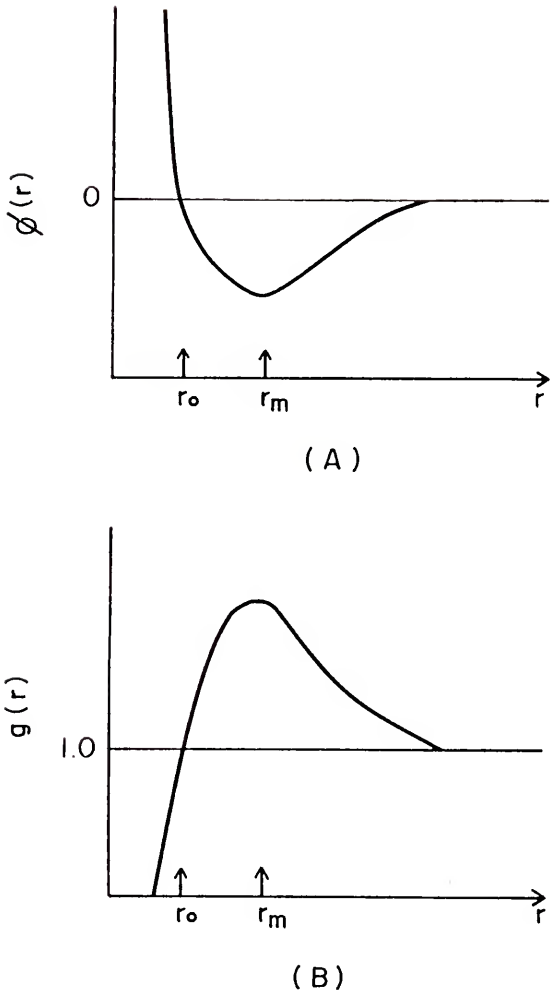

Figure 1-1. The relationship between the pair potential, $\phi(r)$, and $g(r)$ for a dilute gas; r is the distance of separation between two atoms.

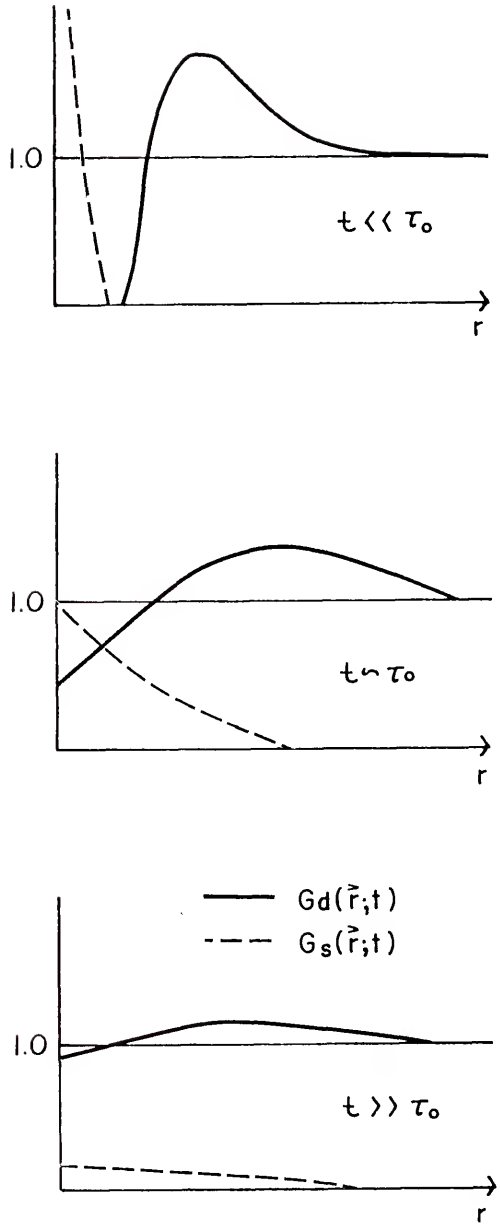

Figure 1-2. Qualitative behavior of the self (G_s) and distinct (G_d) time correlation functions for various times; τ_o is a relaxation time for the fluid structure (17).

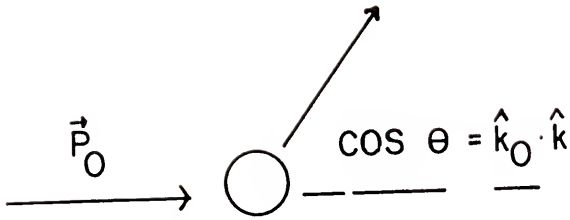

PARTICLE

$$E_0 = \frac{P_0^2}{2m}$$

WAVE

$$\lambda = \frac{\hbar}{|\vec{P}|}$$

$$\vec{k} = \frac{\vec{P}}{\hbar}$$

$$\omega_0 = \frac{E_0}{\hbar}$$

ENERGY CHANGE : $\hbar\omega = E_0 - E$

MOMENTUM CHANGE : $\vec{Q} = \vec{k}_0 - \vec{k}$

Figure 1-3. Incident and scattered radiation.

associated with radiation. The scattering of radiation by matter will involve the distribution of atomic positions, i.e., G(r;t), if the wavelength of the radiation is on the order of the magnitude of the interatomic spacing. If a beam of radiation falls on a sample and wavelets scattered by different atoms have similar amplitudes and phases, then the scattering waves will interfere and the sample acts as a diffraction grating (17). In this case the distribution of scattered intensity contains information on the distribution of atoms in the fluid. Almost any kind of radiation may be used for such experiments - electromagnetic (X-ray, light), electron, neutron, etc. Differences arise due to the differences in the scattering properties of single atoms for each kind of radiation. Table 1-1 (17) shows that neutrons have simpler scattering properties (they do not interact with the electron cloud, only with the nucleus) than the other types of radiation, since they are essentially scattered by a point source.

The usefulness of a given type of radiation depends upon its wavelength and energy and the ease with which these quantities can be determined. Table 1-2 (17) summarizes some data concerning neutrons, electrons and several kinds of electromagnetic radiation. Since the spacing between atoms is on the order of several Angstroms, and the potential well depth is 10^{-1}eV to 10^{-2}eV, the ideal choice of wavelength and energy transfer would be of this order. Examination of Table 1-2 shows that one or the other requirement is satisfied for each case listed, but neutrons are the only form of radiation for which both criteria are satisfied.

The ideal way to discuss neutron scattering is to formulate equations that model the physical process (see Figure 1-4): incident

TABLE 1-1

SCATTERING PROPERTIES OF VARIOUS TYPES OF RADIATION (17)

Radiation	Scattering Center	Size of Scattering Center Relative to Size of Atom
Electromagnetic	Electron density	1
Electrons	Charge density	1
Neutrons	Nucleus	0

TABLE 1-2

WAVELENGTH AND ENERGY OF VARIOUS TYPES OF RADIATION (17)

Radiation	Wavelength, Å	Energy Change*, eV
Electrons	∿0.1	Wide
X-Ray	0.5-2.0	Wide
Light (Raman)	4000	$\sim 10^{-1}$
Light (Brillouin)	4000	$\sim 10^{-5}$
Neutrons	1-10	10^{-1}-10^{-3}

*Indicates the experimentally accessible energy transfer range.

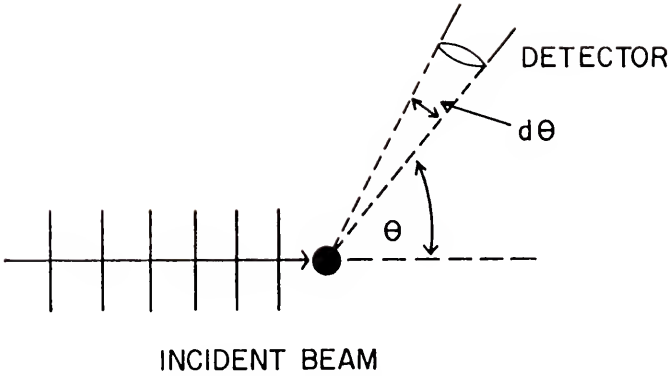

(A)

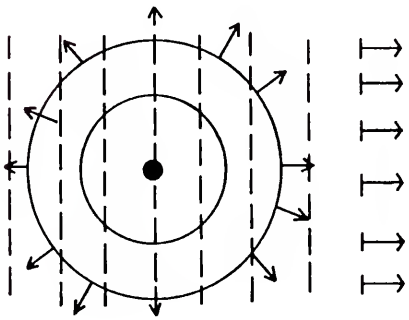

(B)

Figure 1-4. Schematic diagram of the scattering process. The incident (A) and scattered (B) beams are shown as viewed at large distances from the scattering center.

particles, described by a wave packet, approach the target atoms. There follows an interaction with the target atoms, and finally we see two wave packets: the unscattered part of the beam continues in the forward direction, and the scattered particles fly off at some angle. The wave equation describing the scattering for free atoms is

$$(\nabla^2 + k^2)\ \psi(r) = \frac{2m^*}{\hbar^2}\ V(r)\ \psi(r)\ , \tag{1-16}$$

where k is the neutron wave number, $\psi(r)$ is the wave function of the neutron, and V(r) is the scattering potential. The reduced mass, m^*, is defined by

$$m^* \equiv \frac{m_a}{1 + A}\ , \tag{1-17}$$

where m_a is the mass of the atom and A is the ratio of atomic to neutron masses. The solution to equation (1-16), which has the correct boundary condition, may be shown (18) to be

$$\psi(r) = e^{i\vec{k}_o\cdot\vec{r}} - \frac{m^*}{2\pi h^2}\int d\vec{r}\,'\ \frac{e^{ik|\vec{r}-\vec{r}\,'|}}{|\vec{r}-\vec{r}\,'|}\ V(r\,')\ \psi(r\,')\ . \tag{1-18}$$

Here, $\vec{k}_o$ is the wave vector of the incident neutron. Since the scattered neutrons are observed at large distances from the scattering center, only the asymptotic form of $\psi(r)$ is required. Use of the Born approximation, i.e., replacing $\psi(r\,')$ with $\exp(i\vec{k}_o\cdot\vec{r}\,')$, results in

$$\psi(r)_{r\to\infty} = e^{i\vec{k}_o\cdot\vec{r}} - \frac{e^{ikr}}{r}\ [\frac{m^*}{2\pi h^2}\int d\vec{r}\,'e^{i(\vec{k}_o-\vec{k})\cdot\vec{r}\,'}\ V(r\,')]\ . \tag{1-19}$$

We see from equation (1-19) that the solution, $\psi(r)_{r\to\infty}$, is the sum of an incident and a scattered wave, and the scattering amplitude, $f(\theta)$, can be identified as

$$f(\theta) = -\frac{m^*}{2\pi h^2}\int d\vec{r}' \; e^{i(\vec{k}_o-\vec{k})\cdot\vec{r}'} \; V(r') \; , \tag{1-20}$$

with the required cross-section being simply

$$\sigma(\theta) = |f(\theta)|^2 \quad . \tag{1-21}$$

Because the nucleus is almost a point scatterer, Fermi (19) approximated V(r) by

$$V(r) \sim \frac{2\pi h^2}{m^*} \; a \; \delta(r) \; , \tag{1-22}$$

where the constant, a, is called the "scattering length". It is easily seen that the substitution of equation (1-22) into equation (1-20) gives a free-atom scattering cross-section of $4\pi a^2$. For convenience, a scattering length, b, for a "bound atom", is normally used in equation (1-22) in order to introduce the neutron mass, m_n, in place of the reduced mass. This bound atom scattering length is related to the free-atom scattering length through equation (1-23):

$$b = a\left(\frac{1+A}{A}\right) \quad . \tag{1-23}$$

In general the nucleus will have a non-zero spin, I, and the partial wave analysis (17) of the scattering process shows that because of small angular momentum of the neutron for $\lambda \sim 1\mathring{A}$, only s waves contribute. Thus, there are two possible spin states $(I + \frac{1}{2}, I - \frac{1}{2})$, and the scattering lengths of the two spin states will be different (a_+, a_-).

The above discussion has thus far been limited to the scattering of neutrons by a free-atom. In general, however, we must consider the contribution of a collection of atomic nuclei to the scattering

process. The total scattering cross-section is simply

$$\sigma = \sigma_{coh} + \sigma_{incoh} , \tag{1-24}$$

where σ_{coh}, the coherent cross-section, is that contribution to σ due to the interference of waves scattered by different nuclei, and the incoherent cross-section, σ_{incoh}, is that part of σ in which interference between the scattered waves does not occur.

The quantity measured experimentally is the differential scattering cross-section, $\frac{d^2\sigma}{d\Omega d\omega}$, the number of neutrons scattered into a solid angle $d\Omega$ having an energy change $\hbar d\omega$, with

$$\hbar\omega \equiv E_o - E \quad . \tag{1-25}$$

If there is no correlation between the nuclear spins themselves, or between the nuclear spins and particle positions, then

$$\frac{d^2\sigma}{d\Omega d\omega} = \frac{k}{k_o} \left[b^2_{coh} \, S(Q,\omega) + b^2_{incoh} \, S_s(Q,\omega) \right] , \tag{1-26}$$

where $\hbar\vec{Q}$ is the momentum change

$$\hbar\vec{Q} = \hbar(\vec{k}_o - \vec{k}), \tag{1-27}$$

$S(Q,\omega)$ is related to the density-density time-correlation function, $G(\vec{r};t)$, through equation (1-3), and $S_s(Q,\omega)$ is the self-contribution:

$$S_s(Q,\omega) = \int_{-\infty}^{+\infty} dt \; e^{i\omega t} \int d\vec{r} \; e^{-i\vec{Q}\cdot\vec{r}} \; G_s(\vec{r};t) \quad . \tag{1-28}$$

For spin-dependent scattering lengths the differential cross-section may be separated experimentally into the two components in equation (1-28) by recording those neutrons that are depolarized upon scattering, thus enabling $S_s(Q,\omega)$ to be measured separately (17).

CHAPTER 2

STATIC CORRELATIONS IN SIMPLE, DILUTE GASES

2.1 Introduction

In this chapter we consider the problem of obtaining information about intermolecular forces from experimental data on pair and triplet correlation functions for a low density gas. More precisely, numerical calculations on the static structure factor, as well as the pair correlation function, are presented for terms up to ρ^2 in the density expansion of g(r). Calculations are performed using the Barker potential for krypton and xenon, and the three-body contribution to the intermolecular potential is modeled using the Axilrod-Teller potential. Finally, the three-body correlation function is calculated (to first-order in the number density) and compared with the corresponding superposition approximation.

The theory of simple fluids, e.g., rare gases and liquid metals, is usually written in terms of a hierarchy of distribution functions. The simplest of these is the pair correlation function, g(r), which appears extensively in expressions for the thermodynamic properties. Because of its importance, there have been numerous theoretical attempts to calculate g(r) by closure of the hierarchy. These theories involve either an assumed form for the three-body correlation function or an implicit statement concerning it.

While important in the modeling of the pair distribution function, the triplet correlation function also contributes directly to the thermodynamic properties. Barker, Fisher and Watts (20) discuss this and show that with the addition of a triplet term, excellent agreement may be obtained with the measured pressure and energy of argon. They show that the three-body terms contribute 5% of the energy and about 50% of the observed pressure for argon at 100 K and a molar volume of 27 cm^3/mole. The size of this contribution varies with the state conditions, but the pressure contribution is always large, particularly near the triple point. Properties in which the triplet correlation function plays a significant part within the framework of the pair theory include the thermal expansion coefficient and the specific heat. In the pair theory these properties include a large contribution from the triplet correlation function and may not be calculated without a reasonable knowledge of that function (21).

The Fourier transformation of the pair correlation function, S(Q), can be measured through radiation scattering experiments. However, there is no similar method for measuring the triplet correlation function, since radiation scattering cross-sections are too small to give an appreciable sensitivity to the higher functions (10). To overcome this difficulty, Egelstaff and co-workers (14) proposed measuring the isothermal pressure derivative of the static structure factor and show that the first derivative is related to the three-point correlation function and higher derivatives to successively higher-order correlation functions. Using modern radiation scattering techniques Egelstaff et al. measured S(Q) for various liquids as a function of pressure at constant temperature, and differenced the data to obtain the isothermal pressure derivative (14).

An alternative to evaluating $g^{(s)}(q_1,\ldots,q_s)$, the s-particle correlation function, from the distribution function hierarchy (22) is the direct evaluation through equation (2-1):

$$\rho^s g^{(s)}(q_1,\ldots,q_S) \equiv \sum_{N\geq S}^{\infty} \frac{z^N}{h^{3N}(N-S)!} \frac{1}{Z} \int d\vec{q}_{S+1}\ldots d\vec{q}_N \, e^{-\beta U_N(q_1,\ldots q_N)}, \tag{2-1}$$

where Z is the configurational integral

$$Z \equiv \sum_{N\geq 0}^{\infty} \frac{z^N}{h^{3N}N!} \int d\vec{q}_1\ldots d\vec{q}_N \, e^{-\beta U_N(q_1,\ldots,q_N)} , \tag{2-2}$$

$g^{(s)}(q_1,\ldots,q_S)$ is a measure of the correlation between S molecules in a system containing N molecules, and $U_N(q_1,\ldots,q_N)$ is the total potential energy of the N molecules. Assuming a model for the interaction potential, the (Monte Carlo) procedure involves generating a set of configurations proportional to the Boltzmann factor, $\exp[-\beta U_N(q_1,\ldots,q_N)]$, and averaging over the configurations, with equal weight given to each configuration. For the purpose of calculating the total potential energy in any one configuration, it is convenient to separate $U_N(q_1,\ldots,q_N)$ into a sum of terms (23). This sum consists of those for all possible atom pairs ij, all possible triplets, ijk, all possible quadruplets ijkl, and so on, concluding with a final term for the simultaneous interaction of all N molecules:

$$U_N(q_1,\ldots,q_N) = \sum_{i<j} \phi_{ij} + \sum_{i<j<k} \phi_{ijk} + \ldots + \phi_{12\ldots N} . \tag{2-3}$$

The meaning of the terms in equation (2-3) is as follows (23):

> ϕ_{ij} is the mutual potential energy of the pair located at i and j and isolated from the influence of all other molecules,
>
> ϕ_{ijk} is the additional mutual potential energy of the trio located at i,j and k that arises from changes in the electron charge distributions of the isolated pair located at i and j when a third molecule is at location k,
>
> $\phi_{12\ldots N}$ is a potential energy increment, characteristic of the whole system, that is not included in the previous terms.

For the special case of a dilute gas one can proceed rigorously by expanding the correlation function, i.e., equation (2-1), in powers of the density, the form of the expansion being

$$g^{(s)}(q_1,\ldots,q_S) = g_0^{(s)}(q_1,\ldots,q_S) + \rho g_1^{(s)}(q_1,\ldots,q_S) + \ldots , \quad (2\text{-}4)$$

where $g_0^{(s)}$ is completely determined by the potential energy between S molecules, $\phi_{12\ldots S}$, $g_1^{(s)}$ involves the (S+1) particle potential energy, $\phi_{12\ldots S+1}$, as well as $\phi_{12\ldots S}$, and so on. The dependence of the correlation functions on the intermolecular forces for dilute gases is well defined so that one may proceed with some confidence in either direction: from knowledge of the intermolecular forces to the calculation of $g^{(s)}$, or from experimental measurements of the correlation functions, particularly the pair correlation function, to the estimation of the intermolecular potential. In this way, neutron scattering data on low density gases provide a powerful technique for the study of intermolecular forces.

In the next section the magnitudes of the contribution of three-body forces to the low density expansions of $g^{(2)}$ and S(Q) are calculated

to indicate their accessibility to measurement. In Section 2.3 the possibility of using neutron scattering to gain partial information about $g^{(3)}$ is indicated. The need for such information is shown by comparing the low density form of $g^{(3)}$ with the corresponding Kirkwood superposition approximation for pair potentials.

2.2 Two-Body Correlations

In this section the influence of two- and three-body potentials on the density expansion of g(r) is studied numerically. A similar expansion of the static structure factor, S(Q), enables one to identify the non-additive contribution to this experimentally accessible quantity.

A special case (s=2) of equation (2-1), the pair correlation function is defined in the grand canonical ensemble as

$$g(r) \equiv \frac{1}{\rho^2} \sum_{N\geq 3}^{\infty} \frac{z^N}{h^{3N}(N-2)!} \frac{1}{Z} \int d\vec{q}_3 \ldots d\vec{q}_N \, e^{-\beta U_N(\vec{q}_1, \ldots \vec{q}_N)} \quad . \tag{2-5}$$

The evaluation of g(r) becomes exact (in the sense that no approximation for the triplet correlation function is made in closing the hierarchy) in the limit of low density:

$$g(r) = g_0(r) + \rho g_1(r) + \ldots \, , \tag{2-6}$$

with the first two coefficients of the expansion being

$$g_0(r) = 1 + f_{12}$$

and

$$g_1(r) = (1+f_{12}) \int d\vec{q}_3 [f_{13}f_{23} + f_{123}(1+f_{13})(1+f_{23})] \, . \tag{2-7}$$

Here we have introduced the Mayer functions

$$f_{ij} \equiv e^{-\beta\phi_{ij}} - 1$$
$$f_{ijk} \equiv e^{-\beta\phi_{ijk}} - 1 \quad . \tag{2-8}$$

It is clear from equation (2-7) that $g_0(r)$ is a direct measure of the pair potential, ϕ_{ij}, $g_1(r)$ is a function of both ϕ_{ij} and the three-body potential, ϕ_{ijk}, and so on. Note that this expansion is analogous to the virial equation of state: the second virial coefficient depends entirely on the details of the pair potential ϕ_{12}, the third virial coefficient is determined by the three-body potential as well as ϕ_{12}, etc. A study of the three-body potential by Sherwood and co-workers (24) revealed that the third virial coefficient was indeed sensitive to non-additive contributions, as well as details of the two-body potential. However, since the equation of state is determined by integration of the pair correlation function over the distance of separation between two molecules, a study of g(r), as opposed to the virial coefficients, should prove a more sensitive test for models of the two- and three-body potentials.

Practical computations using the above theory require the assumptions of models for the pair and triplet potentials. For the simple gases, argon, krypton, and xenon, it is generally accepted that the pair potential is known with some precision. In particular, Barker and co-workers (12) give the following form for the two-body potential for xenon and krypton:

$$\phi_{ij}(r^*) = \varepsilon[u_0(r^*) + u_1(r^*)], \tag{2-9}$$

where

$$u_0(r^*) = \sum_{i=o}^{5} A_i (r^*-1)^i \, e^{\alpha(1-r^*)} - \sum_{i=o}^{2} \frac{c_{6+2i}}{r^{*6+2i}+\delta}$$

and (2-10)

$$u_1(r^*) = \begin{cases} 0 \quad , & r^* < 1 \\ [P(r^*-1)^4 + Q(r^*-1)^5 \, e^{\alpha'(1-r^*)}], & r^* > 1 \end{cases} .$$

In these expressions ε is the depth of the potential at its minimum and r^* is the intermolecular distance normalized to r_m, the distance at the minimum in the potential. The parameters were determined from a wide range of experimental data, including second virial coefficients, gas transport properties, solid-state data, spectroscopic information on dimers, and measurements of differential scattering cross-sections, and are tabulated in Table 2-1. All subsequent calculations are performed using this potential model, unless otherwise noted.

Figure 2-1 illustrates the behavior of the pair correlation function, using the first three terms in the density expansion for xenon at a reduced density ($\rho^* \equiv \rho r_m^3$) of unity. Although the series does not converge at this density, $\rho^* = 1$ was chosen in order to magnify the contributions of the second and third terms in the expansion.

A means of establishing the range of density for which the expansion of g(r) is applicable is by comparison of equation (2-6) with Monte Carlo calculations. This comparison is very valuable since it enables one to test the density expansion directly. The same potential model is used

TABLE 2-1

BARKER PAIR POTENTIAL (EQUATION (2-10)) PARAMETERS
FOR KRYPTON AND XENON (12)

Parameter	Krypton	Xenon
ε/k, K	201.9	281.0
r_m, Å	4.0067	4.3623
r_o, Å	3.580	3.890
A_o	0.23526	0.2402
A_1	-4.78686	-4.8169
A_2	-9.20	-10.90
A_3	-8.0	-25.0
A_4	-30.0	-50.7
A_5	-205.8	-200.0
C_6	1.0632	1.0544
C_8	0.1701	0.1660
C_{10}	0.0143	0.0323
α	12.50	12.50
δ	0.010	0.010
P	-9.0	59.3
Q	68.67	71.1
δ'	12.5	12.5
n	0.0269	0.0361

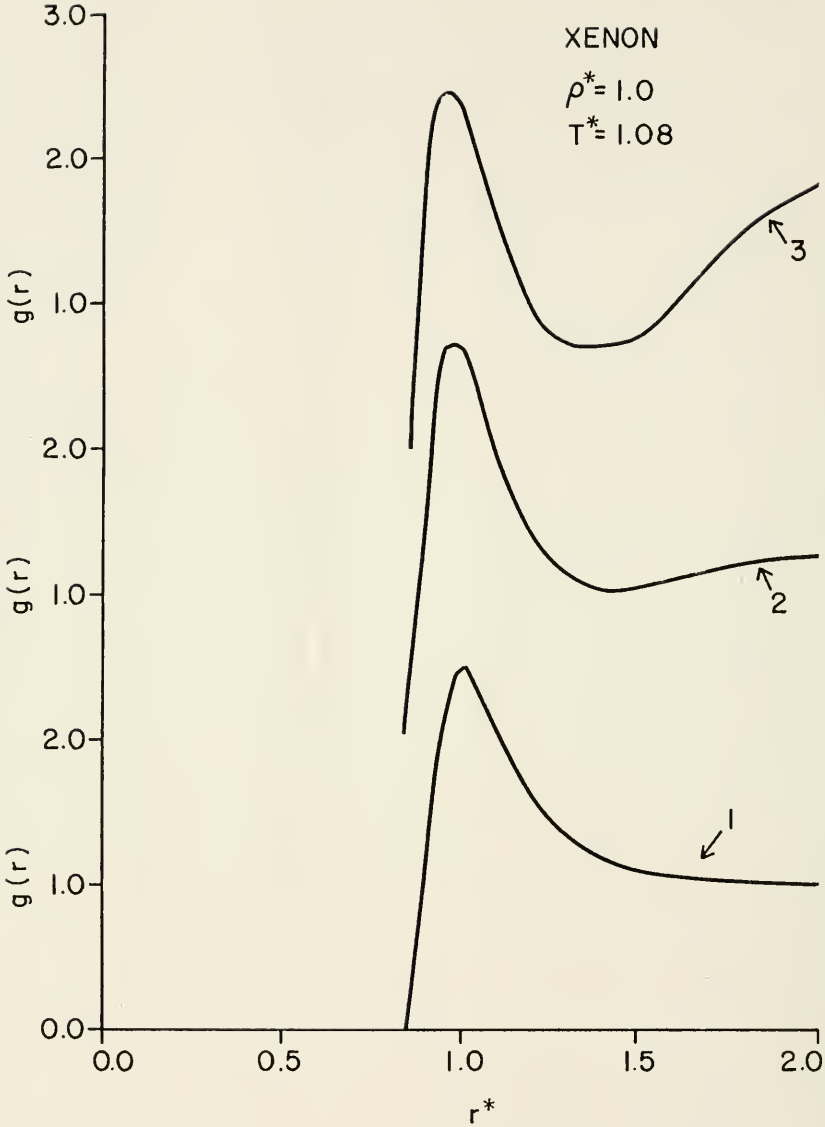

Figure 2-1. Term-by-term comparison of g(r) for xenon assuming pairwise additivity of the potential. The curves labeled 1, 2 and 3 are for terms up to and including g_o, g_1 and g_2 in equation (2-6), respectively; $\rho^* = \rho r_m^3 = 1.0$.

in both the Monte Carlo calculations and the theory so that the comparison tests only the range of convergence of the expansion. Figure 2-2 compares the "exact", i.e., Monte Carlo (25), value of $g(r^*=1)$ with the corresponding density expansion for krypton at 303 K. Terms up to and including $g_2(r)$ were used in the virial calculation (26), and pairwise additivity of the potential energy was assumed. As is evident from the figure, deviations (greater than $\pm$ 2%) from unity become appreciable at a reduced density of 0.40 for krypton at 303 K.

In using experimental data to determine pair potentials it is essential to take account of many-body interactions. In the case of simple gases, Barker _et al_. (12) found that satisfactory agreement[1] between calculated and experimental properties were obtained by including only the third-order triple-dipole (Axilrod-Teller) three-body dispersion interaction,

$$\phi_{123} = \nu \frac{(1 + 3\cos\theta_1\cos\theta_2\cos\theta_3)}{r_{12}^3\, r_{13}^3\, r_{23}^3} , \qquad (2\text{-}11)$$

where the separations r_{ij} and angles θ_i are identified in Figure 2-3. As shown in Figure 2-4, the effect of the triplet dispersion potential on $g_1(r)$ is appreciable for separations $r \sim r_m$.

Experimental information on the pair correlation function, and hence the intermolecular forces, can be obtained through neutron

---

[1] In a study of the three-body potential, Sherwood and co-workers (24) found that satisfactory agreement between theory (assuming a Lennard-Jones 12-6 potential) and experiment for the third virial coefficient could be achieved only by including, in addition to the dispersion contribution, a repulsive contribution for non-additivity. It is important to note that models chosen for the non-additive potential are extremely sensitive to the details of the pair potential.

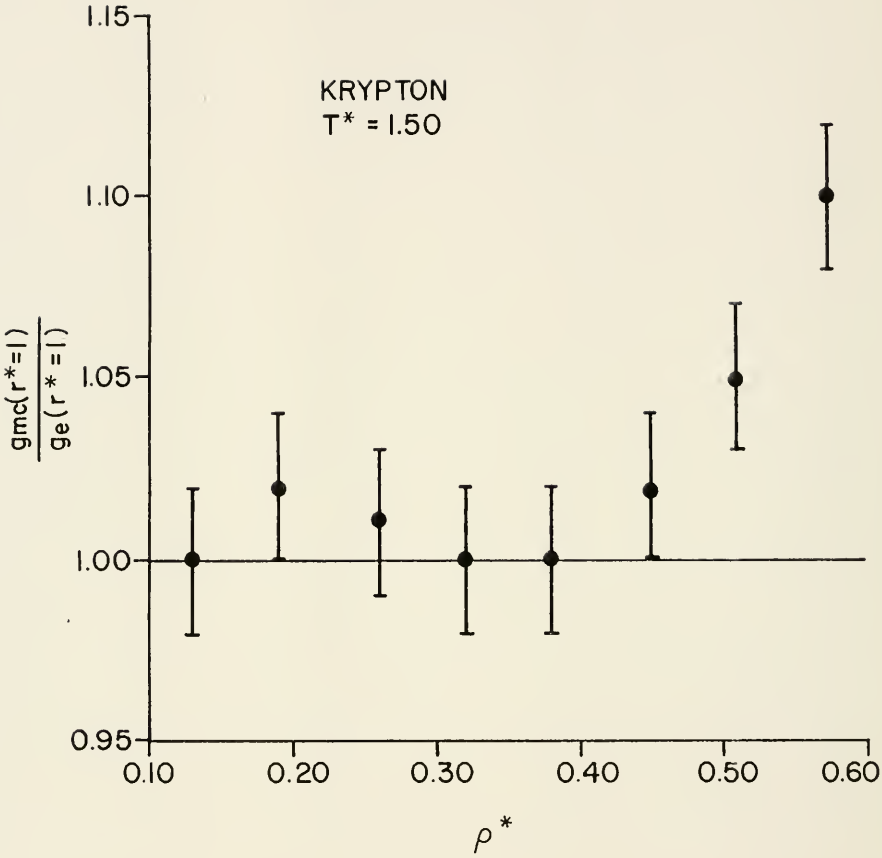

Figure 2-2. Comparison of the Monte Carlo (g_{MC}) calculation of g(r) with equation (2-6) (g_e) for krypton. Pairwise additivity of the potential was assumed, and terms up to and including g_2 were used in calculating g_e. For $\rho^* \leq 0.4$, three terms are sufficient for agreement (estimated error: ±2%) with the MC calculations at $r^* = r/r_m = 1$; $T^* = kT/\varepsilon$.

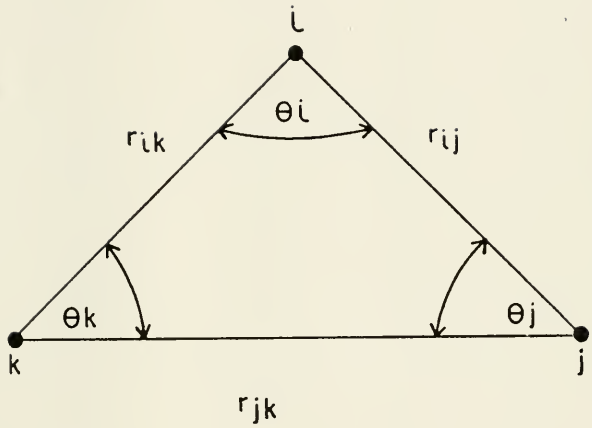

Figure 2-3. Spatial configuration of molecules i,j, and k.

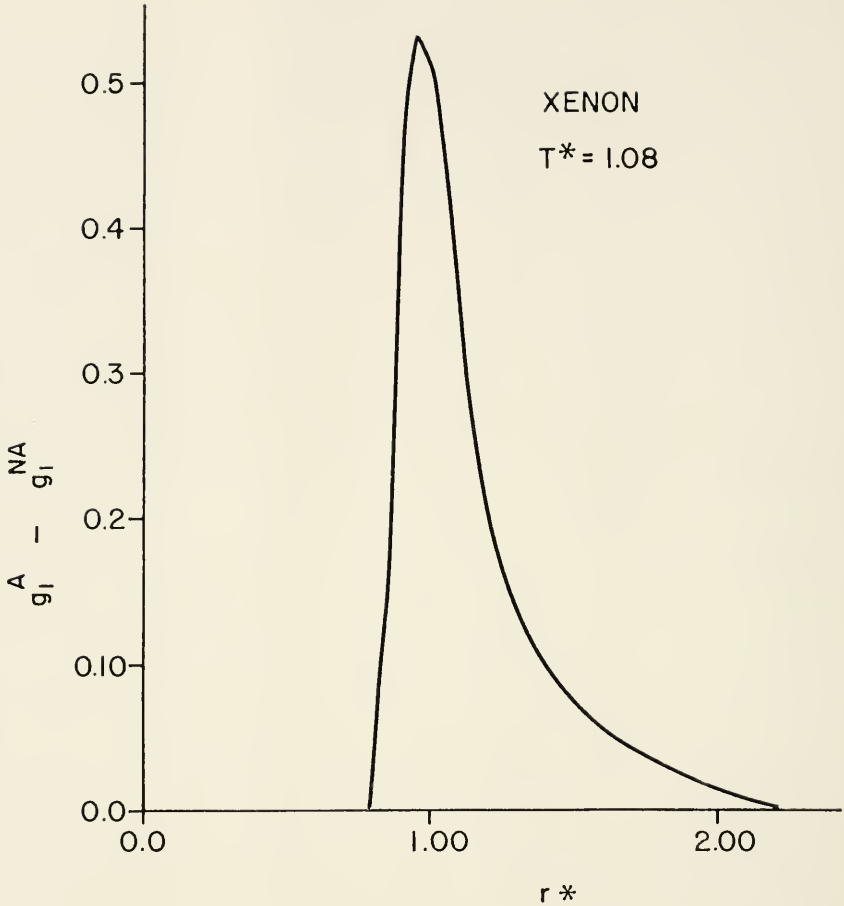

Figure 2-4. Influence of the Axilrod-Teller three-body potential on $g_1(r)$ for xenon; g_1^A, g_1^{NA}, are the values of $g_1(r)$ assuming pairwise additivity and non-additivity (equation (2-11)), respectively; $r^* = r/r_m$, $T^* = kT/\varepsilon$.

scattering or x-ray diffraction measurements, and is contained in the static structure factor, S(Q),

$$S(Q) = 1 + \rho \int d\vec{r}\, e^{i\vec{Q}\cdot\vec{r}}\, [g(r)-1] \ . \qquad (2\text{-}12)$$

An expansion of S(Q) in density is obtained upon substitution of equation (2-6) for g(r) into equation (2-12), and is given below for completeness:

$$S(Q) = 1 + \rho S_1(Q) + \rho^2 S_2(Q) + \ldots \ , \qquad (2\text{-}13)$$

where the coefficients in the expansion are easily identified in terms of g_0, g_1, etc.:

$$\begin{aligned} S_1(Q) &= \int d\vec{r}\, e^{-i\vec{Q}\cdot\vec{r}}\, [g_0(r)-1] \ , \\ S_2(Q) &= \int d\vec{r}\, e^{-i\vec{Q}\cdot\vec{r}}\, g_1(r) \ , \end{aligned} \qquad (2\text{-}14)$$

and so on. Figure 2-5 illustrates the behavior of S(Q), using the first four terms (i.e., up to and including $S_3(Q)$) in the expansion, for xenon at a reduced density of unity. Again, the series does not converge at $\rho^* = 1$, but this density was chosen to magnify the contributions from the terms proportional to the density. As indicated in Figure 2-5, the greatest contribution of the higher-order terms occurs at small Q ($Q<1.5\text{Å}^{-1}$). A similar trend is observed in Figure (2-6) for a reduced density corresponding to one of the experimental state conditions (i.e., $\rho^* = 0.188$). Finally, the effect of non-additivity on $S_2(Q)$ is shown in Figure 2-7, where it is observed that the major contribution of non-additivity occurs at a momentum transfer of unity.

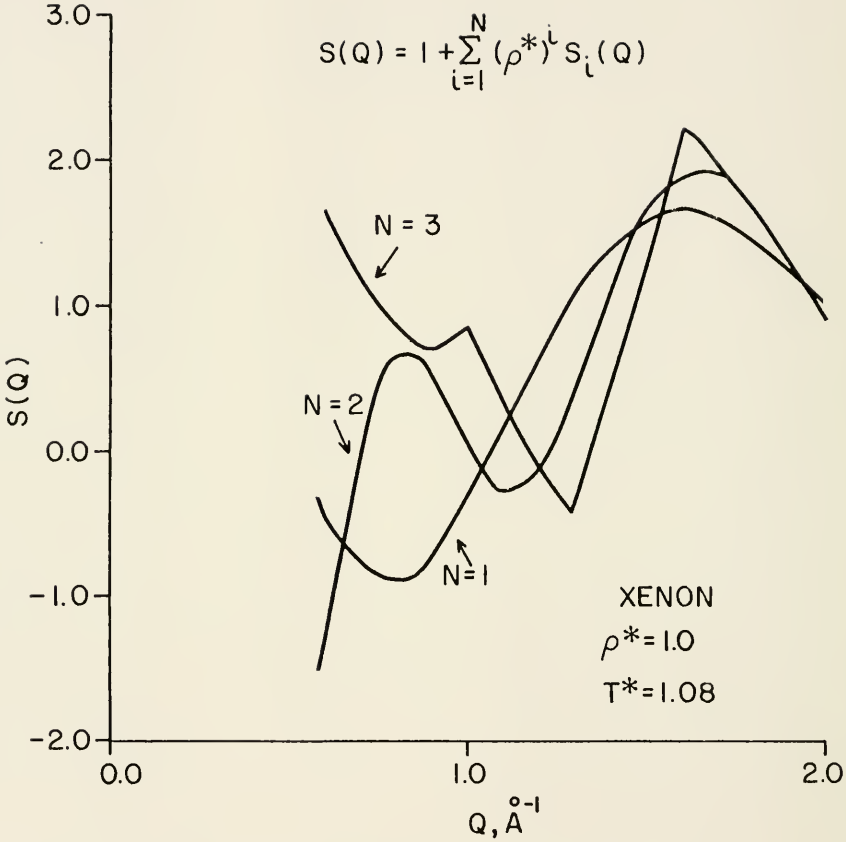

Figure 2-5. Term-by-term comparison of S(Q) for xenon assuming pairwise additivity of the potential. The curves labeled 1, 2, and 3 are for terms up to and including S_1, S_2, and S_3 in equation (2-13), respectively; $\rho^* = \rho r_m^3 = 1.0$.

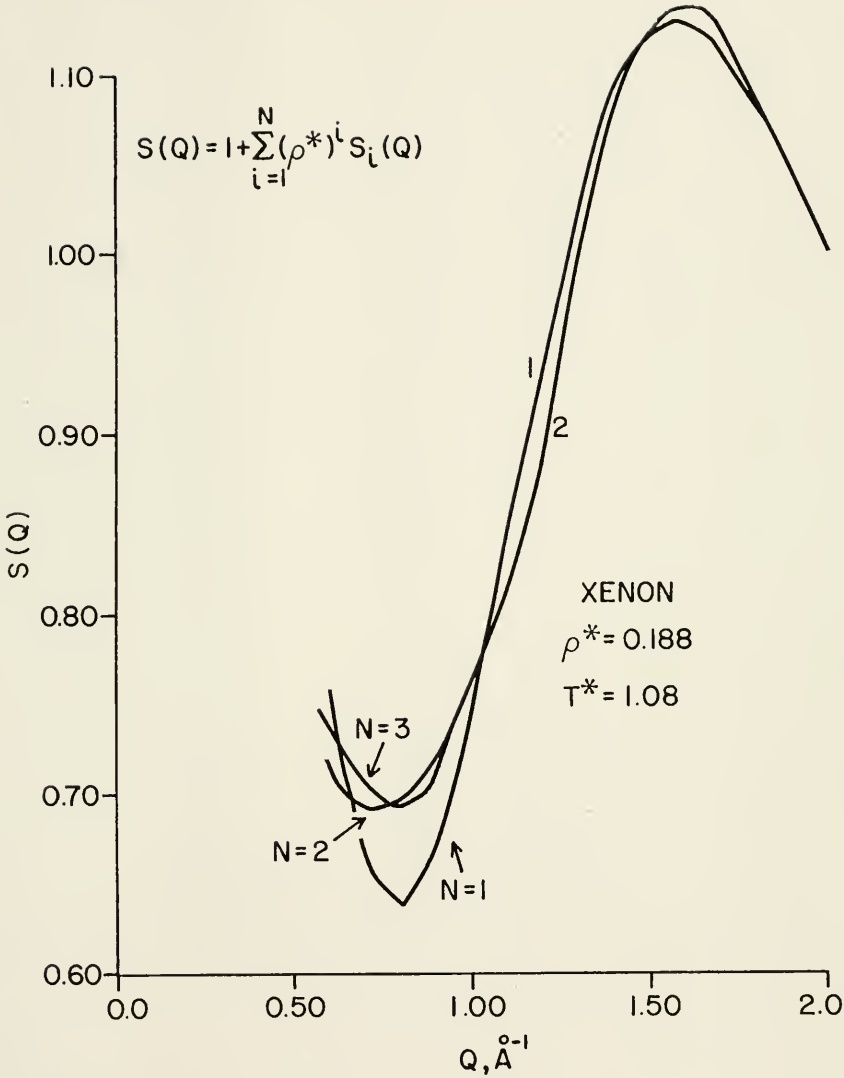

Figure 2-6. Term-by-term comparison of S(Q) for xenon assuming pairwise additivity of the potential. The curves labeled 1,2, and 3 are for terms up to and including S_1, S_2, and S_3 in equation (2-13), respectively; $\rho^* = \rho r_m^3 = 0.188$.

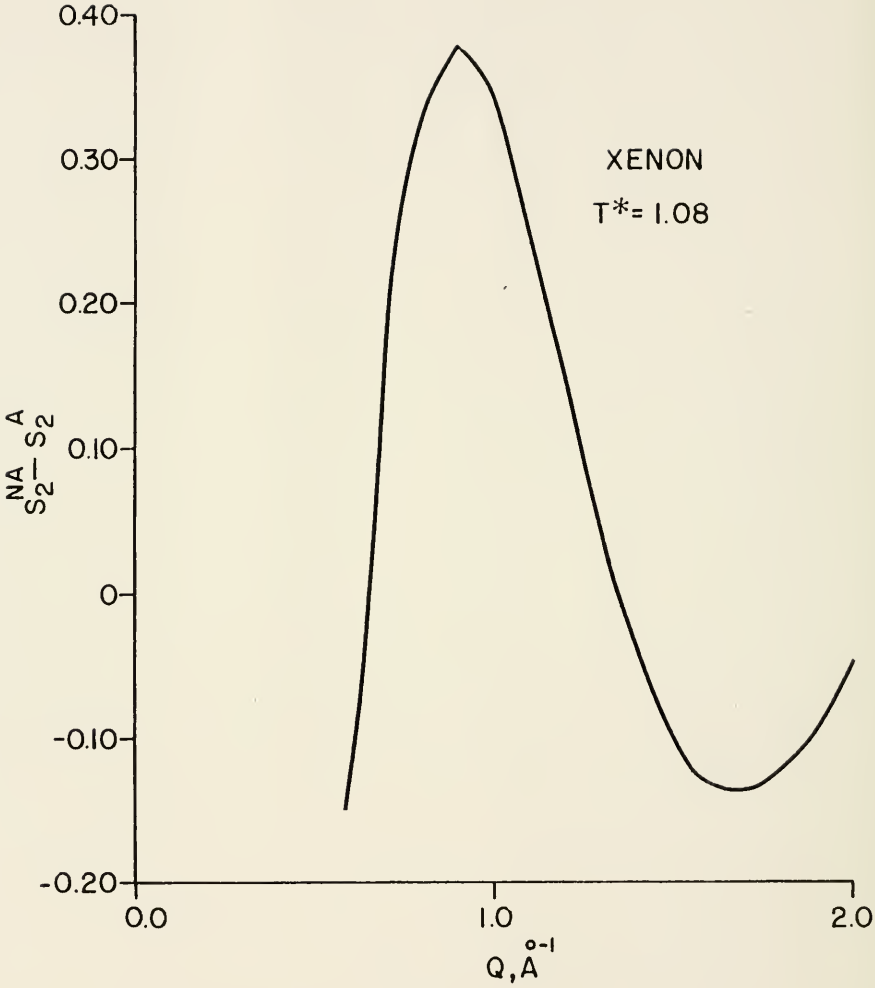

Figure 2-7. Influence of the Axilrod-Teller three-body potential on $S_1(Q)$ for xenon; S_1^{A} , S_1^{NA} are the values of $S_1(Q)$ assuming pairwise additivity and non-additivity (equation (2-11)), respectively.

The results of this section indicate that higher-order terms in the density expansion of S(Q), i.e., $S_2(Q)$, $S_3(Q)$, and so on, do not contribute significantly beyond the first peak in the static structure factor. This is particularly evident in Figure 2-8, a plot of $(S(Q)-1)/\rho^*$ as a function of Q for the upper ($\rho^* = 0.380$) and lower ($\rho^* = 0.156$) densities covered experimentally (see Chapters 5 and 6). Since details of the three-body potential are contained in $S_2(Q)$, it is apparent that precise measurements of S(Q) in the region of $Q = 1.0\text{Å}^{-1}$ are necessary to study the triplet potential experimentally.

2.3 The Triplet Correlation Function

We have indicated the importance of the pair correlation function in predicting thermodynamic properties of equilibrium systems, and the importance of the triplet correlation function in modeling g(r) is established through equation (2-15):

$$kT \frac{\partial g}{\partial \vec{r}_1} + g(r) \frac{\partial \phi_{12}}{\partial \vec{r}_1} + \rho \int d\vec{r}_3 \frac{\partial \phi_{13}}{\partial \vec{r}_1} g^{(3)}(r_1, r_2, r_3) = 0. \qquad (2\text{-}15)$$

Conventional neutron scattering or X-ray diffraction experiments provide a direct measurement of the pair correlation function. Unfortunately, there is no similar method for measuring the triplet correlation function. However, $g^{(3)}$ is related to the pair correlation function through the isothermal pressure derivative (27)

$$\rho kT \left.\frac{\partial g}{\partial P}\right|_T = 2g(r) + \rho \int d\vec{s}[g^{(3)}(r,s) - g(r)] \quad , \qquad (2\text{-}16)$$

so that $g^{(3)}$ is indirectly measured through the isothermal pressure derivative of the static structure factor. Although equation (2-16)

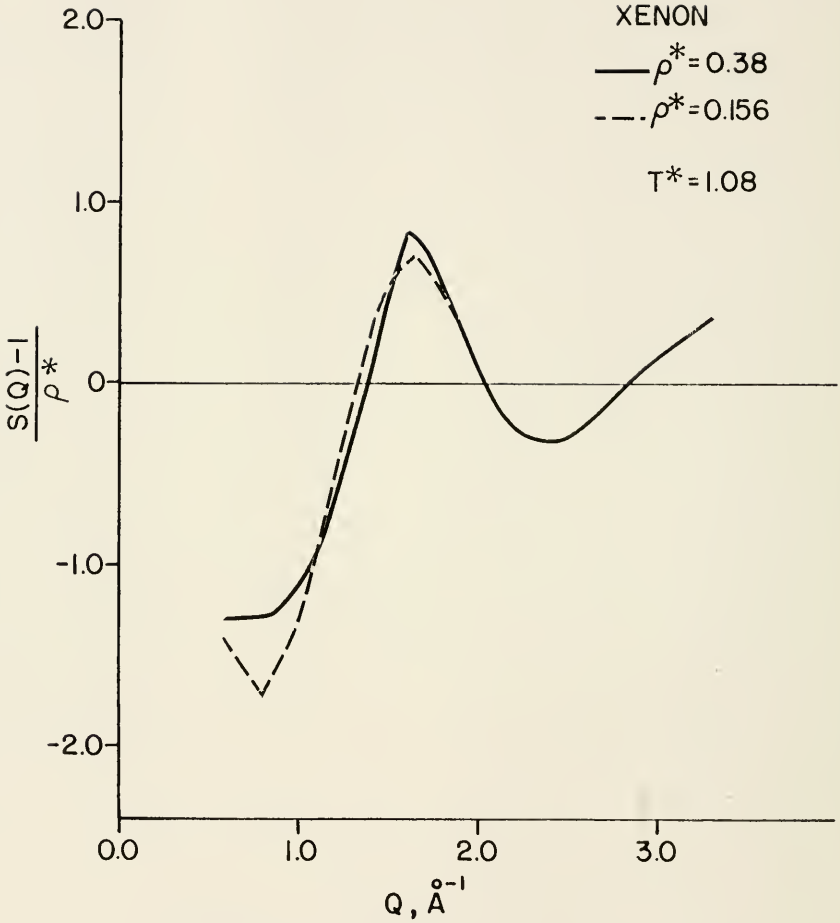

Figure 2-8. Plot of $(S(Q)-1)/\rho^*$ for xenon as a function of Q for the higher (——, $\rho^* = 0.38$) and lower (---, $\rho^* = 0.156$) densities covered experimentally; $\rho^* = \rho r_m^3$, $T^* = kT/\varepsilon$.

cannot be solved exactly for $g^{(3)}$, it does provide a useful guide for modeling the triplet function when coupled with experimental data on $\frac{\partial S(Q)}{\partial P}$. In this section the low density form of the triplet correlation function is calculated and compared with the associated Kirkwood superposition approximation, thereby illustrating the difficulty of modeling such functions.

For a dilute gas, no approximation for $g^{(3)}$ is necessary, and the three-point correlation function becomes

$$g^{(3)}(q_1,q_2,q_3) = g_0^{(3)}(q_1,q_2,q_3) + \rho g_1^{(3)}(q_1,q_2,q_3) + \ldots , \quad (2\text{-}17)$$

where the coefficients in the density expansion are

$$g_0^{(3)}(q_1,q_2,q_3) = (1+f_{12})(1+f_{13})(1+f_{23})$$

and

$$g_1^{(3)}(q_1,q_2,q_3) = (1+f_{12})(1+f_{13})(1+f_{23}) \int d\vec{q}_4 \; [f_{14}f_{24}f_{34} \quad (2\text{-}18)$$

$$+ f_{24}f_{34} + f_{14}f_{24} + f_{14}f_{34} + f_{24} + f_{34} - f_{14}] \quad .$$

In identifying $g_0^{(3)}$ and $g_1^{(3)}$, pairwise additivity of the potential energy was assumed. The integral in equation (2-18) for $g_1^{(3)}$ was evaluated using a Monte Carlo technique. The Monte Carlo method was chosen over other integration routines because of its simplicity and rapid convergence. A test of the convergence of $g_1^{(3)}$ is shown in Figure 2-9, where N is the number of configurations generated by the Monte Carlo procedure.

A frequently used approximation for the triplet correlation function is Kirkwood's superposition approximation for $g^{(3)}$,

$$g^{(3)}(q_1,q_2,q_3) = g(q_1,q_2)g(q_1,q_3)g(q_2,q_3) \quad . \quad (2\text{-}19)$$

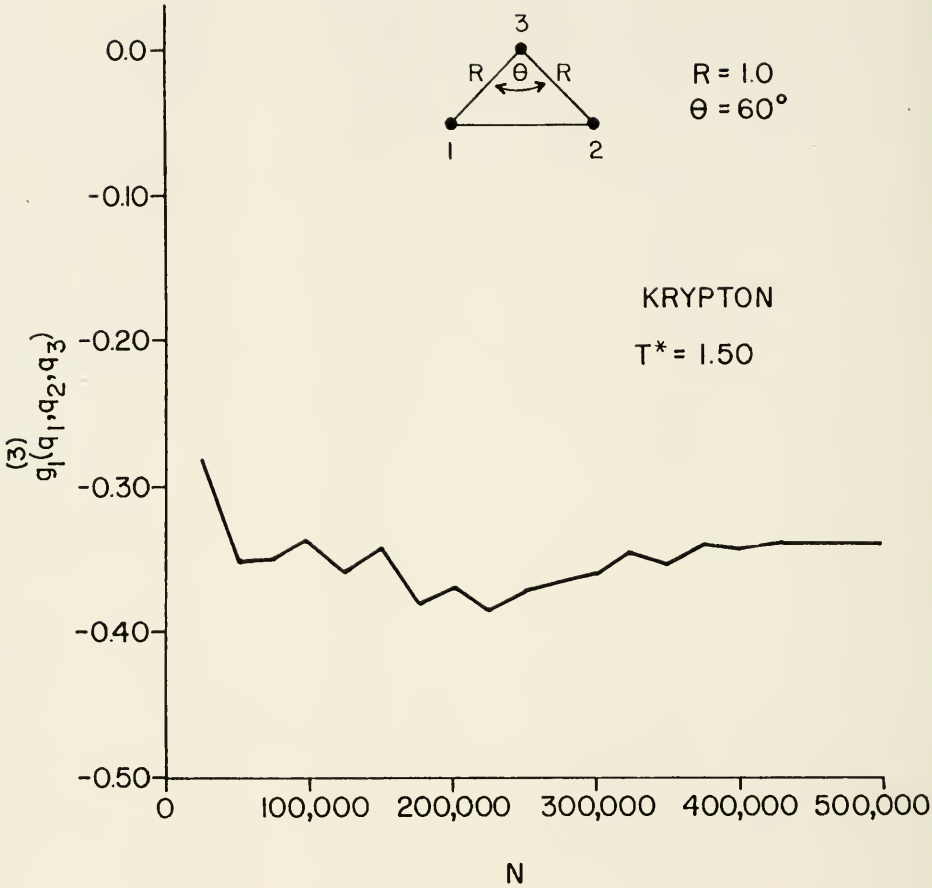

Figure 2-9. Test of the convergence of $g_1^{(3)}$ for krypton; N is the number of configurations generated by the Monte Carlo procedure.

Substitution of the density expansion for the pair correlation function into equation (2-19) results in the following density expansion of the superposition approximation:

$$g_{SA}^{(3)}(q_1,q_2,q_3) = g_{SA,0}^{(3)}(q_1,q_2,q_3) + \rho g_{SA,1}^{(3)}(q_1,q_2,q_3) + \ldots , \quad (2\text{-}20)$$

where the subscript "SA" denotes the superposition approximation, and the corresponding coefficients in the expansion are

$$g_{SA,0}^{(3)}(q_1,q_2,q_3) = g_0^{(3)}(q_1,q_2,q_3)$$

and (2-21)

$$\begin{aligned} g_{SA,1}^{(3)}(q_1,q_2,q_3) = {} & g_0(q_1,q_2)\ g_0(q_1,q_3)\ g_1(q_2,q_3) \\ & + g_1(q_1,q_2)\ g_0(q_1,q_3)\ g_0(q_2,q_3) \\ & + g_0(q_1,q_2)\ g_1(q_1,q_3)\ g_0(q_2,q_3) \ . \end{aligned}$$

It is apparent that the superposition approximation becomes exact in the limit of zero density. Figure 2-10 compares the superposition approximation for $g^{(3)}$ with that predicted by equation (2-17) for a reduced density of unity. The three-particle configuration is indicated in Figure 2-10. Although the superposition approximation gives the correct zero-density limit, the second-order term, $g_{SA,1}^{(3)}$, is clearly inconsistent with the direct numerical evaluation of $g_1^{(3)}$. Again note that a reduced density of unity was chosen to magnify the discrepancy between the two expressions.

A study of the pressure derivative of Monte Carlo results for the pair correlation function provides another test of models for the three-point function. Comparisons of this type can be extremely

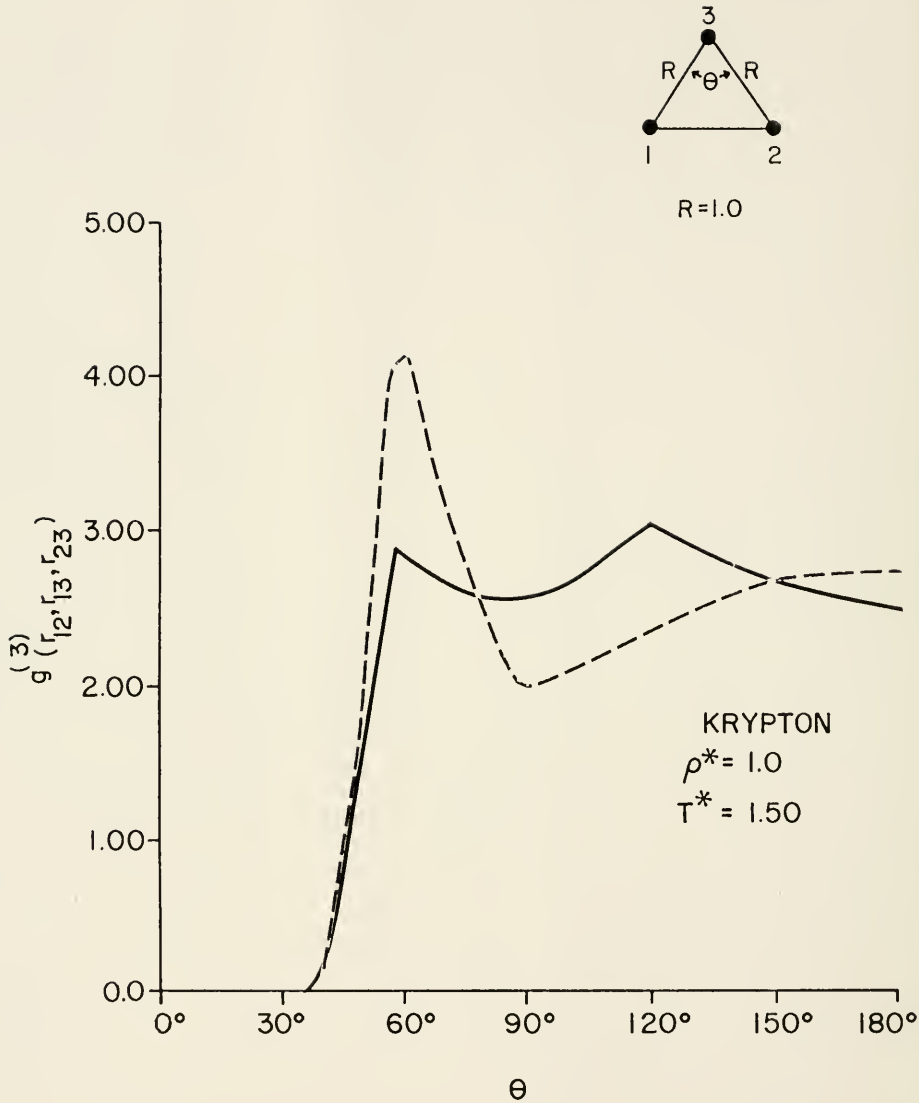

Figure 2-10. Comparison of the superposition approximation for $g^{(3)}$ (---, equation 2-20) with that predicted by equation (2-17) (——) for terms up to and including $g_1^{(3)}$; $\rho^* = \rho r_m^3 = 1.0$.

valuable since the nature of the intermolecular potential is known exactly. Figure 2-11 illustrates the behavior of $\frac{\partial g(r)}{\partial P}$, obtained by differentiating the Monte Carlo results of Verlet (28) for a dense system of Lennard-Jones atoms. Recently, Egelstaff, Page, and Heard (22) have compared several models for the triplet correlation function with experimental measurements of $\frac{\partial S(Q)}{\partial P}$ for liquids rubidium, carbon tetrachloride, and argon. Assuming the interparticle distances vary as $\rho^{-1/3}$, they found that $g^{(3)}$, and hence $\frac{\partial S(Q)}{\partial P}$, can be described quite well by equation (2-22):

$$kT\rho\frac{\partial S(Q)}{\partial P} = -\frac{S(0)}{3}\, Q\, \frac{\partial S(Q)}{\partial Q} \quad . \tag{2-22}$$

A similar comparison (see Figure 2-12) between equation (2-22) and the transformed Monte Carlo results of Verlet illustrates the applicability of Monte Carlo "data" to studying the triplet correlation function. Clearly equation (2-22) is in error as $Q \to 0$, since the isothermal pressure derivative of $S(Q)$ does not vanish, and $S(0)$ and $\frac{\partial S(Q)}{\partial Q}$ are non-zero.

Figure 2-11. Monte Carlo results for $\partial g(r)/\partial P$ for a dense ($\rho^* = 0.83$) system of Lennard-Jones atoms, obtained by differentiating Verlet's (28) Monte Carlo calculations.

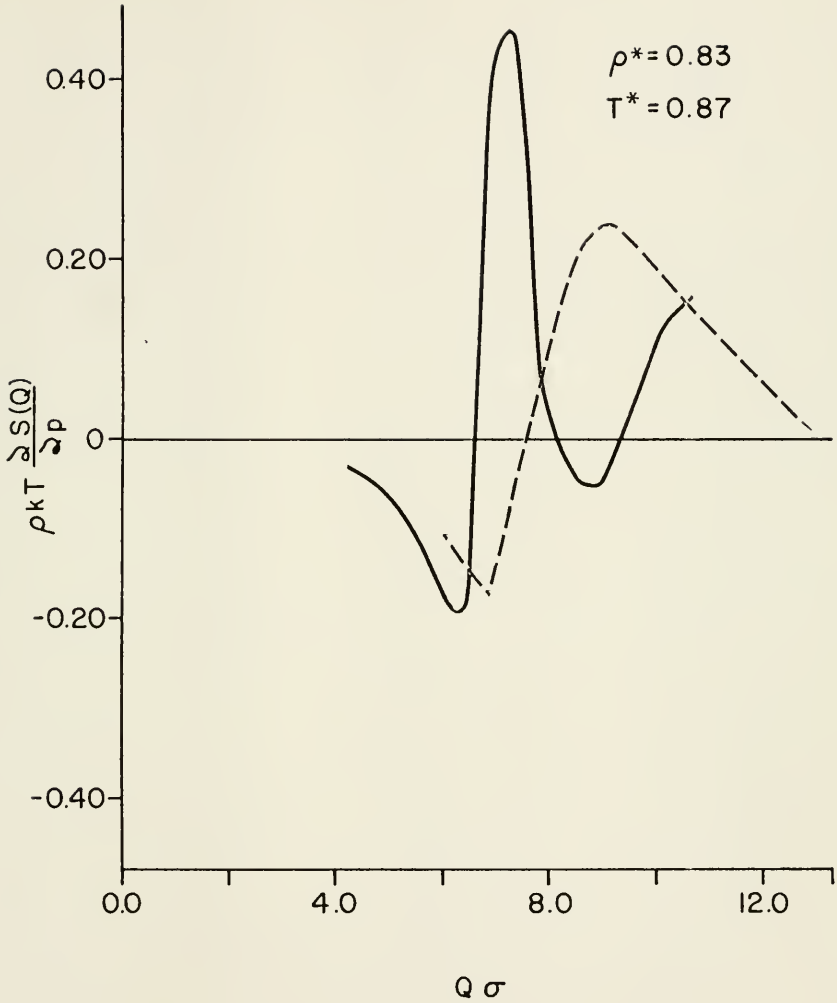

Figure 2-12. Monte Carlo results for $\partial S(Q)/\partial P$ for a dense ($\rho^* = 0.83$) system of Lennard-Jones atoms (——), obtained by Fourier transforming $\partial g(r)/\partial P$ given in Figure 2-11. Also included is $\partial S(Q)/\partial P$ predicted by equation (2-22) (---).

CHAPTER 3

THE FORMAL KINETIC THEORY FOR TIME-DEPENDENT CORRELATION FUNCTIONS

3.1 Introduction

In the study of atomic and molecular processes in fluids, many phenomena can be described in terms of time correlation functions. These functions characterize the decay of spontaneous fluctuations in an equilibrium fluid and, as such, may be observed by radiation scattering measurements. Inelastic scattering experiments have been performed on a wide variety of fluids and solids. The physical relevance of the time correlation functions lies in the fact that they completely describe the linear response of the system to an external disturbance and the linear dissipation of an isolated system approaching equilibrium. For example, virtually all linear transport coefficients, as well as more detailed phenomena such as high frequency sound absorption and collective modes in fluids, may be obtained from time correlation functions. In this chapter the relationship of the dynamic structure factor, $S(Q,\omega)$, to the corresponding linear response time correlation function is established. Some simple and exact properties of $S(Q,\omega)$ are given, along with two formal models which incorporate these properties and which are presently used for semi-phenomenological calculations of $S(Q,\omega)$ for liquids. In Section 3.3 it is shown that a formal kinetic theory for $S(Q,\omega)$ can

provide a microscopic basis for the study of fluids, and the above liquid models are interpreted in this context. Also given in this section is the exact result for a low density gas of hard spheres.

The more general three-point time correlation functions are considered in Section 3.4, where the relationship of these functions to $\frac{\partial S(Q,\omega)}{\partial P}$ is given. A preliminary study of the pressure derivative of the incoherent scattering function by Egelstaff et al. (29) indicates a direct dependence on the pressure derivative of the collision operator. A similar result is found here for $\frac{\partial S(Q,\omega)}{\partial P}$. The isothermal pressure derivative of $S(Q,\omega)$ may be obtained directly from the kinetic theory expression for the triplet time correlation function (presented in Section 3.4), or by differentiation of the kinetic formulation of the two-point function, $S(Q,\omega)$. The formal expression for $\frac{\partial S(Q,\omega)}{\partial P}$, obtained by the latter method, is developed in Section 3.4 and is presented in a form suitable for the introduction of phenomenological models. Finally, $S(Q,\omega)$ is calculated in Section 3.5, using a simple model collision operator, to illustrate the qualitative behavior of $S(Q,\omega)$ and $\frac{\partial S(Q,\omega)}{\partial P}$.

3.2 Properties of $S(Q,\omega)$

3.2.1 Relationship to Linear Response and Sum Rules. The response of a system to an external disturbance can be expressed in terms of a time-dependent correlation function for the unperturbed system (30). For example, if we consider a system initially in equilibrium and apply a time-dependent external field, represented by the addition of a term $V_{ext}(t)B(x_1,\ldots x_N)$ to the Hamiltonian, where $V_{ext}(t)$ is the external field and B is some function of the positions and momentum of the N

molecules in the system, it can be shown (31) that the linear response of a variable $A(x_1,\ldots x_N)$ to the external field may be written as

$$\delta\langle A(t)\rangle = \int_{-\infty}^{t} d\tau\ \chi_{ab}(t-\tau)\ V_{ext}(\tau)\ , \tag{3-1}$$

where the response function, $\chi_{ab}(t)$, is given classically by

$$\chi_{ab}(t) = \begin{cases} \frac{1}{kT}\langle \dot{A}(t)B(o)\rangle_o\ , & t \geq o \\ o\ , & t < o \end{cases} . \tag{3-2}$$

Here, $\delta\langle A(t)\rangle \equiv \langle A\rangle - \langle A\rangle_o$, where $\langle\ldots\rangle$ and $\langle\ldots\rangle_o$ denote the non-equilibrium and equilibrium averages, respectively. Also, $\dot{A}(t)$ represents the time derivative of $A(t)$. It is apparent from equation (3-1) that $\chi_{ab}(t)$ is the time correlation function relating the linear response of the system, i.e., $\delta\langle A(t)\rangle$, to the external field, $V_{ext}(t)$. It is important to note that this general expression does not involve properties of the system outside equilibrium, but instead gives the response in terms of time correlation functions between microscopic quantities at different times for a system in equilibrium.

Of special interest is the case of the density response to an external potential that couples additivity to each particle of the fluid, $V_{ext}(t)B = \sum_{i=1}^{N} V(t;\vec{q}_i)$, where $\vec{q}_i$ is the coordinate of the ith particle. Then equations (3-1) and (3-2) become

$$\langle n(\vec{r},t)\rangle = \int_{-\infty}^{t} d\tau \int d\vec{r}\,'\ \chi(\vec{r}-\vec{r}\,';t-\tau)\ V(\tau,\vec{r}\,'), \tag{3-3}$$

with

$$\chi(\vec{r},\vec{r}\,';t-\tau) \equiv \begin{cases} \frac{-1}{kT}\langle \dot{n}(\vec{r}\,',t)\,n(\vec{r},\tau)\rangle_o\ , & t \geq o \\ o\ , & t < o \end{cases} \tag{3-4}$$

Here, $n(\vec{r})$ is the deviation of the microscopic number density from its equilibrium value,

$$n(\vec{r}) = \sum_{i=1}^{N} \delta(\vec{r}-\vec{q}_i) - \langle \sum_{i=1}^{N} \delta(\vec{r}-\vec{q}_i) \rangle_o \quad . \tag{3-5}$$

There exists a useful relation between the dynamic structure factor, $S(Q,\omega)$, and the density-density response function, χ. Specifically, if one defines the complex susceptibility, $\tilde{\chi}(Q,\omega)$, as the Fourier-Laplace transform of $\chi(\vec{r}-\vec{r}\,';t)$,

$$\tilde{\chi}(Q,\omega) \equiv \frac{-1}{kT} \int_0^{\infty} dt\ e^{i\omega t} \langle \dot{n}_{-Q}(t) n_Q(o) \rangle \ , \tag{3-6}$$

where $n_Q(t)$ is the Fourier transform of $n(\vec{r},t)$,

$$n_Q(t) \equiv \int d\vec{r}\ e^{-i\vec{Q}\cdot\vec{r}}\ n(\vec{r},t) \ ,$$

then it is possible to relate $S(Q,\omega)$ to the density-density response function (See Appendix A):

$$S(Q,\omega) = \frac{2kT}{\rho\omega}\ \tilde{\chi}''(Q,\omega) \quad , \tag{3-7}$$

where $\tilde{\chi}''(Q,\omega)$ is the imaginary part of $\tilde{\chi}(Q,\omega)$. The real part of the complex susceptibility, $\tilde{\chi}'(Q,\omega)$, is related to $\tilde{\chi}''(Q,\omega)$ through equation (3-8),

$$\tilde{\chi}'(Q,\omega) = \fint_{-\infty}^{+\infty} \frac{d\omega'}{\pi}\ \frac{\tilde{\chi}''(Q,\omega')}{\omega'-\omega} \quad , \tag{3-8}$$

where $\fint$ denotes a principal-part integration, so that the general result exists:

$$\tilde{\chi}(Q,\omega) = \int_{-\infty}^{+\infty} \frac{d\omega'}{\pi} \frac{\tilde{\chi}''(Q,\omega')}{\omega'-\omega-i\varepsilon} , \qquad \varepsilon \to o^+$$

or

$$\tilde{\chi}(Q,\omega) = \frac{\rho}{kT} \int_{-\infty}^{\infty} \frac{d\omega'}{\pi} \omega' \frac{S(Q,\omega')}{\omega'-\omega} . \tag{3-9}$$

Equations (3-7) and (3-9) are valuable in the development of models for $S(Q,\omega)$ based on the structure of $\tilde{\chi}(Q,\omega)$. For example, the frequency moments (sum rules) of $\tilde{\chi}''(Q,\omega)$ are equilibrium properties of the fluid which, in principal, can be calculated given the interaction potential and the equilibrium (static) correlation functions. The sum rules are developed from the definition of the frequency moments of $\tilde{\chi}(Q,\omega)$:

$$\tilde{\chi}(Q,\omega) = - \sum_{n \geq o}^{\infty} \left(\frac{1}{\omega}\right)^{n+1} M_n(Q) , \tag{3-10}$$

with

$$\begin{aligned} M_n(Q) &\equiv \int_{-\infty}^{+\infty} \frac{d\omega}{\pi} \omega^n \tilde{\chi}''(Q,\omega) \\ &= \left(i \frac{d}{dt}\right)^n \tilde{\chi}''(Q,t) \Big|_{t=o} , \end{aligned} \tag{3-11}$$

where $M_n(Q)$ is the nth frequency moment of $\tilde{\chi}''(Q,\omega)$. A high frequency expansion for $\tilde{\chi}(Q,\omega)$ in terms of the moments is developed in Appendix A. Since $S(Q,\omega)$ is related to the response function through equation (3-7), the following properties of $S(Q,\omega)$ hold:

$$\int_{-\infty}^{+\infty} \frac{d\omega}{2\pi} \omega^{n+1} S(Q,\omega) = \frac{kT}{\rho} M_n(Q) . \tag{3-12}$$

For monatomic fluids, the first two non-vanishing moments are (31):

$$M_1(Q) = \frac{\rho Q^2}{m}$$

$$M_3(Q) = \frac{\rho Q^2}{m}\left[3Q^2 v_o^2 + \frac{\rho}{m}\int d\vec{r}\, g(r)\,(1-\cos\vec{Q}\cdot\vec{r})(\hat{Q}\cdot\vec{\nabla})^2\phi(r)\right] . \tag{3-13}$$

Here, v_o is the thermal velocity $(kT/m)^{1/2}$, m is the atomic mass, $\hat{Q}$ is the unit vector along $\vec{Q}$, and $\phi(r)$ is the pair potential. The utility of equation (3-12) is illustrated in Section 3.5.

3.2.2 Free-Particle and Hydrodynamic Limits. From the definition of $S(Q,\omega)$ in Chapter 1, we may write

$$S(Q,\omega) = \int_{-\infty}^{+\infty} dt\, e^{i\omega t}\int d\vec{r}\, e^{-i\vec{Q}\cdot\vec{r}}\left(\frac{1}{\rho}\right)\langle n(\vec{r},t)n(\vec{o},o)\rangle_o . \tag{3-14}$$

For large ω the exponential oscillates rapidly giving little contribution to the time integral, unless it is correspondingly small, i.e., $\omega t \sim 1$. Therefore, the large ω-dependence is governed by the short time behavior of $\langle n(\vec{r},t)n(\vec{o},o)\rangle_o$. But, for short times the particles do not have time to collide with each other. Hence, the motion of each particle is governed by the mean field of its neighbors. This mean field will be obtained in Section 3.3; we note here that, as expected, the mean field is small for low density gases since the number of neighbors within the force range is small. In this case the short time behavior is essentially that of free particles, and $n(\vec{r},t)$ becomes

$$n(\vec{r},t) = \sum_{i=1}^{N}\delta\left(\vec{r}-\vec{q}_i-\frac{\vec{p}_i}{m}t\right) - \left\langle\sum_{i=1}^{N}\delta\left(\vec{r}-\vec{q}_i-\frac{\vec{p}_i}{m}t\right)\right\rangle_o . \tag{3-15}$$

Similarly, the average $\langle \ldots \rangle_o$ reduces to that for non-interacting particles, and $S(Q,\omega)$ may be straightforwardly evaluated to give

$$S(Q,\omega) = S^{(o)}(Q) \left(\frac{m}{2\pi kT}\right)^{1/2} \frac{e^{-\left(\frac{m}{2kT}\right)\frac{\omega^2}{Q^2}}}{Q} , \tag{3-16}$$

where $S^{(o)}(Q)$ approaches unity in the low density limit.

At the other extreme we may consider equation (3-14) for small ω and small Q. In this case the integration samples $\langle n(\vec{r},t)n(\vec{o},o)\rangle_o$ on a space and time scale large compared to molecular dimensions. According to Onsager (32), under such conditions the decay of fluctuations should be governed by the macroscopic fluid equations. For a simple fluid these are the linear Navier-Stokes hydrodynamic equations (33),

$$\text{mass:} \quad \frac{\partial \rho'}{\partial t} + \rho \, \vec{\nabla}\cdot\vec{v} = o \tag{3-17}$$

$$\begin{aligned} \text{momentum:} \quad & \rho \frac{\partial \vec{v}}{\partial t} + \frac{c_o}{\nu} \vec{\nabla}\rho' + \frac{c_o \beta_T \rho}{\nu} \vec{\nabla}T' \\ & - \left(\frac{4}{3}\eta_S + \eta_B\right) \nabla^2\vec{v} \\ & - \eta_s[\nabla^2\vec{v} - \vec{\nabla}(\vec{\nabla}\cdot\vec{v})] = o \end{aligned} \tag{3-18}$$

$$\text{energy:} \quad \rho c_v \frac{\partial T'}{\partial t} - c_v \frac{(\nu-1)}{\beta_T} \frac{\partial \rho'}{\partial t} - \lambda \nabla^2 T' = o \quad , \tag{3-19}$$

where ρ' and T' denote deviations from the equilibrium number density, ρ, and the temperature, T, respectively. The ratio of the specific heat at constant pressure (c_p) to that at constant volume (c_v) is denoted by ν; η_S and η_B represent the shear and bulk viscosities, respectively; λ is the thermal conductivity, β_T is the thermal

expansion coefficient ($\equiv \frac{1}{V}\left(\frac{\partial V}{\partial T}\right)_P$), and c_o is the low frequency limit of the sound velocity ($= v\left(\frac{\partial P}{\partial \rho}\right)_T$). These equations may be solved to find $\rho'(\vec{r},t) = T_t \rho'(\vec{r},o)$, where T_t is used to symbolically denote the solution to the hydrodynamic equations. The Onsager assumption then takes the form

$$\langle n(\vec{r},t)n(\vec{o},o)\rangle_o \sim T_t \langle n(\vec{r},o)n(\vec{o},o)\rangle_o \ . \tag{3-20}$$

The time independent correlation function, $\langle n(\vec{r},o)n(\vec{o},o)\rangle_o$, may be evaluated in terms of the pair correlation function, as discussed in Chapter 2. Use of equation (3-20) to determine $S(Q,\omega)$ known as the Landau-Placzek procedure (33,34), gives

$$S(Q,\omega) = S(Q)\left\{\left(\frac{c_p - c_v}{c_p}\right)\frac{2\lambda Q^2/\rho c_p}{\left(\frac{\lambda Q^2}{\rho c_p}\right)^2 + \omega^2} + \frac{c_v}{c_p}\left[\frac{\Gamma Q^2}{(\Gamma Q^2)^2 + (\omega + c_o Q)^2} + \frac{\Gamma Q^2}{(\Gamma Q^2)^2 + (\omega - c_o Q)^2}\right]\right\} \tag{3-21}$$

with

$$\Gamma = \frac{1}{2}\left[\frac{\frac{4}{3}\eta_S + \eta_B}{\rho} + \frac{1}{\rho}\left(\frac{\lambda}{c_v} - \frac{\lambda}{c_p}\right)\right] .$$

Figure 3-1 illustrates the qualitative hydrodynamic behavior of $S(Q,\omega)$. In this hydrodynamic theory of fluctuations, density fluctuations can be described in terms of pressure fluctuations and temperature fluctuations. The two hydrodynamic modes of a simple fluid may therefore be characterized as entropy fluctuations at constant pressure (heat flow) which give rise to the central peak (Rayleigh line), and pressure fluctuations at constant entropy (adiabatic sound propagation)

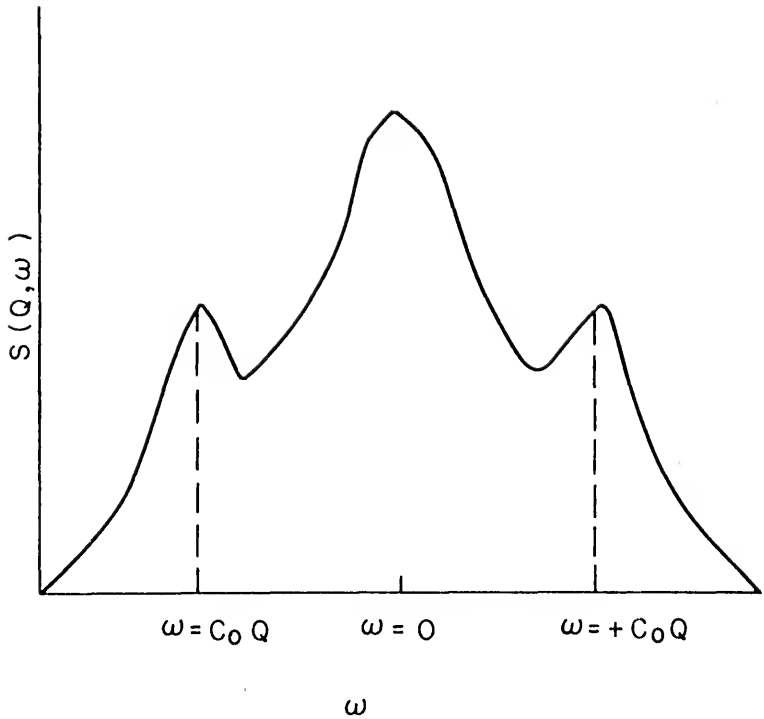

Figure 3-1. Qualitative behavior of the dynamic structure factor, $S(Q,\omega)$, in the hydrodynamic limit.

which are responsible for the two shifted peaks (Brillouin lines). Two side peaks are observed because scattering can occur from waves traveling with the same speed but in opposite directions. These lines are broadened somewhat by dissipative processes which tend to dampen the waves (34).

There are several serious limitations to equation (3-21) for $S(Q,\omega)$. In addition to being only applicable in the hydrodynamic region, i.e., small (Q,ω), there appear a variety of parameters in equation (3-21) whose values are not given by fluid mechanics: these are the thermodynamic derivatives, e.g., c_p, c_v, β_T, c_o, and the transport coefficients η_S, η_B, and λ. While this severely limits equation (3-21) in a predictive sense, it does have its advantages experimentally: it is possible to extract thermodynamic and transport properties from experimental values of $S(Q,\omega)$ in the hydrodynamic limit. Experiments (35,36,37) have shown light scattering to be an excellent technique for obtaining values for the speed of sound, c_o ($\pm$ 0.2%), and effective for determining transport coefficients ($\pm$ 5-10%). In addition, the total scattered intensity yields the isothermal compressibility ($= \frac{1}{\rho}\left(\frac{\partial\rho}{\partial P}\right)_T$) and the ratio of the central peak to the two side peaks (the Landau-Placzek ratio) leads to values of γ.

Additional information is provided by the hydrodynamic theory for $S(Q,\omega)$. In particular (38),

$$\lim_{\substack{\omega\to o \\ Q\to o}} \left[\frac{\omega^4 S(Q,\omega)}{Q^4}\right] = \frac{kT}{\pi m^2}\left(\frac{4}{3}\eta_S + \eta_B\right)$$

and

$$\lim_{\substack{\omega \to o \\ Q \to o}} [Q^2 S(Q,\omega)] = \frac{\rho^2 \; kT \; \beta_T^{\,2}}{\pi\lambda} , \tag{3-22}$$

which again place useful constraints on models for $S(Q,\omega)$, as indicated in the next section.

3.2.3 Formal Models for Liquids. The volume of experimental neutron scattering data on liquids in the past two decades prompted the need for theoretical models to analyze and interpret the data. The hydrodynamic and free-particle limits just discussed are inappropriate as are the frequency moment expansions. The reason for this is that the Q and ω values sampled by neutron scattering correspond to length and time scales of molecular rather than macroscopic dimensions. There have been many suggestions for the reformulation of expressions for $S(Q,\omega)$ that incorporate as much of the known properties of $S(Q,\omega)$ explicitly and contain the unknown properties in a form that is hopefully suitable for approximation. Here we shall mention only two such formulations: the generalized hydrodynamic model of Martin (30) and Ailawadi, Zwanzig, and Rahman (39), and a more recent generalized mean field model developed by Kugler (40).

The generalized hydrodynamic model is based on the assumption that the shape of $S(Q,\omega)$ should be qualitatively that predicted by the Landau-Placzek solution, but that the various constants (sound velocity, viscosity, and so on) should be replaced by functions of Q and ω, which reduce to the proper constants in the hydrodynamic limit, but more generally may vary with these variables. It is possible to make these

replacements formally in such a way as to yield an exact expression for $S(Q,\omega)$. The form given by Martin (30) is

$$S(Q,\omega) = \frac{2}{\beta m} \frac{Q^4 D(Q,\omega)}{\left(\omega^2 - \frac{Q^2}{\beta m S(Q)} + \omega^2 Q^2 \int \frac{d\omega'}{\pi} \frac{D(\omega',Q)}{\omega'^2-\omega^2}\right)^2 + (\omega Q^2 D(Q,\omega))^2}, \tag{3-23}$$

where the real function, $D(Q,\omega)$, is called the "damping function". The problem now becomes one of determining the frequency - and wavelength - dependent function $D(Q,\omega)$, known formally in terms of $\tilde{\chi}(Q,\omega)$. A phenomenological approach to this problem is through the use of a dispersion relation which insures that $S(Q,\omega)$ will have the correct hydrodynamic limit. Additional constraints on $D(Q,\omega)$ are provided by the sum rules and the expressions (3-22) for $S(Q,\omega)$ in terms of the transport properties. In this way the damping function is constrained for large ω by the moment requirements and yields the proper transport coefficients in the low-frequency and long-wavelength limit. The result is an expression for $S(Q,\omega)$ which, in effect, interpolates between the hydrodynamic and free-particle limits of the spectrum. In Section 3.3 a more detailed expression for the damping function is provided in terms of the collision operator of the linear kinetic equation for $S(Q,\omega)$.

In a similar spirit Kugler (40) has recently suggested that $S(Q,\omega)$ be constructed from $\tilde{\chi}(Q,\omega)$, where $\tilde{\chi}(Q,\omega)$ is written in the form

$$\tilde{\chi}(Q,\omega) = \tilde{\chi}_o(Q,\omega) + \tilde{\chi}_o(Q,\omega)\ \tilde{\phi}(Q,\omega)\ \tilde{\chi}(Q,\omega). \tag{3-24}$$

This "Dyson-like" equation defines $\tilde{\phi}(Q,\omega)$. Then, using equation (3-7), $S(Q,\omega)$ is given by

$$S(Q,\omega) = \frac{2kT}{\rho\omega} \frac{\tilde{\chi}_o'' - \tilde{\phi}''(\tilde{\chi}_o' + \tilde{\chi}_o''^2)}{(1+\tilde{\phi}'\tilde{\chi}_o' - \tilde{\phi}''\tilde{\chi}_o'')^2 + (\tilde{\phi}''\tilde{\chi}_o' + \tilde{\phi}'\tilde{\chi}_o'')^2} \quad . \tag{3-25}$$

Here, $\tilde{\chi}_o'$ and $\tilde{\chi}_o''$ are the real and imaginary parts of the ideal gas function, $\tilde{\chi}_o$, and $\tilde{\phi}'$ and $\tilde{\phi}''$ are the real and imaginary parts of "an effective and wave-number dependent interaction", $\tilde{\phi}$, which generalizes the static mean field approximations. The phenomenological determination of $\tilde{\phi}(Q,\omega)$ proceeds in a manner similar to that for the damping function, $D(Q,\omega)$, in the generalized hydrodynamic model. Kugler uses, in addition to the sum rules, empirical data on $S(Q, \omega=o)$. A microscopic formulation of $\tilde{\phi}(Q,\omega)$ is given in Section 3.3, where $\tilde{\phi}(Q,\omega)$ is expressed in terms of the kinetic theory collision operator.

3.3 Formal Kinetic Theory

To improve upon the phenomenological descriptions of $S(Q,\omega)$ mentioned in the last section, a more detailed study of the dynamics at the molecular level is required. In this section the formal kinetic theory for two-point time correlation functions, similar to that developed by Lebowitz, Percus, and Sykes (41), and others (42), is given. The results are exact, although formal, and therefore place no limitations on Q and ω or on the thermodynamic state conditions. In this sense the kinetic theory formulation of $S(Q,\omega)$ is similar to the formal models of the last section containing ingredients that require modeling or a detailed many-body analysis. The difference with kinetic theory is that the description lies at a more microscopic

level so that approximations are introduced in a more fundamental manner where they can be better controlled and corrected. For example, in generalized hydrodynamics approximations are introduced for the damping function, $D(Q,\omega)$, a quantity for which there is no simple physical interpretation or understanding. In contrast, the corresponding quantity studied in kinetic theory is the collision operator representing the collisional properties in phase space; while still complicated, its structure and relationship to the underlying equations of motion is much closer.

3.3.1 Outline of the Method and Results. The time-dependent pair correlation function, $G(\vec{r};t)$, may be expressed in terms of a single particle reduced distribution function, $\psi^{(1)}(x_1;t)$, as follows (43):

$$G(\vec{r};t) = \frac{1}{\rho} \langle n(\vec{r},t)\ n(\vec{o},o)\rangle$$

$$= \frac{1}{\rho} \sum_{N\geq o} \frac{z^N}{h^{3N} N!} \frac{1}{\Omega} \int dx_1 \ldots dx_N \sum_{i=1}^{N} \delta(\vec{q}_i) e^{-\beta H_N}\ n(\vec{r},t)$$

or

$$G(\vec{r};t) = \int dx_1\ \delta(\vec{q}_1)\ \psi^{(1)}(x_1;t)\ . \tag{3-26}$$

Here, x_i denotes the position and momentum of the ith particle, and the reduced distribution functions, $\psi^{(s)}(x_1,\ldots,x_S;t)$, are defined by

$$\rho^S\ \psi^{(s)}(x_1,\ldots,x_S;t) \equiv \sum_{N\geq S} \frac{z^N}{h^{3N}(N-S)!} \frac{1}{\Omega} \int dx_{S+1} \ldots dx_N e^{-\beta H_N}\ n(\vec{r},t). \tag{3-27}$$

It may be shown by direct differentiation that the $\psi^{(s)}$ satisfy the BBGKY hierarchy of equations. The first equation of this hierarchy is

$$\left(\frac{\partial}{\partial t} + \frac{\vec{p}_1}{m} \cdot \nabla_1\right) \psi^{(1)}(x_1;t) = \rho \int dx_2\, \theta_{12}\, \psi^{(2)}(1,2;t) \ , \qquad (3\text{-}28)$$

with

$$\theta_{12} \equiv - \vec{F}(1,2) \cdot (\vec{\nabla}p_1 - \vec{\nabla}p_2) \ . \qquad (3\text{-}29)$$

In equation (3-29), $\vec{F}(1,2)$ is the force on particle 1 due to particle 2. The object of kinetic theory is to obtain an equation for the time evolution of $\psi^{(1)}(x_1;t)$, i.e.,

$$\left(\frac{\partial}{\partial t} + \frac{\vec{p}_1}{m} \cdot \vec{\nabla}_1\right) \psi^{(1)}(x_1;t) = C[\psi^{(1)}(x_1;t)] \ . \qquad (3\text{-}30)$$

Once such an equation is obtained, $G(\vec{r},t)$ may be computed from its solution via equation (3-26).

Equation (3-28) provides the starting point for obtaining the kinetic equation for $\psi^{(1)}(x_1;t)$. Because of the special nature of the initial conditions on the reduced distribution functions, it is possible to express $\psi^{(2)}(x_1,x_2;t)$ as a functional of $\psi^{(1)}(x_1;t)$:

$$\psi^{(2)}(x_1,x_2;t) = \Psi(x_1,x_2;t|\psi^{(1)}) . \qquad (3\text{-}31)$$

A study of this functional shows that it may be split into two parts,

$$\psi^{(2)}(x_1,x_2;t) = \Psi(x_1,x_2;t=o|\psi^{(1)}(t))$$
$$+ \int_0^t d\tau K(x_1,x_2;t-\tau|\psi^{(1)}(\tau)) , \qquad (3\text{-}32)$$

where the first term on the right side may be evaluated explicitly in terms of the equilibrium properties of the fluid, e.g., g(r). Substitution of equation (3-32) for $\psi^{(2)}$ into equation (3-28) gives the desired kinetic equation,

$$\left(\frac{\partial}{\partial t} + \frac{\vec{p}_1}{m} \cdot \vec{\nabla}_1\right) \psi^{(1)}(x_1;t) = B[\psi^{(1)}(t)] + \int_0^t d\tau\, M(t-\tau|\psi^{(1)}(\tau)) \tag{3-33}$$

with

$$B[\psi^{(1)}(t)] \equiv \int dx_2\, \theta_{12}\, \Psi(x_1,x_2;t=o|\psi^{(1)}(t))$$

and (3-34)

$$M(t-\tau|\psi^{(1)}(\tau)) \equiv \int dx_2\, \theta_{12}\, K(x_1,x_2;t-\tau|\psi^{(1)}(\tau)).$$

The dynamic structure factor may now be obtained from equations (3-34) and (3-26), with the result

$$S(Q,\omega) = 2\ \mathrm{Real}\left\{\int d\vec{p}\, [-i\omega + \frac{i\vec{Q}\cdot\vec{p}}{m} - \hat{B} - \hat{M}]^{-1}\, f_o(p)\, S(Q)\right\}, \tag{3-35}$$

where $\hat{B}$ and $\hat{M}$ denote the Fourier-Laplace transforms of the operators B and M, respectively. The operator $\hat{B}$ is found to have the structure of a Vlasov integral operator, so that equation (3-35) may be further reduced to

$$S(Q,\omega) = \frac{2kT}{\rho\omega}\ \frac{I''(Q,\omega)}{[1-kTC(Q)I'(Q,\omega)]^2 + [kTC(Q)I''(Q,\omega)]^2}\ . \tag{3-36}$$

Here, C(Q) is the Fourier transformed equilibrium direct correlation function and I' and I'' are, respectively, the real and imaginary parts of the function

$$I(Q,\omega) \equiv \frac{\rho}{kT} \int d\vec{p}\,[-i\omega + i\,\frac{\vec{Q}\cdot\vec{p}}{m} - \hat{M}(Q,\omega)]^{-1}\; i\,\frac{\vec{Q}\cdot\vec{p}}{m}\, f_0(p) . \qquad (3\text{-}37)$$

Equation (3-36) is the main result of the kinetic theory formulation; it is similar to the formal models for liquids, e.g., generalized hydrodynamics, in that it is expressed in terms of a single function, in this case $I(Q,\omega)$, still to be determined. However, a more detailed representation of $I(Q,\omega)$ is provided through (3-37). In particular, approximations to $I(Q,\omega)$ may be obtained on a microscopic basis through approximations to $\hat{M}(Q,\omega)$.

<u>3.3.2 Derivation of the Formal Kinetic Equation</u>. It can be seen from equation (3-27) that the functions $\psi^{(s)}(x_1,\ldots,x_s;t)$ satisfy the usual BBGKY hierarchy of equations, the first two being

$$\frac{\partial}{\partial t}\,\psi^{(1)} + \frac{\vec{p}_1}{m}\cdot\vec{\nabla}_1\,\psi^{(1)} = \rho \int dx_2\;\theta_{12}\;\psi^{(2)}(x_1,x_2;t) \qquad (3\text{-}38)$$

and

$$\frac{\partial}{\partial t}\,\psi^{(2)} + \tilde{L}(1,2)\;\psi^{(2)} = \rho \int dx_3[\theta_{13} + \theta_{23}]\;\psi^{(3)}(x_1,x_2,x_3;t)\ , \qquad (3\text{-}39)$$

with the two-particle operators, θ_{12} and $\tilde{L}(1,2)$, defined as

$$\theta_{12} \equiv [\vec{\nabla}_1\phi(q_{12})]\cdot(\vec{\nabla}p_1 - \vec{\nabla}p_2)$$

and (3-40)

$$\tilde{L}(1,2) \equiv \frac{\vec{p}_1}{m}\cdot\vec{\nabla}_1 + \frac{\vec{p}_2}{m}\cdot\vec{\nabla}_2 - \theta_{12}\ .$$

Here, $\phi(q_{12})$ is the pair-potential between molecules 1 and 2, $\vec{\nabla}_i$ denotes the gradient with respect to $\vec{r}_i$, and $\vec{\nabla}p_i$ denotes the gradient with respect to $\vec{p}_i$. In equation (3-38),

$$[\frac{\partial}{\partial t} + \frac{\vec{p}_1}{m} \cdot \vec{\nabla}_1]$$

represents the change in $\psi^{(1)}(x_1;t)$ associated with the free-streaming of a single particle, while the right-side of equation (3-38) is that contribution to the change in $\psi^{(1)}$ due to two-body correlations. For convenience, equation (3-38) is written as

$$[-i\omega + \frac{\vec{p}_1}{m} \cdot \vec{\nabla}_1]\ \psi^{(1)}(x_1;\omega) = \psi^{(1)}(x_1;t=o) + \rho \int dx_2\ \theta_{12}\ \psi^{(2)}(x_1,x_2;\omega)\ , \tag{3-41}$$

where the Laplace transform,

$$\psi^{(1)}(x_1;\omega) \equiv \int_0^\infty dt\ e^{i\omega t}\ \psi^{(1)}(x_1;t)\ , \tag{3-42}$$

has been introduced. A similar expression for the transform of $\psi^{(2)}$, $\psi^{(3)}$, etc., exists.

Equation (3-41) is not useful as it stands since it does not form a closed expression for $\psi^{(1)}(x_1;t)$. However, as noted by Lebowitz, Percus, and Sykes (41), the functions $\psi^{(s)}(x_1,\ldots,x_s;t)$ are linear functionals of the single-particle function $\delta(\vec{r}-\vec{q}_1)$. To see this, we write $\psi^{(1)}(x_1;\omega)$ and $\psi^{(2)}(x_1,x_2;\omega)$ as

$$\psi^{(1)}(x_1;\omega) = \int_0^\infty dt\ e^{i\omega t}\ \{\frac{1}{\rho} \sum_{N\geq 2} N \int dx_2\ldots dx_N\ e^{iL_N t}\ f_N\ [1+\sum_{i=2}^{N} P_{i1}]\}\delta(\vec{r}-\vec{q}_1) \tag{3-43}$$

and

$$\psi^{(2)}(x_1,x_2;\omega) = \int_0^\infty dt\, e^{i\omega t} \{\frac{1}{\rho^2} \sum_{N\geq 3} N(N-1) \int dx_3 \ldots dx_N\, e^{iL_N t} f_N[1+\sum_{i=2}^{N} P_{i1}]\}$$

$$\times\ \delta(\vec{r}-\vec{q}_1) \quad , \tag{3-44}$$

where

$$f_N \equiv \frac{1}{N!} (\frac{z}{h^3})^N \frac{e^{-\beta H_N}}{\boxed{H}} \tag{3-45}$$

Also, $e^{iL_N t}$ is the N-particle time evolution operator, where L_N is defined as

$$L_N \equiv i[\sum_{i=1}^{N} \frac{\vec{p}_i}{m} \cdot \frac{\partial}{\partial \vec{q}_i} - \sum_{i=1}^{N} \frac{\partial \phi}{\partial \vec{q}_i} \cdot \frac{\partial}{\partial \vec{p}_i}] \ ,$$

and the permutation operator is defined such that

$$h(x_j) = P_{ji} h(x_i) \ . \tag{3-46}$$

By defining

$$\hat{U}(x_1;\omega) \equiv \frac{1}{\rho} \int_0^\infty dt\, e^{i\omega t} \sum_{N\geq 2} N \int dx_2 \ldots dx_N\, e^{iL_N t} f_N [1+\sum_{i=2}^{N} P_{i1}]$$

and (3-47)

$$\hat{U}(x_1,x_2;\omega) \equiv \frac{1}{\rho^2} \int_0^\infty dt\, e^{i\omega t} \sum_{N\geq 3} N(N-1) \int dx_3 \ldots dx_N\, e^{iL_N t} f_N [1+\sum_{i=2}^{N} P_{i1}] \ ,$$

we see that

$$\psi^{(1)}(x_1,\omega) = \hat{U}(x_1,\omega)\ \delta(\vec{r}-\vec{q}_1) \tag{3-48}$$

and

$$\psi^{(2)}(x_1,x_2;\omega) = \hat{U}(x_1,x_2;\omega)\ \delta(\vec{r}-\vec{q}_1) \ . \tag{3-49}$$

By writing

$$\delta(\vec{r}-\vec{q}_1) = \hat{U}^{-1}(x_1;\omega)\ \psi^{(1)}(x_1,\omega)\ , \tag{3-50}$$

and substituting for $\delta(\vec{r}-\vec{q}_1)$ into equation (3-49) for $\psi^{(2)}(x_1,x_2;\omega)$, the latter may be expressed as a linear functional of $\psi^{(1)}$:

$$\psi^{(2)}(x_1,x_2;\omega) = \Psi^{(2)}(x_1,x_2;\omega|\psi^{(1)}(\omega))\ , \tag{3-51}$$

with

$$\Psi^{(2)}(x_1,x_2;\omega|\psi^{(1)}(\omega)) \equiv \hat{U}(x_1,x_2;\omega)\ \hat{U}^{-1}(x_1;\omega)\ \psi^{(1)}(x_1;\omega)\ . \tag{3-52}$$

Substitution of this result for $\psi^{(2)}$ into the first equation of the BBGKY hierarchy, equation (3-41), gives the desired, formally exact, closed kinetic equation:

$$[-i\omega + \frac{\vec{p}_1}{m}\cdot\vec{\nabla}_1]\ \psi^{(1)}(x_1;\omega) = \psi^{(1)}(x_1;t=o) \tag{3-53}$$

$$+\ \rho\int dx_2\ \theta_{12}\ \Psi^{(2)}(x_1,x_2;\omega|\psi^{(1)}(\omega))\ ,$$

where the initial condition, $\psi^{(1)}(x_1;t=o)$, is determined from equation (3-27) (for t=o) to be[1]

$$\psi^{(1)}(x_1;t=o) = f_o(p_1)[\delta(q_1) + \rho(g(r)-1)]\ . \tag{3-54}$$

Here, $f_o(p_1)$ is the Maxwell-Boltzmann distribution function,

$$f_o(p) = (\frac{1}{2\pi mkT})^{3/2}\ e^{-\frac{p^2}{2mkT}}\ . \tag{3-55}$$

---

[1]For self correlations,

$$\psi^{(1)}(x_1;t=o) = f_o(p_1)\delta(q_1).$$

It is useful to express the time correlation functions, in so far as possible, in terms of the static correlations, which are assumed to be known. This is accomplished by separating explicitly the t=o ($\omega=\infty$) limit of $\psi^{(2)}(x_1,x_2;\omega)$:

$$\psi^{(2)}(x_1,x_2;\omega) = \Psi^{(2)}(x_1,x_2;t=o|\psi^{(1)}(\omega)) + P^{(2)}(x_1,x_2;\omega|\psi^{(1)}(\omega)), \tag{3-56}$$

where $P^{(2)}(x_1,x_2;\omega|\psi^{(1)}(\omega))$ is defined formally (see equation (3-52)) as

$$\begin{aligned} P^{(2)}(x_1,x_2;\omega|\psi^{(1)}(\omega)) \equiv [&\hat{U}(x_1,x_2;\omega)\ \hat{U}^{-1}(x_1;\omega) \\ &- \hat{U}(x_1,x_2;t=o)\ \hat{U}^{-1}(x_1;t=o)]\ \psi^{(1)}(x_1;\omega). \end{aligned} \tag{3-57}$$

It should be noted that equation (3-56) is the Laplace transform of equation (3-32), thereby establishing that result.

The t=o functional, $\Psi^{(2)}(x_1,x_2;t=o|\psi^{(1)}(\omega))$, is obtained directly (see Appendix B for details) by considering equations (3-47) and (3-52), with the result

$$\begin{aligned} \Psi^{(2)}(x_1,x_2;t=o|\psi^{(1)}(\omega)) = g(\vec{q}_{12})\ [&f_o(x_1)\ \psi^{(1)}(x_2;\omega) \\ &+ f_o(x_2)\ \psi^{(1)}(x_1;\omega)] + \rho\ f_o(x_1)\ f_o(x_2) \int dx_3\ f(\vec{q}_1,\vec{q}_2,\vec{q}_3)\ \psi^{(1)}(x_3;\omega)\ , \end{aligned} \tag{3-58}$$

where $g(\vec{q}_{12})$ is the pair correlation function for molecules 1 and 2 separated a distance $\vec{q}_{12}$. The equilibrium function $f(\vec{q}_1,\vec{q}_2,\vec{q}_3)$ is defined by

$$f(\vec{q}_1,\vec{q}_2,\vec{q}_3) \equiv H(\vec{q}_1,\vec{q}_2,\vec{q}_3) - \rho \int d\vec{q}_3' H(\vec{q}_1,\vec{q}_2,\vec{q}_3')C(\vec{q}_3 - \vec{q}_3')\ , \tag{3-59}$$

where

$$H(\vec{q}_1,\vec{q}_2,\vec{q}_3) \equiv h(\vec{q}_1,\vec{q}_2,\vec{q}_3) - h(\vec{q}_{12})h(\vec{q}_{13}) - h(\vec{q}_{12})h(\vec{q}_{23}), \qquad (3\text{-}60)$$

$C(\vec{q})$ is the direct correlation function, and $h(\vec{q}_1,\vec{q}_2,\vec{q}_3)$ is related to the equilibrium two- and three-particle correlation functions (44) by

$$g(\vec{q}_{12}) = h(\vec{q}_{12}) + 1 \qquad (3\text{-}61)$$

and

$$g^{(3)} = h(\vec{q}_1,\vec{q}_2,\vec{q}_3) + h(\vec{q}_{12}) + h(\vec{q}_{13}) + h(\vec{q}_{23}) + 1 . \qquad (3\text{-}62)$$

Hence we see that the t=o functional, $\Psi^{(2)}(x_1,x_2;t=o|\psi^{(1)})$, is entirely determined by the two- and three-particle equilibrium correlation functions.

The result, equation (3-58), may be used in equation (3-63),

$$B[\psi^{(1)}(\omega)] \equiv \rho \int dx_2\ \theta_{12}\ \Psi^{(2)}(x_1,x_2;t=o|\psi^{(1)}(\omega)), \qquad (3\text{-}63)$$

where $B[\psi^{(1)}(\omega)]$ is the mean field contribution to $\psi^{(2)}(x_1,x_2;t)$ and is given by (see Appendix B)

$$B[\psi^{(1)}(\omega)] = \rho\ f_o(x_1)\ \frac{\vec{p}_1}{m} \cdot \vec{\nabla}_1 \int dx_2\ C(\vec{q}_{12})\ \psi^{(1)}(x_2;\omega)\ , \qquad (3\text{-}64)$$

to yield the following formal kinetic equation for the single-particle reduced distribution function:

$$[-i\omega + \frac{\vec{p}_1}{m} \cdot \vec{\nabla}_1 - B]\ \psi^{(1)}(x_1;\omega) = \psi^{(1)}(x_1;t=o) + \rho \int dx_2\ \theta_{12}\ P^{(2)}(x_1,x_2;\omega|\psi^{(1)}(\omega)). \qquad (3\text{-}65)$$

Fourier transforming equation (3-65) yields the final result:

$$[-i\omega + i\,\frac{\vec{Q}\cdot\vec{p}}{m} - \hat{B} - \hat{M}(Q,\omega)]\;\tilde{\psi}^{(1)}(\vec{p};Q,\omega) = S(Q)\;f_o(p) \quad , \tag{3-66}$$

where "$\sim$" denotes the transformed quantity

$$\tilde{\psi}^{(1)}(\vec{p};Q,\omega) \equiv \int_0^\infty dt\; e^{i\omega t} \int d\vec{r}\; e^{-i\vec{Q}\cdot\vec{r}}\;\psi^{(1)}(\vec{p};\vec{r},t)$$

and $S(Q)\;f_o(p)$ is the Fourier transform of $\psi^{(1)}(x_1;t=o)$ (see equation (3-54)). Here, $C(Q)$ is the Fourier transform of the direct correlation function and is related to the static structure factor through equation (3-67):

$$C(Q) = \frac{S(Q)-1}{\rho S(Q)} \quad . \tag{3-67}$$

A formal solution for $\tilde{\psi}^{(1)}(\vec{p};Q,\omega)$ in terms of the collision operator, $\hat{M}(Q,\omega)$, begins with Fourier transforming equation (3-64) for $B[\cdot]$ and substituting the result into equation (3-66):

$$[-i\omega + i\,\frac{\vec{Q}\cdot\vec{p}}{m} - \hat{M}(Q,\omega)]\;\tilde{\psi}^{(1)}(\vec{p};Q,\omega)$$

$$= S(Q)\;f_o(p) + \rho\;f_o(p)C(Q)\;\frac{i\vec{Q}\cdot\vec{p}}{m}\int d\vec{p}_2\;\tilde{\psi}^{(1)}(\vec{p}_2;Q,\omega)\,. \tag{3-68}$$

By integrating equation (3-68) over momentum, and solving for $\int d\vec{p}_2\;\psi^{(1)}(\vec{p}_2;Q,\omega)$, one finds

$$\int d\vec{p}\;\;\tilde{\psi}^{(1)}(\vec{p};Q,\omega) = -\frac{1}{i\omega}\,S(Q)\;\left[\frac{1-\frac{kT}{\rho}\,I(Q,\omega)}{1-kTC(Q)I(Q,\omega)}\right] \quad , \tag{3-69}$$

where $I(Q,\omega)$ is a function of the collision operator (see equation (3-37)). Substitution of equation (3-69) for $\int d\vec{p}\;\;\tilde{\psi}^{(1)}(\vec{p};Q,\omega)$ into equation (3-68) yields the desired result:

$$\tilde{\psi}^{(1)}(\vec{p};Q,\omega) = R(\vec{p};Q,\omega)\ f_o(p)\ S(Q)\ F(Q,\omega)\ ,$$

$$F(Q,\omega) \equiv 1 - \frac{\rho C(Q)}{i\omega}\left(i\,\frac{\vec{Q}\cdot\vec{p}}{m}\right)\left[\frac{1 - \frac{kT}{\rho}\,I(Q,\omega)}{1 - kTC(Q)\ I(Q,\omega)}\right]\ , \tag{3-70}$$

$$R(\vec{p};Q,\omega) \equiv \left[-i\omega + i\,\frac{\vec{Q}\cdot\vec{p}}{m} - \hat{M}(Q,\omega)\right]^{-1}\ .$$

Since the dynamic structure factor, $S(Q,\omega)$, is the Fourier-Laplace transform of $G(\vec{r};t)$, and $G(\vec{r};t)$ is given as an explicit function of $\psi^{(1)}(\vec{p};\vec{r},t)$ in equation (3-26), equation (3-69) then yields:

$$S(Q,\omega) = \frac{2kT}{\rho\omega}\ \frac{I''(Q,\omega)}{[1 - kTC(Q)\ I'(Q,\omega)]^2 + [kTC(Q)\ I''(Q,\omega)]^2}\ . \tag{3-71}$$

Here, $I'(Q,\omega)$ and $I''(Q,\omega)$ are, respectively, the real and imaginary parts of $I(Q,\omega)$. Equation (3-71) exposes the dependence of $S(Q,\omega)$ on the initial correlations (through $C(Q)$). The initial dynamics, i.e., the contribution to $S(Q,\omega)$ when $\hat{M}(Q,\omega) = 0$, may be extracted from $I(Q,\omega)$ by writing

$$I(Q,\omega) = I_o(Q,\omega) + I_c(Q,\omega)\ , \tag{3-72}$$

with

$$I_o(Q,\omega) \equiv \frac{\rho}{mkT}\int d\vec{p}\ \frac{i\vec{Q}\cdot\vec{p}}{-i\omega + \frac{i\vec{Q}\cdot\vec{p}}{m}}\ f_o(p)$$

and (3-73)

$$I_c(Q,\omega) \equiv \frac{\rho}{mkT}\int d\vec{p}\left(-i\omega + i\,\frac{\vec{Q}\cdot\vec{p}}{m}\right)^{-1}\hat{M}(Q,\omega)R(\vec{p};Q,\omega)\ i\vec{Q}\cdot\vec{p}\ f_o(p)$$

The collisionless part, $I_o(Q,\omega)$, may be calculated in terms of the plasma dispersion function (45), and all the collisional effects on $S(Q,\omega)$ enter through the single function $I_c(Q,\omega)$.

3.3.3 Generalized Enskog Models. The evaluation of $S(Q,\omega)$ via equation (3-71) requires that the collision operator, $\hat{M}(Q,\omega)$, be known. In general, the determination of $\hat{M}(Q,\omega)$ is a complex many-body problem to which a great deal of attention is presently being directed. Unfortunately, detailed knowledge of $\hat{M}(Q,\omega)$ for general central potentials has been obtained only for the rather academic case of weak coupling (expansion of $\hat{M}$ to second order in the potential) or the more realistic but restrictive case of a dilute gas. For dense gases, or even moderately dense gases (such as those corresponding to the experimental conditions of this thesis) much less is known beyond such general properties as the sum rules similar to those discussed in Section 3.2.1, conservation laws, etc. An exception, however, is the special case of a fluid interacting via a hard core potential. A hard core potential is defined to be one such that

$$\phi(r) = \begin{cases} \infty \ , & r < r_o \\ \phi_c(r), & r > r_o \end{cases} \quad ,$$

where $\phi_c(r)$ is an arbitrary continuous function of r. Two examples to be considered in Chapter 7 are the hard sphere potential (ϕ_c=o) and the Sutherland potential ($\phi_c = -\varepsilon \left(\frac{r_o}{r}\right)^6$). Because the hard core collisions require essentially zero time to complete, the short time behavior of the kinetic equation contains many of the collisional effects which would require a finite time to develop for the case of a system with purely continuous potentials. Furthermore, the short time behavior of the hard core system may be calculated exactly, without any limitations on the density. It may be obtained just as

has been described in Section (3.3.1), evaluating the t=o two-particle functional $(\Psi^{(2)}(x_1,x_2;t=o|\psi^{(1)}))$ with close attention to the changes due to a discontinuous potential. The exact kinetic equation then has the form (41)

$$[-i\omega + \frac{i\vec{Q}\cdot\vec{p}}{m}]\,\tilde{\psi}^{(1)} - \frac{i\vec{Q}\cdot\vec{p}}{m}\, f_o(p)\,[C(Q) - g(r_o)\,C_o(Q)]$$
$$\times \int d\vec{p}\,\tilde{\psi}^{(1)}(\vec{p};\vec{Q},\omega) = f_o(p)\,S(Q) + \hat{M}_E[Q|\tilde{\psi}^{(1)}] \qquad (3\text{-}74)$$
$$+ \Delta\hat{M}[Q,\omega|\tilde{\psi}^{(1)}] \quad ,$$

where $g(r_o)$ is the equilibrium pair correlation function at hard sphere diameter, r_o, and $C(Q)$ and $C_o(Q)$ are, respectively, the hard core direct correlation function and the low density hard sphere $C_o(Q)$. The Q-dependent "Enskog" collision operator, $M_E(Q)$, is independent of frequency and defined by

$$M_E[Q|\tilde{\psi}^{(1)}] = \rho\, g(r_o) \int d\vec{p}_2 \int d\Omega\, \left(\frac{\vec{p}_1-\vec{p}_2}{m}\right)\cdot\hat{r}_o\, [f_o(p_2)\,\tilde{\psi}(p_1)$$
$$-f_o(p_2')\,\tilde{\psi}^{(1)}(p_1') + e^{i\vec{Q}\cdot\vec{r}_o} f_o(p_1)\tilde{\psi}^{(1)}(p_2) - e^{-i\vec{Q}\cdot\vec{r}_o} f_o(p_1')\,\tilde{\psi}^{(1)}(p_2')],$$

(3-75)

where $\vec{p}$ and $\vec{p}'$ are the pre- and post-collision momenta for collisions at the core, respectively, and the prime on the Ω-integration denotes a restriction to the forward hemisphere. The phase factors $\exp[\pm\, i\vec{Q}\cdot\vec{r}_o]$ arise from non-local spatial effects in collisions between particles of finite size. Finally, $\Delta\hat{M}$ denotes the contribution to the collision operator from particles scattered by the continuous part of the potential, $\phi_c(r)$, and collisions occurring over a finite time. The significant aspect of equation (3-74) is that with the

neglect of $\Delta\hat{M}$, the equation is as tractable as the ordinary Boltzmann equation for hard spheres. The name "generalized Enskog" equation is chosen because the collision operator $\hat{M}_E$ reduces for hard spheres (ϕ_c=o) to that written down by Enskog (46) in an attempt to extend the Boltzmann equation to higher densities (indeed, for hard spheres the low density limit equation of (3-74) is precisely the linearized Boltzmann equation).

The hard sphere Enskog equation is known to predict fairly good transport coefficients for moderately dense gases, with r_o as an adjustable parameter to simulate real (e.g. Lennard-Jones) potential models. The density dependence is represented fairly well in such calculations although the temperature independence of $g^{hs}(r_o)$ in $\hat{M}_E$ is an obvious shortcoming. Much less is known about the use of other hard core potentials. However, the presence of a non-zero ϕ_c does give rise to a temperature dependence beyond that of the ideal gas. Regarding equation (3-74), the effect of ϕ_c appears in two distinct places. The first is to give rise to additional collisional effects in $\Delta\hat{M}$. In addition, however, ϕ_c can also change considerably the value of C(Q) in the mean field operator and $g(r_o)$ in the Enskog operator. Further discussion of the importance of $\phi_c(r)$ is given in Chapter 7 where the generalized Enskog models are used to analyze the experimental data.

3.3.4 Connection with Liquid Models. In Section 3.2, models (e.g., equations (3-23) and (3-25)) were presented for the dynamic structure factor, $S(Q,\omega)$, which incorporate as much as possible of the known properties of $S(Q,\omega)$ explicitly and which contain the unknown behavior in frequency- and wavelength-dependent functions (e.g., $D(Q,\omega)$ and $\tilde{\phi}(Q,\omega)$). The kinetic theory developed in the present section for two-point time-correlation functions resulted in equation (3-71), a formally exact expression for the dynamic structure factor in terms of the collision operator, $\hat{M}(Q,\omega)$, representing the collisional properties in phase space. The following relates $\hat{M}(Q,\omega)$ to the damping function, $D(Q,\omega)$, appearing in the hydrodynamic theory for $S(Q,\omega)$, and the "effective frequency and wavenumber dependent interaction," $\tilde{\phi}(Q,\omega)$, of Kugler's model.

Begin by defining a complex function, $\mathcal{D}(Q,\omega)$, as

$$\mathcal{D}(Q,\omega) \equiv \lim_{\varepsilon\to 0^+} \int_{-\infty}^{+\infty} \frac{dz}{\pi} \frac{D(Q,\omega)}{z-\omega-i\varepsilon} \quad . \tag{3-76}$$

From the relationship

$$\lim_{\varepsilon\to 0^+} \left[\frac{1}{z-\omega-i\varepsilon}\right] = \lim_{\varepsilon\to 0^+} \left[\frac{z-\omega}{(z-\omega)^2+\varepsilon^2}\right] + i \lim_{\varepsilon\to 0^+} \left[\frac{\varepsilon}{(z-\omega)^2+\varepsilon^2}\right], \tag{3-77}$$

and the definition of the δ-function,

$$\delta(x) \equiv \frac{1}{\pi} \lim_{\varepsilon\to 0^+} \left[\frac{\varepsilon}{x^2+\varepsilon^2}\right] \quad , \tag{3-78}$$

we see that $\mathcal{D}(Q,\omega)$ becomes

$$\mathcal{D}(Q,\omega) = \int_{\infty}^{\infty} \frac{dz}{\pi} \frac{D(Q,z)}{z-\omega} + i\, D(Q,\omega) \quad . \tag{3-79}$$

Equation (3-23) for $S(Q,\omega)$ can therefore be written as

$$S(Q,\omega) = \frac{2Q^2}{\omega\beta m} \frac{\omega Q^2 \mathcal{J}'(Q,\omega)}{(\omega^2 - \frac{Q^2}{\beta m S(Q)} + \omega Q^2 \mathcal{J}'(Q,\omega)^2 + (\omega Q^2 \mathcal{J}'(Q,\omega))^2} \tag{3-80}$$

or, equivalently,

$$S(Q,\omega) = -\frac{2Q^2}{\omega\beta m} \operatorname{Im} [\omega^2 - \frac{Q^2}{\beta m S(Q)} + \omega Q^2 \mathcal{J}(Q,\omega)]^{-1} \quad , \tag{3-81}$$

where Im {...} denotes the imaginary part of {...}. In equation (3-80), $\mathcal{J}(Q,\omega)$ and $\mathcal{J}'(Q,\omega)$ are, respectively, the real and imaginary parts of $\mathcal{J}(Q,\omega)$. Equating equations (3-81) and (3-71) then yields $D(Q,\omega)$ in terms of the collision operator:

$$D(Q,\omega) = \frac{kT}{\rho\omega S(Q)^2} [\frac{v_o^2 \, I''(Q,\omega)}{(1 - \frac{kT}{\rho} I'(Q,\omega)^2 + (\frac{kT}{\rho} I''(Q,\omega))^2}] \quad , \tag{3-82}$$

where $I'(Q,\omega)$ and $I''(Q,\omega)$ have been previously defined (see equation (3-37)) in terms of $\hat{M}(Q,\omega)$, and v_o is the thermal velocity, $(\frac{kT}{m})^{\frac{1}{2}}$.

To express $\tilde{\phi}(Q,\omega)$ in terms of the collision operator, we note that equation (3-24) can be rewritten as

$$\tilde{\phi}(Q,\omega) = \frac{\chi_o(Q,\omega) - \tilde{\chi}(Q,\omega)}{\chi_o(Q,\omega)\,\tilde{\chi}(Q,\omega)} \quad , \tag{3-83}$$

where the ideal gas (i.e., $\phi(q_{12}) = 0$) value of $\tilde{\chi}(Q,\omega)$, $\tilde{\chi}_o(Q,\omega)$ is given by

$$\tilde{\chi}_o(Q,\omega) = I_o(Q,\omega), \tag{3-84}$$

with $I_1(Q,\omega)$ defined in equation (3-73). Also, from equations (3-9) and (3-6) it may be verified that

$$\tilde{\chi}(Q,\omega) = \left[\frac{I(Q,\omega)}{1 - kT\ C(Q)\ I(Q,\omega)}\right] \tag{3-85}$$

Use of this in equation (3-83), then yields the desired result:

$$\tilde{\phi}(Q,\omega) = -\frac{C(Q)}{kT} - \frac{I_c(Q,\omega)}{I_o(Q,\omega)\ I(Q,\omega)}\ , \tag{3-86}$$

where $I_c(Q,\omega)$ is defined in equation (3-73).

There are many other exact representations for $S(Q,\omega)$ that have been discussed and compared elsewhere (47). In practice the utility of these expressions depends upon the judicious choice of an unknown function, e.g., $D(Q,\omega)$ in equation (3-23) or $\tilde{\phi}(Q,\omega)$ in equation (3-25). The advantage of the kinetic theory approach is that it provides more details of the structure of these functions, e.g., equations (3-82) or (3-86), before approximations need to be introduced. Of course, the collision operator, $\hat{M}(Q,\omega)$, is still only defined formally, but many of its exact properties (sum rules, connection with hydrodynamics, conservation laws) are known (48) and it may be expected that simple models for $\hat{M}(Q,\omega)$ (in phase space) may yield considerably more sophisticated results for $D(Q,\omega)$ or $\tilde{\phi}(Q,\omega)$ than modeling these functions directly. For example, $\hat{M}(Q,\omega)$ is known to be independent of the frequency for small ω and vanish for large ω. Any model for $\hat{M}(Q,\omega)$ preserving this property will automatically yield an approximation for $S(Q,\omega)$ that interpolates from the free-particle to the hydrodynamic limits, provided $\hat{M}(Q,\omega)$ contains the hydrodynamic subspace exactly.

3.4 Triplet Correlations and the Isothermal Pressure Derivative of $S(Q,\omega)$

Recently, Egelstaff, Gray and Gubbins (49) have pointed out that the measurement of the dynamic structure factor, $S(Q,\omega)$, may provide important constraints on the time-dependent triplet correlation function, $G_3(\vec{r}',o,\vec{r}'',o;\vec{r},t)$. They show that

$$\frac{\partial S(Q,\omega)}{\partial P} = \int dt\, e^{i\omega t} \int d(\vec{r}-\vec{r}')e^{-i\vec{Q}\cdot(\vec{r}-\vec{r}')} \frac{\partial G_2(\vec{r}',o;\vec{r},t)}{\partial P} \tag{3-87}$$

and

$$\rho kT \frac{\partial G_2(\vec{r}',o;\vec{r},t)}{\partial P} = \int d\vec{r}'' \, [G_3(\vec{r}',o;\vec{r}'',o,\vec{r},t) - G_2(\vec{r}',o;\vec{r}'',o)\, G_2(\vec{r}',o;\vec{r},t)] \,, \tag{3-88}$$

where $G_3(\vec{r}',o;\vec{r}'',\vec{r},t)$ is defined as

$$G_3(\vec{r}',o;\vec{r}'',\vec{r},t) \equiv \frac{1}{\rho} \langle n(\vec{r}',o)\; n(\vec{r}'',o)\; n(\vec{r},t)\rangle \,. \tag{3-89}$$

Equations (3-87) and (3-88) provide the connection between the measurable property, $\frac{\partial S(Q,\omega)}{\partial P}$, and the triplet function $G_3(\vec{r}',o;\vec{r}'',o;\vec{r},t)$. In this section the formal kinetic theory of Section 3.3 is applied to the two-time three-space point correlation functions, of which $G_3(\vec{r}',o;\vec{r}'',o;\vec{r},t)$ is a special case. The isothermal pressure derivative of $S(Q,\omega)$, obtained by direct differentiation of equation (3-71) for $S(Q,\omega)$, is derived and presented in a form suitable for the introduction of phenomenological models for the dynamic structure factor.

To obtain maximum generality, correlation functions of three phase variables A, B, and Y, will be considered, where A, B, and Y are of the form

$$A(t) = \sum_{i=1}^{N} a(x_i) - \left\langle \sum_{i=1}^{N} a(x_i) \right\rangle , \tag{3-90}$$

etc. The two-time three-space correlation function is defined as

$$F(t) \equiv \frac{1}{\rho} \langle A(o)\ B(o)\ Y(t) \rangle \quad . \tag{3-91}$$

Of special interest is the case where A, B and Y are local number densities; in particular, the function $G_3(\vec{r}',o;\vec{r}'',o;\vec{r},t)$ is obtained when $a(x_i) = \delta(\vec{r}'-\vec{q}_i)$, $b(x_i) = \delta(\vec{r}''-\vec{q}_i)$, and $y(x_i) = \delta(\vec{r}-\vec{q}_i)$.

With the definitions for $\psi^{(s)}(x_1,\ldots,x_s;t)$, $(s=1,\ldots,N)$, and use of equation (3-90) for A, B, and Y, the correlation function F(t) may be expressed as

$$F(t) = \int dx_1\ a(x_1)\ b(x_1)\ \psi^{(1)}(x_1;t)$$

$$+ \rho \int dx_1\ dx_2\ a(x_1)\ b(x_2)\ [\psi^{(2)}(x_1,x_2;t)$$

$$- f_o(x_1)\ \psi^{(1)}(x_2;t) - f_o(x_2)\ \psi^{(1)}(x_1;t)]. \tag{3-92}$$

There are several important features concerning equation (3-92) for F(t). First we note that the two-time three-space correlation function is determined completely by terms appearing in the expression for the two-time two-space correlation function. Also, the exact functional form of $\Psi(x_1,x_2;t=o|\psi^{(1)}(t))$ is known (Appendix B or equation (3-58)) so that F(t) may be expressed entirely in terms of $\psi^{(1)}(t)$, equilibrium correlation functions, and $K(x_1,x_2;t-\tau|.)$. Substituting equation (3-32) for $\psi^{(2)}(x_1,x_2;t)$ into equation (3-92) yields

$$F(t) = \int dx_1\ a(x_1)\ b(x_1)\ \psi^{(1)}(x_1;t)$$

$$+ \rho \int dx_1\ dx_2\ a(x_1)\ b(x_2)\ [\psi^{(2)}(x_1,x_2;t=o|\psi^{(1)}(x_1;t))$$

$$- f_o(x_1)\ \psi^{(1)}(x_2;t) \tag{3-93}$$

$$- f_o(x_2)\ \psi^{(1)}(x_1;t)] + \rho \int dx_1\ dx_2\ a(x_1)\ b(x_2) \int_0^t d\tau$$

$$\times\ K(x_1,x_2;t-\tau|\psi^{(1)}(x_1;t).$$

Furthermore, for short times F(t) can be calculated without consideration of the form of $K(x_1,x_2;t-\tau|.)$, since the last term in equation (3-93) vanishes for short times. Also, for short times the kinetic equation for $\psi^{(1)}(x_1;t)$ simplifies to the Vlasov equation

$$[\frac{\partial}{\partial t} + \frac{\vec{p}}{m} \cdot \vec{\nabla} - B]\ \psi^{(1)}(x_1;t) = o \quad , \tag{3-94}$$

where the Vlasov operator, B, is given by equation (3-64). Equation (3-94) may be solved exactly for use in the first three terms of equation (3-93). This short-time result for F(t) neglects collisions responsible for finite momentum transfer and is therefore not adequate for times greater than (or on the order of) a typical collision time. True collisional effects require detailed knowledge of $K(x_1,x_2;t-\tau|\cdot)$. The latter is defined formally through equation (3-32), so that equations (3-65) and (3-93) form a closed expression for the (two-time three-space) triplet correlation function.

Evaluation of equation (3-32) to give an explicit form for $K(x_1,x_2;t-\tau|\cdot)$ is, in general, quite difficult, depending on the system being considered. For weakly coupled or dilute fluids, small parameter

expansions (50) are straightforward. The low density Boltzmann limit of F(t) may be obtained directly from the low density limit of $K(x_1,x_2;t-\tau|\cdot)$ and that of the equilibrium correlation functions, e.g., g(r), with the result (43)

$$F_o(t) = \int dx_1\ a(x_1)\ b(x_1)\ \psi^{(1)}(x_1;t) + \rho \int dx_1\ \psi^{(1)}(x_1;t)\ \Gamma_o^{-1}(p_1)\, t J[a(x_1),b(x_2)]\ , \tag{3-95}$$

where $\psi^{(1)}(x_1;t)$ satisfies the kinetic equation

$$\frac{\partial}{\partial t}\psi^{(1)} + \frac{\vec{p}_1}{m}\cdot\nabla_1\psi^{(1)} = \rho I[\psi^{(1)}]\ . \tag{3-96}$$

Here, the operators J and I, the non-linear and the linearized Boltzmann operators, respectively, and are defined by

$$J[a(x_1),\ b(x_2)] \equiv \int dx_2\ \theta_{12}\mathcal{J}(1,2)\ f_o(p_1)f_o(p_2) \times [a(x_1)\ b(x_2) + a(x_2)\ b(x_1)]\ , \tag{3-97}$$

and

$$I[\psi^{(1)}] \equiv \int dx_2\ \theta_{12}\mathcal{J}(1,2)\ [f_o(p_1)\ \psi^{(1)}(x_2;t) + f_o(p_2)\ \psi^{(1)}(x_1;t)]\ .$$

In equations (3-97) and (3-98), $\mathcal{J}(1,2)$ is defined by

$$\mathcal{J}(1,2) \equiv \lim_{t\to\infty} S_{-t}(1,2)\ S_t^o(1,2)\ , \tag{3-99}$$

where $S_t(1,2)$ is the time development operator for two particles, according to Hamilton's equations of motion with interaction $\phi(\vec{q}_{12})$, and $S_t^o(1,2)$ is the corresponding operator without interaction (51).

The appearance of the non-linear operator, J, is a significant difference from the kinetic theory results for two-point correlation functions.

The general result, equation (3-93), simplifies somewhat for the special case of $G_3(\vec{r}',o;\vec{r}'',o;\vec{r},t)$. This triplet function is obtained using $a(x_i) = \delta(\vec{r}-\vec{q}_i)$, $b(x_i) = \delta(\vec{r}''-\vec{q}_i)$, and $y(x_i) = \delta(\vec{r}-\vec{q}_i)$, with the result

$$\begin{aligned} G_3(\vec{r}',o;\vec{r}'',o;\vec{r},t) &= \delta(\vec{r}'-\vec{r}'')\ G_2(\vec{r}',o;\vec{r},t) \\ &+ \rho h(\vec{r}'-\vec{r}'')\ [G_2(\vec{r}'',o;\vec{r},t) + G_2(\vec{r}',o;\vec{r},t)] \\ &+ \rho^2 \int d\vec{r}'''\ f(\vec{r}',\vec{r}'',\vec{r}''')\ G_2(\vec{r}''',o;\vec{r},t) \\ &+ \rho \int d\vec{p}_1\ d\vec{p}_2 \int_0^t d\tau\ K(x_1,x_2;t-\tau|\psi^{(1)}(\tau)) \ . \end{aligned} \tag{3-100}$$

The t=o limit of G_3 is

$$\begin{aligned} G_3(\vec{r}',o;\vec{r}'',o;\vec{r},o) &= \delta(\vec{r}'-r'')\ G_2(\vec{r}',o;\vec{r},o) \\ &+ \rho h(\vec{r}'-\vec{r}'')\ [G_2(\vec{r}'',o;\vec{r},o) + G_2(\vec{r}',o;\vec{r},o)] \\ &+ \rho^2 \int d\vec{r}'''\ f(\vec{r}',\vec{r}'',\vec{r}''')\ G_2(\vec{r}''',o;\vec{r},o) \ . \end{aligned} \tag{3-101}$$

This result may be used to simplify the first three terms in equation (3-100). To do this, define an inverse to $G_2(\vec{r}',o;\vec{r},o)$ by

$$\int d\vec{r}''\ G_2(\vec{r}',o;\vec{r}'',o)\ G_2^{-1}(\vec{r}'',o;\vec{r},o) = \delta(\vec{r}'-\vec{r}) \ . \tag{3-102}$$

Then, equation (3-100) may be written as

$$G_3(\vec{r}',o;\vec{r}'',o;\vec{r},t) = \int d\vec{r}_1\, d\vec{r}_2\, G_3(\vec{r}',o;r'',o;\vec{r}_1,o)$$

$$\times\, G_2^{-1}(\vec{r}_1,o;\vec{r}_2,o)\, G_2(\vec{r}_2,o;\vec{r},t)$$

$$+\, \rho \int d\vec{p}_1\, d\vec{p}_2 \int_0^t d\tau\, K(x_1,x_2;t-\tau|\psi^{(1)}(\tau)). \qquad (3\text{-}103)$$

The first term on the right side of equation (3-103) is what one might reasonably guess as a convolution approximation to G_3, relating it to $G_2(\vec{r}',o;\vec{r},t)$. Since this expression is exact at t=o, such a guess would satisfy the lowest-order sum rule for G_3. The inverse function, G_2^{-1}, is found to be (see Appendix C)

$$G_2^{-1}(\vec{r}',o;\vec{r},o) = \delta(\vec{r}'-\vec{r}) - \rho C(\vec{r}'-\vec{r}) \;, \qquad (3\text{-}104)$$

where C(r) is the direct correlation function.

To calculate $\frac{\partial S(Q,\omega)}{\partial P}$, it is useful to take the transform of equation (3-103) with respect to space and time,

$$\tilde{G}_3(\vec{Q}',\vec{Q};\omega) = G_3(\vec{Q}',\vec{Q};t=o)\; S^{-1}(Q)\; S(Q,\omega)$$

$$+\, \rho \int dx_1\, dx_2\, e^{i\vec{Q}'\cdot(\vec{q}_1+\vec{q}_2) + i\vec{Q}\cdot\vec{q}_1}\, P^{(2)}(x_1,x_2;\omega|\psi^{(1)}),$$

where S(Q) and C(Q) are related through equation (3-67).

Finally, the pressure derivative of $S(Q,\omega)$ follows from equations (3-105), (3-87) and (3-88):

$$\frac{\partial}{\partial P} S(Q,\omega) = \left(\frac{\partial S(Q)}{\partial P}\right) \frac{S(Q,\omega)}{S(Q)}$$

$$+\, \frac{1}{\rho kT} \int dx_1\, dx_2\, e^{i\vec{Q}\cdot\vec{q}_1}\, P^{(2)}(x_1,x_2;\omega|\psi^{(1)}) \quad . \qquad (3\text{-}106)$$

The first term in equation (3-106) may be determined entirely from calculation or measurement of $S(Q,\omega)$ and $\frac{\partial S(Q)}{\partial P}$. The remaining term depends directly on the functional $P^{(2)}$. As indicated by equation (3-65), the problem of deriving a suitable kinetic equation for the usual two-point correlation functions centers on the analysis of $P^{(2)}$. This is a difficult many-body problem in general, and the measurement of $S(Q,\omega)$ has been a valuable guide and test for approximate kinetic models. It is expected that measurement of the pressure derivative, $\frac{\partial S(Q,\omega)}{\partial P}$, will provide additional information in this regard.

3.5 Model Calculations

In this section, $S(Q,\omega)$ and its isothermal pressure derivative are estimated using a simple model for the collision operator. The extent to which information on $P^{(2)}(x_1,x_2;\omega|\psi^{(1)}(\omega))$ can be extracted from measurements on $S(Q,\omega)$ and $\frac{\partial S(Q,\omega)}{\partial P}$, is illustrated by comparing $\frac{\partial \ln S(Q,\omega)}{\partial P}$ with $\frac{\partial \ln S(Q)}{\partial P}$ as a function of ω for fixed Q, as suggested by equation (3-106).

A method for modeling operators in kinetic equations has been described by Gross[2] (52). Here, the analysis is performed using the simplest of these models, a single relaxation time approximation. The result is based on the assumption of only two points in the spectrum of $\hat{M}(Q,\omega)$. One point, zero, corresponding to the eigenfunction 1, follows from the conservation of particle number. The rest of the

---

[2] The details of kinetic modeling are discussed more generally in the next chapter.

spectrum of the exact operator is approximated by a single degenerate point denoted by $\lambda(Q,\omega)$. With these assumptions, the collision operator may be written as

$$M(Q,\omega) = -\lambda(Q,\omega)\ (1-P)\ , \tag{3-107}$$

with M related to $\hat{M}$ through equation (3-108),

$$M \equiv f_o^{-1}\ \hat{M}\ f_o\ , \tag{3-108}$$

and where P is the projection operator, defined for functions of momentum, h(p), by

$$Ph(p) \equiv \int d\vec{p}\ f_o(p)\ h(p)\ . \tag{3-109}$$

The single relaxation time model conserves particle number, by construction, but violates energy and momentum conservation. It is easy to incorporate the latter here by generalizing P to project onto the five-dimensional subspace (see Chapter 4) of these conserved quantities, but in the interest of simplicity the single relaxation time model will suffice. The dynamic structure factor, $S(Q,\omega)$, depends on $M(Q,\omega)$ only through the function $I(Q,\omega)$, as shown in equation (3-37). Use of equation (3-107) for $M(Q,\omega)$ in equation (3-37) yields

$$I(Q,\omega) = \frac{\rho}{kT}\ [1 + i\omega\ \frac{F(Q,\omega)}{1-\lambda(Q,\omega)F(Q,\omega)}]\ , \tag{3-110}$$

where $F(Q,\omega)$ is

$$F(Q,\omega) \equiv \int d\vec{p}\ [-i\omega + i\ \frac{\vec{Q}\cdot\vec{p}}{m} + \lambda(Q,\omega)]^{-1}\ f_o(p). \tag{3-111}$$

To specify the function $\lambda(Q,\omega)$, the fact that $M(Q,\omega)$ must vanish as $\frac{1}{\omega}$ for large ω may be imposed by choosing the "viscoelastic" form (53)

$$\lambda(Q,\omega) = \frac{A(Q)\ \tau(Q)}{1 - i\omega\ \tau(Q)} \quad . \tag{3-112}$$

The function $A(Q)$ was determined by requiring the fourth frequency moment of $S(Q,\omega)$ to be satisfied exactly (see equation (3-13)), with the result

$$A(Q) = \rho\ \frac{Q^2}{m}\ [\frac{C(Q)}{kT} + \frac{1}{Q}\int d\vec{r}g(r)\ (1-\cos\ \hat{Q}.\vec{r})(\hat{Q}.\vec{r})^2\phi(r)]. \tag{3-113}$$

The remaining parameter, $\tau(Q)$, was determined in terms of $S(Q,\omega=o)$, as suggested by Kugler (40).

The functions $S(Q)$, $C(Q)$, and $A(Q)$ were calculated using Verlet's (28) Monte Carlo data for the pair correlation function, $g(r)$, for argon near its triple point. The function, $\tau(Q)$, was determined from Sköld's experimental data (54), and has been assumed to be a slowly varying function of the pressure. Appendix D contains the details for the calculations of this section.

Figure 3-2 shows a comparison of the static liquid structure factor, $S(Q)$, and its corresponding pressure derivative. Figures 3-3 through 3-5 are a comparison of $S(Q,\omega)$ with its pressure derivative at three values of Q accessible via neutron scattering. Finally, Figure 3-6 shows the difference between the logarithmic derivative of $S(Q,\omega)$ and the corresponding derivative of $S(Q)$, suggested by the rearrangement of equation (3-106):

$$\frac{\partial \ell n S(Q,\omega)}{\partial P} = \frac{\partial \ell n S(Q)}{\partial P} + \frac{1}{\rho kTS(Q,\omega)}\int dx_1\ dx_2\ e^{i\vec{Q}\cdot\vec{q}_1}\ P^{(2)}(x_1,x_2;\omega|\psi^{(1)}). \tag{3-114}$$

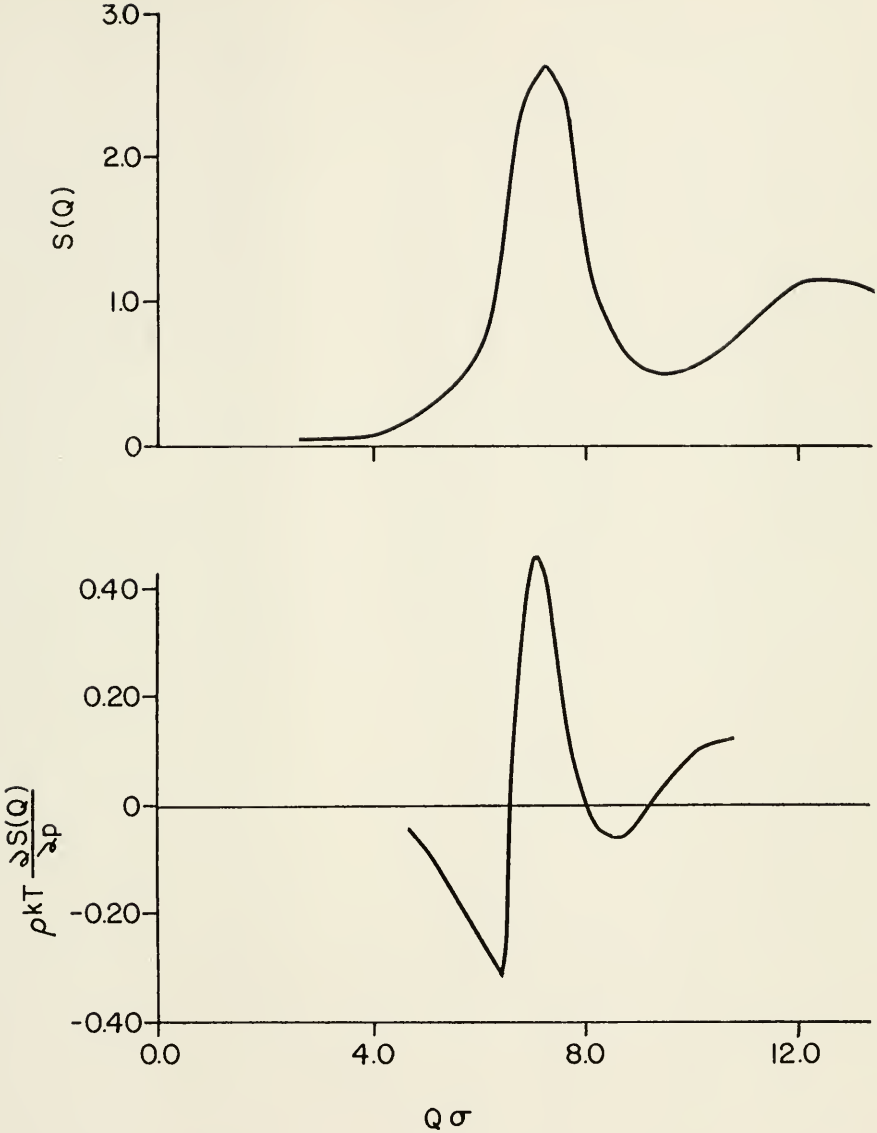

Figure 3-2. The static structure factor, S(Q), and $\partial S(Q)/\partial P$, for liquid argon near its triple point (T = 86.56 K, ρ = 1.402 gram/cm^3).

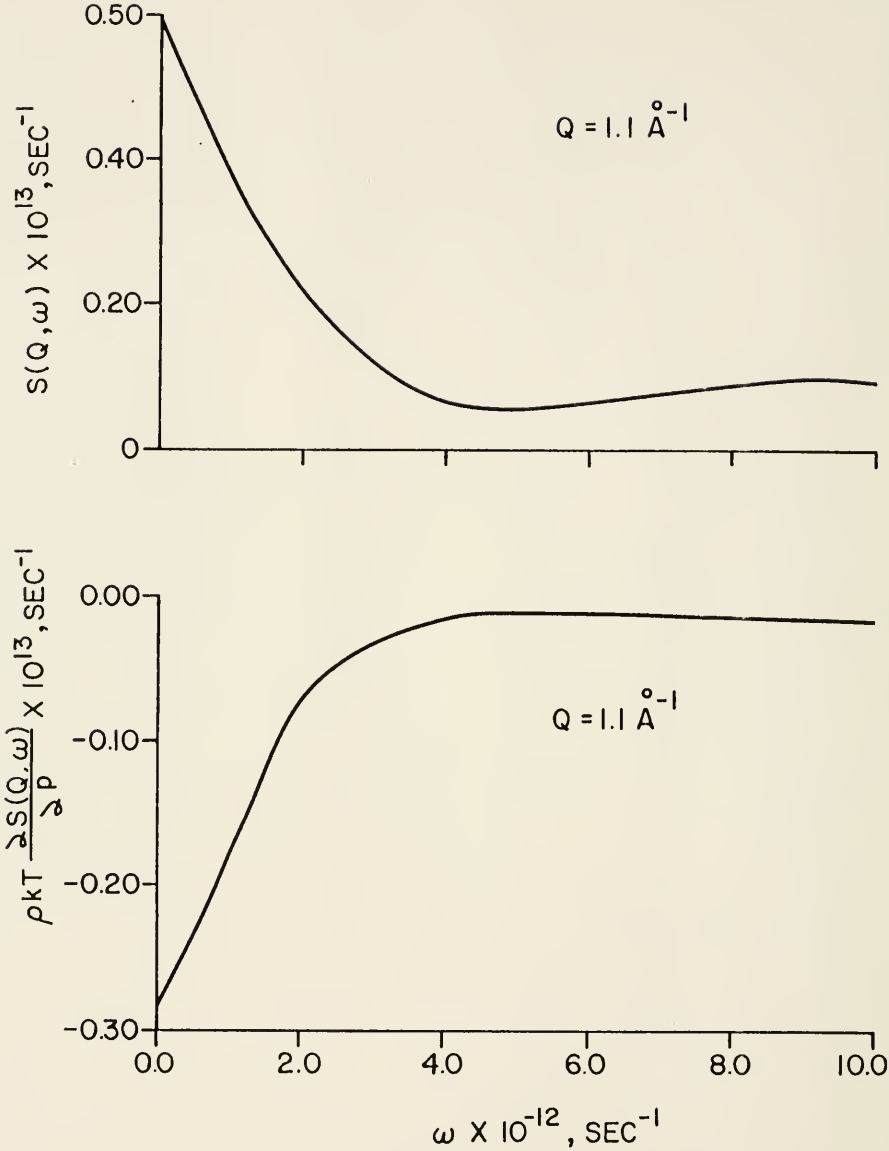

Figure 3-3. The dynamic structure factor, $S(Q,\omega)$, and $\partial S(Q,\omega)/\partial P$ for liquid argon near its triple point ($T = 86.56$ K, $\rho = 1.402$ gram/cm^3) at $Q = 1.1$ Å^{-1}.

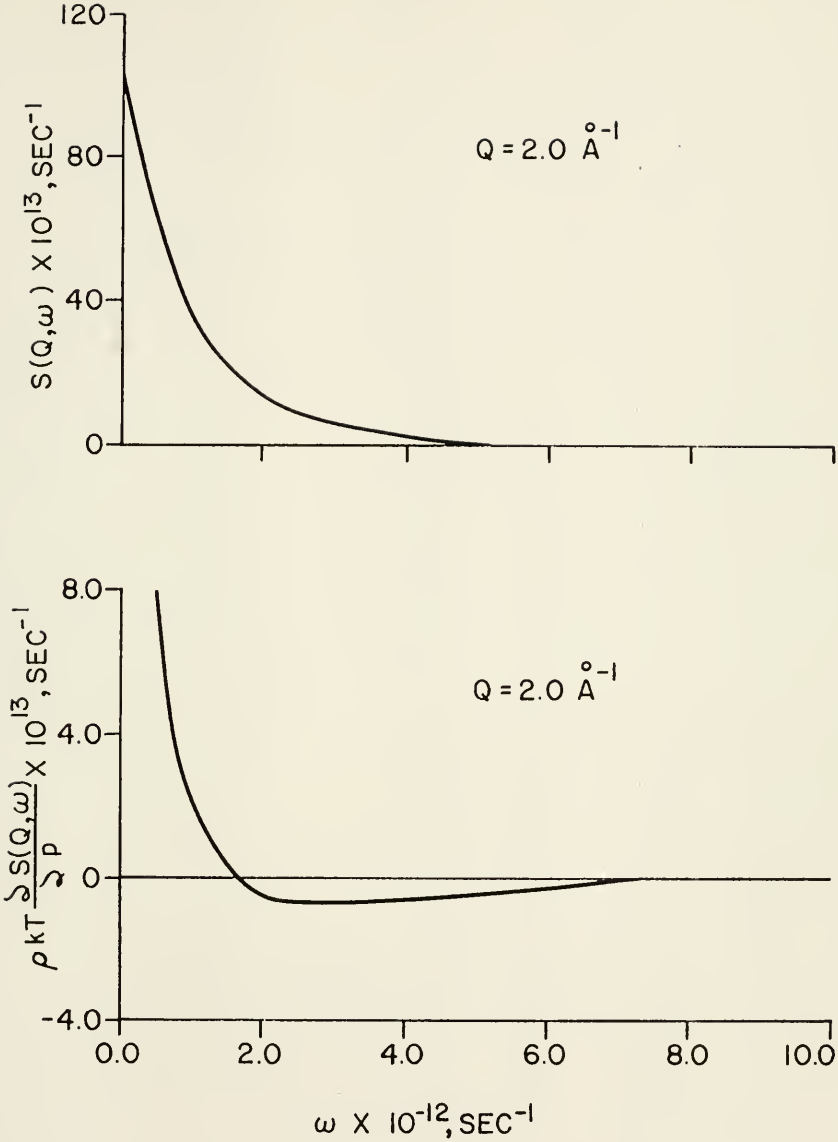

Figure 3-4. Same as Figure 3-3 except that Q = 2.0 Å^{-1}.

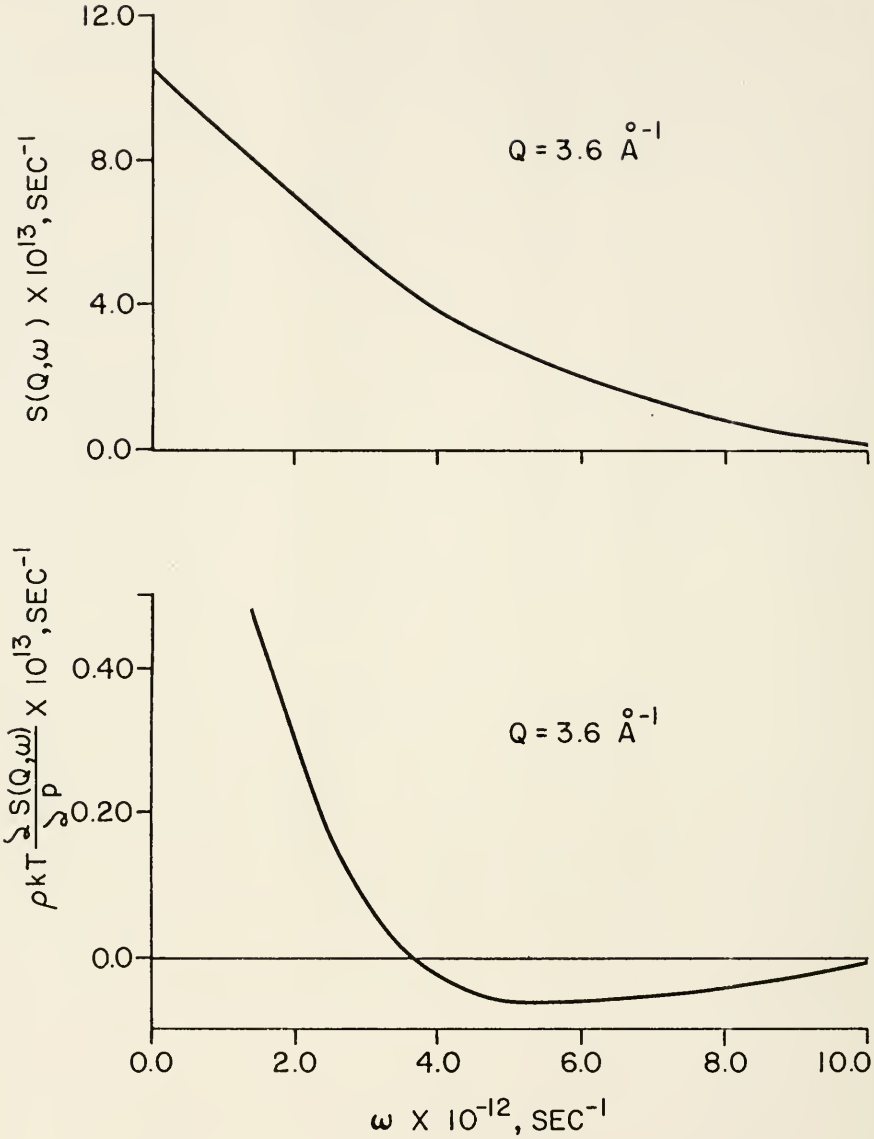

Figure 3-5. Same as Figure 3-3 except that Q = 3.6 $\mathring{A}^{-1}$.

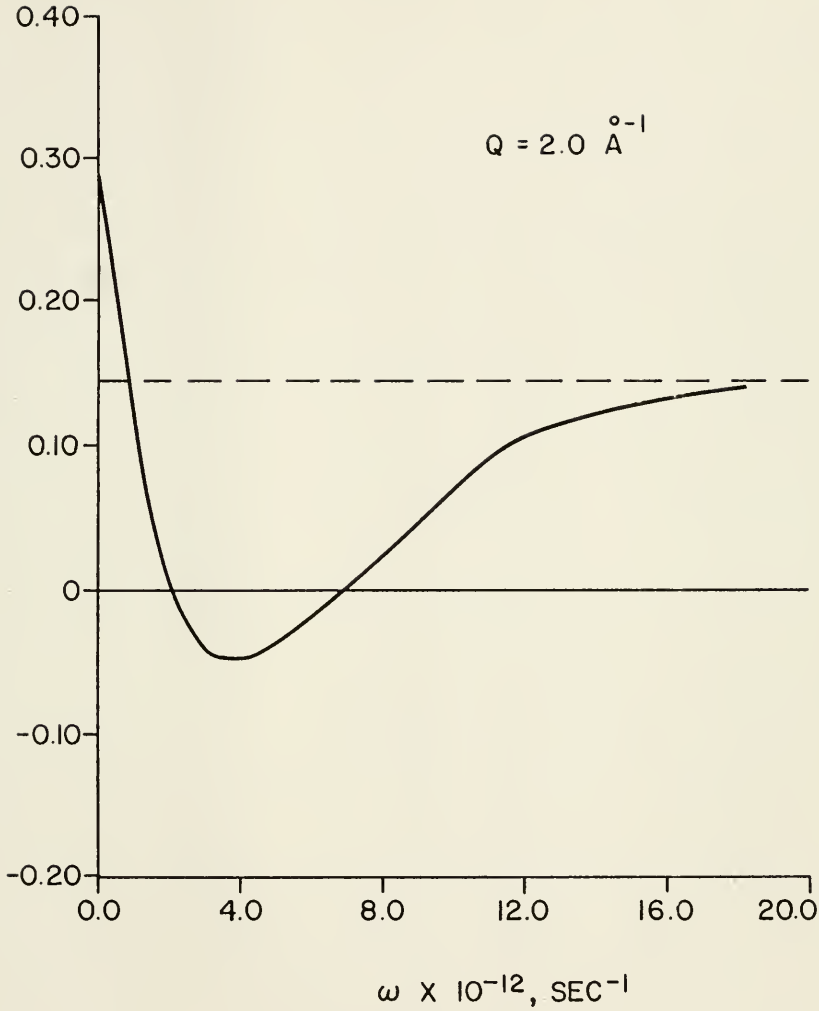

Figure 3-6. Comparison of $\partial \ln S(Q)/\partial P$ (---) and $\partial \ln S(Q,\omega)/\partial P$ (——) for liquid argon near its triple point (T = 86.56 K, ρ = 1.402 gram/cm^3) at Q = 2.0 Å^{-1}.

The two would be equal if the second term in equation (3-114) could be neglected. As the figure shows, such an approximation is good only for large ω (limit $t \to o$), in which case $P^{(2)}$ vanishes. The structure exhibited in Figure 3-6 is thus a measure of the degree to which $P^{(2)}$ may be probed experimentally in this manner. With the recent development of high flux neutron sources, and high resolution spectrometers, the required precision with which $S(Q,\omega)$ must be measured to study $P^{(2)}(x_1,x_2;\omega|\psi^{(1)}(\omega))$ experimentally should be possible.

3.6 Concluding Remarks

In this chapter the formal kinetic theory for two-time three-space correlation functions, as well as for the conventional two-time case, was developed in terms of the function $P^{(2)}(x_1,x_2;\omega|\psi^{(1)}(\omega))$. It was found that the formal kinetic theory for triplet (two-time, three-space) time correlation functions, equation (3-93), depends entirely on elements appearing in the kinetic theory for two-time correlation functions. However, the kernel of the collision operator, $P^{(2)}(x_1,x_2;\omega|\psi^{(1)}(\omega))$, appears explicitly, in contrast to its occurrence in the two-point theory only through the collision operator, $\hat{M}(Q,\omega)$. For this reason it is hoped that the direct dependence of the pressure derivative on the three-point correlation function will allow a more sensitive experimental test of models for $P^{(2)}(x_1,x_2;\omega|\psi^{(1)}(\omega))$. The direct calculation of the pressure derivative in Section 3.5 indicates the expected form for these experiments, and reflects essentially the pressure dependence of $\hat{M}(Q,\omega)$. This information, when coupled with similar measurements of the temperature derivative of $S(Q,\omega)$ (55), should assist in the construction and test of approximate linear kinetic models.

CHAPTER 4

KINETIC MODELING OF THE DYNAMIC STRUCTURE FACTOR

4.1 Introduction

In Chapter 3 a formal kinetic equation, equation (3-66), for the (Fourier and Laplace transformed) distribution function, $\tilde{\psi}^{(1)}(\vec{p};Q,\omega)$, was derived in terms of the generalized collision operator, $\hat{M}(Q,\omega)$, and the dynamic structure factor, $S(Q,\omega)$, was expressed as a function of $\hat{M}(Q,\omega)$ in equation (3-35):

$$S(Q,\omega) = 2\ \mathrm{Real}\left\{\int d\vec{p}\left[-i\omega + i\,\frac{\vec{Q}\cdot\vec{p}}{m} + \hat{B} - \hat{M}(Q,\omega)\right]^{-1} f_o(p)\ S(Q)\right\} \quad . \tag{3-35}$$

There are two distinct problems associated with the evaluation of $S(Q,\omega)$ from this result. The first concerns the construction of an explicit expression or approximation for the operator $\hat{M}(Q,\omega)$ from its formal definition, equation (3-34). Such a construction requires a detailed study of the many-body problem; presently, firm theoretical understanding of $\hat{M}(Q,\omega)$ is limited to small parameter expansions, such as low density or weak coupling results, although considerable progress on dense gases and even liquids has been made in recent years. This thesis will not be concerned with such studies beyond the hard core results presented in Chapter 3. The second problem

involved in determining $S(Q,\omega)$ from equation (3-35) is related to the more technical or mathematical problem of evaluating the integral on the right side of equation (3-35) for a given operator, $\hat{M}(Q,\omega)$, (or approximation to $\hat{M}(Q,\omega)$) whose properties are known. This is the problem of kinetic modeling and is the central theme of this chapter.

Kinetic modeling refers to the replacement of the given collision operator by a model collision operator which is more tractable from a computational point of view, but which preserves the important properties of the given collision operator. The most common method of kinetic modeling is the Gross-Jackson (56) method, which is described in the next section. Briefly, this method represents the collision operator in terms of a finite number (say N) of "matrix elements" of the collision operator with respect to a chosen complete set of functions of the momentum. The remaining matrix elements are approximately represented by the single $(N+1)^{st}$ matrix element. In this way, $S(Q,\omega)$ may be determined from a set of N coupled linear equations. This method has been used successfully by Sugawara, Yip, and Sirovich (57) for the linearized Boltzmann equation and more recently by Mazenko, Wei and Yip (58) for the generalized Boltzmann equation, equation (3-74), for a system of hard spheres.

The drawback of the Gross-Jackson method is that the number, N, of matrix elements, and hence coupled equations to be solved, is large if substantial accuracy is desired. For the problem considered here such accuracy is required in order to make as faithful a correspondence as possible between the measured $S(Q,\omega)$ and the theoretically chosen $\hat{M}(Q,\omega)$. For hard spheres the above authors find they must choose

$N > 30$ to achieve an accuracy in $S(Q,\omega)$ on the order of 2 per cent. The calculations are non-trivial for such a large number of matrix elements and may be expected to be considerably more complex for more realistic potential models.

A method for optimizing the Gross-Jackson procedure is also suggested in this chapter. The objective of this optimized kinetic model is to significantly reduce the order, N, required without a substantial reduction in accuracy. Although preliminary, the optimization scheme is tested for the Fokker-Planck and Boltzmann-Lorentz kinetic equations to calculate the self structure factor, $S_s(Q,\omega)$, and found to be quite good when compared with existing results.

4.2 Gross-Jackson Kinetic Modeling

The expression for $S(Q,\omega)$, equation (3-35), contains both the mean field operator, $\hat{B}$, and the collision operator, $\hat{M}$; however, the effect of the operator $\hat{B}$ may be calculated explicitly (see equations (3-70) and (3.74) for hard spheres) so that $S(Q,\omega)$ may be written as

$$S(Q,\omega) = 2 \text{ Real} \left\{ \frac{S(Q) \int d\vec{p}\, f_o(p)\, Y(p)}{1-\rho[C(Q)-g(r_o)C_o(Q)] \int d\vec{p}\, f_o(p)\, \frac{i\vec{Q}\cdot\vec{p}}{m}\, Y(p)} \right\} . \tag{4-1}$$

Here, $Y(p)$ is defined by

$$Y(p) \equiv [-i\omega + \frac{i\vec{Q}\cdot\vec{p}}{m} - M(Q,\omega)]^{-1}\, 1 , \tag{4-2}$$

and the operator $M(Q,\omega)$, rather than $\hat{M}(Q,\omega)$, has been introduced for convenience:

$$M(Q,\omega) \equiv f_o^{-1}(p)\, \hat{M}(Q,\omega)\, f_o(p) . \tag{3-108}$$

The problem of calculating $S(Q,\omega)$ therefore reduces to a determination of $Y(p)$ through kinetic modeling of $M(Q,\omega)$.

The Gross-Jackson kinetic model for evaluating the dynamic structure factor is based on the formal decomposition of a given collision operator, $M(Q,\omega)$. In this section the expansion technique is discussed in more detail, and a relatively simple, N=6, kinetic model for the generalized Enskog collision operator is used to calculate $S(Q,\omega)$. To facilitate the description, it is useful to introduce a scalar product notation,

$$(a,b) \equiv \int d\vec{p}\ f_o(p)\ a^*(p)\ b(p), \tag{4-3}$$

where a and b are arbitrary functions of $\vec{p}$ and * denotes complex conjugation. Further, let $\{\psi_\alpha(p)\}$ denote a complete set of functions of $\vec{p}$. Then, an arbitrary function, $a(p)$, may be expanded in terms of the set $\{\psi_\alpha(p)\}$,

$$a(p) = \sum_{\alpha=1}^{\infty} \psi_\alpha(p)\ (\psi_\alpha, a)\ . \tag{4-4}$$

The operator, $M(Q,\omega)$, may be completely characterized by its matrix elements with respect to the set $\{\psi_\alpha(p)\}$. To show this consider the action of $M(Q,\omega)$ on an arbitrary function $b(p)$ and denote the result by $a(p)$:

$$a(p) \equiv M(Q,\omega)\ b(p)\ .$$

Then, the expansion of $b(p)$ according to equation (4-4) gives

$$M(Q,\omega)\ b(p) = \sum_{\alpha=1}^{\infty} \psi_\alpha(p)\ (\psi_\alpha, Mb)\ .$$

A further expansion of b yields the desired result:

$$M(Q,\omega)\ b(p) = \sum_{\alpha=1}^{\infty} \sum_{\beta=1}^{\infty} \psi_\alpha(p)\ M_{\alpha\beta}(Q,\omega)\ (\psi_\beta, b)\ , \tag{4-5}$$

where the matrix elements $M_{\alpha\beta}(Q,\omega)$ are defined by

$$M_{\alpha\beta}(Q,\omega) \equiv (\psi_\alpha,\ M\ \psi_\beta)\ . \tag{4-6}$$

Equation (4-5) is exact, as no approximations have been introduced to this point. The details of the collision operator are contained in the matrix elements $M_{\alpha\beta}(Q,\omega)$ and in general there are infinitely many such matrix elements. The object of kinetic modeling is to approximate M in a form requiring only a finite number of matrix elements, with successively better approximations requiring more matrix elements. However, it is not possible to simply truncate the expansion of equation (4-5), as this would imply a restriction on the range and domain of M to functions expandable in only a finite number of the $\{\psi_\alpha\}$. To describe a more general approximation scheme, we first separate M into its contributions in the subspace of the first N ψ_α's plus the remainder:

$$\begin{aligned} M(Q,\omega)\ b(p) = & \sum_{\alpha=1}^{N} \sum_{\beta=1}^{N} \psi_\alpha(p)\ M_{\alpha\beta}(\psi_\beta, b) \\ & + \sum_{\alpha=1}^{N} \sum_{\beta=N+1}^{\infty} \psi_\alpha(p)\ M_{\alpha\beta}(\psi_\beta, b) \\ & + \sum_{\alpha=N+1}^{\infty} \sum_{\beta=1}^{N} \psi_\alpha(p)\ M_{\alpha\beta}(\psi_\beta, b) \\ & + \sum_{\alpha=N+1}^{\infty} \sum_{\beta=N+1}^{\infty} \psi_\alpha(p)\ M_{\alpha\beta}(\psi_\beta, b)\ . \end{aligned} \tag{4-7}$$

The objective now is to approximate the last three terms in equation (4-7), while preserving the exact form of M relative to the first N ψ_α's. Regarding the last three terms, we note that if the set $\{\psi_\alpha\}$ were eigenfunctions of $M(Q,\omega)$, then

$$M_{\alpha\beta} \to M_{\alpha\alpha}\ \delta_{\alpha\beta}\ .$$

For a suitably chosen complete set of functions $\{\psi_\alpha\}$, the matrix elements may also be assumed to be approximately diagonal. Therefore, the first approximation is to set $M_{\alpha\beta} = M_{\alpha\alpha}\ \delta_{\alpha\beta}$ in the last three terms in equation (4-7), with the result

$$M(Q,\omega)\ b(p) \to \sum_{\alpha=1}^{N} \sum_{\beta=1}^{N} \psi_\alpha(p)\ M_{\alpha\beta}(Q,\omega)\ (\psi_\beta, b)$$

$$+ \sum_{\alpha=N+1}^{\infty} \psi_\alpha(p)\ M_{\alpha\alpha}(Q,\omega)\ (\psi_\alpha, b)\ .$$

The second and final approximation is to represent all of the matrix elements for $\alpha \geq N + 1$ by the single degenerate value $\lambda_N \equiv M_{N+1,N+1}$, i.e.,

$$M(Q,\omega)\ b(p) \to \sum_{\alpha=1}^{N} \sum_{\beta=1}^{N} \psi_\alpha(p)\ M_{\alpha\beta}(Q,\omega)\ (\psi_\beta, b)$$

$$+ \lambda_N \sum_{\alpha=N+1}^{\infty} \psi_\alpha(p)\ (\psi_\alpha, b)\ , \tag{4-8}$$

with

$$\lambda_N \equiv M_{N+1,N+1}\ . \tag{4-9}$$

This defines the Gross-Jackson kinetic model of order N. It requires the exact matrix elements in the N-dimensional subspace of the first N ψ_α's and represents the operator in the orthogonal subspace by the single matrix element λ_N.

Further use of equation (4-4) in equation (4-8) allows the latter to be rewritten as

$$M_N(Q,\omega)\ b(p) = \sum_{\alpha=1}^{N} \sum_{\beta=1}^{N} M_{\alpha\beta}(Q,\omega)\ \psi_\alpha(p)\ (\psi_\beta, b)$$

$$+ \lambda_N(Q,\omega)\ [b(p) - \sum_{\alpha=1}^{N} \psi_\alpha(p)\ (\psi_\alpha, b)]\ , \qquad (4\text{-}10)$$

where the notation M_N is used to denote the Nth order Gross-Jackson kinetic model for $M(Q,\omega)$. Comparing equation (4-10) with equation (4-5), we see that the approximate collision operator M_N is exactly equal to the true collision operator in the subspace spanned by the set $\{\psi_\alpha\}$, for $\alpha \leq N$. Equation (4-10) is an approximate representation of the true collision operator with details of the given collision operator incorporated through the matrix elements $M_{\alpha\beta}$, although only approximately so for $\alpha > N$. For greater accuracy, the subspace may be increased by choosing a larger N.

To this point no statement has been made concerning the selection of the set $\{\psi_\alpha\}$. While somewhat arbitrary, the choice of $\{\psi_\alpha\}$ can be simplified by consideration of the characteristics of the collision operator. For example, from the fact that binary collisions conserve the number, momentum, and energy of the particles at $Q=o$, it follows that there is a five-fold degenerate eigenvalue of $M(Q,\omega)\big|_{Q=o}$, $\lambda=o$. In this case, the first five eigenfunctions might be chosen as $\{1, \frac{\vec{p}}{m}, \frac{p^2}{2m}\}$, corresponding to the number density, momentum, and kinetic energy. It is expected that when many elements are contained within $\{\psi_\alpha\}$, the choice of the set will be less important.

As an example of Gross-Jackson kinetic modeling, we consider a simple, N=6, model for the generalized Enskog collision operator (see equations (3-74) and (3-75)). The first five ψ_α's are chosen to ensure the conservation of particle number, momentum, and kinetic energy (as $Q \to o$),

$$\psi_1 = 1$$

$$\{\psi_2, \psi_3, \psi_4\} = \{ (\frac{\beta}{m})^{\frac{1}{2}} p_x, (\frac{\beta}{m})^{\frac{1}{2}} p_y, (\frac{\beta}{m})^{\frac{1}{2}} p_z\} \quad ,$$

$$\psi_5 = (\frac{2}{3})^{\frac{1}{2}} [\frac{\beta p^2}{2m} - \frac{3}{2}] \quad ;$$

ψ_6 is chosen to yield the thermal conductivity (in the limit $Q \to o$) as obtained from the solution of the Boltzmann equation,

$$\psi_6 = (\frac{\beta}{10m})^{\frac{1}{2}} p_z [\frac{\beta p^2}{m} - 5] \; ;$$

the eigenvalue, λ_6, is chosen to yield the corresponding ($Q \to o$) Boltzmann expression for the shear viscosity,

$$\lambda_6 = (\frac{\beta}{m})^2 (p_y p_z, M\, p_y\, p_z) \; .$$

Returning to equations (4-1) and (4-2) for $S(Q,\omega)$ and $Y(p)$, we replace M by M_6 to get the N=6 kinetic model approximation. From equation (4-10),

$$M_6(Q,\omega)\; b(p) = \lambda_6(Q,\omega)\; b(p) + \sum_{\alpha=1}^{6} \sum_{\beta=1}^{6} \mu_{\alpha\beta}(Q,\omega)\; \psi_\alpha(p)\; (\psi_\beta, b) \; , \tag{4-11}$$

and

$$\mu_{\alpha\beta}(Q,\omega) \equiv M_{\alpha\beta}(Q,\omega) - \lambda_6(Q,\omega)\ \delta_{\alpha\beta} \quad , \tag{4-12}$$

where again b(p) is an arbitrary function of momentum. Use of equation (4-11) in equation (4-2) gives for Y(p)[1]

$$Y(p) = R_N\ 1 \ ,$$

with

$$R_N \equiv [-i\omega + \frac{i\vec{Q}\cdot\vec{p}}{m} - M_6(Q,\omega)]^{-1} \quad ,$$

or equivalently

$$Y(p) = R_{oo}1 + R_{oo} \sum_{\alpha=1}^{6} \sum_{\beta=1}^{6} \mu_{\alpha\beta}\ \psi_\alpha(p)\ (\psi_\beta,\ Y) \ , \tag{4-13}$$

where

$$R_{oo} \equiv [-i\omega + \frac{i\vec{Q}\cdot\vec{p}}{m} - \lambda_6(Q,\omega)]^{-1} \quad . \tag{4-14}$$

In the equation for Y(p), equation (4-13), there are six unknowns, i.e., (ψ_β, Y) for $\beta = 1,\ldots,6$, requiring six independent equations. The six linearly independent equations are generated by successively multiplying equation (4-13) by ψ_α (for $\alpha \leq 6$) and carrying out the required momentum integration. Details of this procedure are given in Appendix E, along with the final results for $S(Q,\omega)$.

The N=6 kinetic model is used in Chapter 7 to analyze the neutron scattering measurements of $S(Q,\omega)$ for low density xenon gas. An estimate on the accuracy of this model can be obtained by comparing the N=6 model with the corresponding N=30 kinetic model

---

[1]For convenience the same notation is used for the approximate Y(p).

solution of Mazenko et al. (58) for a dilute hard sphere gas. It is convenient (for calculation purposes) to define the following dimensionless variables:

$$R(x,y) \equiv \frac{\sqrt{2}}{\pi} Q\, v_o\, S(Q,\omega)$$

with

$$x \equiv \frac{\omega}{\sqrt{2}\, Q\, v_o}$$

$$y \equiv \frac{4\rho^*}{Q\, r_o} \quad . \tag{4-15}$$

Here, ρ^* is the reduced number density ($\equiv \rho r_o^3$), and r_o is the hard sphere radius. Figure 4-1 compares the N=6 kinetic model (·) with the fully converged, N=30, solution (——) of Mazenko and coworkers (58) for y = 0.067 (This corresponds to a reduced density of 0.010 and a hard sphere radius $\sim$ 3 Å, yielding Q $\sim$ 0.20 $Å^{-1}$). Clearly, in this region of Q space the N=6 kinetic model is in excellent agreement with the fully converged solution. Unfortunately, the additional results (for ρ^* = 0.010) given by Mazenko et al. (58) (i.e., y = 0.50, y = 1.17, y = 3.0) correspond to a Q range (i.e., Q = 0.030, Q = 0.010, Q = 0.004) not covered experimentally, thereby limiting the comparison of the two models to Figure 4-1. Considerably larger errors are expected in the transition region (y $\sim$ 1) thus requiring larger N for accurate kinetic modeling.

4.3 Optimization of the Gross-Jackson Kinetic Model

In general, the calculation of the dynamic structure factor by expanding the collision operator in a complete set of orthogonal functions, $\{\psi_\alpha\}$, requires a large number of terms (N > 30 for the

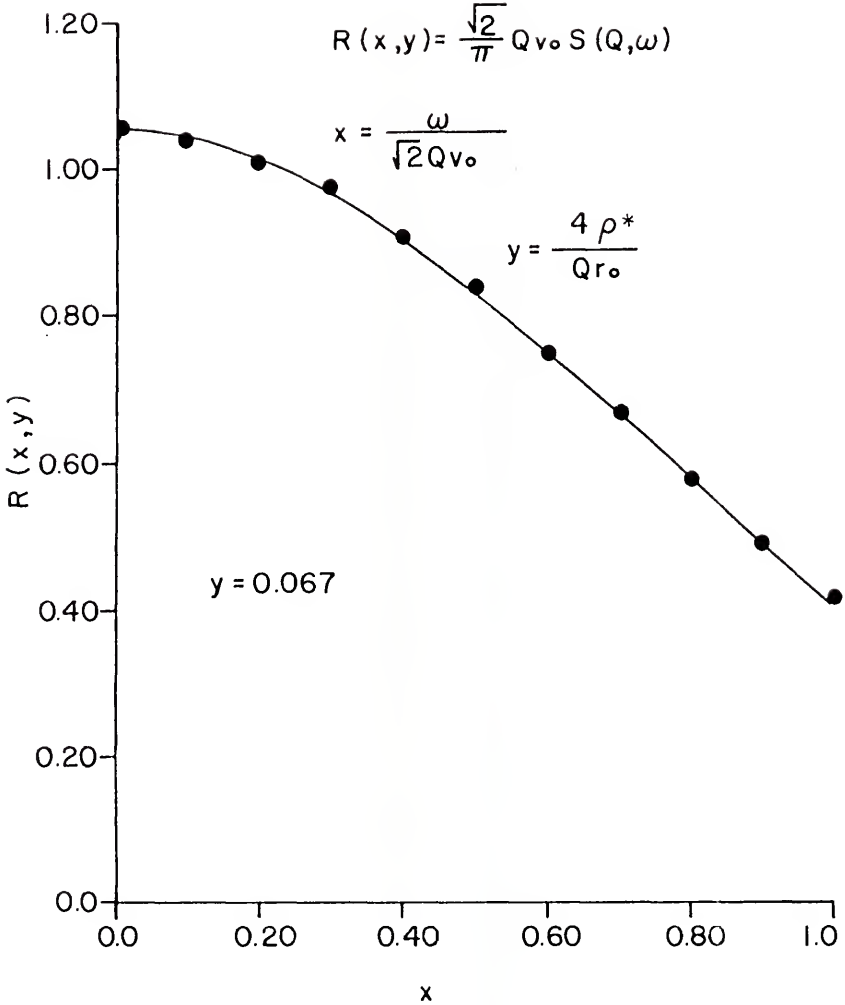

Figure 4-1. The dynamic structure factor, $S(Q,\omega)$, for the N = 6 Gross-Jackson kinetic model (•). Included is the fully converged, N = 30, solution (——).

generalized Enskog collision operator) if considerable accuracy ($\sim$ 2%) is desired. The solution of the modeled kinetic equation becomes quite complicated since the higher-order matrix elements, $M_{\alpha\beta}$, are expressed as rather involved nested sums; the computation time required to determine $S(Q,\omega)$ is on the order of a few hours on an IBM 360/168 computer (59) for the N=30 hard sphere kinetic model discussed in the previous section. In view of these results, a new approach to kinetic modeling is proposed in this section, which may be useful when more realistic potential models or more complex collision operators are considered. This technique differs from the standard Gross-Jackson modeling by replacing the eigenvalue λ_N (see equation (4-9)) with an appropriately chosen function, $\lambda(Q,\omega)$. In this way it is hoped to incorporate in $\lambda(Q,\omega)$ more of the important part of the spectrum of $M(Q,\omega)$ in the subspace of the ψ_α's for $\alpha > N$, so that low-order kinetic models may be used in the analysis of $S(Q,\omega)$ without significant loss in accuracy.

4.3.1 Formal Expression for $\lambda(Q,\omega)$. Returning to equation (4-1), we note the identity

$$(1, \frac{i\vec{Q}\cdot\vec{p}}{m} Y) = 1 + i\omega\ (1, Y)\ , \tag{4-16}$$

where use has been made of the fact that

$$(1, Ma) = 0$$

for arbitrary a (by conservation of particle number). Then, equation (4-1) may be written as

$$S(Q,\omega) = 2\ S(Q)\ \text{Real}\ \{\frac{I(Q,\omega)}{1-\rho[C(Q)-g(r_o)C_o(Q)][1+i\omega I(Q,\omega)]}\}, \quad (4\text{-}17)$$

with

$$I(Q,\omega) \equiv (1,Y)\ . \quad (4\text{-}18)$$

From equation (4-2), Y(p) is given by

$$Y = R\ 1\ , \quad (4\text{-}19)$$

and

$$R \equiv [-i\omega + \frac{i\vec{Q}\cdot\vec{p}}{m} - M(Q,\omega)]^{-1}\ . \quad (4\text{-}20)$$

Replacing the given collision operator, $M(Q,\omega)$, with a model collision operator, $M_o(Q,\omega)$, yields an approximate solution, $Y_o(p)$,

$$Y_o = R_o\ 1 \quad (4\text{-}21)$$

with

$$R_o \equiv [-i\omega + \frac{i\vec{Q}\cdot\vec{p}}{m} - M_o(Q,\omega)]^{-1}\ . \quad (4\text{-}22)$$

The exact and approximate solutions are then related by

$$Y(p) = Y_o(p) + R_o(M-M_o)\ Y(p), \quad (4\text{-}23)$$

as follows from the identity

$$R = R_o + R_o(M-M_o)\ R. \quad (4\text{-}24)$$

Correspondingly, $S(Q,\omega)$ may be expressed as

$$S(Q,\omega) = S^{(o)}(Q,\omega) + \Delta S(Q,\omega)\ , \quad (4\text{-}25)$$

where $S^{(o)}(Q,\omega)$ is the approximate $S(Q,\omega)$ determined by the replacement of M by M_o,

$$S^{(o)}(Q,\omega) \equiv 2\, S(Q)\ \text{Real}\ \left\{ \frac{I^{(o)}(Q,\omega)}{1-\rho\,[C(Q)-g(r_o)C_o(Q)]\,[1+i\omega I^{(o)}(Q,\omega)]} \right\} \tag{4-26}$$

with

$$I^{(o)}(Q,\omega) \equiv (1,\ Y_o)\ . \tag{4-27}$$

The form of $\Delta S(Q,\omega)$ is easily identified by comparison of equations (4-25) and (4-17), but for the time being it is sufficient to observe that $\Delta S(Q,\omega)$ is proportional to the difference $I-I^{(o)}$,

$$\begin{aligned} \Delta S(Q,\omega) &\ \alpha\ I-I^{(o)} \\ &\equiv \Delta I\ . \end{aligned} \tag{4-28}$$

The optimization of a given method of kinetic modeling may now be described. We assume that a kinetic model, M_o, may be parameterized by a complex parameter, λ. Then λ is chosen to minimize the contribution from $\Delta S(Q,\omega)$ in equation (4-25) and hence improve the approximation, $S^{(o)}(Q,\omega)$, to $S(Q,\omega)$. In particular, $\lambda(Q,\omega)$ is chosen to make $\Delta I = 0$ so that, with equation (4-28), $\Delta S(Q,\omega)$ also vanishes. One then has, formally,

$$S(Q,\omega) = S^{(o)}(Q,\omega)\ . \tag{4-29}$$

Thus, the kinetic model, $M_o(\lambda)$, is parameterized in such a way as to yield the same $S(Q,\omega)$ as the given collision operator, M. It must be expected, of course, that the expression for λ obtained from

$$\Delta I(\lambda) = 0 \tag{4-30}$$

will be itself difficult to evaluate. However, it may also be expected that equation (4-30) is much less sensitive to approximations than $S(Q,\omega)$ itself.

As a specific example of the optimization scheme, consider M_o to be the Nth-order Gross-Jackson kinetic model, equation (4-10),

$$M_o(\lambda)b(p) = \sum_{\alpha=1}^{N} \sum_{\beta=1}^{N} M_{\alpha\beta}(Q,\omega)\ \psi_\alpha(p)\ (\psi_\beta,b)$$

$$+ \lambda[b(p) - \sum_{\alpha=1}^{N} \psi_\alpha(p)\ (\psi_\alpha,b)]\ , \qquad (4\text{-}31)$$

where the Gross-Jackson constant λ_N (given by equation (4-9)) has been replaced by the complex parameter, λ. With the choice of equation (4-31), $S^{(o)}(Q,\omega)$ may be calculated as described for the usual Gross-Jackson model. However, now the parameter λ is chosen according to equation (4-30),

$$\Delta I(\lambda) = 0$$

$$= (1,[Y-Y_o]\ 1)$$

or, using equation (4-23) for the difference, $Y-Y_o$, λ is chosen such that

$$(1,\ R_o[M-M_o]\ R\ 1) = 0\ . \qquad (4\text{-}32)$$

From the discussion of Section 4.2 it is clear that M and M_o are identical in the subspace of the first N ψ_α's, so that equation (4-32) refers to the properties of the collision operator, M, in the orthogonal subspace. Defining $M_\perp$ by

$$M_{\perp} b(p) \equiv M\, b(p) - \sum_{\alpha=1}^{N} \sum_{\beta=1}^{N} M_{\alpha\beta}\, \psi_{\alpha}(p)\, (\psi_{\beta}, b) \;, \tag{4-33}$$

equations (4-31) and (4-32) give the desired expression for λ:

$$\lambda(Q,\omega) = \frac{(1,\ R_o\ M_{\perp} R1)}{(1,\ R_o[1-P_N]\ R1)} \quad . \tag{4-34}$$

Here, $(1-P_N)$ is a projection operator orthogonal to the first N ψ_{α}'s,

$$(1-P_N)\ b(p) = b(p) - \sum_{\alpha=1}^{N} \psi_{\alpha}(p)\ (\psi_{\alpha}, b) \ . \tag{4-35}$$

This choice (equation (4-34)) makes the order N kinetic model yield the exact $S(Q,\omega)$. All of the details of the collision operator in the subspace orthogonal to the first N ψ_{α}'s are contained in the expression for $\lambda(Q,\omega)$. Of course, the latter is now very difficult to compute. However, it may be expected that the variation of $\lambda(Q,\omega)$ with Q and ω is much milder than that of $S(Q,\omega)$ (indeed this is shown to be true below) and therefore more amenable to approximation. One such approximation to equation (4-34) can be made by noting that the condition (4-32) implies

$$(Y_o^*,\ M_{\perp} Y) = 0 \quad ,$$

so that the two functions, Y and Y_o are equal in some subspace, i.e.,

$$(1,\ Y) = (1,\ Y_o) \ ,$$

or equivalently,

$$(1,\ R1) = (1,\ R_o 1) \quad .$$

This suggests expanding R about R_o, as a general approximation to R. To lowest order, replacing R1 in equation (4-35) with $R_o 1$ yields the final expression for λ:

$$\lambda(Q,\omega) = \frac{(1,\ R_o\ M_\perp R_o 1)}{(1,\ R_o[1-P_N]R_o 1)} \quad . \tag{4-36}$$

We now briefly summarize the results of this section. The difference between the optimized kinetic model presented above and the standard Gross-Jackson kinetic model discussed in Section 4.2 centers around the identification of the eigenvalue λ_N. In particular, the Gross-Jackson recipe identifies λ_N as the matrix elements $(\psi_{N+1},\ M\psi_{N+1})$, whereas the optimized model replaces λ_N with a well-defined function of Q and ω(equation (4-34)) by requiring

$$S(Q,\omega) = S^{(o)}(Q,\omega).$$

The parameter λ (determined in this way) has the property such that

$$\lim_{Q\to 0} \lambda(Q,\omega) = \lambda_N \quad . \tag{4-37}$$

For cases in which Q is not small, $\lambda(Q,\omega)$ is determined from the matrix element (in the approximation of equation (4-36))

$$\lambda(Q,\omega) \propto (Y_o^*,\ M\ \ Y_o) \quad .$$

As a function of $\vec{p}$, $Y_o(Q,\omega;\vec{p})$ would require an expansion in terms of all of the set $\{\psi_\alpha\}$, for accurate representation. Because of this, it is hoped that $\lambda(Q,\omega)$ determined from equation (4-36) may better sample the spectrum of $M(Q,\omega)$ in the orthogonal subspace so that

low-order kinetic models may be used in the analysis of $S(Q,\omega)$. In Section 4.4 the calculation of the self structure factor, $S_s(Q,\omega)$, provides a test of the optimized kinetic model. The results are good, and the functional dependence of λ on Q and ω is found to be surprisingly simple.

4.4 Model Calculations

Because the self structure factor, $S_s(Q,\omega)$, is somewhat more tractable (in a mathematical sense) than $S(Q,\omega)$, and is directly accessible experimentally through radiation scattering measurements, calculation of $S_s(Q,\omega)$ provides a good test of the optimized kinetic model developed in Section 4.3. In the case of self correlations,

$$S(Q) = 1,$$

$$C(Q) = 0 = C_o(Q)$$

and the formal expression for the self structure factor becomes (see, for example, equations (4-17) and (4-18))

$$S_s(Q,\omega) = 2 \text{ Real } \{I_s(Q,\omega)\} \ , \tag{4-38}$$

where $I_s(Q,\omega)$ is defined as

$$I_s(Q,\omega) \equiv (1, Y^s) \ , \tag{4-39}$$

and

$$Y^s(p) \equiv [-i\omega + \frac{i\vec{Q}\cdot\vec{p}}{m} - M_s(Q,\omega)]^{-1} \ . \tag{4-40}$$

A test of the optimized kinetic model for the Fokker-Planck and Boltzmann-Lorentz kinetic equations follows.

4.4.1 The Fokker-Planck Kinetic Equation. This simple example was chosen because the Fokker-Planck collision operator is physically realistic for Brownian particles and, more important, an exact solution of the kinetic equation for self correlations exists. For the Fokker-Planck collision operator,

$$M_s = \gamma_o[\vec{\nabla}_v - \beta m \vec{v}] \cdot \vec{\nabla}_v \ , \tag{4-41}$$

where γ_o is the Stokes friction constant, $I_s(Q,\omega)$ is shown by Lebowitz, Percus and Sykes (41) to be

$$I_s(Q,\omega) = (i\omega + DQ^2)^{-1} \ [1 + e^{K^2} \ K^{-2(T+Q^2)}$$

$$x \int_0^{K^2} dt \ e^{-t} \ t^{(T+Q^2)}] \ . \tag{4-42}$$

The parameters D, K, and T are defined as

$$D \equiv (\frac{1}{\beta m})^2 \frac{1}{\gamma_o} \ ,$$

$$K \equiv (\frac{1}{\beta m})^{3/2} \frac{Q}{\gamma_o} \ ,$$

and

$$T \equiv \frac{-i\omega}{\beta m \gamma_o} \ . \tag{4-43}$$

A simple model for the Fokker-Planck collision operator is the N=1 Gross-Jackson model (see equation (4-10))

$$M_1(Q,\omega) \ b(p) = \psi_1(\psi_1, M_s \ \psi_1) \ (\psi_1, b)$$

$$+ \lambda_1[b - \psi_1(\psi_1, b)] \ , \tag{4-44}$$

with

$$\lambda_1 \equiv (\psi_2, M_s \psi_2) \ . \tag{4-45}$$

With the choice

$$\psi_1 = 1 \ ,$$

$$\psi_2 = \left(\frac{\beta}{m}\right)^{\frac{1}{2}} p_z \ ,$$

$M_1(Q,\omega)$ may be compactly expressed as

$$M_1 = \lambda_1 [1-P_1] \tag{4-46}$$

and

$$\lambda_1 = \left(\frac{\beta}{m}\right) (p_z, M_s p_z)$$

$$= -\beta m \gamma_o \ , \tag{4-47}$$

where the projection operator, P_1, projects onto the function 1,

$$P_1 b(p) \equiv 1(1,b) \ ,$$

and equation (4-41) for $M_s(Q,\omega)$ was used to determine λ_1. The friction constant, γ_o, was chosen such that the self diffusion coefficient for the Fokker-Planck equation is the same as that given by the Boltzmann-Lorentz equation (see Section 4.4.2):

$$\lambda_1 = -\frac{8}{3} \left(\frac{\pi kT}{m}\right)^{\frac{1}{2}} \rho \ r_o^2$$

$$= -\beta m \gamma_o$$

or

$$\gamma_o = \frac{8}{3\pi} \left(\frac{\pi kT}{m}\right)^{3/2} \rho \; r_o^2 \; . \tag{4-48}$$

For this model, $I_s(Q,\omega)$ reduces to

$$I_s^{(o)}(Q,\omega) = \frac{J_o(Q,\omega)}{1 + \lambda_1 \; J_o(Q,\omega)} \quad , \tag{4-49}$$

where

$$J_o(Q,\omega) \equiv \frac{-i}{Q} \left(\frac{\beta m}{2}\right)^{\frac{1}{2}} \quad \Phi(z) \; ,$$

and the plasma dispersion function, $\Phi(z)$, is defined as

$$\Phi(z) \equiv \frac{1}{\sqrt{\pi}} \int_{-\infty}^{+\infty} dt \; \frac{e^{-t^2}}{t-z} \quad , \tag{4-50}$$

$$z \equiv \left(\frac{\beta m}{2}\right)^{\frac{1}{2}} \; \frac{\omega - i\lambda_1}{Q} \quad . \tag{4-51}$$

Although the choice

$$\lambda_1 = \left(\frac{\beta}{m}\right) \; (p_z, \; M_s \; p_z)$$

provides a good approximation to the self structure factor in the limit as $Q \to 0$, this choice is rather poor for the remaining (Q,ω) spectrum. As discussed in Section 4.3, the replacement of λ_1 with the optimally determined eigenvalue $\lambda(Q,\omega)$, expressed in terms of the Fokker-Planck operator in equation (4-34), should provide a better representation of $M_s(Q,\omega)$ over the entire (Q,ω) range. If we make the approximation leading to equation (4-36), we obtain the following expression for $\lambda(Q,\omega)$:

$$\lambda(Q,\omega) = \frac{(1,\ R_{oo}\ M_s\ R_{oo})}{(1,\ R_{oo}[1-P_1]\ R_{oo}} \quad , \tag{4-52}$$

where

$$R_{oo} \equiv [-i\omega + \frac{i\vec{Q}\cdot\vec{p}}{m} - \lambda(Q,\omega)]^{-1} \ .$$

Equation (4-52) is evaluated (using equation (4-41) for M_s) in Appendix F, with the result

$$\lambda(Q,\omega) = (\frac{\gamma_o \beta m}{3})\ [\frac{1-z^2+(\frac{3}{2} - z^2)z\phi(z)}{1+z\phi(z)+\frac{1}{2}\phi^2(z)}] \ , \tag{4-53}$$

where z is now a function of $\lambda(Q,\omega)$. Because $\lambda(Q,\omega)$ appears on the right side of equation (4-53), some type of iteration sheme is required to determine $\lambda(Q,\omega)$.

It is now easy to confirm the property of equation (4-37). In the limit of small Q, or large Z,

$$\phi(z) \to -\frac{1}{z} - \frac{1}{2z^3} - \ldots \ ,$$

so that

$$\lambda(Q,\omega) \to -\beta m \gamma_o \ ,$$

which is identical with equation (4-47).

The improvement of the optimized kinetic model over the N=1 Gross-Jackson kinetic model is apparent in Figure 4-2, a plot of $R_s(x,y)$ $(\equiv \frac{\sqrt{2}}{\pi} Qv_o S_s(Q,\omega))$ versus the reduced frequency, $x(\equiv \frac{\omega}{\sqrt{2}\ Qv_o})$, at a fixed $y(\equiv \frac{4\rho^*}{Qr_o})$. Since the characteristics of the line shape of $S_s(Q,\omega)$ are well represented by the half-width at half-maximum, $x_{\frac{1}{2}}$, defined by (60)

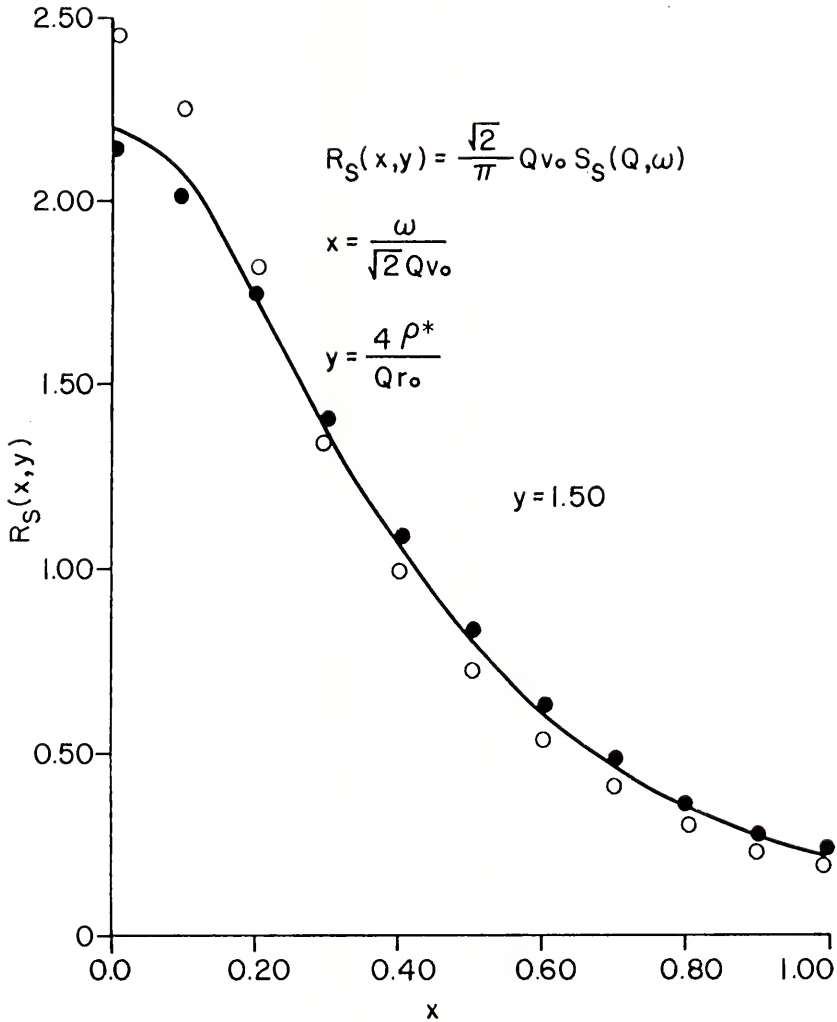

Figure 4-2. The self structure factor, $S_S(Q,\omega)$, for the Fokker-Plank model; exact solution (——), N = 1 Gross-Jackson (∘) and optimized (•) kinetic models.

$$R_s(x_{\frac{1}{2}}, y) \equiv \frac{1}{2} R_s(x=o, y) \ , \tag{4-54}$$

Figure 4-3, where $x_{\frac{1}{2}}$ is shown as a function of y, together with Figure 4-2, indicates that the optimized kinetic model for the Fokker-Planck collision operator is far superior to the N=1 Gross-Jackson kinetic model over the entire Q-range.

4.4.2 The Boltzmann-Lorentz Kinetic Equation. For a dilute gas of hard spheres, the collision operator for self correlations becomes

$$M_s[b(p)] = \rho \int d\vec{p}_2 \int' d\Omega \left| \frac{\vec{p}_1 - \vec{p}_2}{m} \right| \cdot \hat{r}_o \ f_o(p_1) \ f_o(p_2)$$

$$\times \ [b(p_1) - b(p_1')] \ . \tag{4-55}$$

Again we consider the N=1 Gross-Jackson kinetic model; the optimized kinetic model expression for $\lambda(Q,\omega)$ (see equation (4-52)) is

$$\lambda(Q,\omega) = \frac{(1, \ R_{oo} \ M_s \ R_{oo})}{1 + z\bar{\Phi}(z) + \frac{1}{2} \bar{\Phi}^2(z)} \ , \tag{4-56}$$

where $(1, \ R_{oo} \ M_s \ R_{oo})$ is given by (see Appendix G for details)

$$(1, \ R_{oo} \ M_s \ R_{oo}) = I_1^{(s)}(Q,\omega) + I_2^{(s)}(Q,\omega),$$

$$I_1^{(s)}(Q,\omega) = \frac{4r_o^2\rho}{v_o Q^2} \int_0^\infty dg \ g^2 \ e^{-g^2} \int_0^\infty dG \ e^{-G^2}$$

$$\times \ \left[\frac{1}{G+Z_+} + \frac{1}{G-Z_-} - \frac{1}{G-Z_+} - \frac{1}{G-Z_-}\right] ,$$

$$I_2^{(s)}(Q,\omega) = \frac{2r_o^2\rho}{v_o Q^2} \int_0^\infty dg \ g e^{-g^2} \int_0^\infty dG \ e^{-G^2} \ \times \ [F_1^2(Q,\omega) + F_2^2(Q,\omega)] \ ,$$

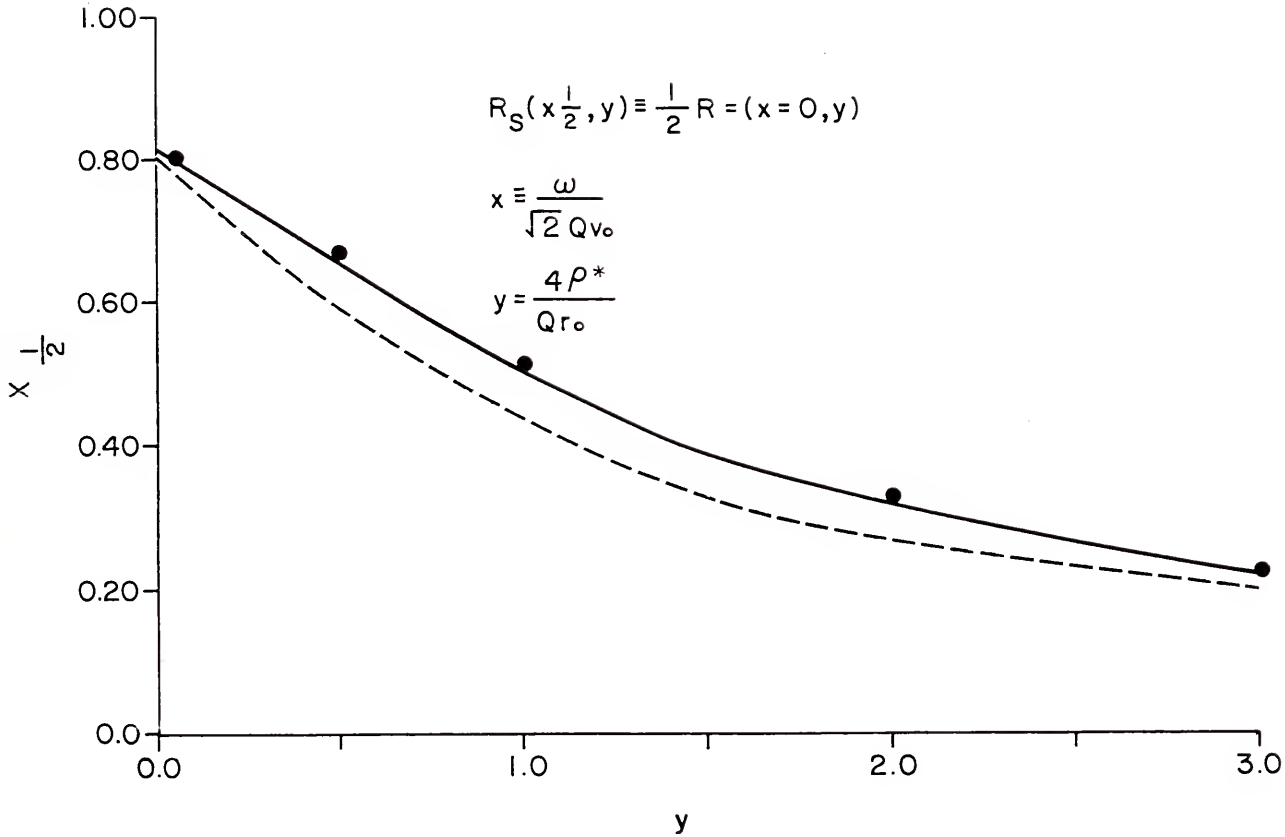

Figure 4-3. Half-width at half-maximum ($x_{\frac{1}{2}}$) for the Fokker-Plank model; exact solution (——), N = 1 Gross-Jackson (---), and optimized (•) kinetic models.

$$F_1(Q,\omega) \equiv \ln\left[\frac{G+Z_-}{G+Z_+}\right] ,$$

$$F_2(Q,\omega) \equiv \ln\left[\frac{G-Z_-}{G-Z_+}\right] ,$$

$$Z_+ \equiv \sqrt{2}\, Z + g ,$$

$$Z_- \equiv \sqrt{2}\, Z - g , \qquad (4\text{-}57)$$

and Z and $\varphi(Z)$ are defined by equations (4-51) and (4-50), respectively. The $Q \to 0$ (or large Z) limit of equation (4-56) is shown in Appendix F to yield λ_1, i.e.,

$$\lim_{Q\to 0} \lambda(Q,\omega) \to \frac{\beta}{m} (p_z, M_s\, p_z) .$$

which is consistent with equation (4-37).

As in the case of the Fokker-Planck collision operator, some type of iteration procedure is required to solve equation (4-56) for $\lambda(Q,\omega)$; successive substitution of the real and imaginary parts of $\lambda(Q,\omega)$ was found to be the most efficient procedure. Not more than four iterations were necessary to satisfy

$$[(\Delta\lambda_R)^2 + (\Delta\lambda_I)^2]^{\frac{1}{2}} \leq 0.01,$$

where $(\Delta\lambda_i)$ is the difference between successive values of the real (λ_R) or imaginary (λ_I) parts of $\lambda(Q,\omega)$. Less than 30 seconds on an IBM 370 computer were necessary to determine $\lambda(Q,\omega)$ at five values of the frequency for a given Q, using a combined Gaussian (N_G=48) - trapizoidal numerical integration scheme to evaluate $I_1^{(s)}(Q,\omega)$ and $I_2^{(s)}(Q,\omega)$.

As shown in Figures 4-4, 4-5 and 4-6, the optimized kinetic model (——) agrees favorably with the fully converged (N=30) model of Mazenko et al. (58). Included for comparison are the simple N=1 model (-•-•-) and the N=6 kinetic model (-∘-∘-) discussed in Section 4.2. The optimized kinetic model is seen in Figure 4-6, a plot of $x_{\frac{1}{2}}$ versus y, to be superior to these two models over the entire range of Q.

Finally, Figure 4-7 illustrates the functional dependence of $\lambda(Q,\omega)$ on the reduced frequency, x ($\equiv \frac{\omega}{\sqrt{2}\, Qv_o}$), for two values of y ($\equiv \frac{4\rho^*}{Qv_o}$). In general, λ_I was found to be a linearly increasing function of x, whereas λ_R decreased with x; the rate of change of λ_R and λ_I are a function of the parameter y. This simple behavior could prove valuable in speeding up the iteration of equation (4-36) for $\lambda(Q,\omega)$, and suggests λ to be a well-behaved function of both Q and ω. These figures also verify the speculation that $\lambda(Q,\omega)$ is structurally simpler than $S(Q,\omega)$ and hence probably more easily approximated.

4.5 Concluding Remarks

In this chapter the formal decomposition of the collision operator was discussed, a simple, N=6, kinetic model for $S(Q,\omega)$ was compared with the fully converged (N=30) results of Mazenko et al. (58) for a dilute, hard sphere gas, and a new (optimized) kinetic model was developed. The N=6 kinetic model was found to agree well with its fully converged (N=30) counterpart (assuming $\rho^* = 0.01$ and $Q \sim 0.20\ \text{Å}^{-1}$); unfortunately, no results exist for comparison in the experimental region of interest ($\rho^* \sim 0.25$, $Q \sim 1.0\ \text{Å}^{-1}$).

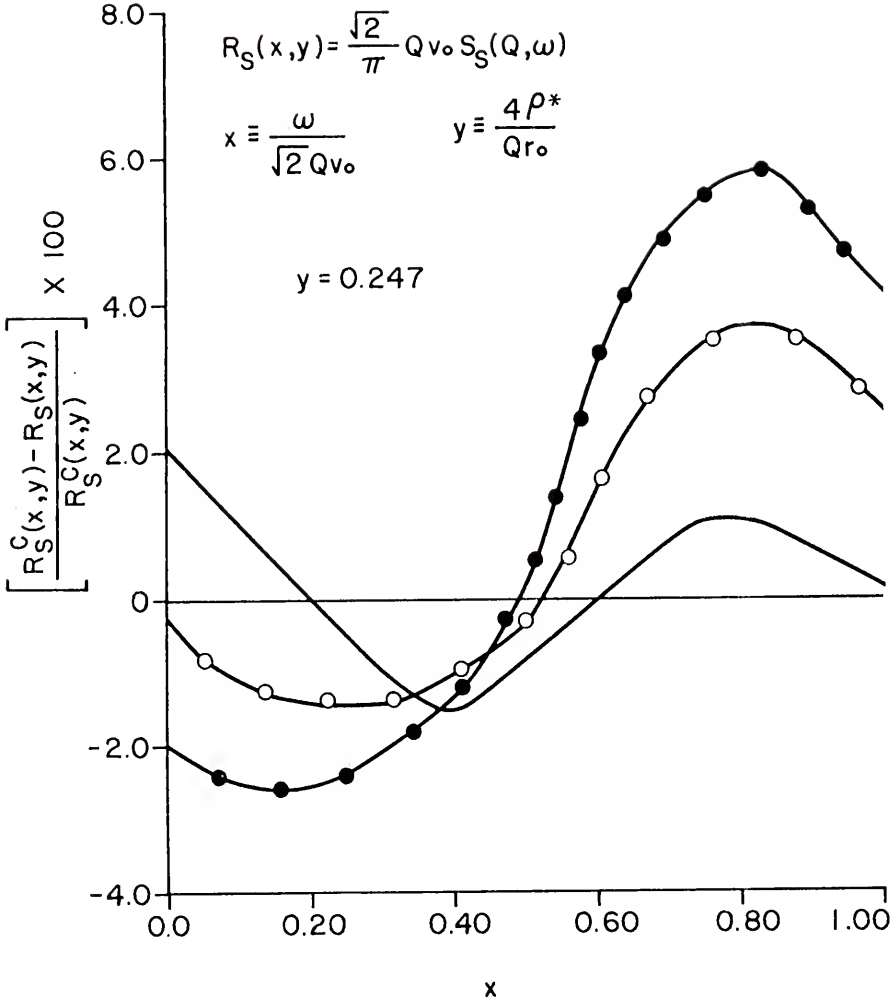

Figure 4-4. Percent deviation of the N = 1 (-•--•-), the N = 6 (-o-o-) and the optimized (——) kinetic models from the fully converged, N = 30, solution, $R_S^C(x,y)$.

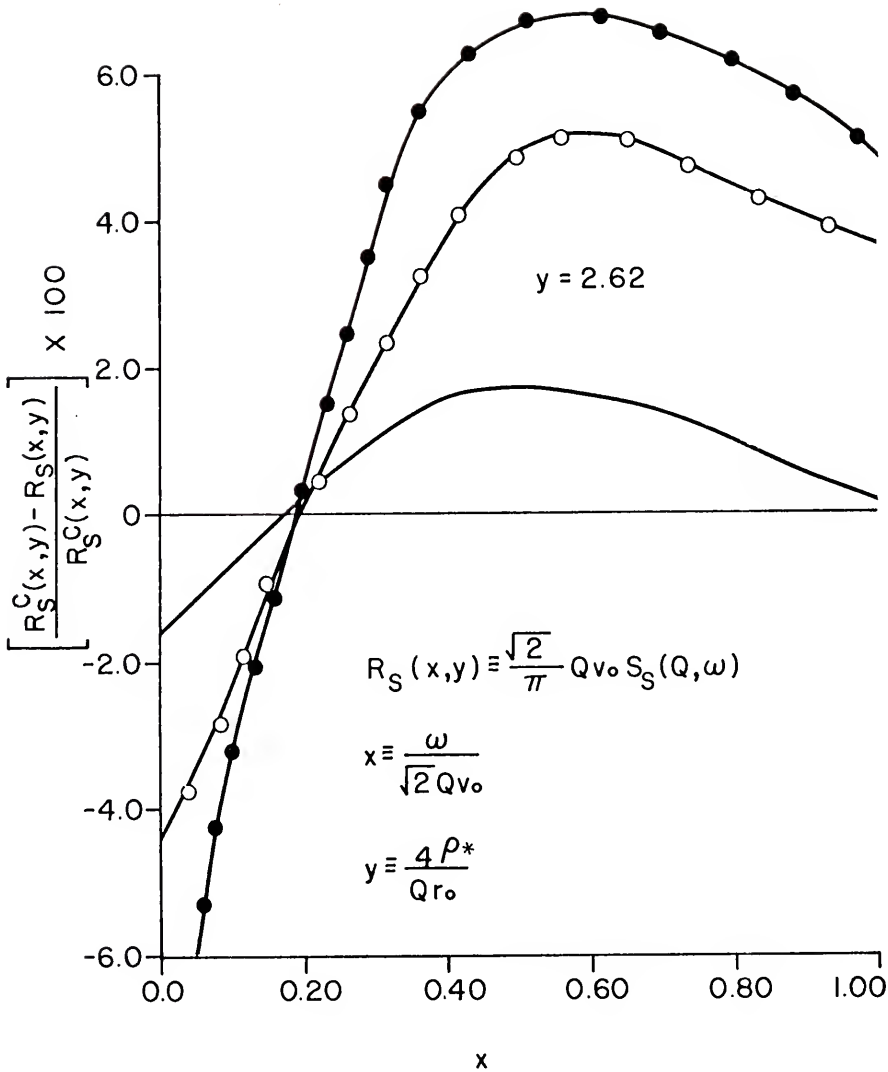

Figure 4-5. Same as Figure 4-4 except that y = 2.62.

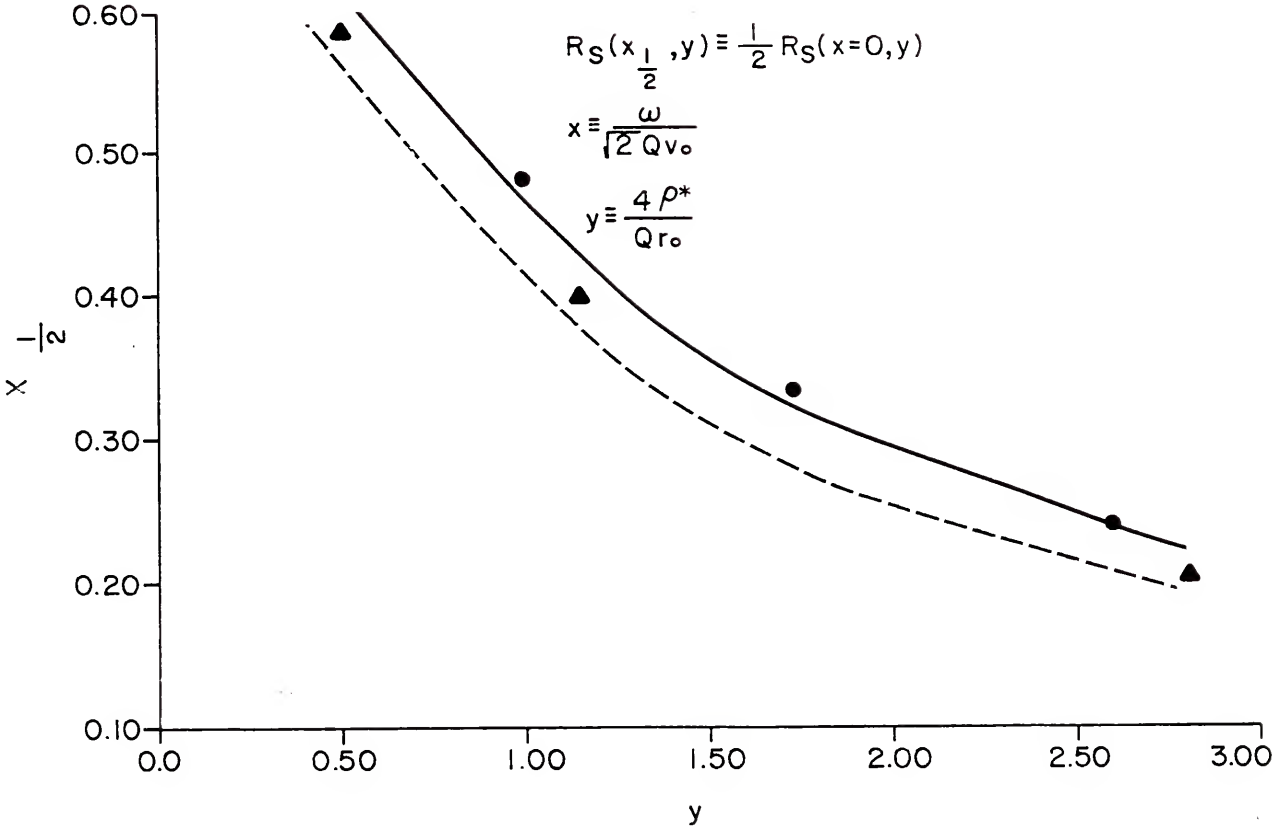

Figure 4-6. Half-width at half-maximum ($x_{\frac{1}{2}}$) for a dilute gas of hard spheres; exact solution (——), the N = 1 (---), N = 6 (▲) and the optimized (•) kinetic models.

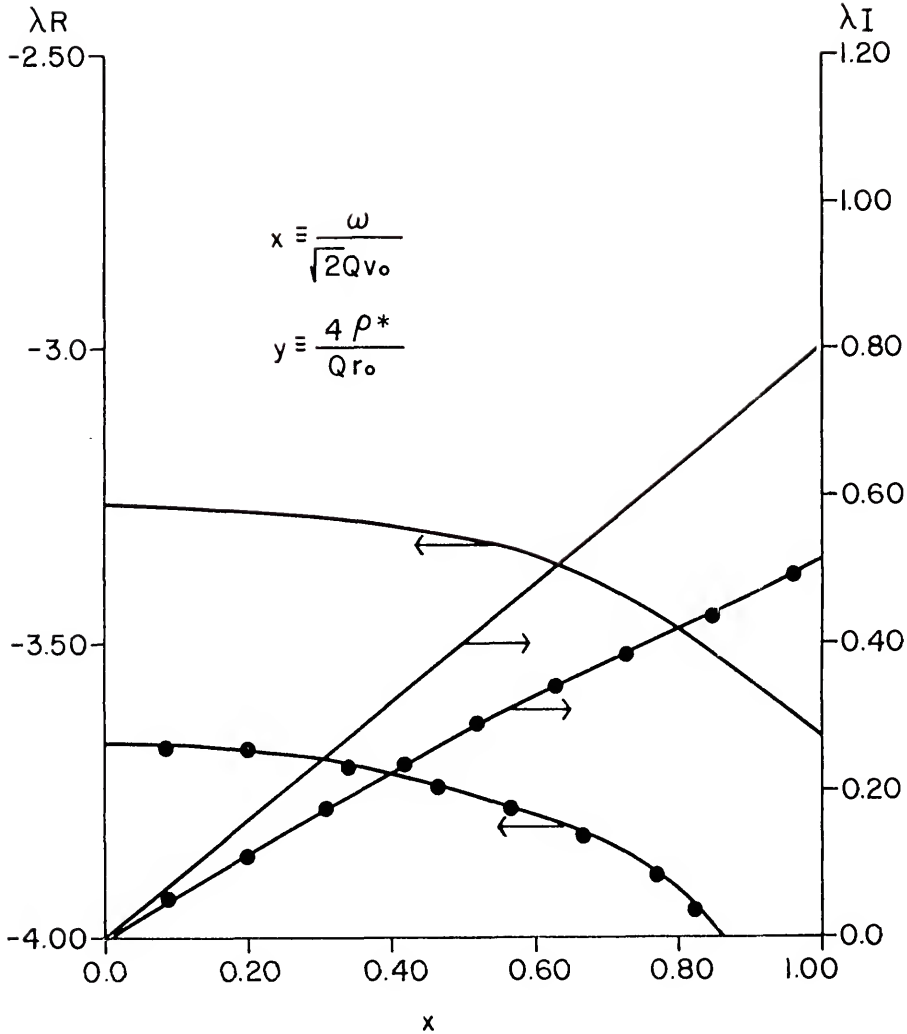

Figure 4-7. Behavior of the real (λ_R) and imaginary (λ_I) parts of the optimized kinetic model eigenvalue (equation (4-56)) for a dilute, hard sphere gas; y = 0.247 (——), y = 1.00 (-·-·-).

The optimized kinetic model developed in Section 4.3 was found to be far superior to the N=1 model when compared with the exact solution of the Fokker-Planck kinetic equation for self correlations. The calculation of $S_s(Q,\omega)$ for a more realistic collision operator, the Boltzmann-Lorentz operator for self correlations, again showed that the optimized kinetic model is a vast improvement over both the N=1 and N=6 Gross-Jackson kinetic models. Although details have not been worked out, the success of the optimized kinetic model for self correlations suggests that equally favorable results for $S(Q,\omega)$ should be attainable using a low-order kinetic model for the generalized Enskog collision operator.

CHAPTER 5

NEUTRON SCATTERING TIME-OF-FLIGHT SPECTROMETRY

5.1 Introduction

Sir James Chadwick's (61) discovery of neutrons in 1932 followed the Joliot-Curie studies on alpha irradiation of beryllium. The flux from these very weak sources was increased slowly by using more intense alpha emitters, but it was not until the advent of the fission reactor in 1942 that neutron beams could be produced which were intense enough for even very simple diffraction studies. Development of better and more specialized sources increased neutron fluxes from 10^5 to 10^{16} neutrons per square centimeter per second, thereby making it possible to obtain precise neutron scattering data on dilute and moderately dense gases.

Since the neutron wavelength is of the order of the interatomic spacing, the inelastic scattering of neutrons yields information about the structure and dynamics, i.e. $G(\vec{r};t)$, of the fluid on a microscopic scale. The distribution, in terms of the solid angle, $d\Omega$, and energy transfer, $\hbar d\omega$, of scattered neutrons is related to the fluid structure through equation (1-26):

$$\frac{d^2\sigma}{d\Omega d\omega} = \frac{k}{k_o} \left[b_{coh}^2 S(Q,\omega) + b_{incoh}^2 S_s(Q,\omega) \right] . \qquad (1\text{-}26)$$

Here, b_{coh} and b_{incoh} are the coherent and incoherent scattering lengths, respectively, $\vec{k}_o$ ($\equiv \vec{p}_o/\hbar$, where $\vec{p}_o$ is the incident neutron

momentum) is the incident neutron wave vector, $\vec{k}$ is the scattered neutron wave vector, and $\frac{d^2\sigma}{d\Omega d\omega}$, the differential scattering cross-section, is the number of neutrons scattered into the solid angle $d\Omega$ with an energy change $\hbar d\omega$. For atomic fluids, the dynamic structure factor, $S(Q,\omega)$, and the self structure factor, $S_s(Q,\omega)$, are related to the density-density time correlation functions through equations (1-3) and (1-28)[1]:

$$S(Q,\omega) = \int_{-\infty}^{+\infty} dt\ e^{i\omega t} \int d\vec{r}\ e^{-i\vec{Q}\cdot\vec{r}} G(\vec{r};t)\ , \qquad (1\text{-}3)$$

$$S_s(Q,\omega) = \int_{-\infty}^{+\infty} dt\ e^{i\omega t} \int d\vec{r}\ e^{-i\vec{Q}\cdot\vec{r}} G_s(\vec{r};t)\ . \qquad (1\text{-}28)$$

In equations (1-3) and (1-28), $\hbar\vec{Q}$ is the momentum change and $\hbar\omega$ is the energy change associated with the scattering process:

$$\begin{aligned} \hbar\vec{Q} &= \vec{p} - \vec{p}_o \\ \hbar\omega &= E - E_o\ . \end{aligned} \qquad (5\text{-}1)$$

A schematic layout for the measurement of the differential scattering cross-section is shown in Figure 5-1. The ratio of the scattered neutron intensity as recorded by the detector to the incident neutron intensity is converted to $\frac{d^2\sigma}{d\Omega d\omega}$ after correcting for unwanted effects, e.g., multiple scattering. Details of the data analysis are given in Chapter 6.

A frequently used technique for determining the dynamic characteristics of a "black box" process, i.e., a system whose internal structure is unknown, is to measure the system's response to a time-

---

[1] The corresponding expressions for molecular fluids are given by Egelstaff et al. (62).

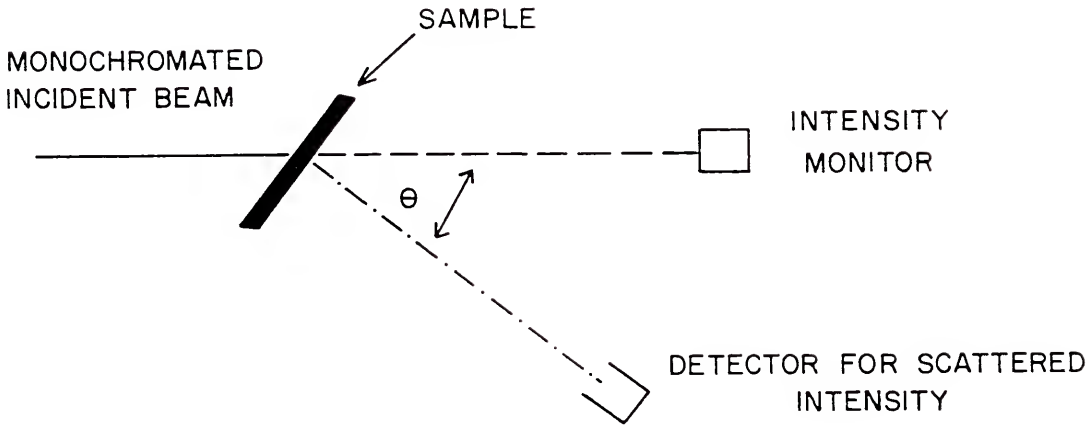

Figure 5-1. Schematic layout for the measurement of $d^2\sigma/d\Omega d\omega$.

dependent forcing function. The same approach is applicable to the study of the time-dependent microstructure of an equilibrium system: the response of the system to a known forcing function, in this case a monoenergetic pulse of neutrons, is used to provide information on the dynamic structure factor, $S(Q,\omega)$. The concept of the neutron scattering time-of-flight experiment is briefly summarized in Figure 5-2. The upper left graph in Figure 5-2 shows the velocity distribution of a beam of thermal neutrons emerging from a reactor. In order to determine the momentum and energy changes of the neutrons, it is necessary to know the incident neutron velocity (denoted v_o). This is accomplished by passing the neutron beam through a monochromator, in this case a crystal which diffracts neutrons with the velocity v_o at a Bragg angle θ_B according to the Bragg relation

$$n\lambda_o = 2\ d \sin \theta_B \quad \text{for } n = 1,2,\ldots \tag{5-2}$$

Here, d is the spacing between parallel-layer planes within the crystal. The monochromated beam then passes through the sample, and the resulting changes in neutron intensities as a function of detector angle and neutron velocity are recorded as shown in the lower left drawing of Figure 5-2. An analysis of the time-of-flight spectra then yields the dynamic structure factor.

Inelastic neutron scattering differs from diffraction experiments in that the latter records the scattered intensity as a function of detector angle (or momentum transfer) only, yielding $S(Q)$, the static structure factor. The connection between $S(Q)$ and $S(Q,\omega)$ is made through equation (5-3):

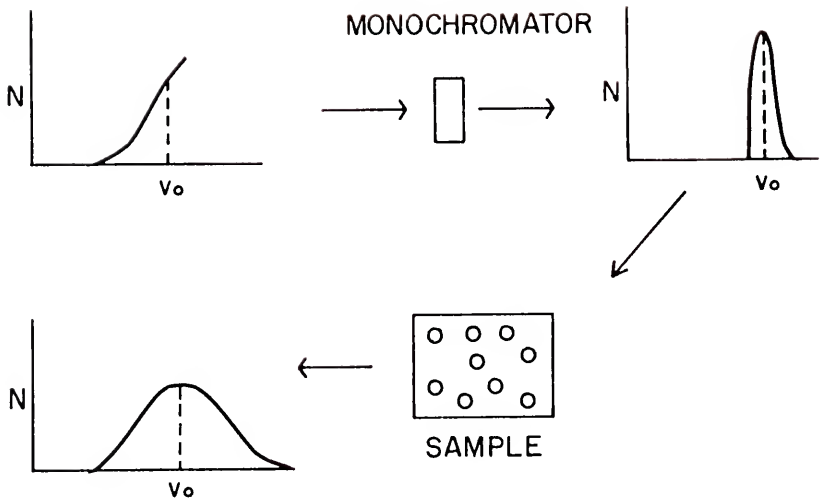

Figure 5-2. Illustration of the time-of-flight measurement; N is the neutron intensity and v_o is the known incident neutron velocity.

$$S(Q) = \int_{-\infty}^{+\infty} d\omega \; S(Q,\omega) \; . \tag{5-3}$$

Consequently, X-ray or elastic neutron scattering measurements of $S(Q)$ involve an integration of $S(Q,\omega)$ over ω at constant Q. Because of this, diffraction experiments provide no information on the dynamic behavior of the fluid (17).

5.2 The Correlation Method in Time-of-Flight Experiments

In a time-of-flight experiment, the incident neutron beam is modulated in time by a rotating disc of constant angular frequency made from neutron absorbing material and having a pattern of slits and bridges as shown in Figure 5-3. This narrow, monoenergetic pulse is scattered by the sample. The time-of-flight distribution, $Z(T)$, at the detector, which is described mathematically by the convolution of the incident beam, $M(t)$, with a function $U(t)$ characterizing the scattering system, plus an additive background, $B^{o}(t)$, is given by (63)

$$Z(t) = U * M + B^{o}(t) \; , \tag{5-4}$$

where $U * M$ is the convolution

$$U * M = \int_{0}^{T_e} dt' \; U(t) \quad M(t-t') . \tag{5-5}$$

Here, T_e is the experiment run time. Since $U(t)$ is related to the scattering cross-section, a time-of-flight experiment can be identified as a stable, homogeneous linear system (64) with $M(t)$ the forcing function, $Z(t)$ the total output, and $U(t)$ representing the

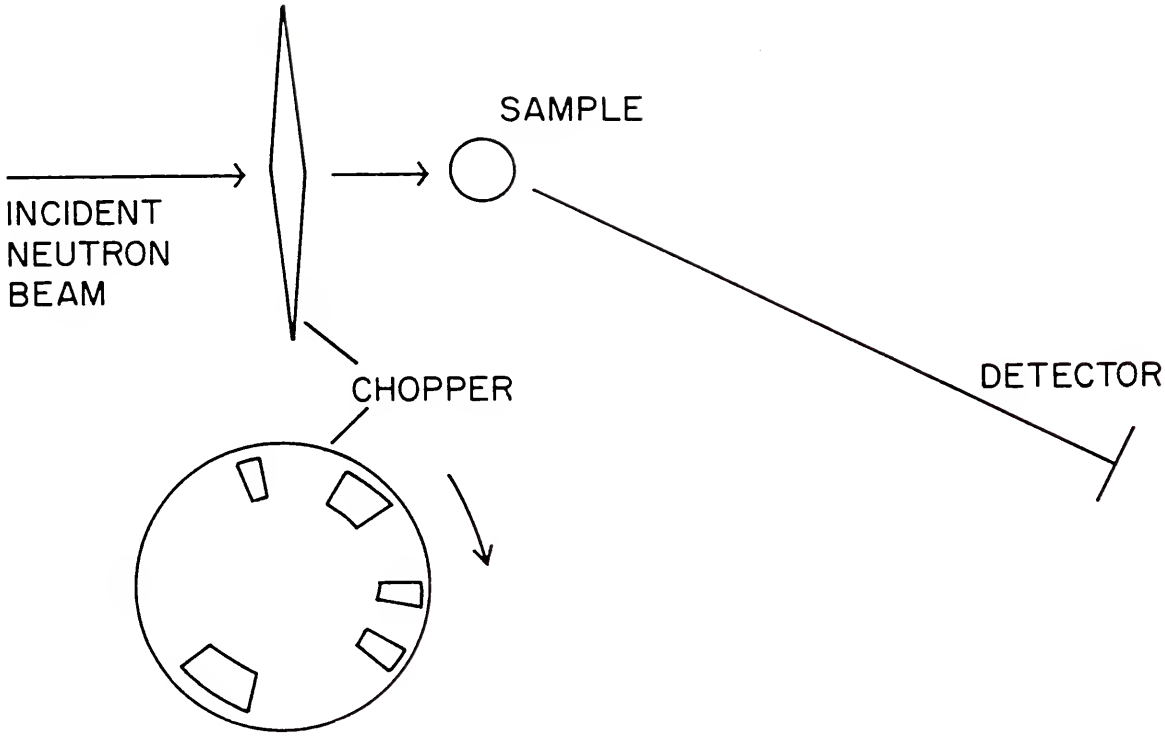

Figure 5-3. The mechanical chopper.

so-called system response function (not to be confused with the "transfer function," defined as the Laplace transform of U(t).)

Here we are concerned with the correlation method using as M(t) (pseudo) randomly modulated primary beams. The simplest modulation function is a sequence of rectangular pulses with M(t) equal to one or zero during equi-distant time intervals θ (see Figure 5-4). However, other pulse shapes may appear in practice. Furthermore, the modulation function of a mechanical chopper is periodic in time with a period $T_m = N\theta$ ($\leq T_e$), where N is the number of intervals per period.

The shape of an elementary pulse of width θ is denoted by $\phi(t)$, and a sequence of pulses is characterized by a periodic sequence of N numbers, $a_{i+N} = a_i$, with values zero and one, $a_i = \{0,1\}$. If t_i is the center of the time interval θ, then the modulation function M(t) is simply the superposition of pulses at all times where $a_i = 1$, i.e.,

$$M(t) = \sum_i a_i \, \phi(t-t_i) \quad . \tag{5-6}$$

The binary sequence {0,1} consists of m "on-states", i.e., the chopper will emit m neutron pulses per period T_m, and the duty cycle of the sequence is defined by

$$c \equiv \frac{m-1}{N-1} \quad . \tag{5-7}$$

The conventional time-of-flight experiment uses one single neutron pulse per period (m=1, c=0), and Z(t) then gives directly the convolution of the scattering function with the pulse shape. The disadvantage of this method is that the available neutron intensity is only utilized during a small fraction of time (typically 1%). The

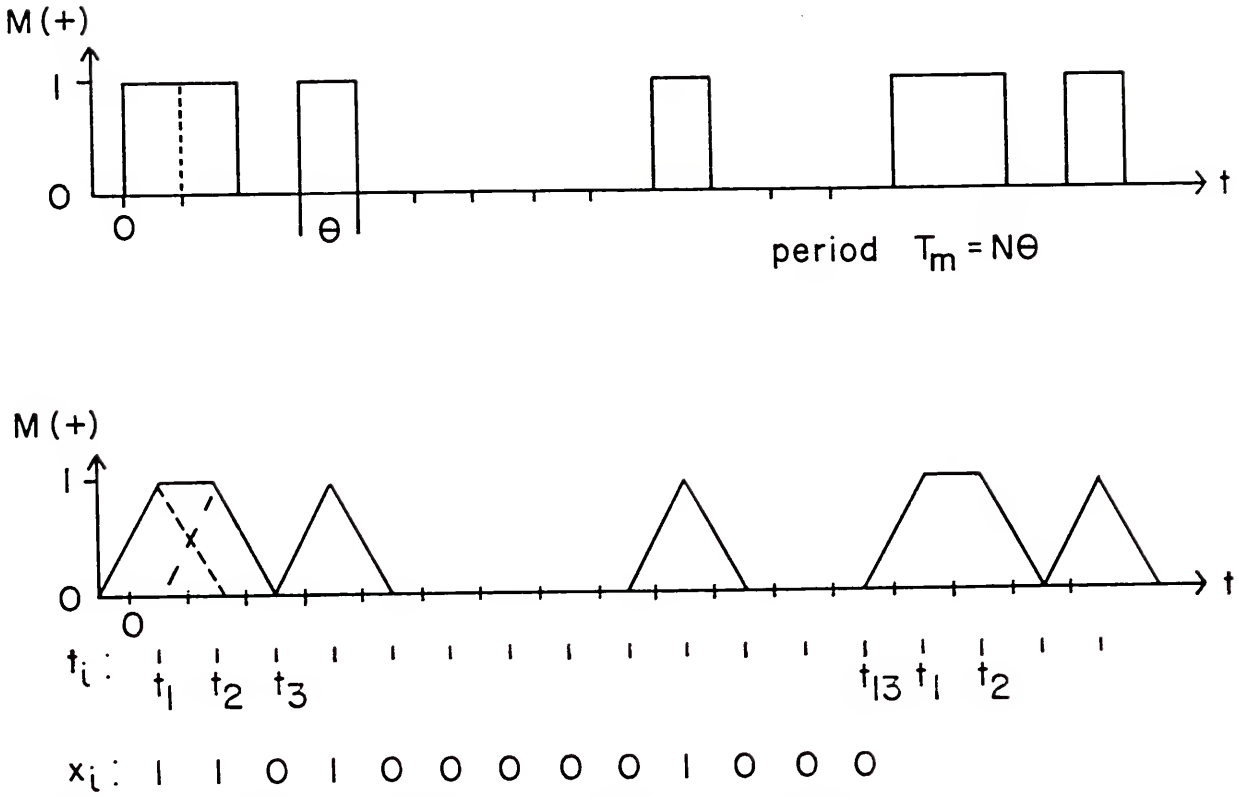

Figure 5-4. The forcing function, M(t), for various pulse shapes; Θ is the pulse width and N is the number of intervals per period.

correlation method may exploit up to 50% of the neutrons by using a modulation function with a suitable duty cycle.

In practice, the time-of-flight distribution, $Z(t)$, is counted in discrete time channels of finite width, c_w. Introducing the ratio of pulse width to channel width, $\nu = \frac{\theta}{c_w}$, and denoting $t_j = (j-1)\nu$, solution of the time-of-flight spectra yields (63)

$$U(\tau) = \frac{1}{m} \sum_{j=o}^{N-1} \left(\frac{a_j - c}{1-c}\right) Z(\tau + t_j) - \frac{B^o}{m} \quad . \tag{5-8}$$

It is not at all obvious whether the correlation method is superior to the conventional single-pulse time-of-flight experiment. In order to compare both methods, the ratio of the variances, i.e., the estimated mean-square statistical errors, of the time-of-flight spectra is generally accepted (65) as a criterion for superiority:

$$\frac{[\Delta^2\ U(\tau)]_{conv}}{[\Delta^2\ U(\tau)]_{corr}} = K(c,N) \quad . \tag{5-9}$$

Here, $K(c,N)$ represents the change in accuracy due to the correlation method using a pseudo-random chopper of the same resolution and the same total running time but with an arbitrary period T_m of the chopper sequence modulation. It turns out that the correlation method can be made superior to the conventional time-of-flight experiment by a suitable choice of the duty cycle. By maximizing $K(c,N)$, Amadori and Hofeld (66) determined the optimum duty cycle for a given number of intervals per period. The two modulation functions used in this study appear in Table 5-1. In addition, van Jan and Scherm (67) show that the usual way of using 50% "open time" in pseudo-random pulsing

TABLE 5-1

PULSING SEQUENCES USED IN THE TIME-OF-FLIGHT EXPERIMENT

Sequence 1	Sequence 6
N=121 c=0.325	N=156 c=0.194
Positions i with $a_i = 1$	Positions i with $a_i = 1$
0, 1, 2, 3, 6, 7, 10, 11, 15, 17, 18, 22, 28, 20, 36, 39, 46, 47, 49, 51, 61, 69, 70, 71, 74, 75, 77, 79, 86, 88, 89, 93, 95, 101, 102, 106, 109, 112, 115	0, 1, 2, 4, 13, 20, 23, 24, 29, 31, 34, 38, 41, 44, 46, 58, 72, 73, 77, 88, 89, 95, 97, 98, 111, 120, 124, 139, 144, 150, 152.

does not always minimize the statistical error. For many applications a duty cycle of 20 to 30% is slightly preferable.

Figure 5-5 illustrates the qualitative features of the correlation technique. The upper graph in Figure 5-5 shows the modulation function, the middle graph gives the neutron intensity measured at the detector, and the bottom graph is the resulting time-of-flight spectrum. In Figure 5-6 the correlated spectrum is seen superimposed on a large oscillatory background. The oscillations in the background arise from the pseudo-random (as opposed to truly random) nature of the pulsing sequence. Since the static structure factor, S(Q), is related directly to the peak area, care must be taken to ensure that the background is removed in a consistent manner for each run. The procedure followed (see Section 6.5) was to subtract from the peak area (width N) equal portions (width N/2) of the background on each side of the central peak. Hopefully, this technique reduces the error contribution due to the pseudo-randomness of the pulsing sequence.

5.3 The Magnetically-Pulsed Time-of-Flight Spectrometer

As indicated in Figure 5-3, the conventional technique for generating a pulsed beam of neutrons is by mechanical means. However, a time-of-flight spectrometer which utilizes a magnetically-pulsed neutron beam has recently been developed by Mook and Wilkinson (68) and is installed at the High Flux Isotope Reactor (HFIR) at the Oak Ridge National Laboratory (ORNL). A schematic diagram of this system is shown in Figure 5-7.

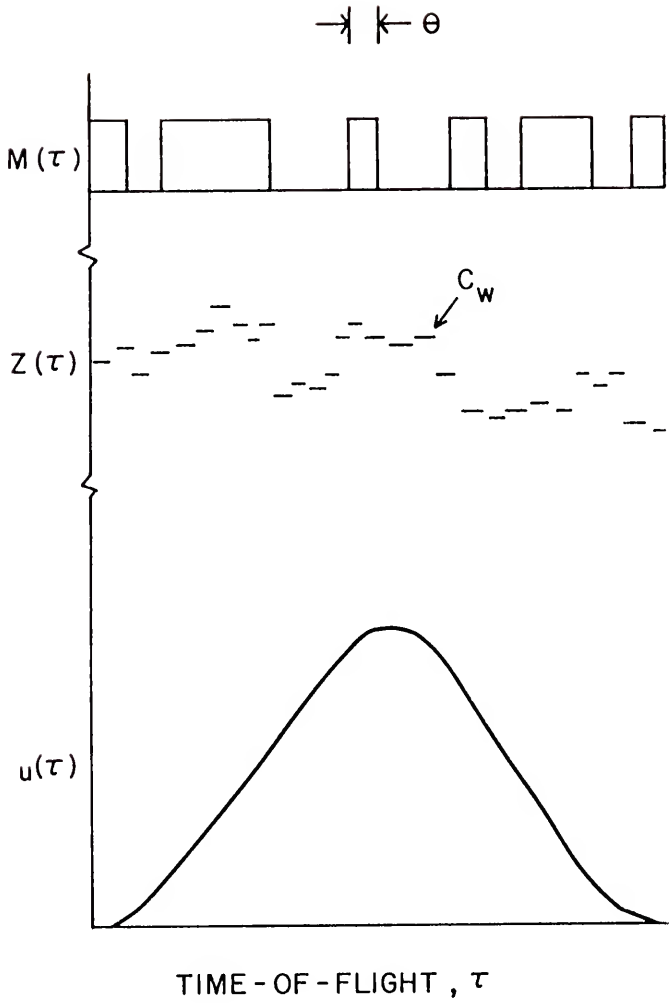

Figure 5-5. Qualitative behavior of the forcing function (M), the time-of-flight distribution (Z), and the correlated time-of-flight spectrum (U); θ is the pulse width and c_w is the channel width.

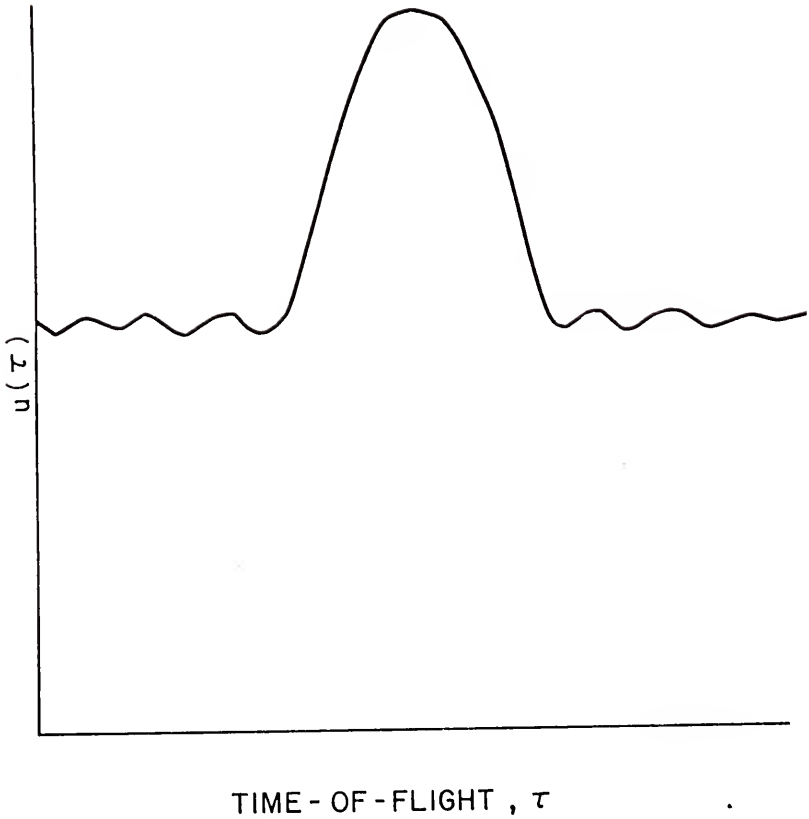

Figure 5-6. Qualitative behavior of the correlated spectrum (U). The background oscillations are attributed to the pseudo-random correlation technique.

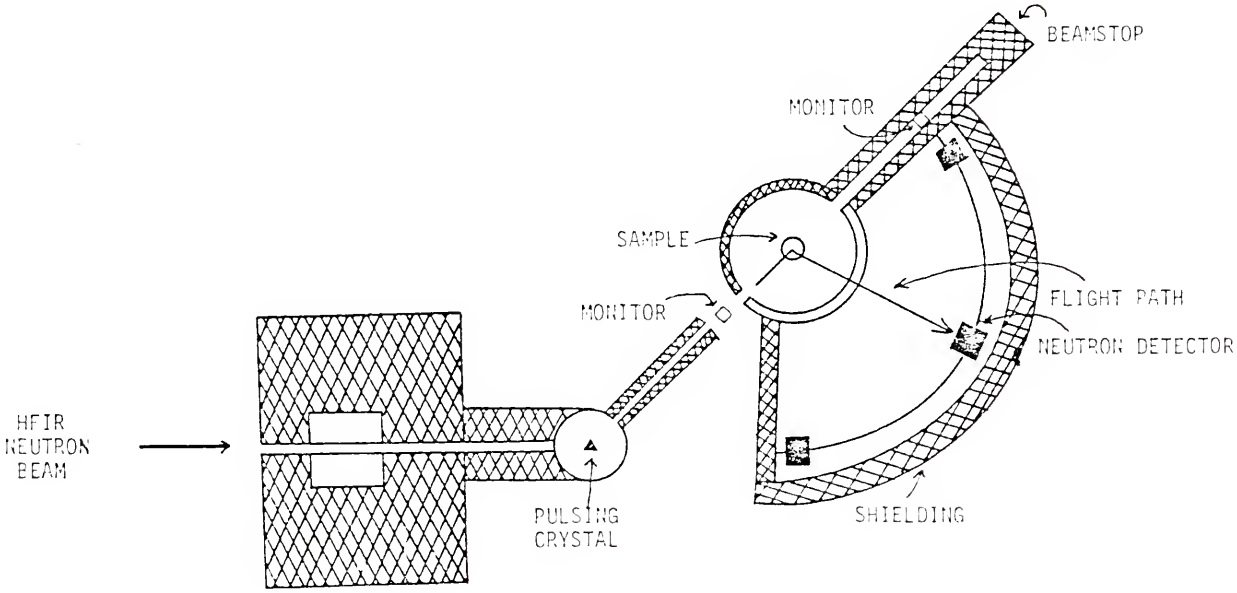

Figure 5-7. Schematic layout of the HFIR magnetically pulsed time-of-flight spectrometer.

The neutron beam (with dimensions 2.5 cm x 3.0 cm) emerging from the reactor[2] is pulsed by diffracting it from a magnetic lithium ferrite crystal in which the moment direction can be switched rapidly. The use of a magnetic crystal to modulate the beam was first suggested by Shull, Wollan, and Strauser (69), who showed that the intensity of a magnetic reflection from a crystal is dependent upon the direction of the atomic magnetic moments within the crystal relative to the scattering vector. When the atomic moments are aligned along the scattering vector, the magnetic intensity is zero, and when the moments are perpendicular to the scattering vector the magnetic moment is maximized. Therefore, if the moment can be changed by an external magnetic field, the magnetically reflected neutron intensity can be varied from zero to the maximum. A neutron pulse is thus produced by applying a pulsed magnetic field to the crystal, and the neutron pulse length and frequency can be changed by simply changing the length and frequency of the applied current pulse that generates the magnetic field.

Based on the Bragg angle and plane spacing of the lithium ferrite crystal, it was decided that an incident beam of neutrons with a wavelength[3] of 2.2 Å, and an incident energy of 16.9 MeV, would provide the optimum characteristics with regard to counting statistics and instrument resolution. It was observed that when the crystal was in

---

[2]The HFIR has a thermal neutron flux of about 10^{15} neutrons per square centimeter per second at the beam tube position.

[3]The incident wavelength was determined from equation (5-2), with a crystal spacing of 4.81 Å, and θ_B equal to 13.22°.

the "off" state, the neutron intensity was not zero, as anticipated, but rather an on-off ratio of 1.5 was found to be typical.

The monochromator-pulser crystal was mounted in a shield, with the sample and flight path assembly attached to this shield in such a way that the scattering angle from the monochromator can be continually varied between 0 and 90 degrees. The distance from the crystal to the sample was 193 cm, and the sample-to-detector distance was 151.7 cm. Scattering angles from the sample extended from 10 to 140 degrees, and high pressure ^{3}He detectors were used to provide 15 separate data channels. Figure 5-8 illustrates the qualitative behavior of the static structure factor, S(Q), for xenon. To cover as much of the Q-range as possible, it was decided to make two separate runs at each density: a low angle run covering the angles 11.8 to 36.5 degrees, and a high angle run from 39.1 to 63.4 degrees. The corresponding Q-range of the two runs is indicated in Figure 5-8, and the placement of the 30 detectors is summarized in Table 5-2. Note that the Q values listed are the elastic momentum transfer,

$$Q_o = \frac{4\pi \sin \theta}{\lambda_o} , \qquad (5\text{-}10)$$

where 2θ is the scattering angle.

The spectrometer was on-line with its own computer, a Digital Equipment Corporation (DEC) PDP 15-30. The pseudo-random code (see Table 5-1), stored in the computer and relayed to the crystal pulser, provided a continuously pulsed neutron beam according to a predetermined coding sequence. Data was taken on-line by the

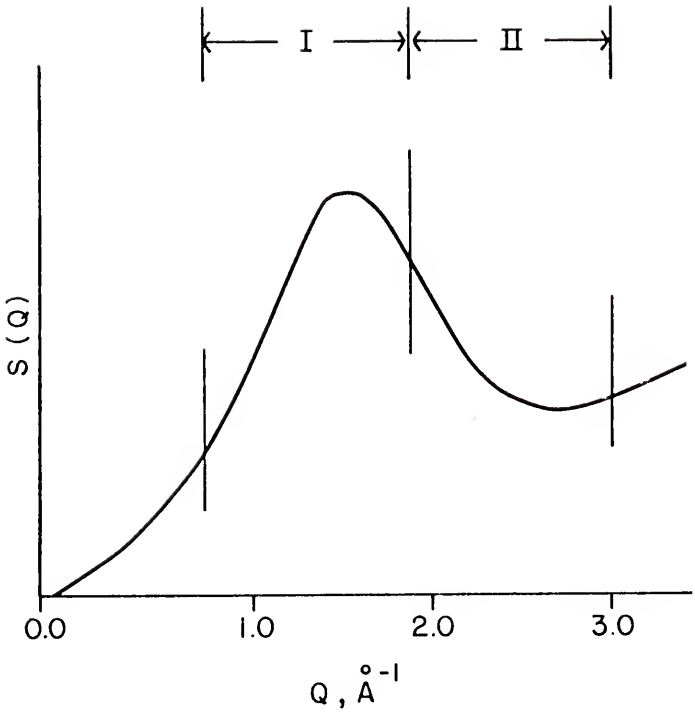

Figure 5-8. Qualitative behavior of the static structure factor, S(Q); Region I: $11.8° \leq 2\theta \leq 36.5°$, Region II: $39.1° \leq 2\theta \leq 63.4°$.

TABLE 5-2

DETECTOR ANGLES

Detector	SET I		SET II	
	2θ	Q_o^*	2θ	Q_o^*
1	11.8	0.585	39.1	1.911
2	13.3	0.660	40.6	1.981
3	14.8	0.736	42.1	2.052
4	16.3	0.812	43.6	2.123
5	17.9	0.887	45.2	2.193
6	20.9	1.040	48.2	2.332
7	22.4	1.110	49.7	2.400
8	23.9	1.183	51.2	2.470
9	25.4	1.258	52.7	2.540
10	27.0	1.332	54.3	2.604
11	30.0	1.480	57.3	2.740
12	31.5	1.550	58.8	2.803
13	33.0	1.622	60.3	2.870
14	35.5	1.743	61.8	2.935
15	36.5	1.780	63.4	3.000

*Elastic momentum transfer, Q_o, is calculated from equation (5-10) for $\lambda_o = 2.2$ Å.

DEC PDP 15-30 and, after neutron counts had accumulated for a specified length of time, the data was cross-correlated (see equation (5-8)) and the spectra displayed on a large oscilloscope screen and simultaneously stored on DEC tape for later examination. All data taken was later transferred to IBM tape and analyzed at the University of Florida.

Before leaving this section, a discussion of possible sources of error peculiar to this apparatus is appropriate. To begin with, there is a large contribution to the time-of-flight spectrum due to air scattering. In an ideal world the air would be replaced with helium (low σ_s), thereby significantly reducing the superimposed background. In the second place, cadmium vanes were placed between each detector to act as collimators. These vanes were not mechanically secured so that any physical disturbance to the shielding could possibly shift their positions relative to the detectors. Finally, the magnetic crystal was pulsed with an RF field, leading to RF pickup by the detectors. Although attempts were made to eliminate it by shielding and biasing each detector, the pickup was not at all stable and varied from counter to counter. It is felt that, of the three effects mentioned above, the latter is perhaps the more serious.

5.4 Vessel Design

Prior to the design of the high pressure sample vessel, the following experimental conditions needed to be established:

(1) The pressure-density-temperature range over which the experiment was to be conducted,

(2) The desired fraction of the incident neutron beam to be scattered by the xenon sample.

From the above it is apparent that vessel design is very much a function of the experimental conditions.

As discussed in Chapter 1, information on S(Q) for a low density gas provides information on the pair and triplet intermolecular potentials, and the dynamic structure factor, $S(Q,\omega)$, concerns the two- and three-body dynamics of the gas molecules. For this reason, the density range for xenon corresponding to the second and third virial coefficients, i.e., two- and three-body interactions, was identified and established as part of the desired pressure-density range to be covered experimentally. To minimize experimental difficulties, 303 K was chosen as the temperature at which the experiment was to be run. Figure 5-9 illustrates the pressure-density-temperature relationship for xenon, and Figure 5-10 plots density as a function of pressure for a temperature of 303 K. Also shown (dashed line) is the third virial coefficient region, calculated from the equation of state

$$\frac{P}{RT} = \rho - 126.51\ \rho^2 + 6551\ \rho^3 \ . \qquad (5\text{-}11)$$

Values for the second and third virial coefficients are the experimental values given by Dymond and Smith (70).

In calculating the solid line in Figure (5-10), it was assumed that corresponding states between argon and xenon is valid, i.e.,

$$\left(\frac{P^*V^*}{T^*}\right)_{xenon} = \left(\frac{P^*V^*}{T^*}\right)_{argon} , \qquad (5\text{-}12)$$

where the state variables (P, V, T) are reduced by their critical values. The equation of state used for argon is that given by McCarty <u>et al</u>. (71):

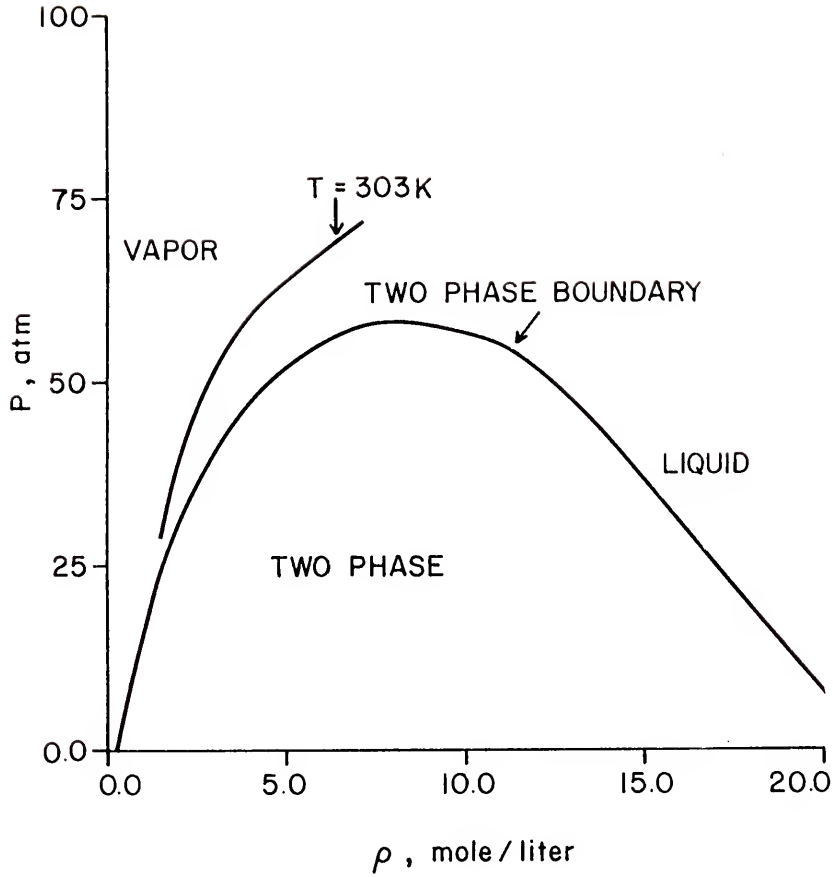

Figure 5-9. Phase diagram for xenon; T = 303 K is the experimental run temperature.

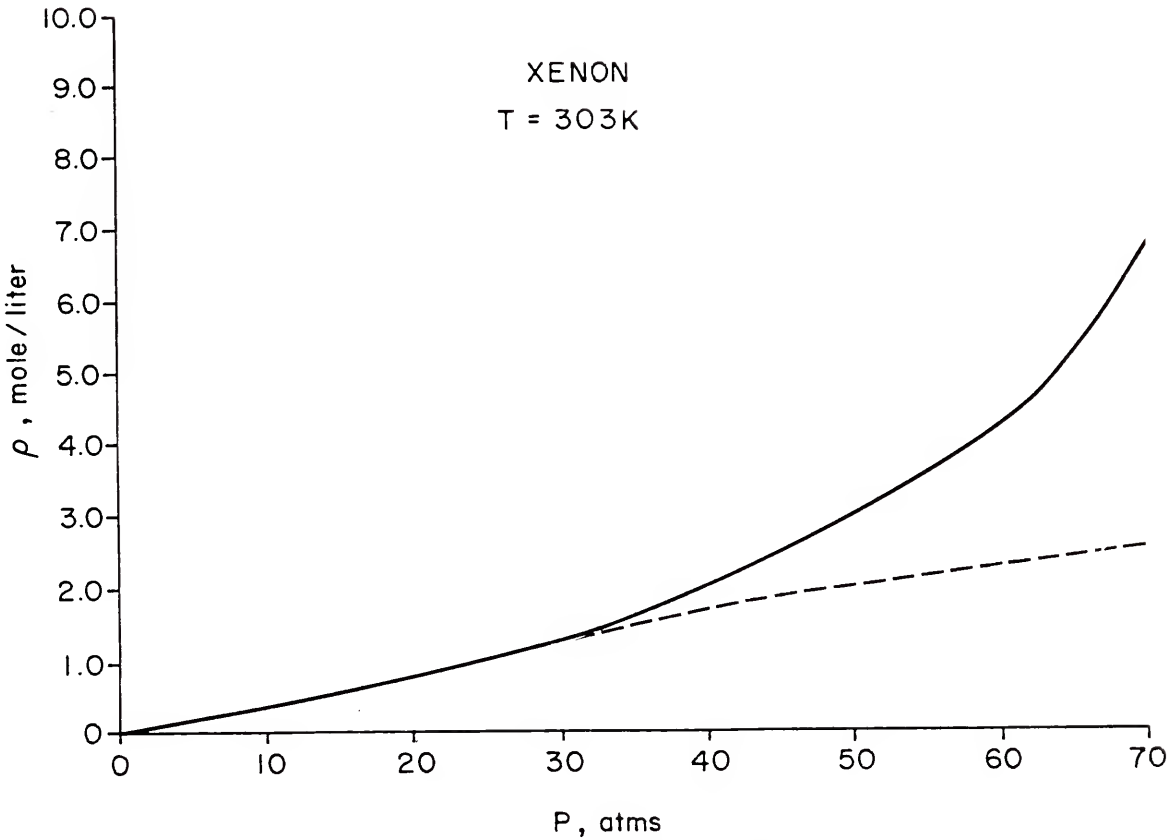

Figure 5-10. Xenon density as a function of pressure at T = 303 K. The solid line is the equation of state, equation (5-10), and the dashed line is the virial equation, equation (5-11).

$$\frac{P}{\rho T} = R + \rho\left(N_1 + \frac{N_2}{T} + \frac{N_3}{T^2} + \frac{N_4}{T^3} + \frac{N_5}{T^5}\right)$$

$$+ \rho^2\left(N_6 + \frac{N_7}{T}\right) + \rho^3 N_8$$

$$+ \rho^2\left(\frac{N_9}{T^3} + \frac{N_{10}}{T^4} + \frac{N_{11}}{T^5}\right) \exp(-N_{16}\rho^2)$$

$$+ \rho^4\left(\frac{N_{12}}{T^3} + \frac{N_{13}}{T^4} + \frac{N_{14}}{T^5}\right) \exp(-N_{16}\rho^2)$$

$$+ \rho^5\left(\frac{N_{15}}{T}\right) . \qquad (5\text{-}13)$$

The parameters (for argon) appearing in equation (5-13) can be found in Table 5-3; the critical properties for xenon and argon are given in Table 5-4. A test of the equation of state was made by comparing equations (5-12) and (5-13) with the experimental data of Beattie _et al_. (72) for xenon at 298 K (see Figure 5-11). As shown, the equation of state accurately describes the pressure-density behavior of xenon.

It is generally accepted (73) that scattering of 10% of the incident neutron flux by the xenon atoms is sufficient to give good counting statistics while simultaneously minimizing the multiple scattering of neutrons in the sample. If one assumes a slab geometry of thickness d, then the fraction of incident neutrons scattered by the sample is given by (74)

$$\frac{I_o - I}{I_o} = 1 - e^{-\sigma_s \rho d} , \qquad (5\text{-}14)$$

TABLE 5-3

EQUATION OF STATE (EQUATION (5-16)) PARAMETERS
FOR ARGON AND XENON

$N_1 = 0.25978374 \times 10^{-2}$	$N_9 = 0.48141071 \times 10^{3}$
$N_2 = -0.987358670$	$N_{10} = 0.64565346 \times 10^{5}$
$N_3 = -0.67273638 \times 10^{2}$	$N_{11} = -0.11485282 \times 10^{8}$
$N_4 = -0.26494177 \times 10^{4}$	$N_{12} = -0.648354880$
$N_5 = 0.97631231 \times 10^{7}$	$N_{13} = 0.46524812 \times 10^{3}$
$N_6 = 0.70478556 \times 10^{-4}$	$N_{14} = 0.10933578 \times 10^{5}$
$N_7 = -0.46767764 \times 10^{-2}$	$N_{15} = 0.6943953 \times 10^{-6}$
$N_8 = 0.22640765 \times 10^{-5}$	$N_{16} = 0.480 \times 10^{-2}$

$R = 0.082056160$

TABLE 5-4

CRITICAL PARAMETERS FOR ARGON AND XENON

	Argon	Xenon
T_c, K	150.86	289.81
P_c, atm	48.34	57.89
ρ_c, mole/ℓ	13.41	8.32

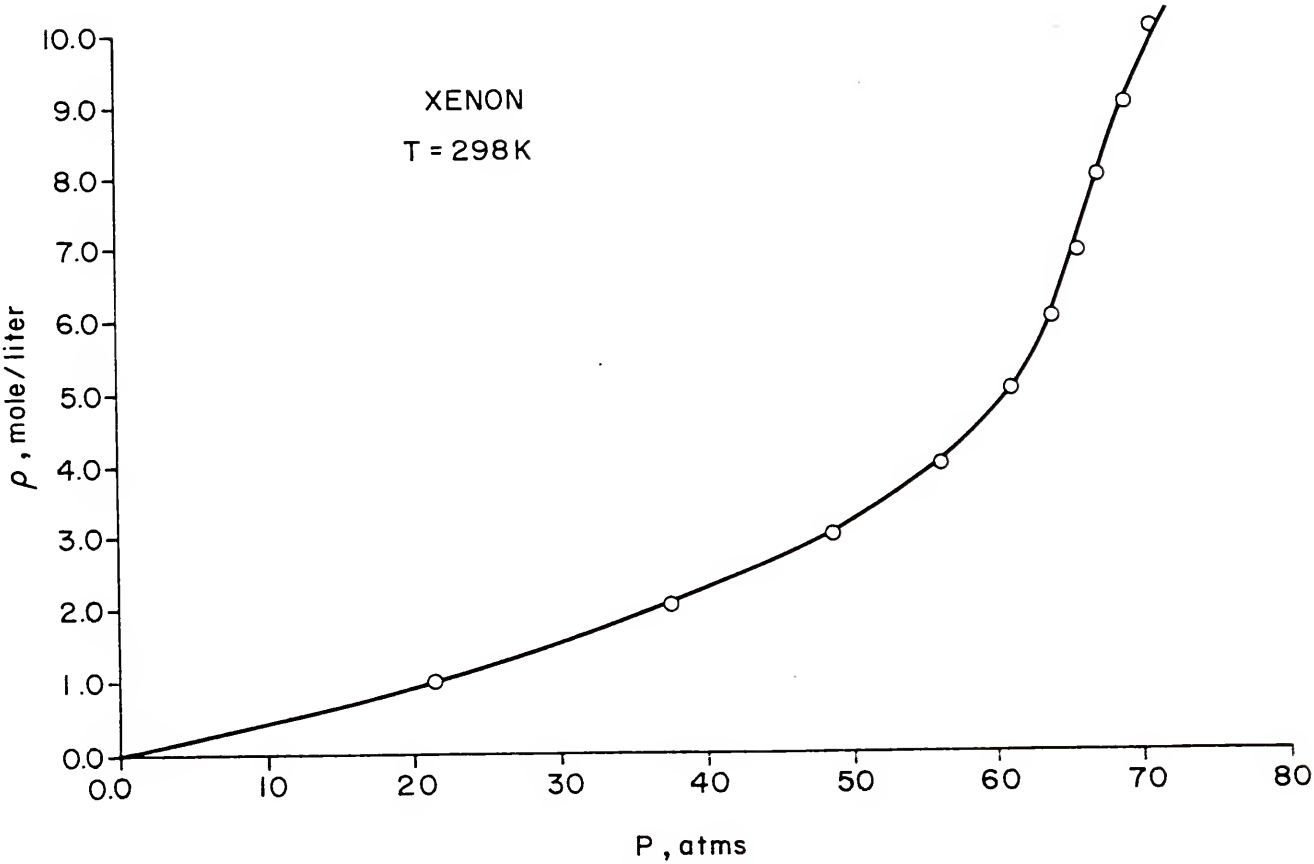

Figure 5-11. Comparison of the equation of state (equation (5-13)) with the experimental data of Beattie et al. (72) for xenon at 298 K; the solid line is equation (5-13), and (∘) is data.

where I_o is the incident neutron intensity and (I_o-I) is the intensity of the scattered neutrons. In equation (5-14), ρ is the sample number density and σ_s is the scattering cross section. Assuming an expansion of the exponential to be a valid approximation, an explicit expression for the vessel diameter is obtained:

$$d = \frac{1}{\rho\sigma_s} \left(\frac{I_o-I}{I_o}\right) \quad . \tag{5-15}$$

Since the vessel is to be used for a wide range of densities, it was decided to have 10% scattering by the xenon molecules at an intermediate density of 5 moles per liter. This yields a vessel diameter of 7 cm for σ_s = 4.3 barns.[4]

The wall thickness of the vessel, t_w, is related to the vessel diameter, the yield strength of the vessel material, σ_y, and the pressure of the sample through (75) the equation

$$t_w = (K-1)\frac{d}{2} \quad , \tag{5-16}$$

with

$$K^2 \equiv \left(\frac{\sigma_y+P}{\sigma_y-P}\right) \quad . \tag{5-17}$$

Because of a combination of small scattering cross-section (σ_s < 1 barn) and a high yield strength (σ_y = 40,000 psi), a polycrystalline aluminum alloy (6061-T6) was chosen as the vessel construction material. Using a safety factor of 1.5, i.e., 1.5 times the desired maximum experimental pressure, as a design criteria, the required vessel wall thickness was found from equation (5-16) to be one-sixteenth of

---

[4] 1 barn = 10^{-24} cm^2.

an inch. This vessel, according to the design specifications, can withstand up to 135 atm pressure.

The ends of the cylinder (see Figure 5-12) form a circular flange having an O-ring seating and a thick base plate closure. The vessel is sealed by teflon O-rings, housed in partially enclosed grooves between the vessel flange and the base. To reduce the multiple scattering of neutrons, a solid aluminum cylinder, coated with cadmium, a strong neutron absorber, was attached internally to each end plate. The length and diameter of each cylinder was determined by the beam dimensions and the vessel diameter, respectively. Finally, the bases were secured by eight high-tensile half-inch bolts. The vessel was pressure tested with nitrogen to 135 atm with no measurable changes in vessel dimensions. Detailed drawings of the sample vessel appear in Appendix H.

5.5 Filling Procedure

The gas transfer lines and sample pressure vessel (A) are shown schematically in Figure 5-13. Xenon gas (cylinder C) at a pressure of 54 atm and 99.9% purity, was obtained from the Matheson Gas Company. Prior to filling the sample vessel with xenon gas, the system was evacuated by opening valves 1, 2, and 3. Xenon gas was introduced into the system by first closing valve 3, then opening valve 4. To remove all xenon from the carrier vessel, it was necessary to cool cylinder B to a temperature of approximately 200 K using a dry ice - acetone bath. When thermal equilibrium was reached, valve 2 was closed and the cryopumping vessel (B) heated to room temperature, thus transierring the xenon from cylinder B to

Figure 5-12. Xenon Sample Vessel.

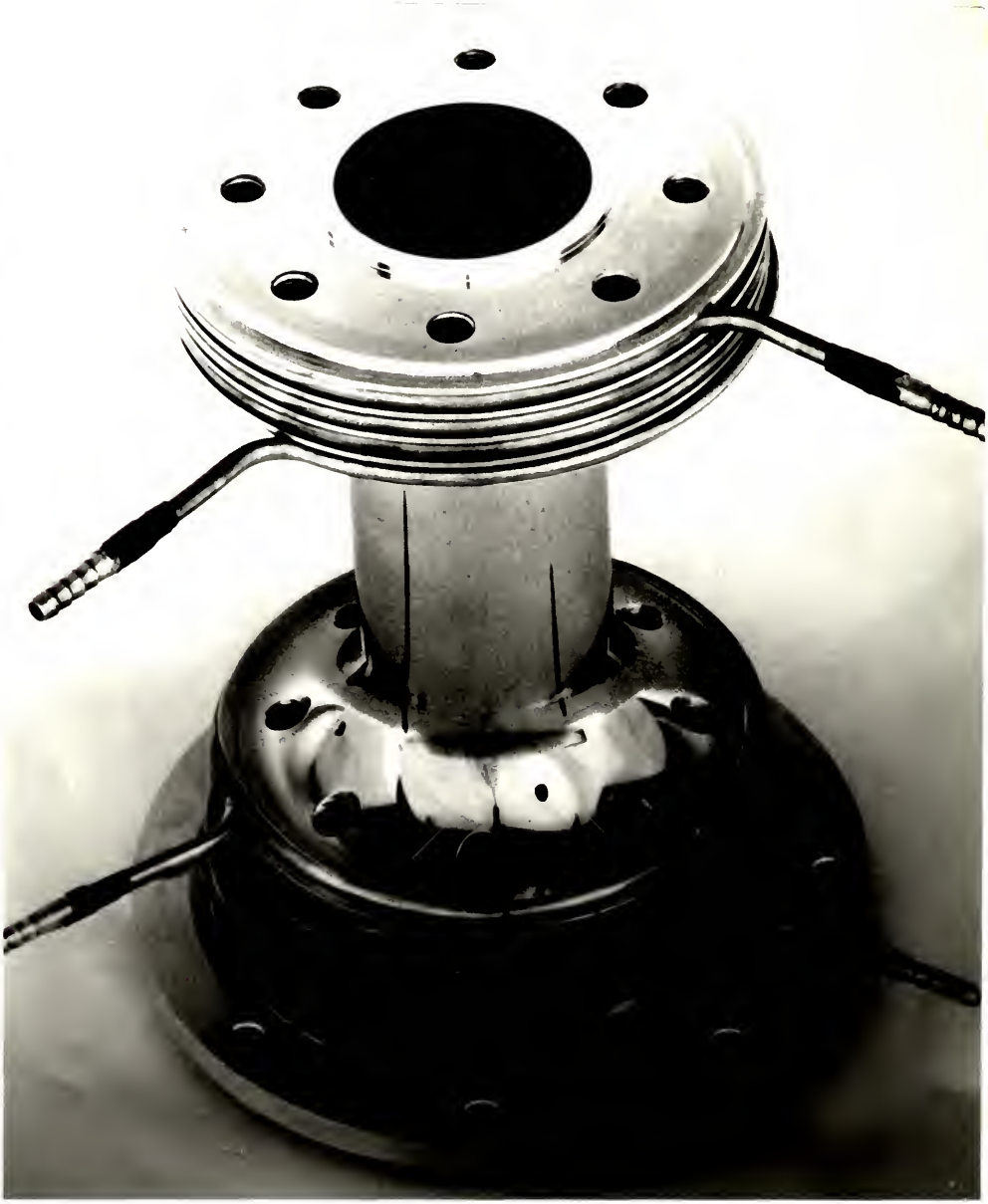

Figure 5-12

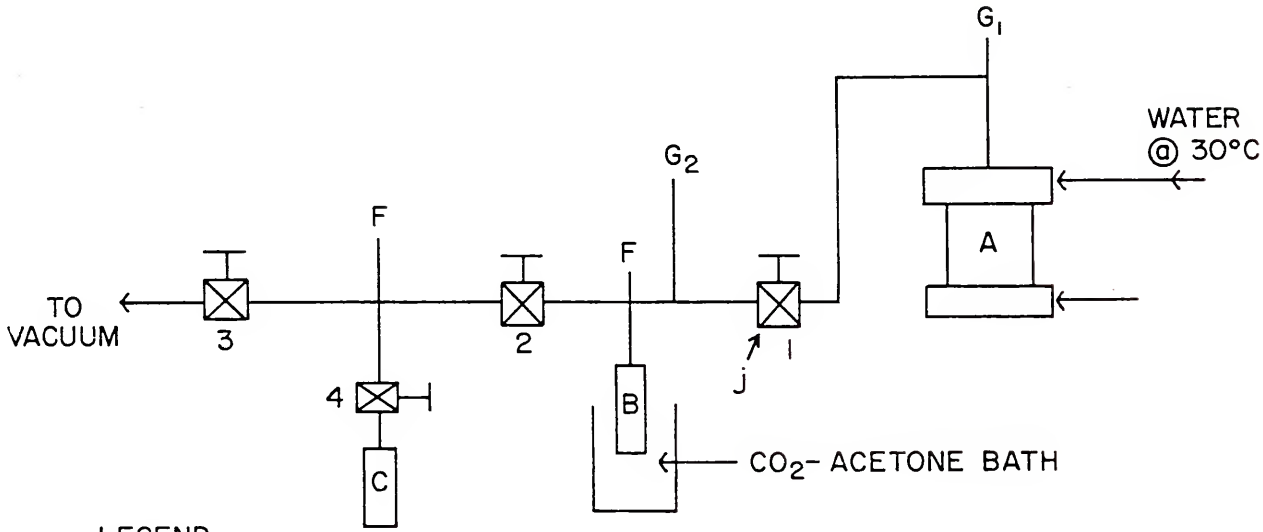

LEGEND

1,2,3,4 - VALVES

A - SAMPLE VESSEL

B - CRYOPUMP

C - XENON CARRIER VESSEL

G_1 - PRESSURE GAUGE, 1500 psi

G_2 - PRESSURE GAUGE, 3000 psi

F - PRESSURE FUSES

Figure 5-13. Schematic layout of the gas transfer lines and the xenon sample vessel (A).

the sample vessel. Once the transfer was complete, valves 1 and 2 were closed and a new carrier cylinder replaced the empty cylinder (C). Valve 3 was then opened and that part of the system exposed to air was again evacuated before introducing more xenon into the system through valve 4. This procedure was followed until the sample vessel (A) reached the desired pressure while at room temperature. Water at 30 C was then circulated through the heating coils on the sample vessel, raising the temperature (and pressure) to the final, desired operating conditions. During high pressure operation, valve 1 was closed and a catcher vessel (D in Figure 5-14), was attached at junction j of Figure 5-13, thereby isolating the sample from the cryopumping system. Upon completion of each run the pressure was lowered by recondensing xenon into the catcher vessel (D).

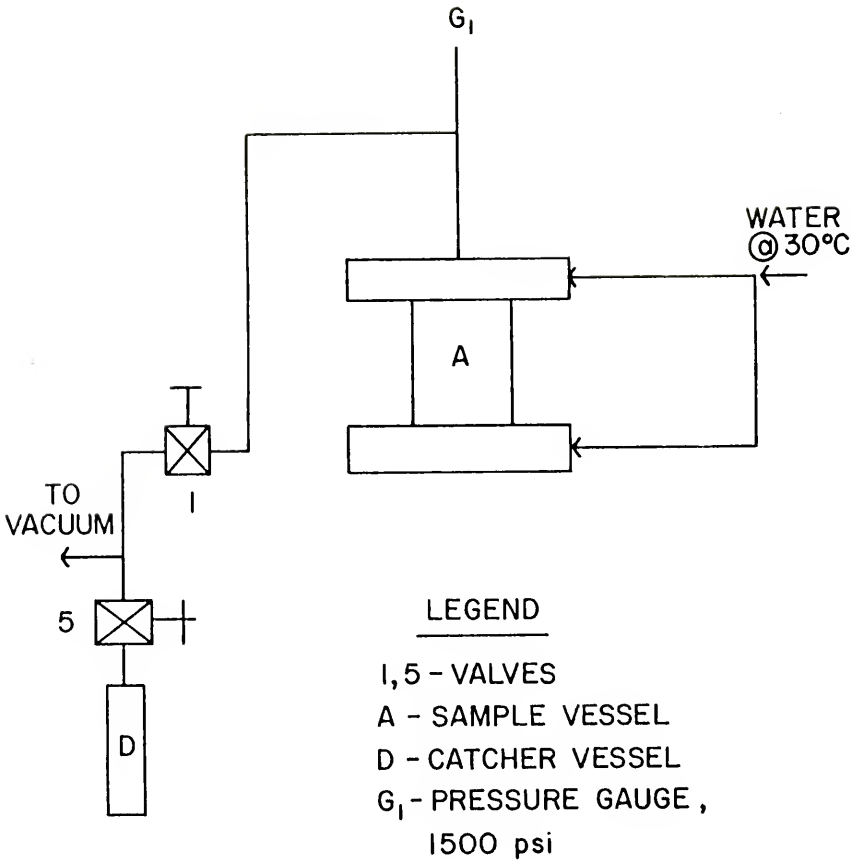

Figure 5-14. Schematic layout of the xenon sample vessel (A) during operation.

CHAPTER 6

DATA REDUCTION

6.1 Introduction

The central quantity of interest in thermal neutron scattering is the dynamic structure factor, $S(Q,\omega)$. The basic task of the theorist is to calculate this quantity with the help of an appropriate miscroscopic model, while that of the experimentalist is to extract $S(Q,\omega)$ from observed scattering data. Apart from corrections for background and instrument resolution, the scattering data are proportional to $S(Q,\omega)$ (and $S_s(Q,\omega)$), provided the sample is such that absorption and multiple scattering can be neglected. However, absorption and multiple scattering, while sometimes small, usually cannot be neglected and the data must therefore be corrected for these quantities. In Chapter 5 the concepts of neutron scattering time-of-flight spectrometry were introduced and details specific to the High Flux Isotope Reactor at the Oak Ridge National Laboratory were discussed. This chapter is concerned with the reduction of the time-of-flight data, and the subsequent extraction of $S(Q,\omega)$ from such data.

The basic equation for the analysis of the time-of-flight data is developed below with the aid of Figure 6-1, typical of the results for the time-of-flight data for xenon. In this figure the

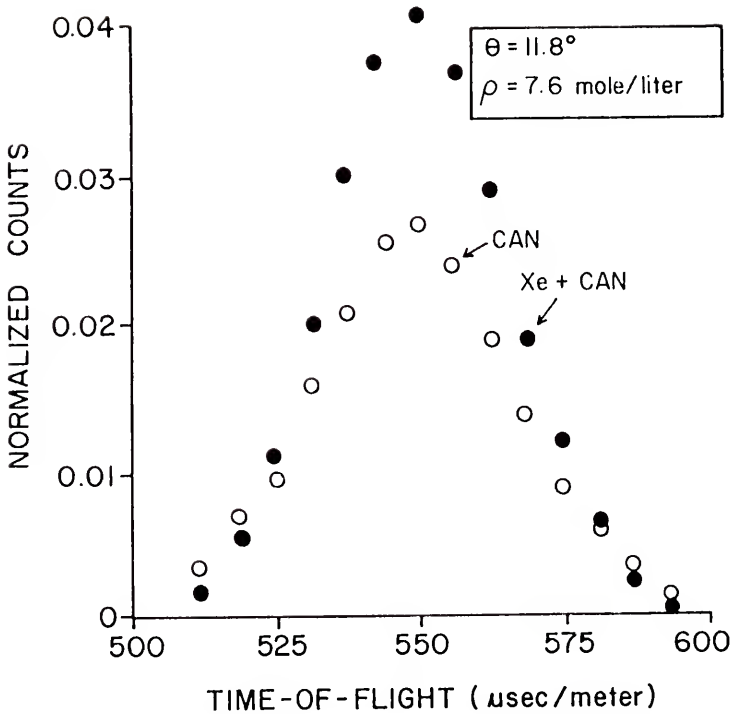

Figure 6-1. Raw time-of-flight data for xenon plus the sample vessel (•) and the sample vessel alone (∘), normalized to the total incident flux.

normalized (to the total incident neutron flux on the sample) neutron counts at a detector angle of 11.8 degrees is shown as a function of time-of-flight for the xenon plus the sample vessel and for the sample vessel itself. To get the spectrum for xenon alone, it is necessary that the contribution from the sample vessel be subtracted from that of the xenon plus the sample vessel. Neglecting absorption and multiple scattering effects,

$$I_{**}^{Xe}(\theta,\tau) = I_{**}^{Xe+SV}(\theta,\tau) - I_{**}^{SV}(\theta,\tau) \quad , \tag{6-1}$$

where $I_{**}(\theta,\tau)$ denotes the neutron intensity, as a function of angle and times-of-flight before corrections for absorption and multiple scattering are made. In equation (6-1), the superscripts (Xe) and (SV) indicate the intensities for the xenon and sample vessel, respectively.

A peculiar feature in Figure 6-1 is observed for low and high times-of-flight: the normalized counts for the xenon plus the sample vessel are less than that for the sample vessel alone. This occurs because xenon is a high absorber of neutrons. Designating $A(\theta,\tau)$ as the absorption correction, equation (6-1) is replaced by

$$I_{*}^{Xe}(\theta,\tau) = \frac{I_{**}^{Xe+SV}(\theta,\tau)}{A^{Xe+SV}(\theta,\tau)} - \frac{I_{*}^{SV}(\theta,\tau)}{A^{SV}(\theta,\tau)} \quad , \tag{6-2}$$

where $I_{*}(\theta,\tau)$ is the neutron intensity after corrections are made for absorption and before correcting for multiple scattering. Figure 6-2 illustrates the effect $A(\theta,\tau)$ has on the data of Figure 6-1. Details of the calculation of $A(\theta,\tau)$ are discussed in section 6.3.

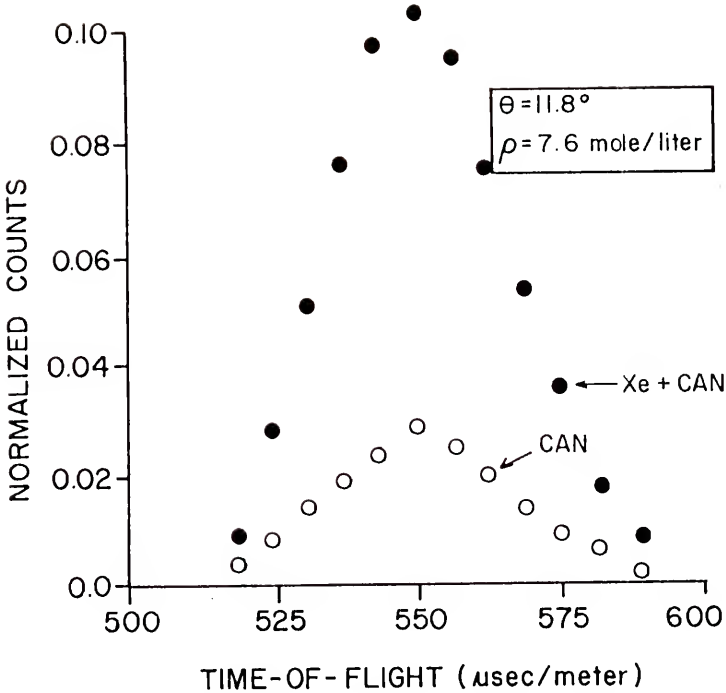

Figure 6-2. Data from Figure 6-1 corrected for neutron absorption; xenon plus sample vessel (•), sample vessel alone (∘).

If $I_n(\theta,\tau)$ is the intensity of neutrons scattered n-times, the total scattering can be written as the sum

$$I_{**}(\theta,\tau) = I_1(\theta,\tau) + M(\theta,\tau) \ , \tag{6-3}$$

where $M(\theta,\tau)$ represents the contribution due to multiple scattering of neutrons,

$$M(\theta,\tau) = I_2(\theta,\tau) + I_3(\theta,\tau) + \ldots \ . \tag{6-4}$$

In the case of elastic scattering, Vineyard (76) introduced the approximation

$$\frac{I_n(\theta)}{I_{n-1}(\theta)} = \frac{I_2(\theta)}{I_1(\theta)} \equiv \delta(\theta) \ , \tag{6-5}$$

where $I_j(\theta)$ is the integrated intensity

$$I_j(\theta) = \int_0^\infty dt \ I_j(\theta,t) \ . \tag{6-6}$$

With this approximation for higher-order scattering, the multiple scattering contribution becomes

$$M(\theta) = \delta(\theta) \ I_{**}(\theta) \ , \tag{6-7}$$

and the single-scattered intensity (elastic) is simply

$$I_1(\theta) = I_{**}(\theta) - M(\theta) \ . \tag{6-8}$$

Equation (6-7) is generalized to inelastic scattering with the assumption that the multiple scattering of neutrons approach thermal equilibrium so their distribution is Gaussian (77) with respect to the time-of-flight:

$$M(\theta,\tau) = \frac{X^4\, M(\theta)}{\tau}\, e^{-X^2} \quad . \tag{6-9}$$

In equation (6-9), $X \equiv \tau_f/\tau$, where τ_f is a parameter determined by fitting to the data (see Section 6.2). Combining equations (6-3) and (6-9), and correcting for absorption, the desired form for the single-scattering intensity becomes

$$I_1(\theta,\tau) = \frac{1}{A(\theta,\tau)}[I_{**}(\theta,\tau) - \frac{X^4}{\tau}\delta(\theta)e^{-X^2}\int_0^\infty dt\; I_{**}(\theta,t)]. \tag{6-10}$$

Again, $I_{**}(\theta,\tau)$ is the neutron intensity before correcting for multiple scattering and absorption, and $I_1(\theta,\tau)$ is the fully-corrected single-scattered intensity.

Because each detector is not exactly alike, calibration runs with vanadium and air were made, and the differential scattering cross-section is corrected accordingly:

$$\frac{d^2\sigma}{d\Omega d\tau} = [\frac{(\sigma\rho)_{van}}{(\sigma\rho)_{xe}}]\; \frac{I_1^{Xe+SV}(\theta,\tau) - I_1^{SV}(\theta,\tau)}{I_1^{V+A}(\theta) - I_1^{A}(\theta)}\;, \tag{6-11}$$

where the single-scattered intensities are calculated using equation (6-10). In equation (6-11), the superscripts (V+A) and (A) are introduced to denote the vanadium plus air and air intensities, respectively.

6.2 Correction for Multiple Scattering

In the calculation of $S(Q,\omega)$ it is necessary to separate the primary scattering of neutrons from the secondary and higher orders of scattering. The problem of multiple scattering events has been treated in a general way (78), in addition to the rigorous Monte

Carlo (79) calculations, and a solution for the multiple scattering of neutrons by infinite slabs of an isotropic scatterer has been derived by Vineyard (76). This calculation separates the primary scatter, in which the neutrons have been diffracted only once, from the secondary scatter, where two diffraction events have occurred, and finally from all subsequent higher-order events.

Blech and Averbach (80) followed Vineyard and calculated the scattering ratio for a cylindrical sample. The ratio of secondary to primary scattering, $\delta(\theta)$, was evaluated numerically and tabulated as a function of μR and R/H, where μ is the sample attenuation and R and H are the cylinder radius and height, respectively. These tabulated values were used to estimated the multiple scattering contribution to the neutron intensities, and the results are summarized in Table 6-1 and Figure 6-3; $\delta(\theta)$ was assumed to be zero for air and independent of angle, as suggested by Blech _et al_. (80).

The generalization of Vineyard's theory of multiple scattering to inelastic scattering assumes that the velocities of the scattered neutrons are Gaussianly distributed (77), as suggested by equation (6-9). Upper and lower bounds on the parameter, τ_f, can be established via physical arguments. For situations where most of the neutrons are scattered elastically then leave the sample, τ_f would correspond to $1/v_o$, where v_o is the average incident neutron velocity. On the other extreme, if the neutrons were scattered several times such that they come to thermal equilibrium before leaving the sample, τ_f would approach $1/v_t$, where v_t is the neutron velocity when in thermal equilibrium with the sample,

TABLE 6-1

RATIO OF TWICE-SCATTERED TO SINGLY-SCATTERED NEUTRONS (δ)

Material	δ
Vanadium	0.051
Aluminum	0.026
Xenon: ρ, $\frac{\text{mole}}{\text{liter}}$	
3.08	0.050
3.80	0.045
4.67	0.040
5.51	0.038
7.60	0.037

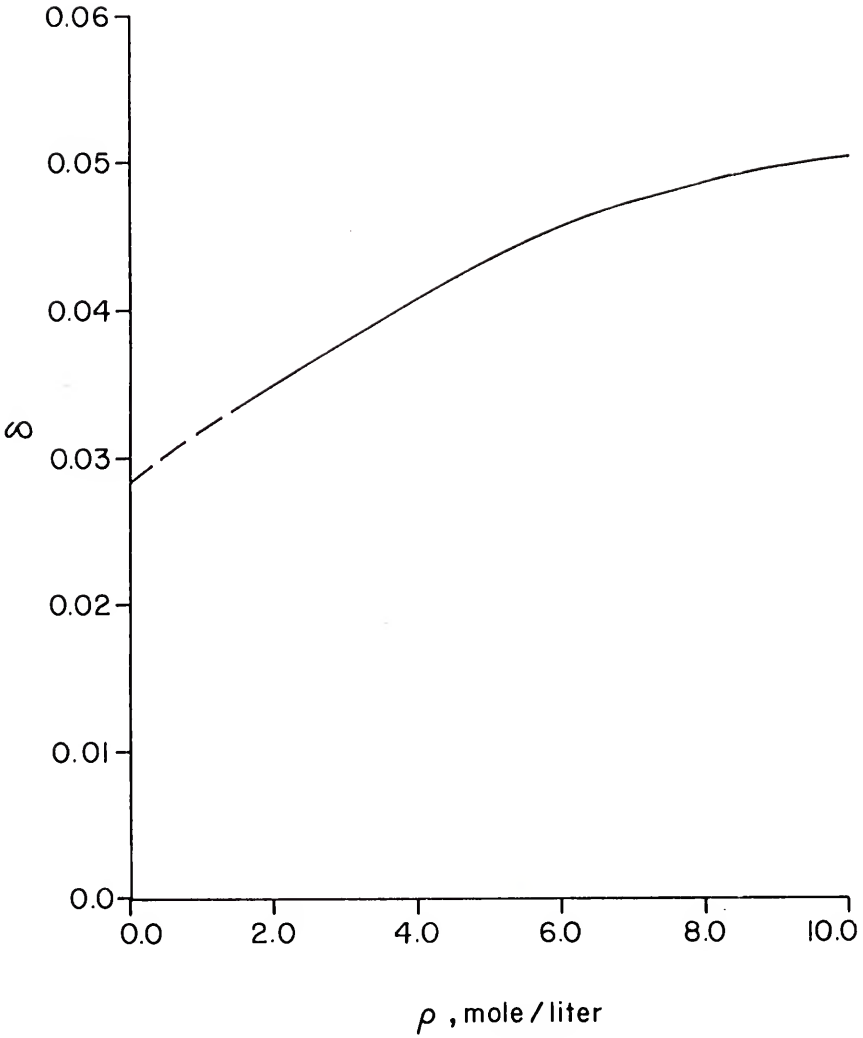

Figure 6-3. The ratio, δ, of twice-scattered neutrons (I_2) to singly scattered neutrons (I_1) as a function of the xenon density; ρ = 0 corresponds to the aluminum sample vessel.

$$v_t = \left(\frac{3kT}{m_n}\right)^{\frac{1}{2}} \quad . \tag{6-12}$$

In equation (6-12), k is Boltzmann's constant, m_n is the neutron mass, and T is the sample temperature. Clearly, if $v_t > v_o$, then

$$365 \frac{\mu_{sec}}{m} = \frac{1}{v_t} < \tau_f < \frac{1}{v_o} = 555 \frac{\mu_{sec}}{m} \quad . \tag{6-13}$$

Figure 6-4, a plot of the multiple scattering contribution (---) superimposed on the experimental time-of-flight spectrum (——), illustrates the procedure followed in estimating τ_f. Since the single scattering is nearly elastic at low angles, and $\delta(\theta)$ and τ_f are assumed to be independent of angle, the wings of the distribution at low angles are determined by the multiple scattering. The parameter τ_f was specified by fitting equation (6-9) to the wings of the experimental data at the lower angles (up to $2\theta=15^o$). In practice it was found that multiple scattering contributed only a small portion ($\sim$ 1%) to the total peak <u>area</u>, so that the value of τ_f was not critical; $\tau_f = 490\ \mu_{sec}/m$ was used in the analysis. This value lies in the range of equation (6-13).

6.3 Correction for Absorption

Theoretical expressions which describe the scattering of neutrons are usually derived by considering a sample so thin that neutron absorption can be neglected. In practice, both the incident and the scattered beams are subject to self-absorption, not only within the sample itself, but to further absorption within the walls of the sample vessel. As with multiple scattering, corrections must be made for absorption before experimental data are treated on an absolute basis.

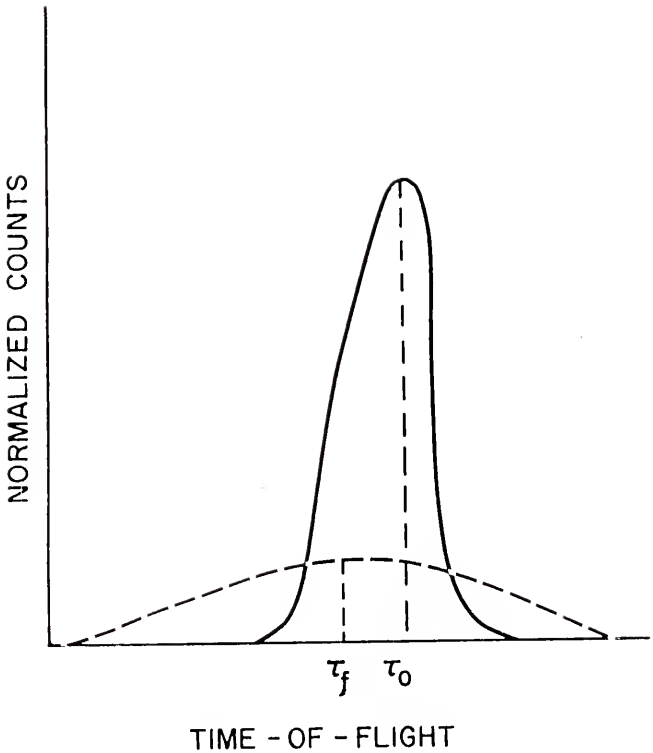

Figure 6-4. Procedure used for estimating τ_f in equation (6-9). The xenon time-of-flight spectrum (——) is shown for low angles, and (---) is the multiple scattering correction of equation (6-9). Note that this figure is <u>not</u> drawn to scale.

Blake (81) presented formulae and tables for the self absorption of X-rays within a cylindrical sample, and Ritter (82) extended the analysis by considering the effect of an annular cell surrounding a sample which is fully exposed to a uniform incident beam. The computations are lengthy and involved, especially if carried out by the graphical technique employed by Ritter. Paalman and Pings (83) placed Ritter's computation into a rigorous mathematical form, and Kendig and Pings (84) generalized the method to incident X-ray beams of arbitrary dimensions. The extension to neutron beams is straightforward and is discussed below.

Assuming that the sample and vessel can be homogenized (see Appendix I), the expression given by Kendig and Pings for the absorption factor, $A(\theta,\tau)$, reduces to the following:

$$A(\theta,\tau) = \{A_s(a) + A_s(b)\}^{-1} \{SR(a,o) + ST(a,o) + SR(b,1) + ST(b,1)\} , \tag{6-14}$$

where

$$SR(d,q) = \frac{\pi R^2}{3m_s^2} \sum_{m=1}^{m_d} (1-\frac{1}{2m}) \sum_{n=1}^{3m} \exp[-\mu_i \ell_s^{(i)}(r_m,\omega_{mn} + q\pi,\theta) - \mu_s \ell_s^{(s)}(r_m,\omega_{mn} + q\pi,\theta)] , \tag{6-15}$$

$$ST(d,q) = \frac{\pi R^2}{3m_s^2} \sum_{m=m_{d+1}}^{m_s} (1-\frac{1}{2m}) \sum_{n=1}^{n_d} \{\exp[-\mu_i \ell_s^{(i)}(r_m,\omega_{mn} + q\pi,\theta) - \mu_s \ell_s^{(s)}(r_m,\omega_{mn} + q\pi,\theta)] + \exp[-\mu_i \ell_s^{(i)}(r_m,\pi-\omega_{mn} + q\pi,\theta) - \mu_s \ell_s^{(s)}(r_m,\pi-\omega_{mn} + q\pi,\theta)]\} , \tag{6-16}$$

$$A_s(d) = \frac{\pi}{2} R^2 - R^2 \cos^{-1} \left(\frac{|d|}{R}\right) + |d| \ (R^2 - d^2)^{\frac{1}{2}} \ , \qquad (6\text{-}17)$$

$$m_d = [m_s \left(\frac{|d|}{R}\right) + \frac{1}{2}] \ , \qquad (6\text{-}18)$$

and

$$n_d = [\frac{3m}{\pi} \sin^{-1} \left(\frac{|d|}{r_m}\right) + \frac{1}{2}] \ . \qquad (6\text{-}19)$$

The brackets in equations (6-18) and (6-19) signify the "greatest integer in." In equations (6-15) and (6-16), m_s is an arbitrary parameter determining the size of the area elements. It was found that a value of 50 for m_s was sufficient to ensure convergence of the summations.

In equations (6-15) and (6-16), μ_i is the total attenuation for the incident beam, μ_s is the total attenuation for the scattered beam, and $\ell_s^{(i)}$ and $\ell_s^{(s)}$ are the corresponding path lengths:

$$\ell_s^{(i)}(r,\omega,\theta) = r \cos \omega + (R^2 - r^2 \sin^2 \omega)^{\frac{1}{2}} \ , \qquad (6\text{-}20)$$

$$\ell_s^{(s)}(r,\omega,\theta) = -r \cos(\omega-2\theta) + [R^2 - r^2 \sin^2(\omega-2\theta)]^{\frac{1}{2}}. \qquad (6\text{-}21)$$

For elastic scattering, $\mu_i = \mu_s$, and the expression for $A(\theta,\tau)$ reduces to that given by Kendig and Pings (84).

It was assumed in all calculations that the total attenuation for a particular wave-length, λ, is given by

$$\mu(\lambda) = [\frac{\lambda}{\lambda_{ref}} \sigma_a(\lambda_{ref}) + \sigma_s] \ \rho_{eff} \ , \qquad (6\text{-}22)$$

where $\sigma_s(\lambda_{ref})$ is the absorption cross-section at the reference wave-length (usually taken as 1.8 Å), σ_s is the scattering cross-section, and ρ_{eff} is the effective sample number density (see Appendix I).

For the incident beam, $\mu_i = \mu(\lambda_o)$, where λ_o is the incident neutron wavelength (2.2 Å). The scattered wavelength, $\lambda_{s,i}$, corresponding to time channel i, is given by

$$\lambda_{s,i} = \left(\frac{h}{m_n \ell_{sd}}\right) i c_w \quad , \tag{6-23}$$

where c_w is the channel width, (12.093 μ_{sec}), h is Planck's constant, ℓ_{sd} is the flight path (1.517 meters), and m_n is the neutron mass. The attenuation of the scattered beam is calculated for each time channel, using equation (6-23) for $\lambda_{s,i}$, and the effect of the change in neutron velocity due to the scattering process is shown in Figure 6-5 for a particular scattering angle (0 degrees) and a xenon density of 7.6 mole/liter. The cross-sections, σ_a and σ_s, for xenon, vanadium, and aluminum are summarized in Table 6-2; $A(\theta,\tau)$ was assumed to be unity for air.

Figure 6-6 is a comparison of the experimental xenon transmissions,

$$A(\theta=o,\ \tau_o) = \frac{(\text{Mon II/Mon I})_{\text{sample}}}{(\text{Mon II/Mon I})_{\text{empty}}} \quad , \tag{6-24}$$

where τ_o is the time-of-flight corresponding to the elastic channel, with the values calculated from equation (6-14), and Mon (...) denotes the integrated counts of monitor (...). The experimental transmissions are reported in Table 6-3 as a function of the xenon density. Also included for completeness are the vanadium and sample vessel transmissions.

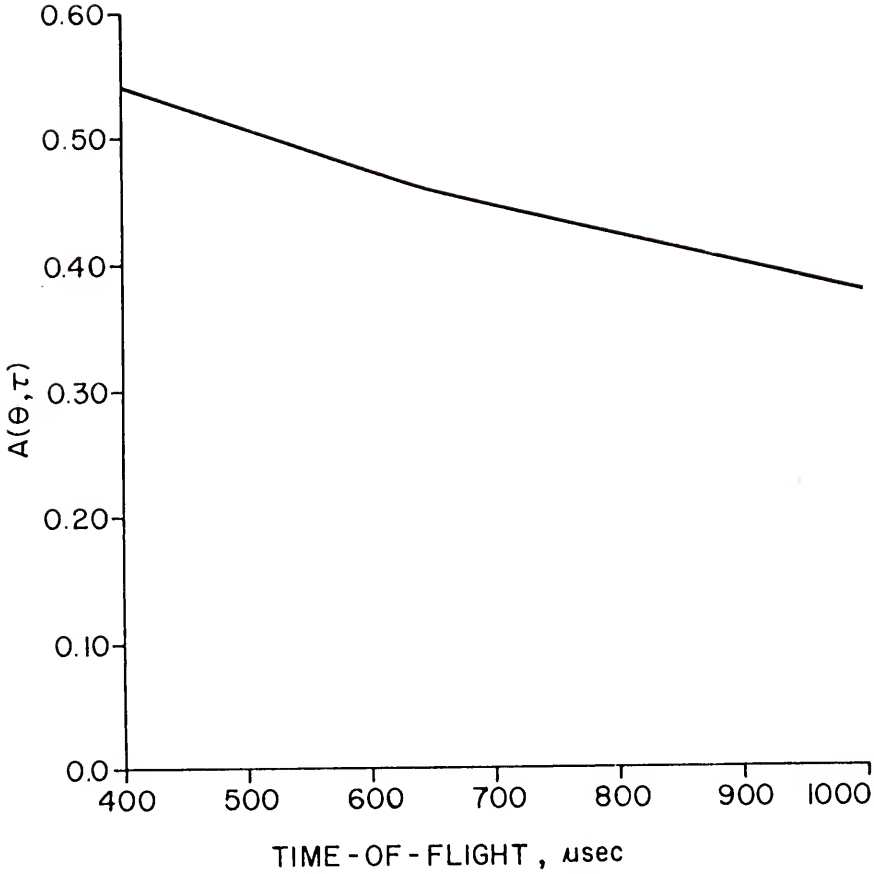

Figure 6-5. Behavior of the absorption correction, $A(\Theta,\tau)$, as a fuction of the time-of-flight; $\Theta = 0°$, $\rho = 7.6$ mole/liter.

TABLE 6-2

ABSORPTION (λ=1.8 Å) AND SCATTERING CROSS-SECTIONS FOR ALUMINUM, XENON AND VANADIUM

Material	σ_a, barn	σ_s, barn
Aluminum	0.235	1.41
Xenon	37.5	4.3
Vanadium	4.98	5.06

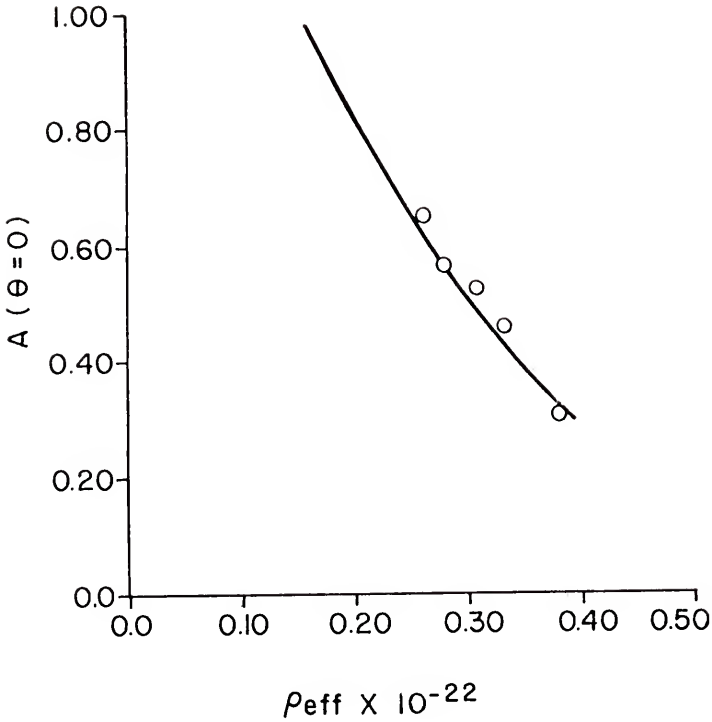

Figure 6-6. Comparison of the experimental transmissions (•), equation (6-24) with the calculated transmissions (——, equation (6-14) for $\Theta = 0°$). The effective xenon number density is obtained by homogenization of xenon plus the sample vessel.

TABLE 6-3

EXPERIMENTAL TRANSMISSIONS

Material	ρ, mole/liter	$A(\theta=0)$
Xenon	3.08	0.65
	3.80	0.57
	4.67	0.52
	5.51	0.46
	7.60	0.31
Aluminum	94.6	0.95
Vanadium	117.0	0.72

6.4 Normalization of Data

In this section the conversion from time-of-flight units to energy units, and the subsequent normalization of $S(Q,\omega)$ to $S(Q)$, is discussed. From the equation

$$\hbar\,\omega_i = E_o - E_i \ , \tag{5-1}$$

and the fact that E_i can be written in terms of the time-of-flight,

$$E_i = \frac{m_n}{2\tau_i^2} \ , \tag{6-25}$$

The following relationship between $d\omega$ and $d\tau$ exists:

$$\tau^3 \frac{d\omega}{d\tau} = c_1 \ , \tag{6-26}$$

where c_1 is defined as the ratio $m_n/\hbar$. In this way the differential scattering cross-section becomes

$$\frac{d^2\sigma}{d\Omega d\omega} = \frac{1}{c_1}\,\tau^3\,\frac{d^2\sigma}{d\Omega d\tau} \ . \tag{6-27}$$

From equation (1-26),

$$\frac{d^2\sigma}{d\Omega d\omega} = \frac{k}{k_o}\,\tilde{S}(Q,\omega) \ , \tag{6-28}$$

where the wave vector, k, is written in terms of the time-of-flight as

$$\hbar k = \frac{m_n}{\tau} \ , \tag{6-29}$$

and the tilde over $S(Q,\omega)$ denotes

$$\tilde{S}(Q,\omega) = b_{coh}^2 S(Q,\omega) + b_{incoh}^2 S_s(Q,\omega) \ , \tag{6-30}$$

the following equation for $\tilde{S}(Q,\omega)$ is obtained:

$$\tilde{S}(Q,\omega) = \left(\frac{\tau^4}{c_1 \tau_0}\right) \frac{d^2\sigma}{d\Omega d\tau} \quad . \tag{6-31}$$

Equation (6-31) is not the final form for $\tilde{S}(Q,\omega)$, however, since consistency should be achieved by normalizing the data to $S(Q)$.

The connection between $S(Q,\omega)$ and the static structure factor is given in equation (5-3) and reproduced below for convenience:

$$S(Q) = \int_{-\infty}^{+\infty} d\omega \, S(Q,\omega) \quad . \tag{5-3}$$

Hence we see that $S(Q)$ involves an integration of $S(Q,\omega)$ over ω at <u>constant</u> Q. In view of the relationship between Q and ω, i.e.,

$$\frac{\hbar^2 Q^2}{2m_n} = 2E_o + \hbar\omega - 2(E_0^2 + \hbar\omega E_o)^{\frac{1}{2}} \cos 2\theta, \tag{6-32}$$

the momentum transfer reduces to that for elastic scattering,

$$Q_o = \frac{4\pi \sin \theta}{\lambda_o} \quad , \tag{5-10}$$

only when the neutron energy, E_o, is high compared to the energy transfer, $\hbar\omega$ (85). In Figure 6-7 the functional dependence of ω on the momentum transfer is illustrated for various scattering angles. As is evident from the figure, Q remains essentailly constant with angle for the experimental conditions of interest.

As implied by equation (6-32), small changes in energy on scattering cause changes in the momentum transfer between the neutron and the xenon atom. For this reason,

$$\int_{-\infty}^{+\infty} d\omega \left(\frac{d^2\sigma}{d\Omega d\omega}\right) = \int_0^{\infty} d\tau \left(\frac{d^2\sigma}{d\Omega d\tau}\right) \tag{6-33}$$

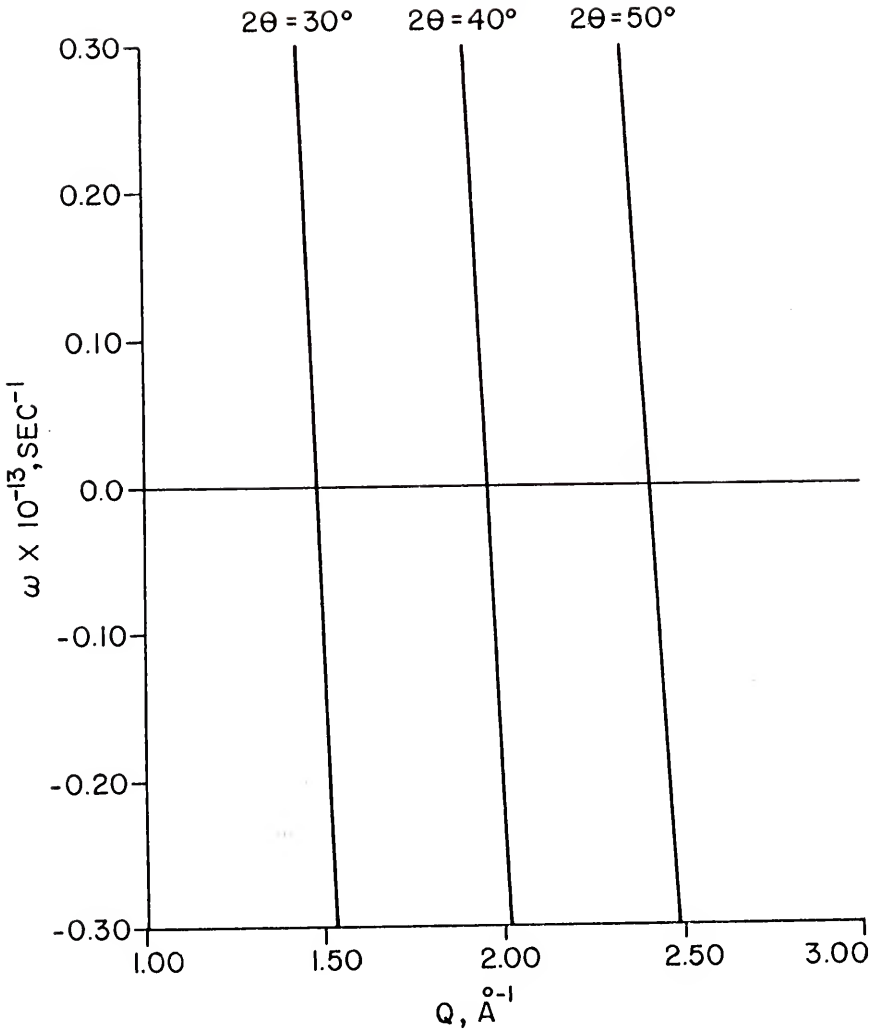

Figure 6-7. An (ω,Q) diagram for various scattering angles, 2θ.

only if $k = k_o$ and Q is not a function of the energy transfer. In the limiting case of the energy transfer being small compared with the incident energy, $\tilde{S}_{eff}(Q)$, determined by the integration

$$\tilde{S}_{eff}(Q) = \int_0^{\infty} d\tau \left(\frac{d^2\sigma}{d\Omega d\tau}\right) , \tag{6-34}$$

is related to the true structure factor,

$$\tilde{S}(Q) = \int_{-\infty}^{+\infty} d\omega \left(\frac{d^2\sigma}{d\Omega d\omega}\right) , \tag{6-35}$$

through (86) equation (6-36):

$$\tilde{S}_{eff}(Q) = \tilde{S}(Q) - \frac{m_n}{2M} \left[\frac{kT}{E_o} - \sin^2(\theta/2)\right] . \tag{6-36}$$

Here, M is the atomic mass of xenon, k is Boltzmann's constant and T is the sample temperature. For xenon at room temperature, the Placzek correction, i.e., the bracketed term in equation (6-36), is negligible so that $\tilde{S}(Q)$ can be determined by direct integration of the time-of-flight spectrum, as implied in equation (6-33).

For comparison with theory, $\tilde{S}(Q,\omega)$ is normalized to $\tilde{S}(Q)$, with the result

$$\tilde{S}(Q,\omega) = \left(\frac{\tau^4}{c_1\tau_0}\right) N(Q) \left(\frac{d^2\sigma}{d\Omega d\tau}\right) , \tag{6-37}$$

where N(Q) is the normalization constant

$$N(Q) = \frac{b^2_{coh}\ S(Q) + b^2_{incoh}}{\int_0^{\infty} d\tau \left(\frac{d^2\sigma}{d\Omega d\tau}\right)} . \tag{6-38}$$

Equation (6-37) is the final form for $\tilde{S}(Q,\omega)$.

6.5 Instrument Resolution and Stability

In Chapter 7 the theoretical results of Chapters 2, 3, and 4 are compared with experimental measurements of $S(Q,\omega)$ and $S(Q)$ for low density xenon gas. Experimental results of this kind, however, include the resolution broadening of the spectrometer and must therefore be compared to theoretical results which have been broadened by the same function. Also crucial to the comparison of theory and experiment is an estimation of instrument stability during the experimental runs. Resolution and stability of the spectrometer are discussed in this section.

6.5.1 Instrument Resolution. The instrument resolution function is deduced from time-of-flight data taken with a vanadium spiral of approximately the same dimensions as the xenon sample vessel. The Debye temperature of crystalline vanadium is $\sim$ 350 K so that at room temperature the scattering is mainly elastic. Also, since the two spin-weighted scattering amplitudes for ^{51}V are almost equal in magnitude but opposite in sign, interference effects can be neglected. Hence, the scattering is isotropic, and the spectrum scattered by vanadium (see Figure 6-8) consists mainly of an elastic peak (86). Figure 6-8 is the resolution function to be convoluted with the kinetic theory in Chapter 7, and represents an average over three separate runs and thirty scattering angles. That the energy resolution of the spectrometer is poor is best seen in Figure 6-9, where the resolution function is superimposed on a typical xenon (i.e., 11.8 degrees) spectrum. From Figure 6-9 one can conclude that a great deal of the width seen in the xenon time-of-flight spectra is due, not to xenon, but to broadening by the spectrometer.

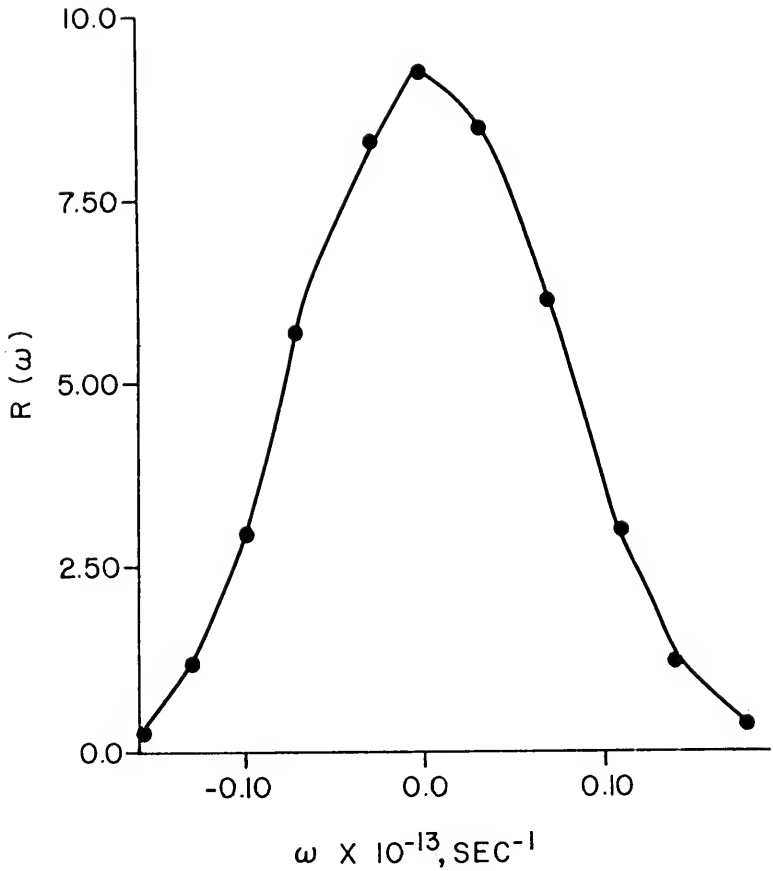

Figure 6-8. The spectrometer resolution function R(ω). The closed circles are the data and the solid line is drawn as a visual aid.

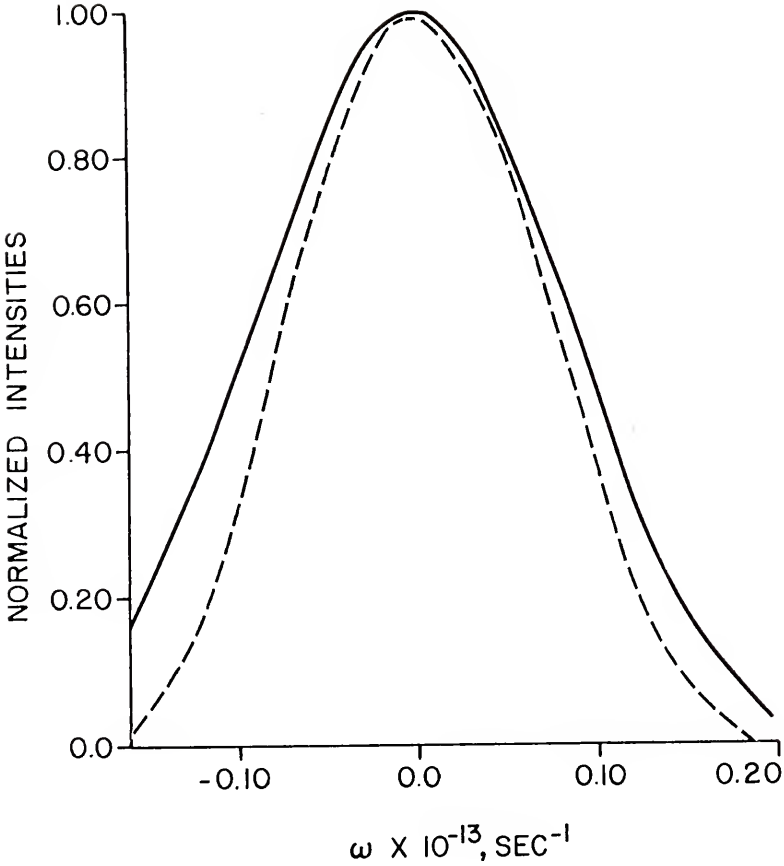

Figure 6-9. Comparison of the spectrometer energy resolution function (---) with a typical xenon spectrum (——). Both are normalized to a peak value of unity for comparison.

6.5.2 Instrument Stability. In Chapter 5 we indicated several possible sources of experimental error. For convenience, we list these below:

(1) Oscillations due to pseudo-random correlation technique (Section 5.2)

(2) Large contribution to time-of-flight spectra from air scattering (Section 5.3)

(3) Loose cadmium vanes (Section 5.3)

(4) RF pickup on detectors (Section 5.3)

One additional source of error not covered above is that due to counting statistics. In particular, if A is the area under the peak (refer to Figure 6-10), and B is the background area, then the uncertainty in the peak area (A-B) is simply $\sqrt{A + B}$. As we discussed in Section 6.1 (see equation (6-11)), the static structure factor is proportional to the ratio

$$T(Q) = \frac{I^{Xe + SV}(Q) - I^{SV}(Q)}{I^{V + A}(Q) - I^{A}(Q)} , \tag{6-39}$$

where I(Q) is the integrated time-of-flight spectrum; (Xe + SV) denotes the xenon plus sample vessel, (V + A) denotes vanadium plus air, and so on. Associated with each peak area is an uncertainty, so that a more appropriate form for equation (6-39) is

$$T(Q) = \frac{I^{Xe}(Q) \pm \Delta I^{Xe}(Q)}{I^{V}(Q) \pm \Delta I^{V}(Q)} , \tag{6-40}$$

where

$$\begin{aligned} I^{Xe}(Q) &\equiv I^{Xe + SV}(Q) - I^{SV}(Q) , \\ I^{V}(Q) &\equiv I^{V + A}(Q) - I^{A}(Q) , \end{aligned} \tag{6-41}$$

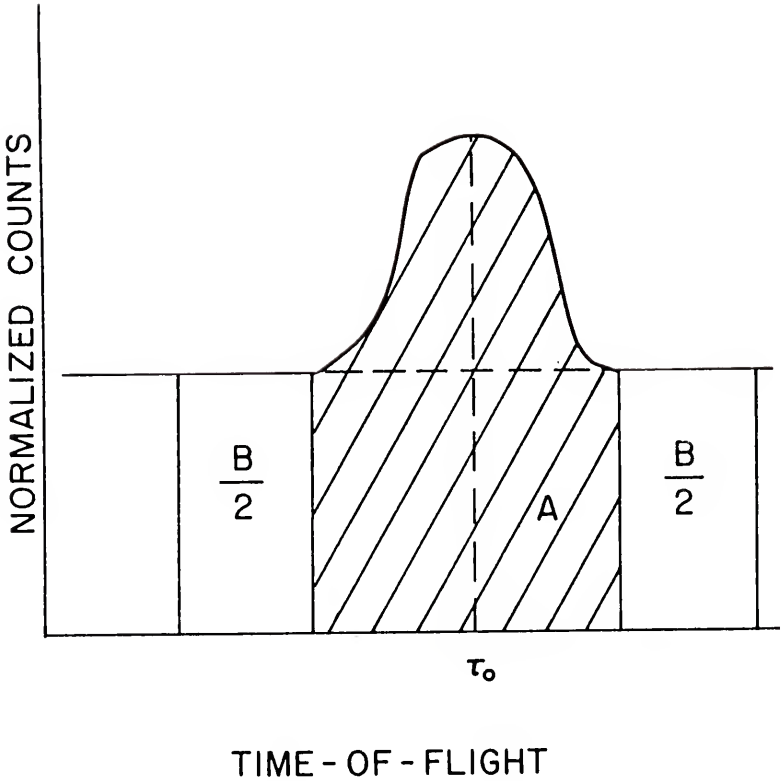

Figure 6-10. Areas used in estimating errors due to counting statistics. The shaded area (A) is the area under the central peak and the two background areas (B/2) are separated from (A) by vertical lines.

and $\Delta I(Q)$ are the associated errors:

$$\Delta I^{Xe}(Q) = ([\Delta I^{Xe + SV}(Q)]^2 + [\Delta I^{SV}(Q)]^2)^{\frac{1}{2}} ,$$

$$\Delta I^{V}(Q) = ([\Delta I^{V + A}(Q)]^2 + [\Delta I^{A}(Q)]^2)^{\frac{1}{2}} . \qquad (6\text{-}42)$$

Using these relationships, the error in $S(Q)$, $\Delta S(Q)$, can be estimated (87):

$$\frac{\Delta S(Q)}{S(Q)} \sim ([\frac{\Delta I^{Xe}(Q)}{I^{Xe}(Q)}]^2 + [\frac{\Delta I^{V}(Q)}{I^{V}(Q)}]^2)^{\frac{1}{2}} . \qquad (6\text{-}43)$$

According to equation (6-43), the error in $S(Q)$ due to counting statistics only is on the order of 1 - 2%. Table 6-4 gives typical values for peak area and background counts for xenon, vanadium, the sample vessel, and air. For the integrated vanadium spectra the error was estimated to be on the order of 2 per cent.

In Figure 6-11, $I^V(Q)$ is plotted as a function of Q for three different (high, low angle) vanadium runs. Included in the figure is the least squares fit of the data (solid line) and a $\pm$ 2% error bar (dashed lines) representing the error due to counting statistics. As indicated in the figure, most of the data lie outside the estimated error limits, implying that the main contribution to the experimental error is due not to counting statistics, but probably must be attributed to one of the four sources mentioned above. This inevitably leads to the conclusion that the spectrometer was somewhat unstable during operation, and therefore it seems reasonable to expect

(1) the data on $S(Q)$ are poor ($\sim$ 5%)

(2) the ratios $\frac{S(Q,\omega)}{S(Q)}$ are acceptable since these errors should cancel one another.

TABLE 6-4

TYPICAL PEAK (Np) AND BACKGROUND (N_B) COUNTS FOR XENON, THE SAMPLE VESSEL, VANADIUM, AND AIR

Material	N_B*	N_p*
Xenon	850525	1205173
Vessel	931588	1301878
Vanadium	607398	1075700
Air	416810	613205

*For a 24 hour run.

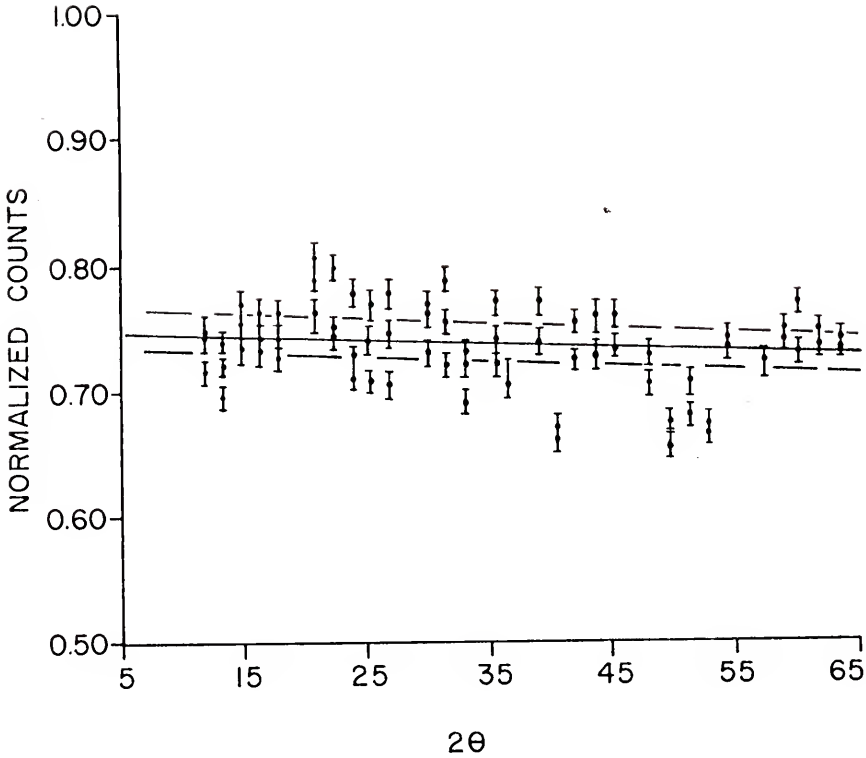

Figure 6-11. Integrated vanadium spectrum (air subtracted) as a function of the scattering angle. The solid line is a least squares fit of the data (•) and the dashed lines denote a ±2% error bar due to counting statistics.

CHAPTER 7

COMPARISON OF THEORY WITH EXPERIMENT

7.1 Introduction

The theme of this thesis has been the theoretical and experimental investigation of the structure and dynamics of a simple gas. In Chapter 2 the problem of obtaining information concerning the intermolecular forces from neutron scattering data was considered. The static structure factor, $S(Q)$, was expanded in powers of the density,

$$S(Q) = 1 + \rho S_1(Q) + \rho^2 S_2(Q) + \dots , \qquad (2\text{-}13)$$

and $S_1(Q)$ was shown to be a direct measure of the pair potential, ϕ_{ij}, $S_2(Q)$ a function of both ϕ_{ij} and the three-body potential, ϕ_{ijk}, and so on. The kinetic theory for the dynamic structure factor, $S(Q,\omega)$, written in terms of a formal collision operator, was presented in Chapter 3, and Chapter 4 was concerned with the problem of solving the kinetic equation once the collision operator has been identified. In particular, $S(Q,\omega)$ was evaluated using the N=6 Gross-Jackson kinetic model for a dilute gas of hard spheres. Finally, Chapters 5 and 6 discussed details of the neutron scattering experiment performed on low density xenon gas at the Oak Ridge National Laboratory.

In this chapter the connection between theory and experimental results is made. Section 7.3 compares the density expansion with

experimental measurements of S(Q). The theoretical calculation of the static structure factor is carried out assuming the Barker pair potential for xenon (see equations (2-9) and (2-10)), and the three-body contribution to the intermolecular potential is modeled using the Axilrod-Teller dispersion potential (equation (2-11)). In Section 7.4 the isothermal pressure derivative of the static structure factor (related to the three-point correlation function in Section 2.3) is obtained by differencing the experimental data for S(Q) at two different pressures. The analysis of the time-of-flight data is performed using the N=6 Gross-Jackson kinetic model for a fluid of hard cores. A comparison of this model (assuming (i) hard spheres and (ii) hard cores having attractive forces) with experimental measurements of $\ddot{S}(Q,\omega)$ (equation (6-30)) is made in Section 7.5. Finally, experimental measurements of the isothermal pressure derivative, $\frac{\partial S(Q,\omega)}{\partial P}$, are presented in Section 7.6.

7.2 Treatment of Data

Corrections (of the time-of-flight spectra) for multiple scattering and absorption of neutrons, and the normalization of the dynamic structure factor to S(Q), were discussed in Chapter 6. In this section, theory and experiment are put on an absolute basis by requiring the experimental values of S(Q) at the second node[1] to agree with the theoretical calculation of S(Q) at the same point.

---

[1] Here, we define a "node" of S(Q) to be a Q-value at which S(Q) = 1. For example, the first node of S(Q) is the Q-value (moving from Q=o) at which S(Q) is unity for the first time.

In Figure 7-1 the qualitative behavior of S(Q) as a function of Q, observed experimentally, is shown. For comparison, the corresponding S(Q) as predicted by the density expansion (equation (2-13)) is included (——). An examination of the time-of-flight spectra (see Figure 7-2) reveals $Q = 2.13\ \mathring{A}^{-1}$ and $Q = 2.19\ \mathring{A}^{-1}$ (shown by arrows in Figure 7-1) to be pathological data points; the strong oscillations in $S(Q,\omega)$ make the calculation of S(Q), i.e., the area under the $S(Q,\omega)$ curve, questionable. Since Bragg scattering by the aluminum vessel was eliminated by placement of the counters, it can only be concluded that $Q = 2.13\ \mathring{A}^{-1}$ and $Q = 2.19\ \mathring{A}^{-1}$ correspond to second-order Bragg scattering. For this reason these values were discarded in the further analysis of the experimental data.

Time-of-flight measurements of vanadium, and the subsequent integrated values, provide the spectrometer energy resolution (discussed in Section 6.5) necessary to put the experimental values of S(Q) on an absolute basis. This is accomplished by the ratio of effective scattering cross-sections, according to equation (6-11). However, because of the instability in the spectrometer, the absolute scale was not reliable and it was decided to match the experimental values of S(Q) at the second node (see footnote 1, and arrow in Figure 7-3) predicted by the density expansion. Applying this technique to the data in Figure 7-1, and neglecting the Q-values corresponding to second-order Bragg scattering, yields Figure 7-3; $S(Q,\omega)$ was adjusted accordingly. This procedure of normalizing S(Q) was followed for all experimental runs.

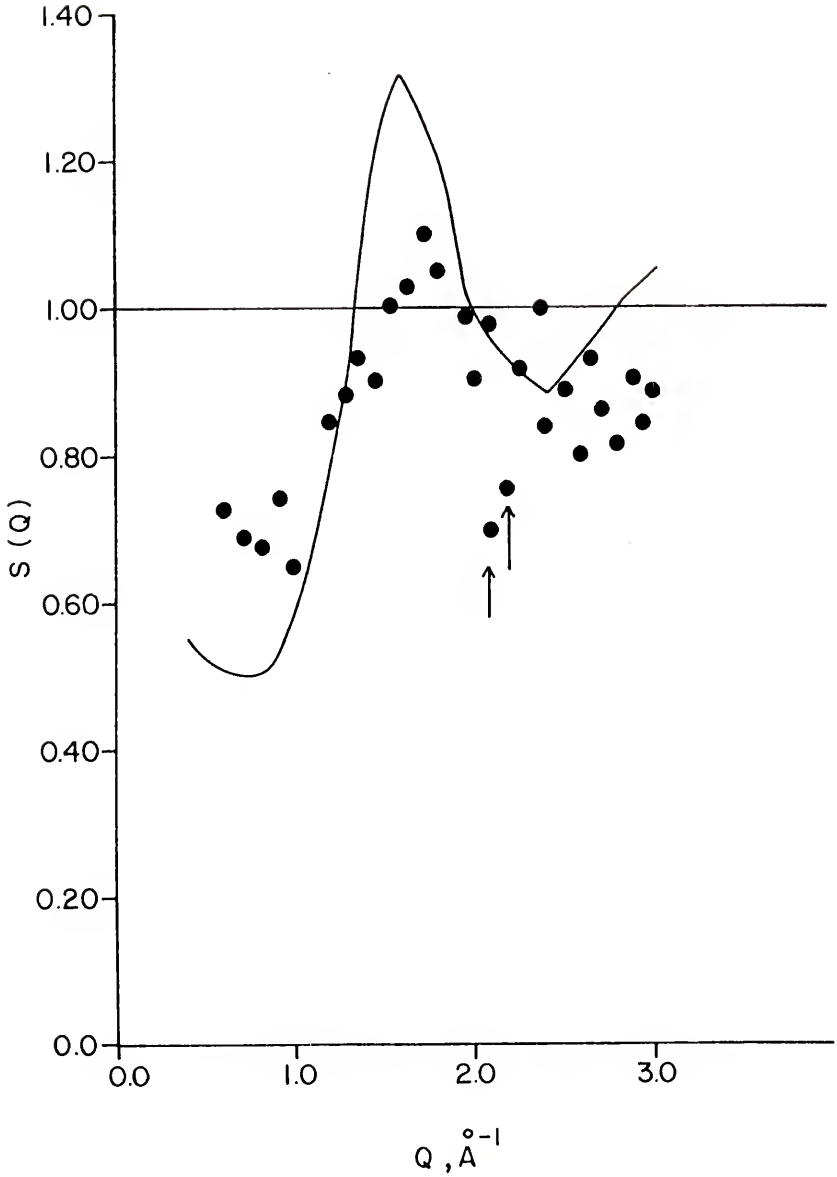

Figure 7-1. Qualitative behavior of the static structure factor observed experimentally (•) and predicted from the density expansion (equation (2-13)) of S(Q) (---). The arrows (Q = 2.13 Å^{-1}, Q = 2.19 Å^{-1}) denote the pathological data points.

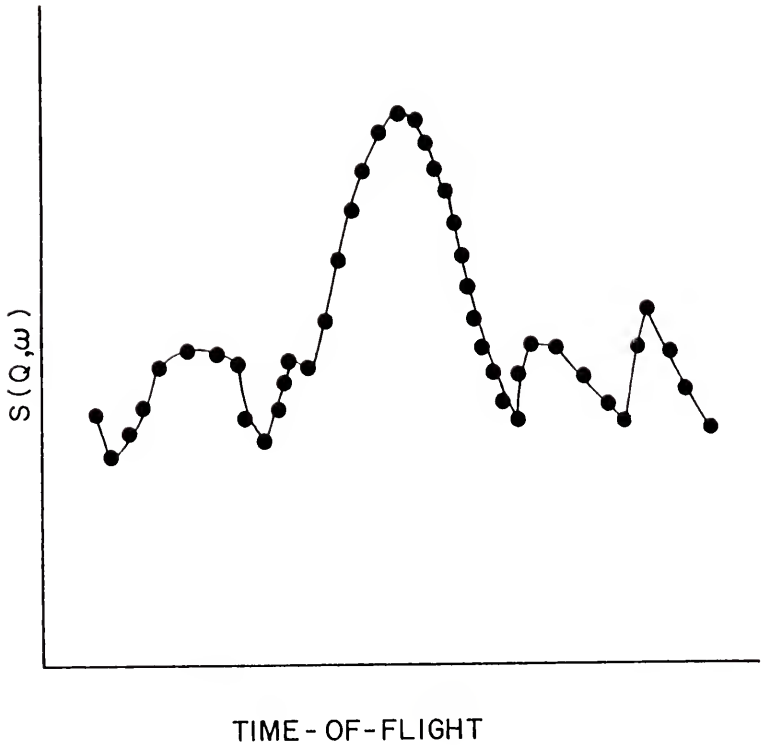

Figure 7-2. Qualitative behavior of $S(Q,\omega)$ for $Q = 2.13$ Å^{-1} and $Q = 2.19$ Å^{-1}. The large oscillations in the background are due to second-order Bragg scattering.

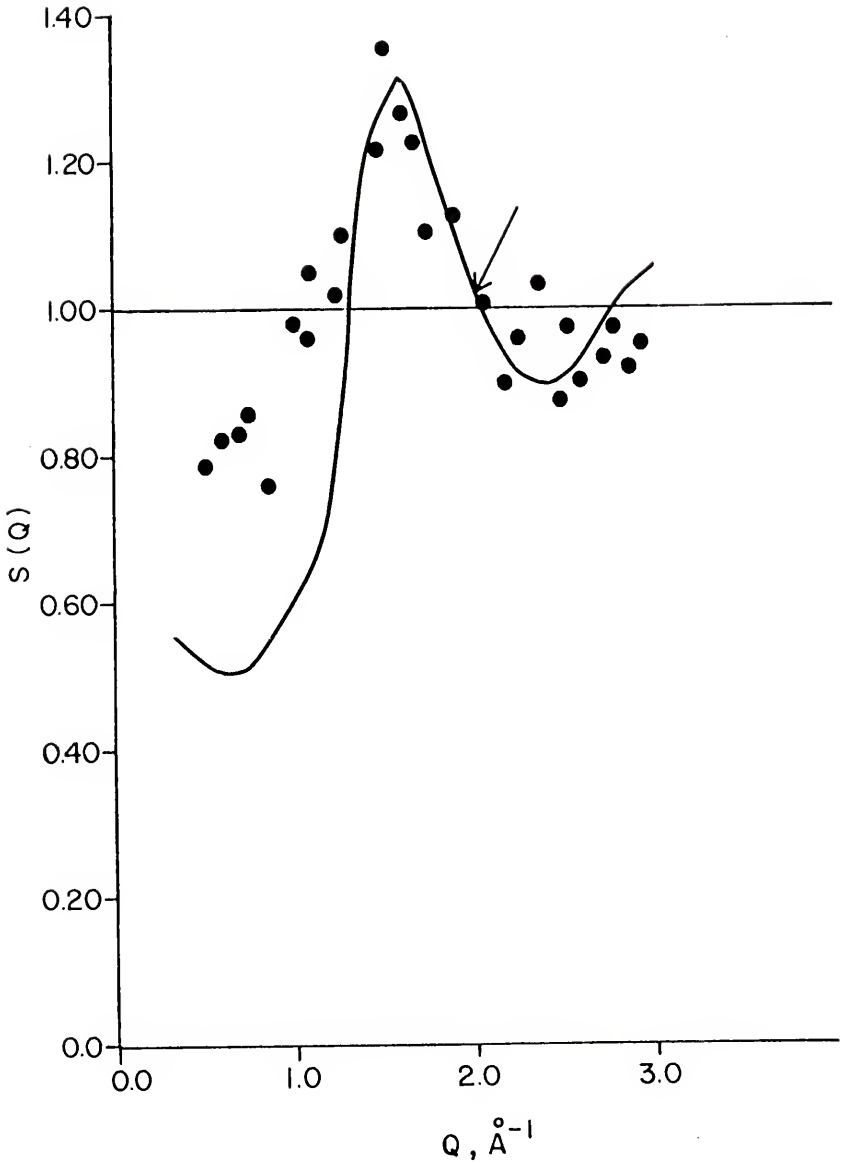

Figure 7-3. Data of Figure 7-1 with S(Q = 2.13 Å^{-1}) and S(Q = 2.19 Å^{-1}) discarded. The remaining S(Q) values are normalized to the second node in S(Q) (arrow).

7.3 The Static Structure Factor

As discussed in Section 6.4, measurements of the differential scattering cross-section, $\frac{d^2\sigma}{d\Omega d\omega}$, yield the dynamic structure factor, $S(Q,\omega)$; $S(Q)$ is then found from equation (7-1):

$$S(Q) = \frac{\tilde{S}(Q) - b^2_{incoh}}{b^2_{coh}} , \tag{7-1}$$

with

$$\tilde{S}(Q) \equiv \int_{-\infty}^{+\infty} d\omega \left(\frac{d^2\sigma}{d\Omega d\omega}\right) . \tag{7-2}$$

After normalizing the data by the procedure discussed in Section 7.2, the experimental values for $S(Q)$ are ready for comparison with the corresponding values predicted by the density expansion of $S(Q)$. The calculation of $S(Q)$ was first performed assuming pairwise additivity of the intermolecular potential for terms up to and including $S_3(Q)$ in the expansion. The comparison of theory (assuming pairwise additivity and the Barker pair potential for xenon) with experiment is shown in Figures 7-4 through 7-8. Table 7-1 summarizes the experimental state conditions and the Q=o intercept, S(o), as calculated from the realtion (17)

$$S(o) = kT \left(\frac{\partial\rho}{\partial P}\right)_T . \tag{7-3}$$

Here, $\left(\frac{\partial\rho}{\partial P}\right)_T$ was determined from the xenon equation of state, equation (5-13).

Despite the large scatter in the experimental $S(Q)$ values, several important conclusions concerning the data can be reached. To date (88), there have been only a few experimental measurements of $S(Q)$ for gases, primarily due to the lack of high intensity neutron

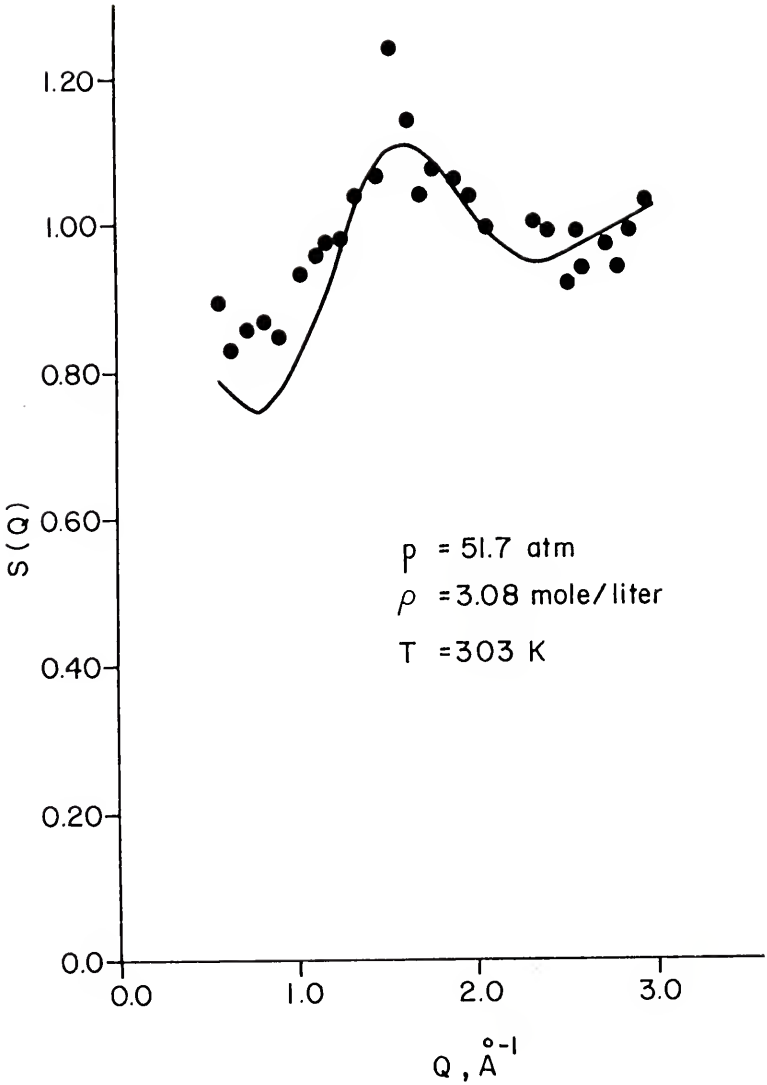

Figure 7-4. Comparison of the density expansion (equation (2-13)) of S(Q) (——) with experiment (·). Pairwise additivity and Barker's pair potential for xenon were assumed for terms up to and including $S_3(Q)$. State conditions: P = 51.7 atm, ρ = 3.08 mole/liter, T = 303 K.

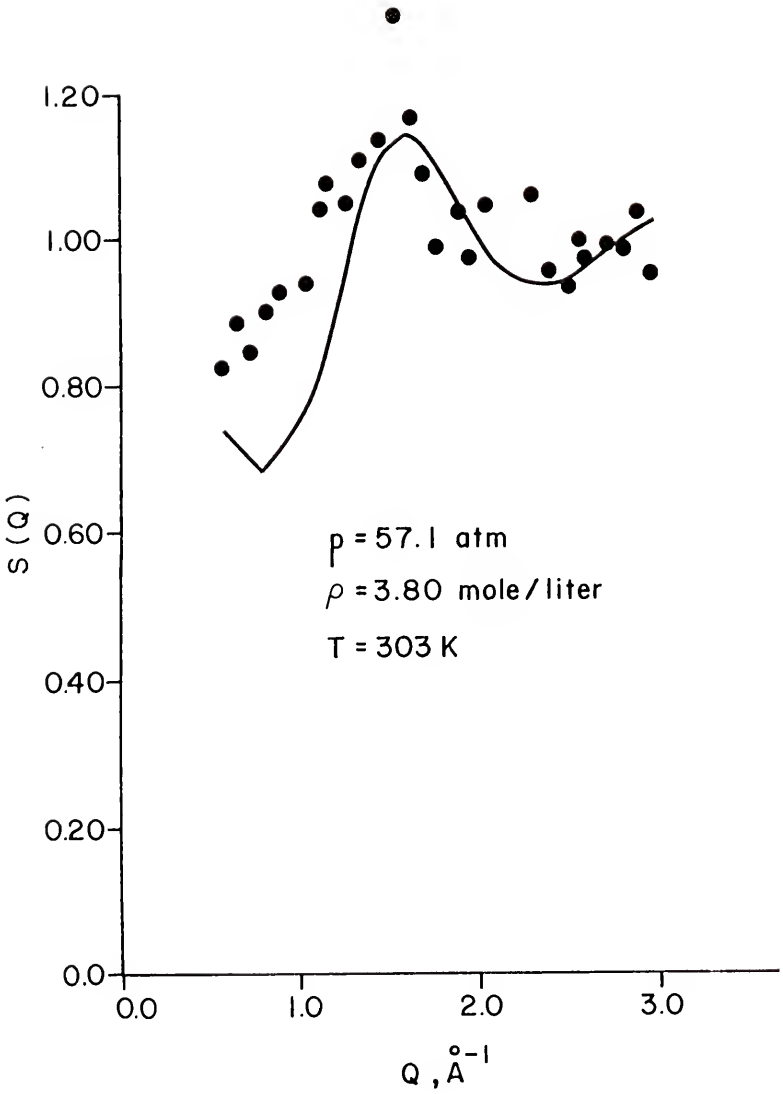

Figure 7-5. Same as Figure 7-4 except: P = 57.1 atm, ρ = 3.80 mole/liter, T = 303 K.

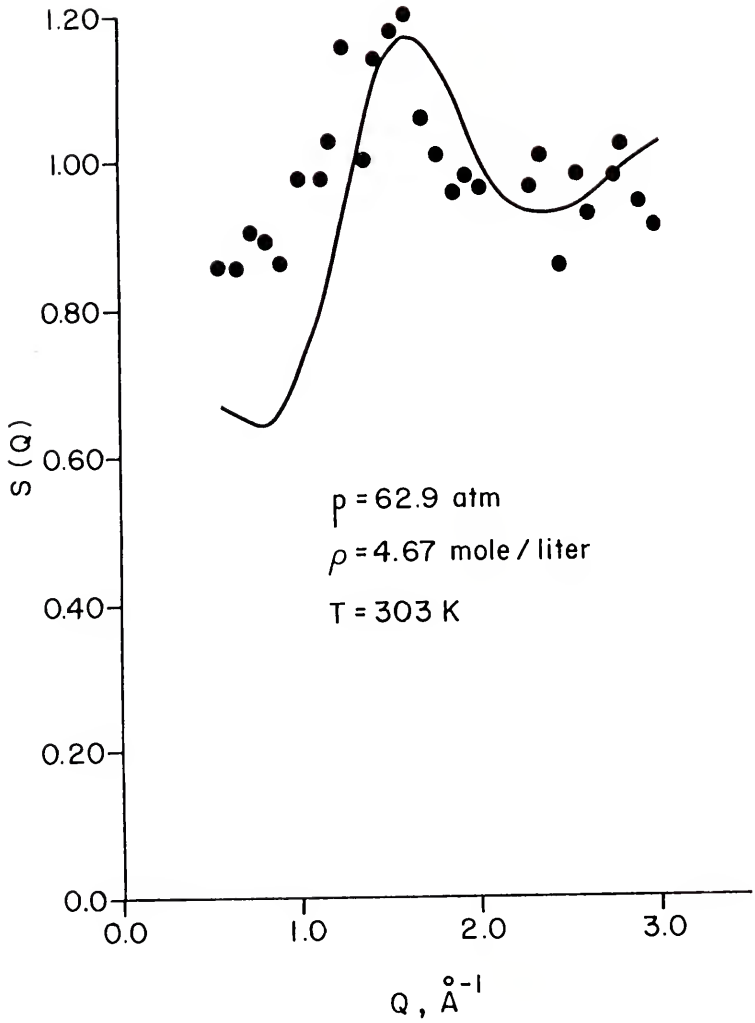

Figure 7-6. Same as Figure 7-4 except: P = 62.9 atm, ρ = 4.67 mole/liter, T = 303 K.

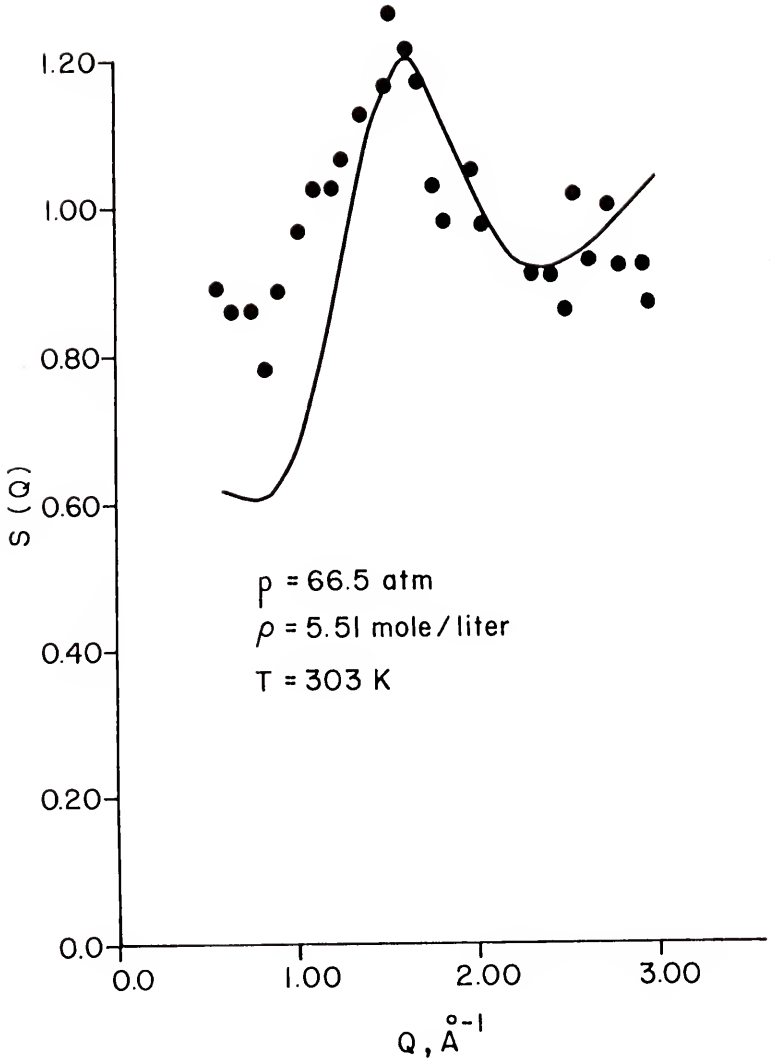

Figure 7-7. Same as Figure 7-4 except: P = 66.5 atm, ρ = 5.51 mole/liter, T = 303 K.

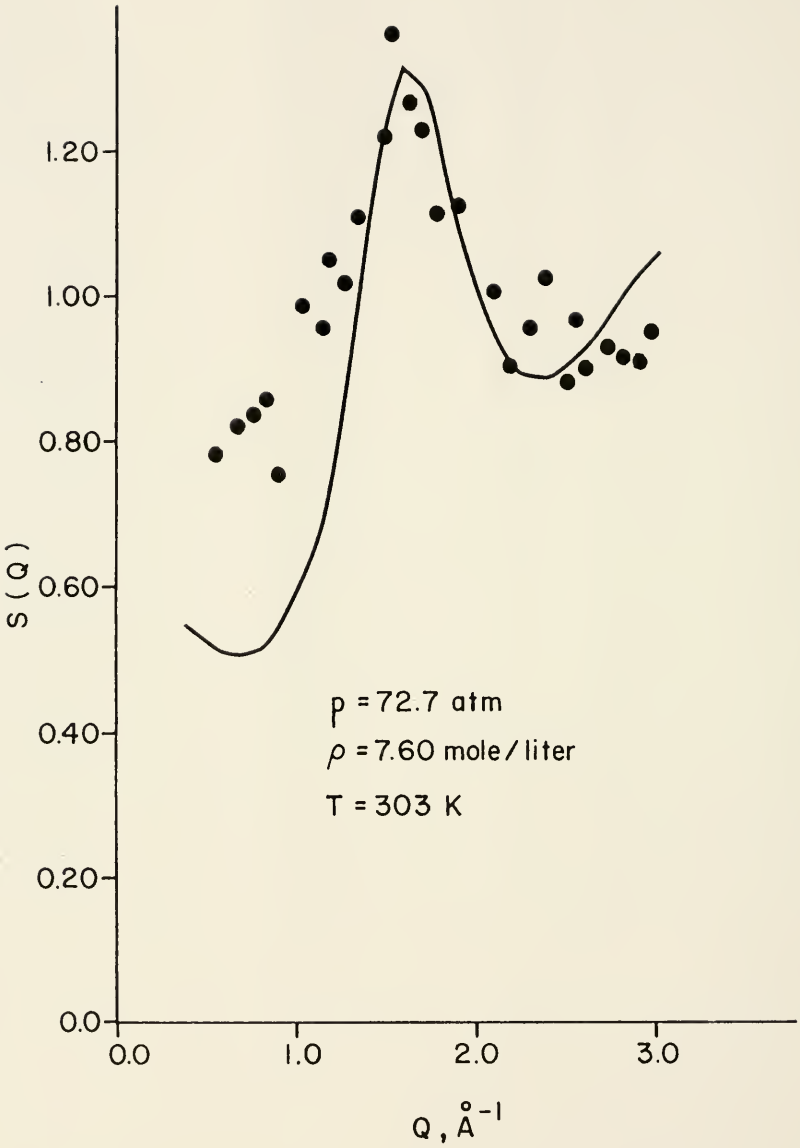

Figure 7-8. Same as Figure 7-4 except: P = 72.7 atm, ρ = 7.60 mole/liter, T = 303 K.

TABLE 7-1

SUMMARY OF EXPERIMENTAL STATE CONDITIONS
ALL RUNS AT T = 303 K

P, atm	ρ, mole/liter	$S^*(0)$
51.7	3.08	2.56
57.1	3.80	3.40
62.9	4.67	4.87
66.5	5.51	8.44
72.7	7.60	21.88

---

*S(o) determined from equation (7-3).

sources. Therefore, the results depicted in Figures 7-4 through 7-8 are gratifying in the sense that definite trends in the experimental data for S(Q) are observed with changes in the density. This in itself indicates the applicability of neutron scattering techniques for studying the structure of dilute gases.

As seen in Figures 7-4 through 7-8, the experimental data and theoretical predictions for S(Q) are in disagreement. One immediate question arises in this comparison between theory and experiment: "have enough terms been included in the density expansion of S(Q) to ensure convergence of the series?" Although the question of convergence can be answered by direct comparison with Monte Carlo results (as discussed in Chapter 2), Figures 7-9 and 7-10 are somewhat more revealing. In these figures the effect of each term in the density expansion of S(Q) is shown for the highest (ρ = 7.60 mole/liter) and lowest (ρ = 3.08 mole/liter) densities covered experimentally; the corresponding experimental data is included for comparison. Based on this term-by-term comparison we find the following:

(1) S(Q) is insensitive to higher terms, i.e., $S_2(Q)$, $S_3(Q)$,..., beyond the first peak in S(Q), so that matching experiment and theory at the second node is valid,

(2) Higher terms tend to produce a steeper slope on the low-Q side of S(Q) (for $Q \sim 1\ \text{Å}^{-1}$), thus widening the gap between theory and experiment in the range

$$1.1\ \text{Å}^{-1} < Q < 1.5\ \text{Å}^{-1} ,$$

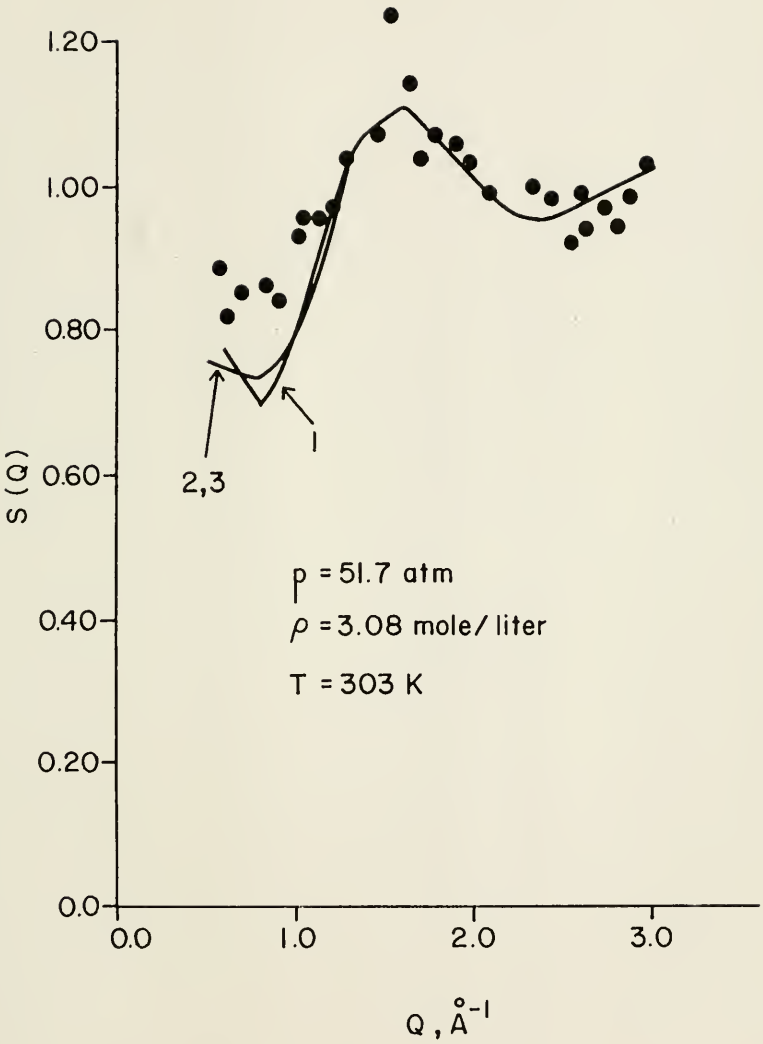

Figure 7-9. Term-by-term comparison of S(Q) for xenon. The curves labeled 1,2, and 3 are for terms up to and including S_1, S_2 and S_3 in equation (2-13), respectively. Pairwise additivity and Barker's pair potential for xenon were assumed. Full circles are experimental values.

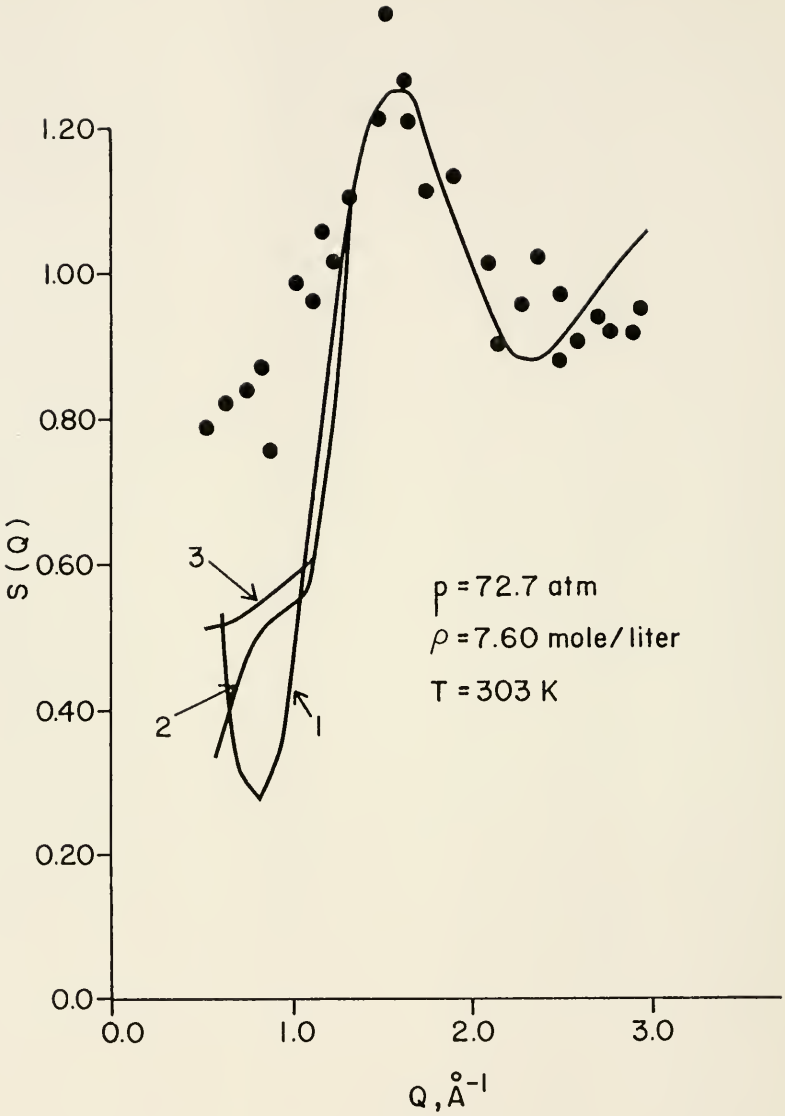

Figure 7-10. Same as Figure 7-9 except: P = 72.7 atm, ρ = 7.60 mole/liter, T = 303 K.

(3) Higher terms tend to fill in the minimum ($Q \sim 0.8$ Å^{-1}), thereby narrowing the discrepancy between theory and experiment in the range

$$0.5 \text{ Å}^{-1} < Q < 1.1 \text{ Å}^{-1} ,$$

and

(4) The truncated expression

$$S(Q) = 1 + \rho S_1(Q) + \rho^2 S_2(Q) + \rho^3 S_3(Q) , \qquad (7\text{-}4)$$

appears to be a good approximation to $S(Q)$ for the density and Q ranges studied experimentally.

These results suggest that the Barker pair potential for xenon may be somewhat in error. The Barker potential was determined (12) from macroscopic data, e.g., second virial coefficients, as was done by Barker for argon (89) and krypton (12). However, because of the lack of accurate data available for xenon (when compared with argon), Henderson (90) has suggested tentatively that Barker's potential may indeed by incorrect, as suggested in Figures 7-4 through 7-8. As a further comparison between theory and experiment, $(S(Q)-1)/\rho^*$ is plotted[2] in Figure 7-11. Included in this figures is the corresponding density expansion for the highest (---, ρ = 7.60 mole/liter) and

---

[2]Note that $(S(Q)-1)/\rho^*$ removes the linear dependence of $S(Q)$ on the density and is therefore sensitive to higher-order terms in the density expansion. Here, $\rho^* \equiv \rho r_m^3$, where r_m is the minimum in the Barker pair potential.

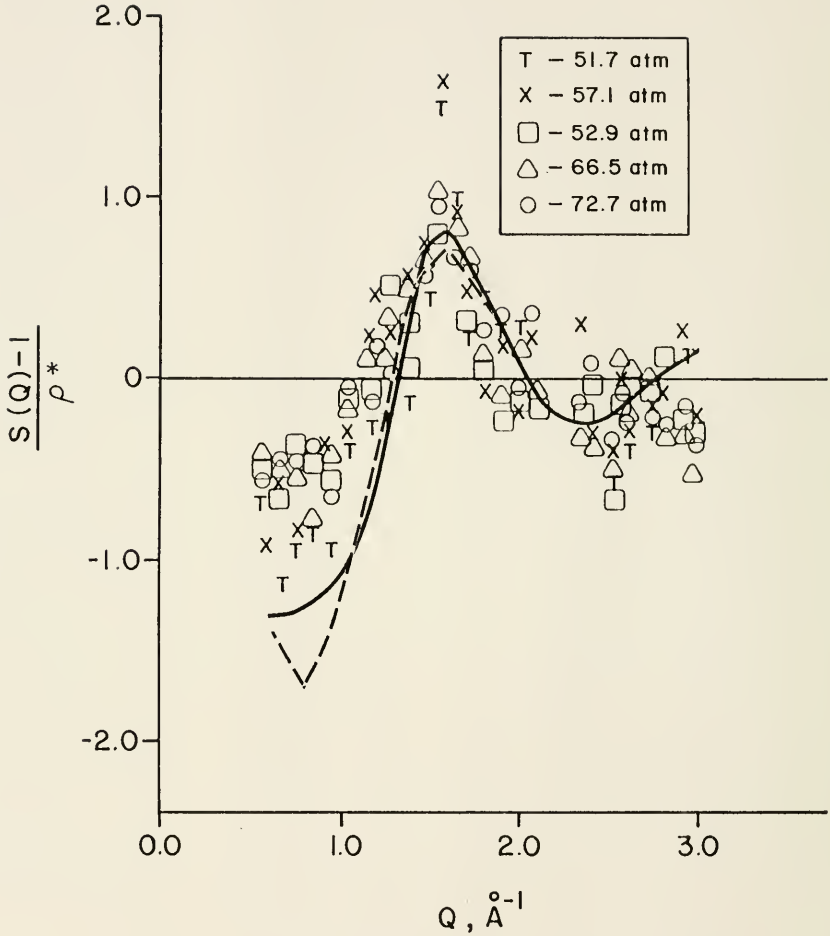

Figure 7-11. Plot of $(S(Q)-1)/\rho^*$ versus Q. Included are the results from equation (2-13) for ρ = 7.60 mole/liter (——) and ρ = 3.08 mole/liter (---). Pairwise additivity and Barker's pair potential for xenon were assumed for terms up to and including $S_3(Q)$.

lowest (---, ρ = 3.08 mole/liter) densities covered experimentally. The fluctuations in the data shown in Figure 7-11 is believed to be due to spectrometer instability as discussed in Section 6.5.2. To further examine the function $(S(Q)-1)/\rho^*$, the data is divided into two groups (corresponding to pressures above and below the critical pressure P_c = 57.89 atms) below Q = 1.0 $\mathring{A}^{-1}$, and averaged[3] at each value of Q; for Q > 1.0 $\mathring{A}^{-1}$, data for all pressures were averaged. The results of the averaging process are shown in Figure 7-12. Included in this figure is the first term in the density expansion, $S_1(Q)$, thus providing a useful comparion between theory and experiment. The solid line (——) in Figure 7-12 is an "eye-ball" fit of the averaged S(Q) points, and serves as a guide in comparing the data with $S_1(Q)$. As shown in the figure, the data and theory are shifted in Q-space, again suggesting Barker's pair potential for xenon to be somewhat erroneous. However, before coming to any firm conclusion, we must first consider the impact of non-additivity in the intermolecular potential on S(Q). To do so, we consider the three-body potential function.

As mentioned in Chapter 2, Barker _et al_. (12) found that satisfactory agreement between calculated and experimental macroscopic properties were obtained by including only the third-order triple-dipole (Axilrod-Teller) three-body dispersion interaction (given by equation (2-11)). Figures 7-13 and 7-14 are the results

---

[3]By averaging at each Q-value it is hoped that a large portion of the fluctuations in S(Q) will be removed.

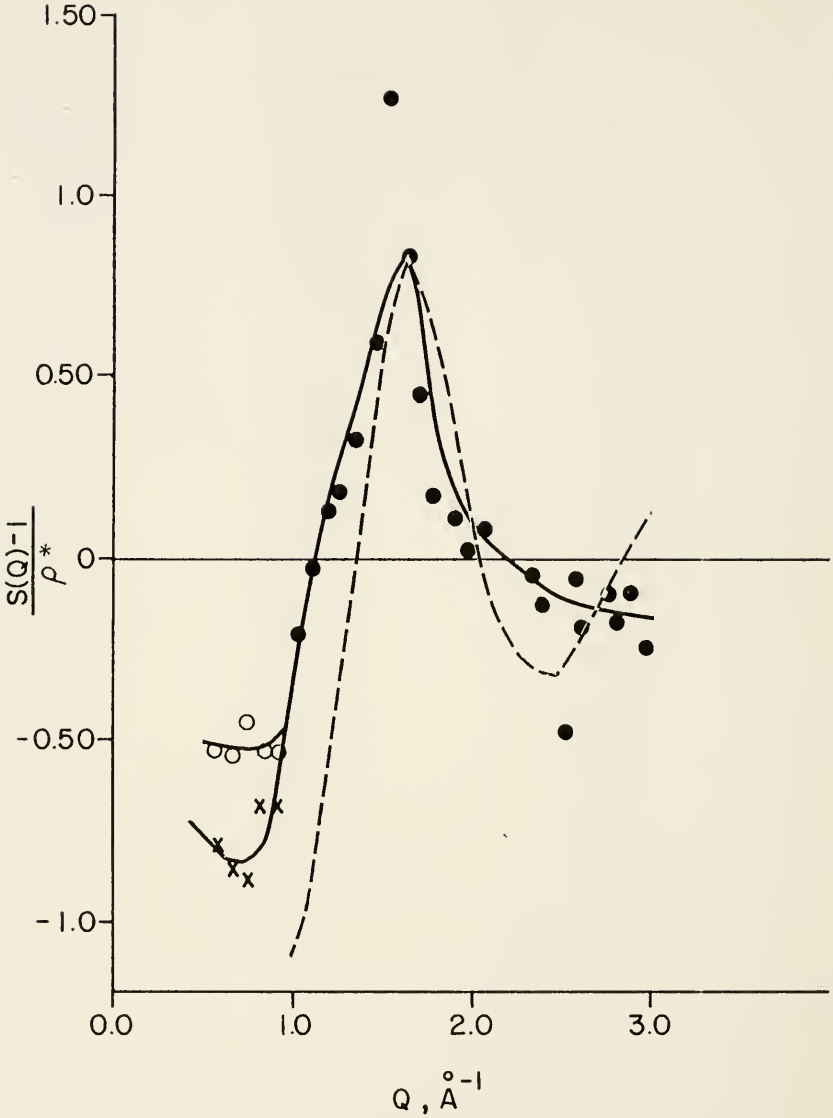

Figure 7-12. Results of averaging the data from Figure 7-11. Open circles (∘) are averages for $P < P_c$, crosses (+) are averages for $P > P_c$, and full circles (•) are averages for all P at fixed Q; P_c is the critical pressure for xenon. Included is the first term in the density expansion, $S_1(Q)$ (---). The solid lines are drawn as a visual aid.

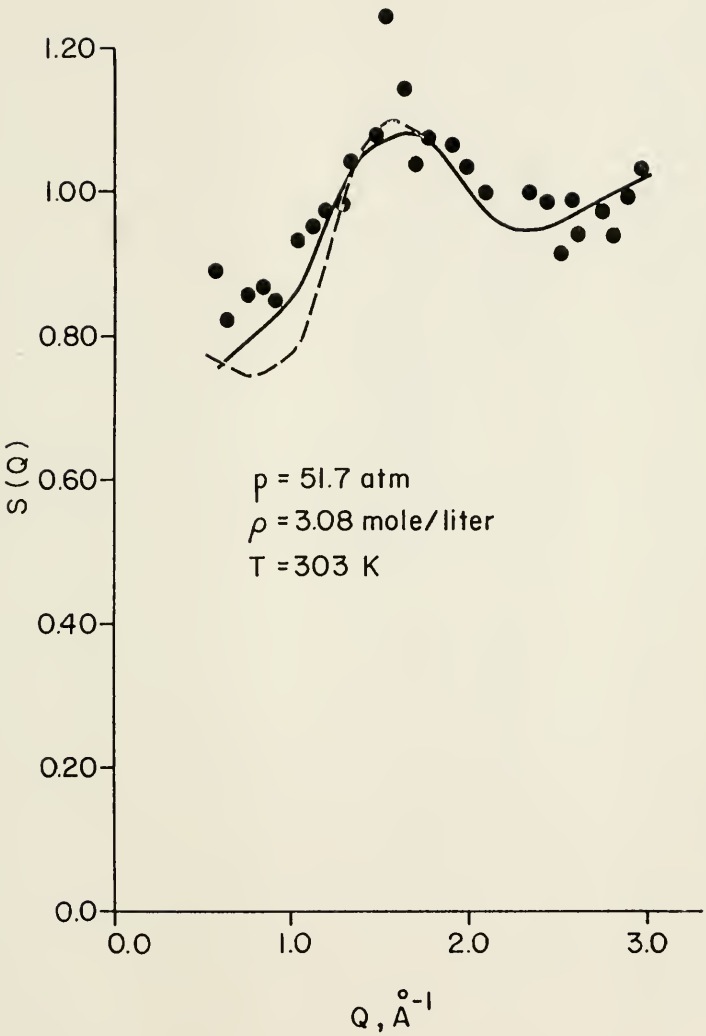

Figure 7-13. The effect of non-additivity of the intermolecular potential on S(Q). Non-additivity in $S_2(Q)$ (---) was modeled using the Axilrod-Teller dispersion potential; the dashed line was calculated assuming pairwise additivity and Barker's potential for xenon for terms up to and including $S_3(Q)$.

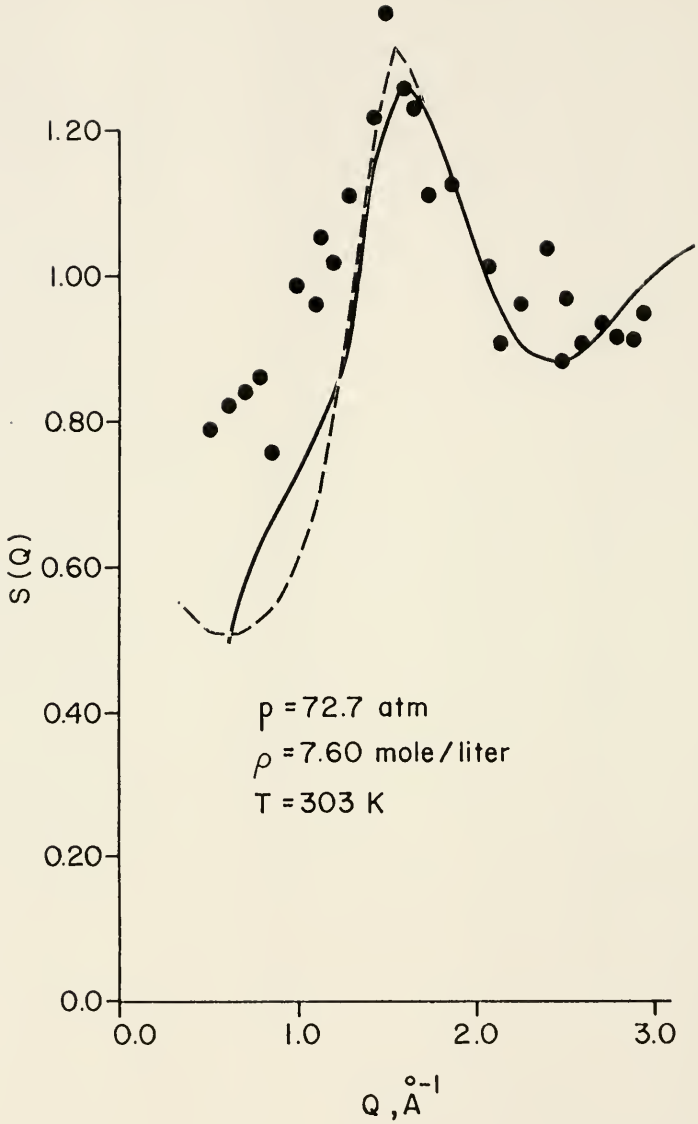

Figure 7-14. Same as Figure 7-13 except: P = 72.7 atm, ρ = 7.60 mole/liter, T = 303 K.

(——) of adding the Axilrod-Teller potential to $S_2(Q)$; $S_3(Q)$ is calculated assuming pairwise additivity in the intermolecular potential energy. For comparison, S(Q) as calculated by assuming pair-wise additivity is included (---) in Figures 7-13 and 7-14. The addition of the non-additive three-body term to $S_2(Q)$ is seen to reduce the discrepancy between theory and experiment. Agreement between the measured values of S(Q) and those predicted assuming the Axilrod-Teller non-additive correction is much better at the lower density, perhaps suggesting that non-additivity in $S_3(Q)$ may be important at the higher densities.

In light of the effect of the Axilrod-Teller three-body dispersion potential on the calculated S(Q) values, it is not possible to distinguish between an error in the pair potential (Figure 7-4) or an error in the three-body potential (Figure 7-13) in explaining the discrepancy between theory and experiment. More data should be taken over the same (and perhaps a lower) density range, concentrating on the region $0.5\ \text{Å}^{-1} < Q < 2.0\ \text{Å}^{-1}$, and the non-additive contribution of the intermolecular potential to $S_3(Q)$ should be investigated. It is likely that a combination of uncertainty in both the pair and three-body potentials contribute to the discrepancy between S(Q) calculated via equation (7-3) and what is observed experimentally.

7.4 The Isothermal Pressure Derivative of S(Q)

In Section 2.4 the relationship between the isothermal pressure derivative, $\frac{\partial S(Q)}{\partial P}$, and the static three-point correlation function, $g^{(3)}(\vec{q}_1, \vec{q}_2, \vec{q}_3)$, was discussed. Here, $\frac{\partial S(Q)}{\partial P}$ is obtained from the experimental data of Section 7.3 by differencing S(Q) at two different pressures:

$$\frac{\partial S(Q)}{\partial P} = \frac{S(Q;P_2) - S(Q;P_1)}{P_2 - P_1} \quad . \tag{7-5}$$

Since the spectrometer has been demonstrated to be unstable, differencing adjacent pressures does not yield satisfactory results for $\frac{\partial S(Q)}{\partial P}$. Therefore, widely spaced pressures are taken to evaluate the isothermal pressure derivative. In Figures 7-15 and 7-16 the dimensionless pressure derivative, $\rho kT \frac{\partial S(Q)}{\partial P}$, is shown as a function of Q for the differences (P_2 = 62.9 atm, P_1 = 51.7 atm) and (P_2 = 72.7 atm, P_1 = 62.9 atm), respectively. The density used to reduce $\frac{\partial S(Q)}{\partial P}$ is the average density between P_2 and P_1,

$$\rho(P) = \frac{\rho(P_2) + \rho(P_1)}{2} \quad ,$$

with

$$P \equiv \frac{P_1 + P_2}{2} \quad . \tag{7-6}$$

The corresponding (theoretical) pressure derivative, calculated from equation (7-4) assuming pairwise additivity and Barker's pair potential for xenon, is included (——) for comparison. Although the pressure differences are essentially the same, the corresponding density differences differ by a factor of two between Figures 7-15 and 7-16. It is therefore not surprising that the scatter in the data is considerably lower in Figure 7-16 ($\Delta\rho \sim 3$ mole/liter) than in Figure 7-15 ($\Delta\rho \sim 1.5$ mole/liter). Nevertheless, the scatter in the experimental data is quite large in both instances and is believed to be the results of spectrometer instability (Section 6.5). For this reason, no definite conclusions can be made concerning the behavior of $\frac{\partial S(Q)}{\partial P}$, and hence $g^{(3)}(\vec{q}_1, \vec{q}_2, \vec{q}_3)$, for gaseous xenon. However, since the

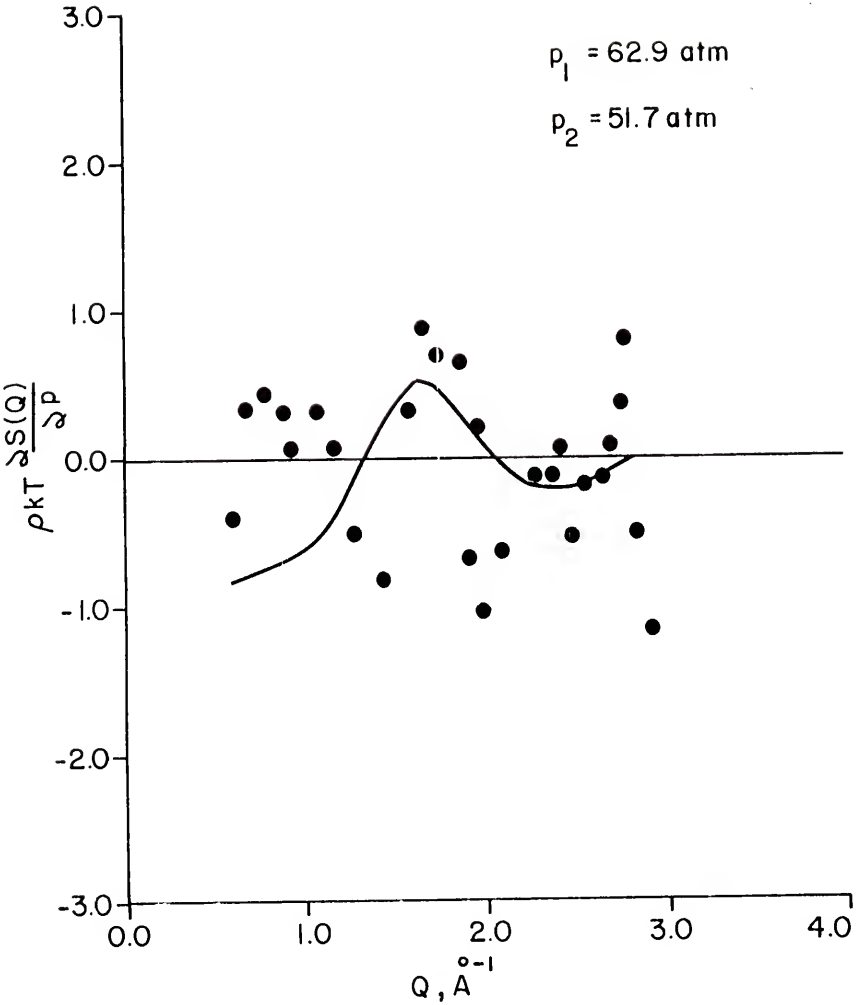

Figure 7-15. Comparison of theory (——) with experiment (•) for $\partial S(Q)/\partial P$. Pairwise additivity and Barker's pair potential for xenon were assumed for terms up to and including $S_3(Q)$; P_2 = 62.9 atm, P_1 = 51.7 atm.

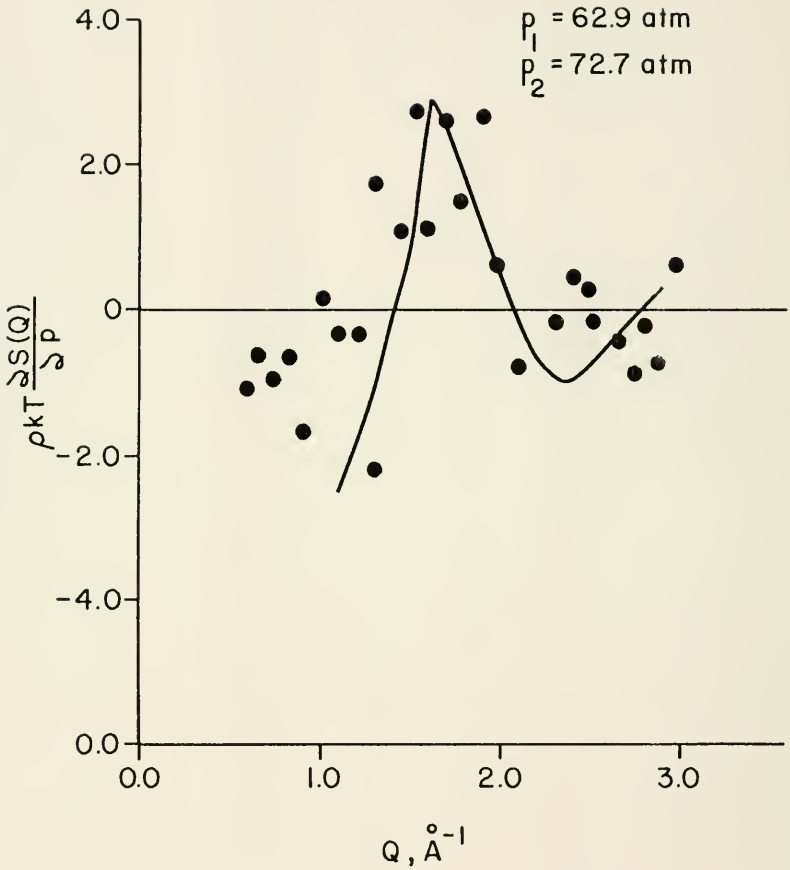

Figure 7-16. Same as Figure 7-15 except: P_2 = 72.7 atm, P_1 = 62.9 atm.

difference

$$S(Q, P_2) - S(Q, P_1)$$

should eliminate random fluctuations for a given detector, these results confirm the belief that the spectrometer behavior was highly eratic with time.

7.5 The Dynamic Structure Factor

In this section we present the kinetic theory analysis of the time-of-flight measurements of $\tilde{S}(Q,\omega)$, defined[4] through equation (6-30):

$$\tilde{S}(Q,\omega) \equiv b^2_{coh}\, S(Q,\omega) + b^2_{incoh}\, S_s(Q,\omega) \ . \qquad (6\text{-}30)$$

In order to achieve a uniform and consistent comparison between theory and experiment, the time-of-flight measurements are normalized to the averaged S(Q) values in the following manner. If F(Q) (given in Table 7-2) is the averaged quantity $(S(Q)-1)/\rho^*$, i.e., the solid line in Figure 7-11, then S(Q) becomes

$$S_a(Q) = 1 + \rho^* F(Q) \quad , \qquad (7\text{-}7)$$

where the subscript "a" denotes the averaged S(Q), and $\tilde{S}(Q,\omega)$ is normalized to $S_a(Q)$ such that

$$\int_{-\infty}^{+\infty} d\omega\, \tilde{S}(Q,\omega) = b^2_{coh}\, S_a(Q) + b^2_{incoh} \ . \qquad (7\text{-}8)$$

---

[4] For xenon,

$$b^2_{coh} = 0.237$$
$$b^2_{incoh} = 0.110 \ .$$

TABLE 7-2

SUMMARY OF F(Q) APPEARING IN EQUATION (7-7)

Q_o, $\mathring{A}^{-1}$	$F_L^*(Q)$	$F_H^*(Q)$
0.58	-0.79	-0.51
0.66	-0.83	-0.52
0.74	-0.82	-0.52
0.81	-0.78	-0.52
0.89	-0.63	-0.51
1.04	-0.33	-0.33
1.11	-0.03	-0.03
1.18	0.10	0.10
1.26	0.24	0.24
1.33	0.44	0.44
1.48	0.60	0.60
1.55	0.80	0.80
1.62	0.83	0.83
1.70	0.63	0.63
1.77	0.40	0.40
1.91	0.26	0.26
1.98	0.08	0.08
2.05	0.05	0.05
2.33	-0.07	-0.07
2.40	-0.10	-0.10
2.47	-0.12	-0.12
2.54	-0.13	-0.13
2.60	-0.13	-0.13
2.74	-0.14	-0.14
2.80	-0.15	-0.15
2.87	-0.14	-0.14
2.94	-0.13	-0.13

---

*$F_L(Q)$ is obtained by averaging for $P < P_c$; $F_H(Q)$ is obtained by averaging for $P > P_c$. For xenon P_c = 57.89 atm.

Figures 7-17 ($P = 51.7$ atm, $\rho = 3.08$ mole/liter, $T = 303$ K) and 7-18 ($P = 72.7$ atm, $\rho = 7.60$ mole/liter, $T = 303$ K) are representative of the experimental time-of-flight spectra observed for gaseous xenon. Here $\tilde{S}(Q,\omega)$, normalized according to equation (7-8), is shown as a function of the frequency, ω, for various values of Q. The static structure factor, $S(Q)$, is included as an additional guide in following the Q-dependence of $\tilde{S}(Q,\omega)$, and the full lines are drawn as a visual aid.

7.5.1 Relationship of $\tilde{S}(Q,\omega)$, $S(Q,\omega)$, and $S_s(Q,\omega)$ to Experiment.

By definition, (equation (6-30)), $\tilde{S}(Q,\omega)$ contains contributions from both $S(Q,\omega)$ and $S_s(Q,\omega)$. These quantities may be evaluated from kinetic theory, once a suitable collision operator $\hat{M}$ is determined, using the kinetic modeling discussed in Chapter 4. Although the details of the choice of collision operator and characteristics of the kinetic theory are not discussed until Sections 7.5.2-7.5.4, it is useful to anticipate the results for the purpose of illustrating the relative magnitudes of $\tilde{S}$, S and S_s. Figure 7-19 illustrates these functions, $S(Q,\omega)$ (---), $S_s(Q,\omega)$ (-·-·-), and $\tilde{S}(Q,\omega)$ (——), calculated from a kinetic theory chosen to give adequate agreement with experiment (see Section 7.5.4). Similarly, Figure 7-20 shows a comparison with the weighting factors (b^2_{coh}, b^2_{incoh}) included, i.e., $b^2_{coh}\, S(Q,\omega)$ (---) and $b^2_{incoh}\, S_s(Q,\omega)$ (-·-·-). As shown, the self structure factor, $S_s(Q,\omega)$, is a significant fraction of $\tilde{S}(Q,\omega)$, particularly for frequencies greater than 0.10×10^{13} Sec^{-1} for xenon at $Q = 0.58$ $\mathring{A}^{-1}$.

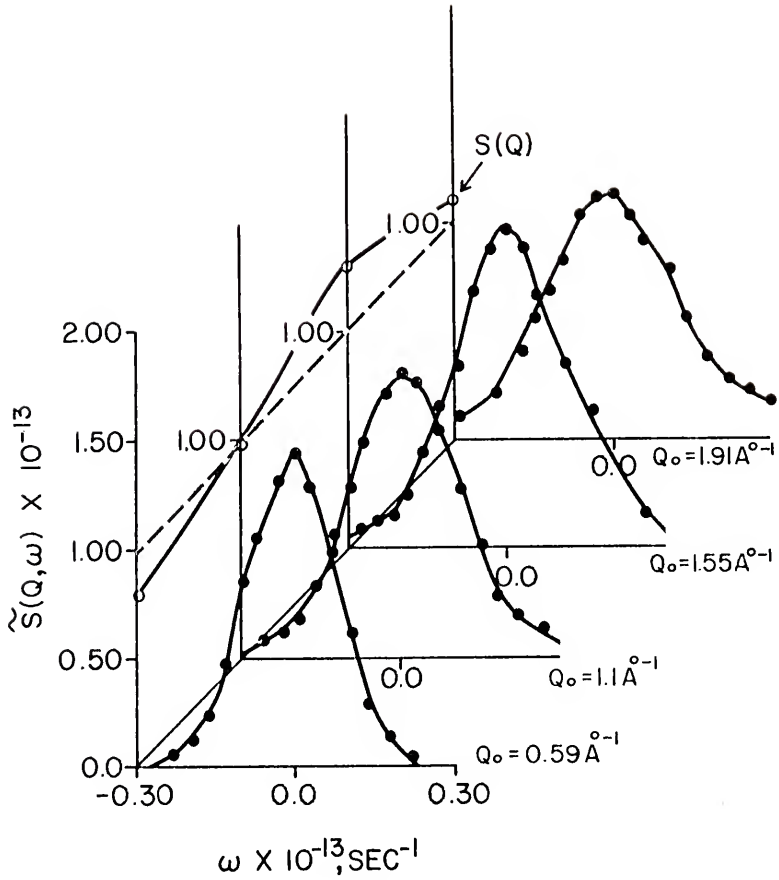

Figure 7-17. The dynamic structure factor, $\tilde{S}(Q,\omega)$, as a function of ω for various Q_o values, Here, $\tilde{S}(Q,\omega)$ is defined in equation (6-30), (•) are experimental points, and (——) is drawn as a visual aid. Also included is the static structure factor, S(Q).

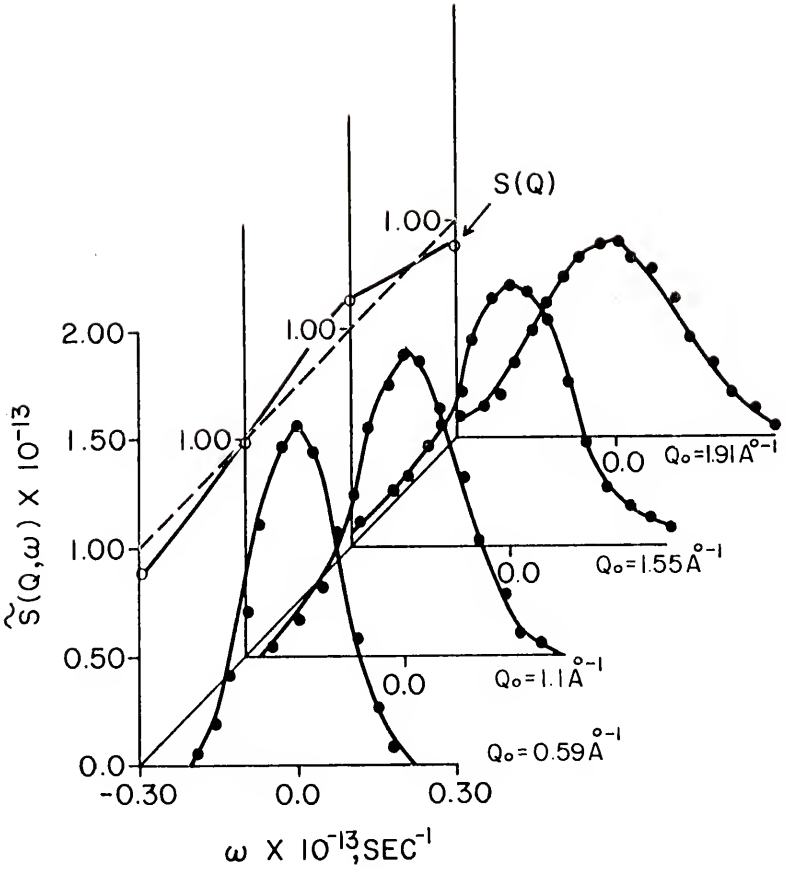

Figure 7-18. Same as Figure 7-17 except: P = 72.7 atm, ρ = 7.60 mole/liter, T = 303 K.

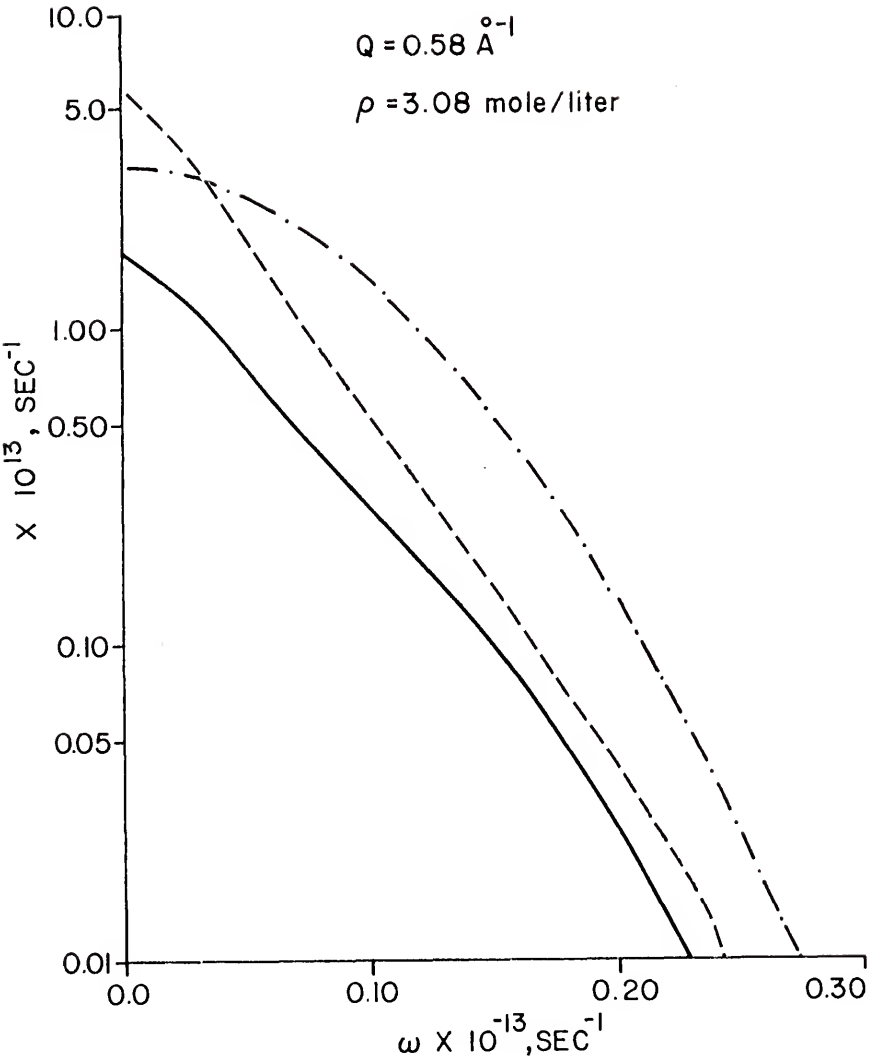

Figure 7-19. Relative magnitudes of $S(Q,\omega)$ (---) and $S_s(Q, \ )$ (-·-·-) as calculated from kinetic theory. Also included is $\tilde{S}(Q,\omega)$ (——) defined in equation (6-30).

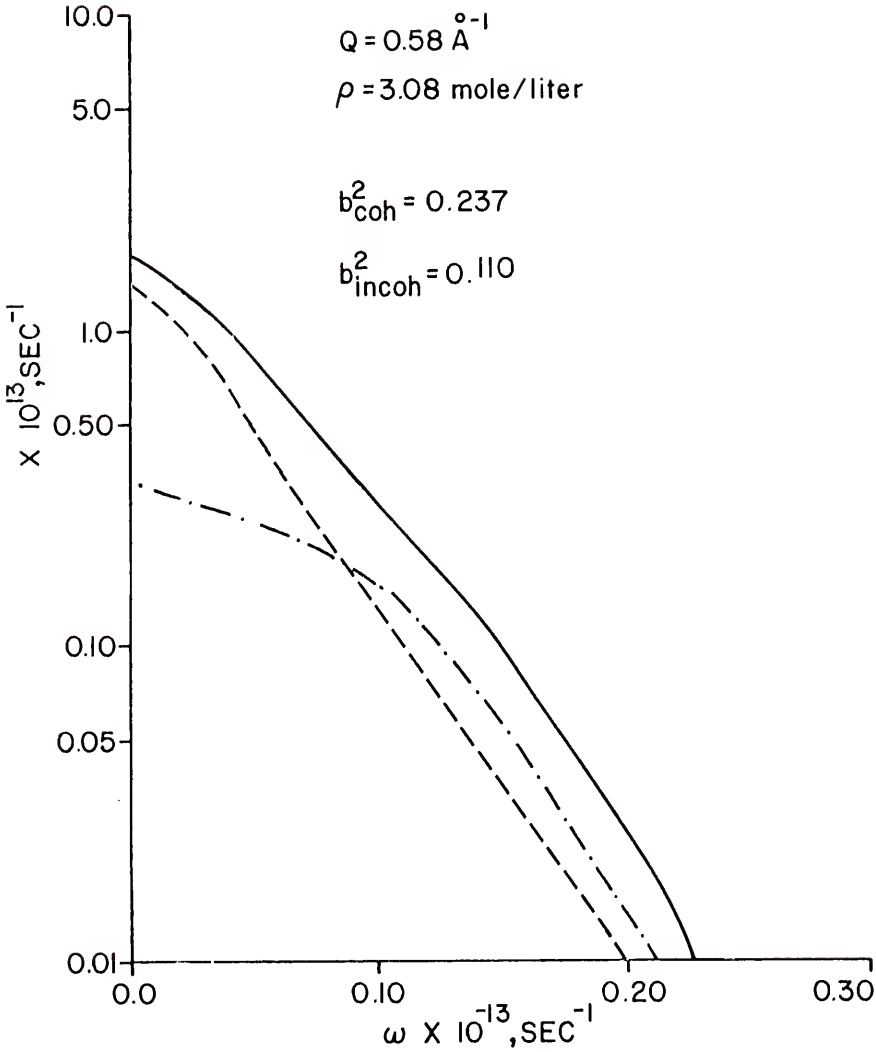

Figure 7-20. Contribution of $b^2_{coh}S(Q,\omega)$ (---) and $b^2_{incoh}S_s(S,\omega)$ (-·-·-) to $\tilde{S}(Q,\omega)$ (——).

To compare kinetic theory with measured values of $\tilde{S}(Q,\omega)$, the kinetic model calculations must first be convoluted with the spectrometer resolution function, $R(\omega)$, as discussed in Section 6.5. We see from Figure 7-21 that the theoretical calculations are significantly broadened by the spectrometer. The solid line (——) in Figure 7-21 is the result of convoluting the kinetic model (---) for $\tilde{S}(Q,\omega)$ with the spectrometer resolution function (-·-·-) according to equation (7-9):

$$\tilde{S}_c(Q,\omega) \equiv \int_{-\infty}^{+\infty} d\omega' \; \tilde{S}(Q,\omega') \; R(\omega-\omega') \; . \tag{7-9}$$

Again, details of the kinetic theory calculation are given in Sections 7.5.2-7.5.4.

7.5.2 Comparison with Free-Particle and Collisionless Theories. Before attempting a detailed analysis of the experimental data it is instructive to consider the general structure of the kinetic equation to distinguish various physical effects and determine the extent to which collisions play a role in accounting for the experimental data. In this and subsequent sections attention will be restricted to a single Q value ($Q = 0.58\ \text{Å}^{-1}$). A more complete analysis of the data of other Q values and higher pressures remains to be done.

We recall from Chapter 3 that the general form of the exact kinetic equation is

$$[-i\omega + \frac{i\vec{Q}\cdot\vec{p}}{m} - \hat{B} - \hat{M}(Q,\omega)]\; \tilde{\psi}^{(1)} = S(Q)\; f_o(p) \tag{3-66}$$

where $\hat{M}$ is the collision operator, $\frac{i\vec{Q}\cdot\vec{p}}{m}$ represents the free streaming of non-interacting particles, and $\hat{B}$ is the mean field operator

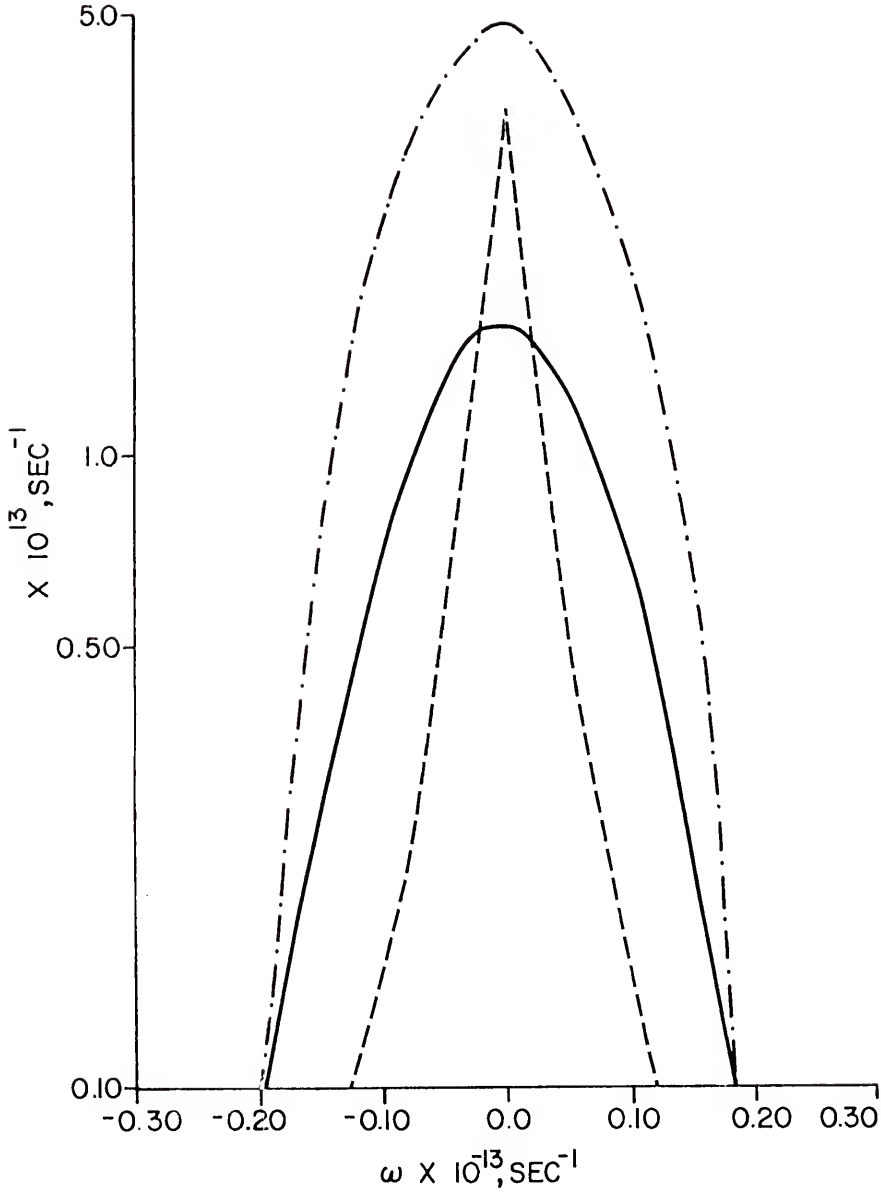

Figure 7-21. The convolution of $\tilde{S}(Q,\omega)$ as calculated from kinetic theory (---) with the spectrometer resolution function, $R(\omega)$ (-•-•-). Here, (—) is the convoluted function, $\tilde{S}_c(Q,\omega)$, defined in equation (7-9).

representing the average mean force on a particle due to correlations with surrounding particles. We distinguish two distinct forms of the mean field operator,

$$\hat{B}[\psi^{(1)}] = \frac{i\vec{Q}\cdot\vec{p}}{m} \rho C(Q) f_o(p) \int d\vec{p}' \tilde{\psi}^{(1)}(\vec{p}';Q,\omega) \qquad (7\text{-}10)$$

for the case of a fluid interacting via a continuous potential, and

$$\hat{B}[\psi^{(1)}] = \frac{i\vec{Q}\cdot\vec{p}}{m} \rho f_o(p)[C(Q)-\rho g(r_o)C_o^{hs}(Q)] \int d\vec{p}_1' \tilde{\psi}^{(1)}(\vec{p}';Q,\omega) \qquad (7\text{-}11)$$

for a hard core fluid (see Section 3.3.3). In both cases the operator is entirely determined in terms of equilibrium data and does not add to the type of information already contained in $S(Q)$. Therefore, ideally we would like the effects of $\hat{M}$ to be clearly measurable in $S(Q,\omega)$ experiments since it is $\hat{M}$ which contains the genuine dynamical information. It is useful then to understand the relative contributions of $\frac{i\vec{Q}\cdot\vec{p}}{m}$, $\hat{B}$, and $\hat{M}$. We have therefore determined $\tilde{S}_c(Q,\omega)$ for two cases: (i) free particles, i.e. replacing equation (3-66) by

$$[-i\omega + \frac{i\vec{Q}\cdot\vec{p}}{m}] \tilde{\psi}^{(1)} = S(Q) f_o(p)$$

and (ii) neglecting collisions, i.e.

$$[-i\omega + \frac{i\vec{Q}\cdot\vec{p}}{m} - \hat{B}] \tilde{\psi}^{(1)} = S(Q) f_o(p) \ . \qquad (7\text{-}12)$$

(The presence of $S(Q)$ in the free particle equation is due to our choice to normalize calculations of $S(Q,\omega)$ to $S(Q)$). Figure 7-22 shows the calculation of $\tilde{S}_c(Q,\omega)$ for free-particles (-•-•-), a collisionless fluid of hard spheres (---), and a collisionless fluid with a continuous potential (——) for xenon at $Q = 0.58$ Å^{-1} and for $\rho = 3.08$ mole/liter. The hard sphere calculation is based on

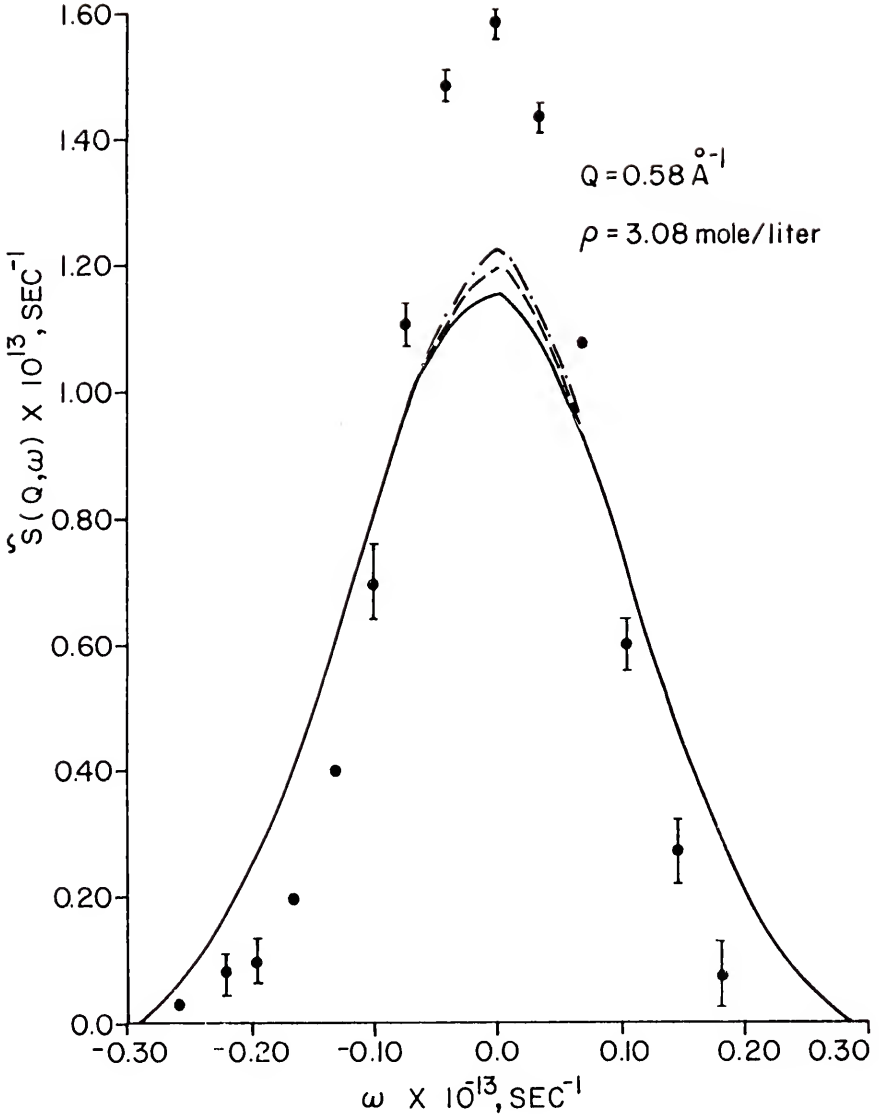

Figure 7-22. Comparison of free-particle (-·-·-) and collisionless theories (---, hard sphere; ——, continuous) with experimental data (·) for $\tilde{S}_c(Q,\omega)$. The error bars are estimated by averaging two experimental runs at ρ = 3.08 mole/liter.

equations (7-11) and (7-12) with C(Q) determined from the Percus-Yevick equation for hard spheres at an r_o chosen to equate the hard sphere S(Q) and the experimental S(Q); $g(r_o)$ was determined by the Carnahan-Starling equation. The calculation for the collisionless fluid with a continuous potential for xenon is based on equations (7-10) and (7-12) with C(Q) determined directly from the experimental data, i.e.,

$$C(Q) = \frac{S(Q)-1}{\rho S(Q)} \tag{3-67}$$

All calculations are normalized to the experimental S(Q).

Three observations may be made from Figure 7-22:

(1) Neither free-particles, nor collisionless fluid calculations can account for the experimental data; hence collisional effects are being observed,

(2) The effect of the mean field in both hard sphere and continuous potential cases broadens $\tilde{S}_c(Q,\omega)$ over the free particle results, that is, they tend to decrease the agreement with experiment, (at this Q-value), and

(3) The effect of the mean field compared to free particles is relatively small, but not entirely negligible.

It is known that collisions narrow $\tilde{S}_c(Q,\omega)$ so that the discrepancy between free particle or collisionless kinetic theories and experimental data must be accounted for in the theory through the operator M. As has been noted in Chapters 3 and 4, no adequate study of $\hat{M}$ exists for a moderately dense fluid with real potentials. However, as discussed in Section 3.3.3 the generalized Enskog models are

able to represent some of the density effects at the price of introducing model potentials with a hard core. Therefore, in the next two sections we study the possibility of representing the experimental data with such model hard core potentials.

Before leaving the collisionless models, one further calculation is of interest. The experimental temperature was 303 K, corresponding to a reduced (Barker) $T^* \equiv kT/\varepsilon = 1.08$. For such a low temperature one might expect the data to be sensitive to the attractive part of the intermolecular potential. To test this effect relative to hard spheres, the Sutherland potential was considered. The pair potential for the Sutherland model is defined to be

$$\phi(r) = \begin{cases} \infty & , r < r_o \\ -\varepsilon\left(\frac{r_o}{r}\right)^6 & , r \geq r_o \end{cases} \quad . \tag{7-13}$$

Figure 7-23 shows a comparison of the free particle (-•-•-), the collisionless Sutherland fluid (——), and experiment. (The choice of parameters for the Sutherland fluid is discussed in Section 7.5.4). The main conclusion of this calculation is that, although the collisionless Sutherland fluid is still inadequate to fit the data, the mean field nevertheless has the effect of narrowing $\tilde{S}_c(Q,\omega)$ and tends to decrease the disagreement between theory and experiment. There is therefore a qualitative difference between the mean field operator for hard spheres and that for attracting spheres. This point will be elaborated on further in Section 7.5.4.

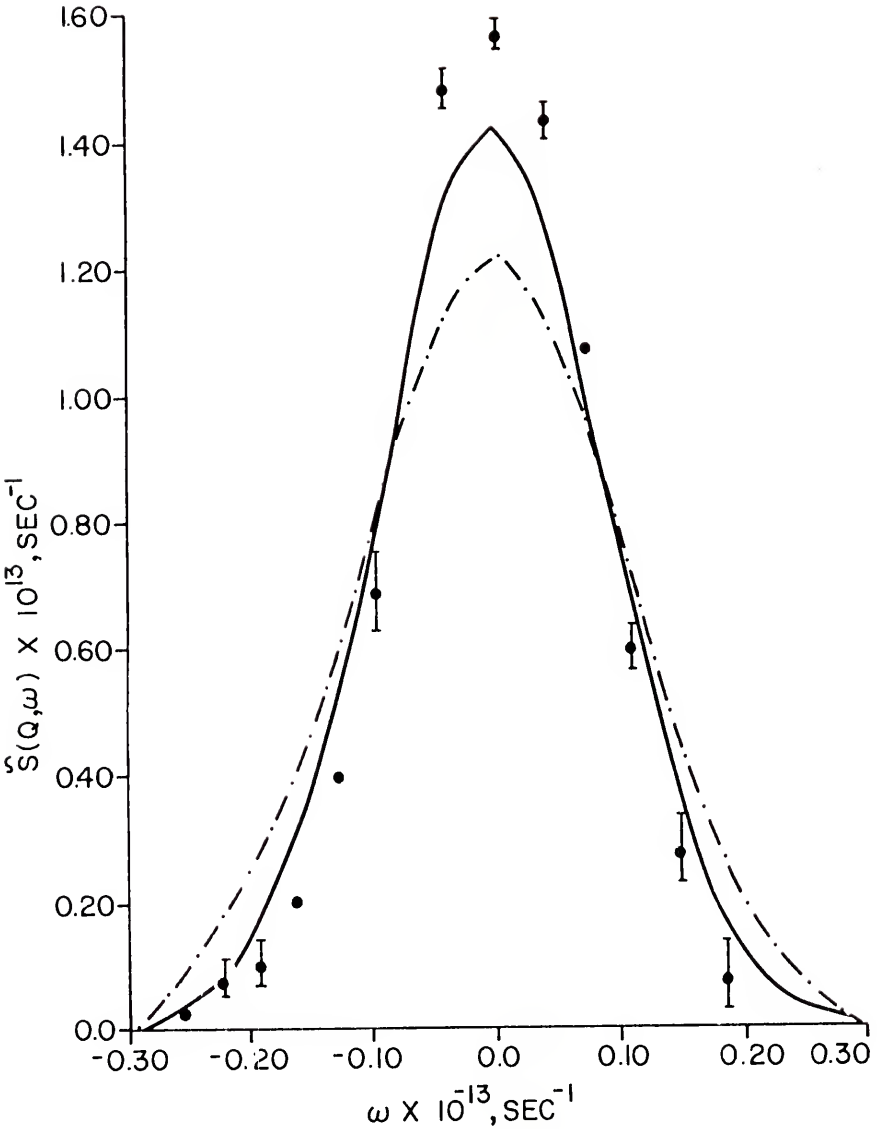

Figure 7-23. Comparison of free-particle (-·-·-) and Sutherland fluid (——) with experiment (·).

7.5.3 Comparison with Generalized Enskog Hard Sphere Fluid.

The previous figures have indicated that collisional effects are required to adequately interpret the data. These collisional effects may be calculated with a realistic potential (e.g., Barker's potential) for dilute xenon gas, but no adequate theory of the collision operator for such potentials exists at the more moderate densities of interest here. However, as noted in Section 3.3.3, more detailed analysis is possible for a moderately dense fluid of particles interacting via a hard core. In this section we consider a system of hard spheres of diameter r_o as a first attempt at understanding the dynamical structure of xenon. The hard sphere potential,

$$\phi(r) = \begin{cases} \infty & r < r_o \\ o & r \geq r_o \end{cases} ,$$

is certainly not very realistic, but with r_o as an adjustable parameter it has been found that a variety of equilibrium and transport data of real fluids can be partially modeled with hard spheres. A study similar to that of this section has been carried out by Furtado et al. (91) in an attempt to model liquid argon with the generalized Enskog kinetic equation for hard spheres. They found that a straightforward evaluation of $S(Q,\omega)$ for hard spheres was not in good agreement with experiment; a similar conclusion is reached here.

The hard sphere kinetic equation (equation (3.74)) was solved to calculate $\hat{S}(Q,\omega)$ using the N=6 Gross-Jackson kinetic model of Chapter 4. (No attempt at optimizing this model or extending it to larger N values was made since the N=6 model is quite accurate at

the measured Q values). The theory requires specification of S(Q), C(Q), r_o, and $g(r_o)$. In all calculations of this chapter, $S(Q,\omega)$ was normalized to the experimental S(Q). Aside from this normalization, all other quantities were calculated for the hard sphere fluid. Specifically, C(Q) was determined from Percus-Yevick theory while $g(r_o)$ was determined from the more accurate Carnahan-Starling equation. We do not consider the errors made in these determinations as bearing significantly on the outcome for $\tilde{S}(Q,\omega)$. The value of the hard sphere diameter was treated as a variable parameter. Figure 7-24 compares the results at r_o = 2.75 Å and r_o = 6.0 Å with the experimental data. The value r_o = 2.75 Å was chosen because at that value the hard sphere S(Q) (from Percus-Yevick) agrees with the experimental S(Q) at Q = 0.58 $Å^{-1}$; the value r_o = 6.0 Å was chosen arbitrarily to show the trend at larger r_o. Figure 7-23 indicates clearly that hard spheres are not an adequate model for xenon at the state conditions studied.

To understand this failure, several points may be observed. First, the result of increasing the collisional effects is to narrow the line and move the theory in the direction of the experiment. This may be observed in Figure 7-24 by noting that the r_o = 6 Å result is narrower than the r_o = 2.75 result (recall the collision frequency increases as r_o^2). However, although r_o has been increased by more than a factor of 2, the narrowing is not very great. The reason for this may be seen by considering the mean field term, proportional to $[C(Q)-g(r_o)C_o(Q)]$. As noted in the last section, the effect of this term for hard spheres is to broaden

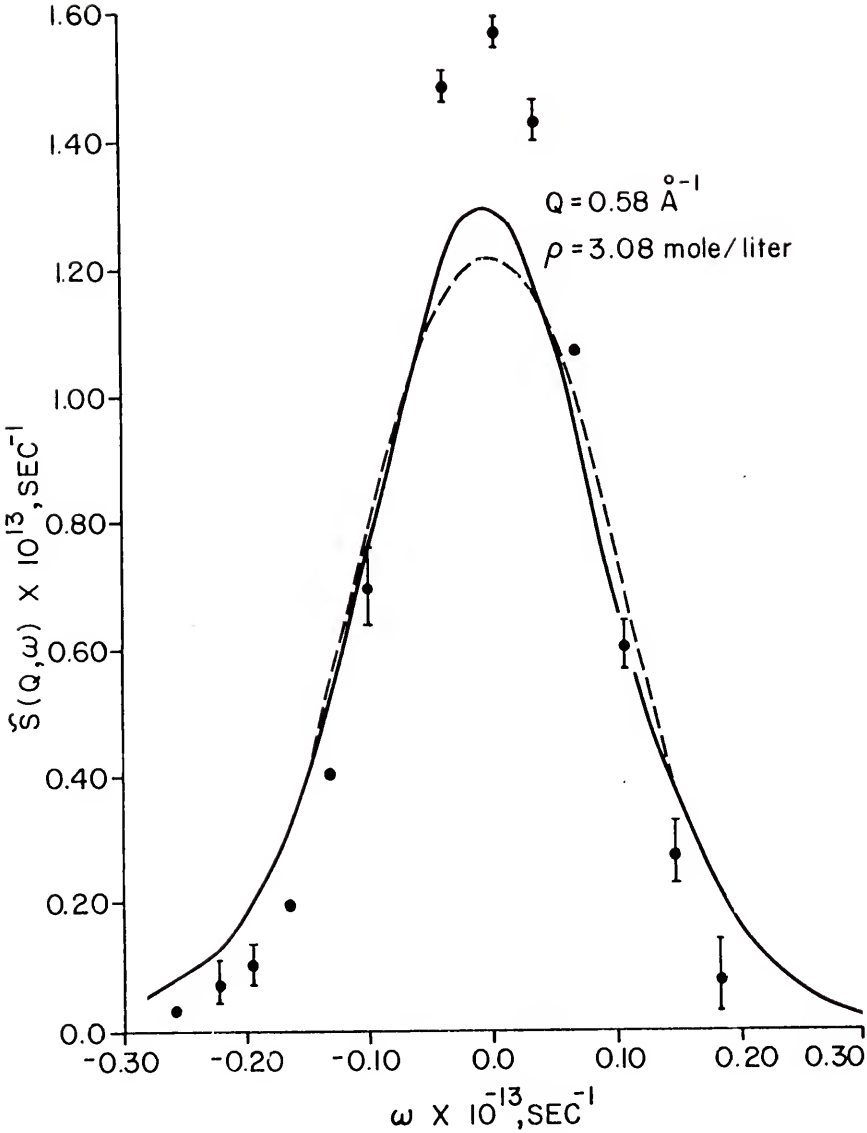

Figure 7-24. Calcualtion of $\tilde{S}_c(Q,\omega)$ using Enskog's theory for hard spheres. Here, (---) is for r_o = 2.75 Å, (——) is for r_o = 6.0 Å, and (·) denotes experimental data.

$S(Q,\omega)$ over its free particle-value (see Figure 7-22). As r_o is increased the influence of this mean field term increases, so that there is a competition between the collisional narrowing and the broadening of the mean field. Figure 7-24 shows that collisions ultimately dominate, but their effective narrowing is considerably reduced. This competition continues for larger r_o so that even for artificially large r_o (which would be difficult to justify in any case) the data apparently cannot be fit with a hard sphere fluid.

7.5.4 Comparison with a Hard Core Fluid with Attractive Forces. In the previous section we found the Enskog theory for hard spheres inadequate to represent $\tilde{S}_c(Q,\omega)$ for xenon at the experimental state conditions. The problem may be traced to the fact that, for values of r_o needed to give reasonable fluid structure (i.e. to fit $S(Q)$) the hard sphere collision frequency is too small to give the proper collisional narrowing. The collision frequency may be increased by increasing r_o, but then the fluid structure is so poorly represented that $C(Q)$ and the corresponding mean field term give unphysical broadening and again the data cannot be fit. An alternative to increasing r_o might be to enhance the collision frequency by increasing $g(r_o)$ artificially (recall $\hat{M}_E$ is proportional to $g(r_o)$). Such a procedure was carried out recently by Furtado et al. (91) to successfully fit $S(Q,\omega)$ for dense argon. The replacement of $g(r_o)$ by an adjustable parameter is similar in spirit to a suggestion of Enskog's (46) in an attempt to extend his hard sphere theory to real potentials. We have carried out a similar analysis of the xenon data and find that the data can indeed be fit with input

of experimental $S(Q)$, $C(Q)$, and variation of r_o and $g(r_o)$. However, such analysis for a hard sphere fluid is so ad hoc and such a departure from theory that it is difficult to interpret or come to any conclusions once the data has been fit. We therefore will not pursue further the hard sphere fluid, but rather conclude that such a potential model is too crude to represent xenon.

In light of the above comments, we must look for a mechanism which can account for a greater collision frequency than that for hard spheres. Some suggestion is provided by the calculations for the collisionless Sutherland model of section 7.5.2, which indicated a definite dependence on the attractive part of the potential at the chosen experimental temperature. This had the effect that the mean field acted in concert with the collisions to narrow $\tilde{S}_c(Q,\omega)$, as opposed to partially offsetting the collisional narrowing in the hard sphere case. Furthermore, $g(r_o)$ will be enhanced by the attractive well with a corresponding increase of the collision frequency. For these reasons, we study in this section the generalized Enskog theory for attractive hard spheres. To recall the definition of Section 3.3.3, the pair potential for attractive spheres is

$$\phi(r) = \begin{cases} \infty \ , & r < r_o \\ \phi_c(r), & r \geq r_o \end{cases} ,$$

where $\phi_c(r)$ is an arbitrary continuous attractive potential. For definiteness the discussion here will be limited to the special case of the Sutherland potential, equation (7-13), although no special importance is implied by this choice. The main point here

is to identify a physical property of the real fluid which must be incorporated in the theory in order to gain agreement with the data.

The generalized Enskog equation for attractive spheres (equation (3-74)) differs from that for hard spheres only in the replacement of the hard sphere C(Q) and $g(r_o)$ by the corresponding values for the attracting sphere fluid. To determine these, the parameters r_o and $\frac{\varepsilon}{k}$ in the Sutherland potential must be chosen. These were picked to give a good representation of the actual g(r) for xenon. Since there is a great deal of flexibility here (between choice of potential model, ϕ_c, and parameters r_o and $\frac{\varepsilon}{k}$) no attempt was made at a careful calculation of g(r) for the Sutherland potential; rather, it was simply assumed to have the form,

$$g_s(r) \sim e^{-\frac{\phi(r)}{kT}} \quad . \tag{7-14}$$

Figure 7-25 shows a comparison of $g_s(r)$ for $r_o = r_m \equiv$ minimum of the Barker potential ($r_m \sim 4.3$ Å) and $\frac{\varepsilon}{k} = 277$ K, and g(r) for Barker's potential from the virial expansion (terms up to and including $g_2(r)$). Also included is the hard sphere (Percus-Yevick) result for the same r_o. Clearly, the Sutherland potential is much better able to model the region of the peak of g(r) than can the hard sphere model. In particular, $g_s(r_o)$ is considerably greater than $g_{hs}(r_o)$.

To calculate $\tilde{S}_c(Q,\omega)$ for the Sutherland model we also need C(Q). It was decided, on the basis of the fact that g(r) could be so well fit by $g_s(r)$, that we could use the experimentally determined C(Q) (equation (7-13)) without significant error. Otherwise,

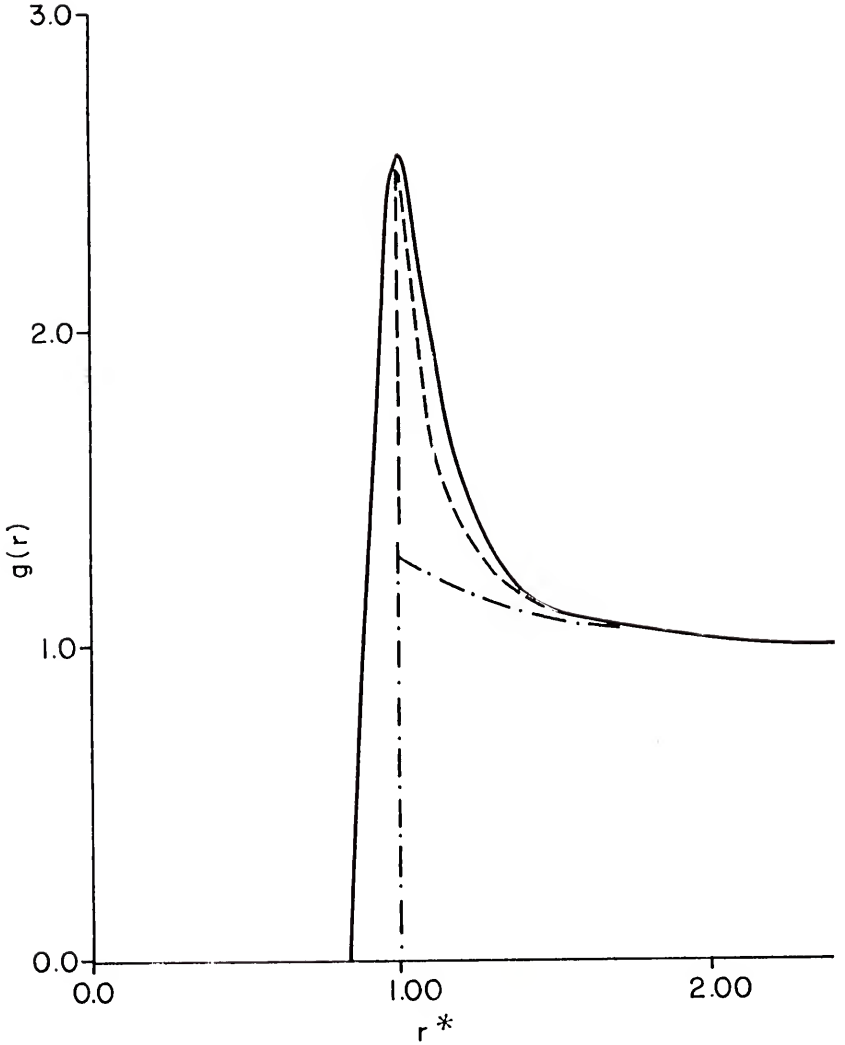

Figure 7-25. Comparison of g(r) as predicted from Percus-Yevick hard spheres (-•-•-, r_o = 6.0 Å^{-1}) and g(r) from the Sutherland potential (---; ε/k = 277.5 K, $r_o = r_{min}$) with the virial calculation (——) of g(r) for Barker's pair potential assuming pairwise additivity for terms up to and including $g_2(r)$ in equation (2-6).

$g_s(r_o)$ and r_o were determined from equation (7-14) and the above mentioned potential parameters. Figure 7-26 shows the comparison of $\tilde{S}_c(Q,\omega)$ for the Sutherland model (——), the hard sphere model (---), and the experimental data (·). The agreement between experiment and the theory for attractive spheres is quite good, while as already noted there is poor agreement for hard spheres. We conclude that the effect of the attractive part of the xenon potential is significant in representing the collisional narrowing.

The treatment of the attractive forces given here is quite superficial and is intended only to show the qualitative difference the inclusion of such forces makes. In particular, no significance is attached to the above values of r_o and $\frac{\varepsilon}{k}$ used to fit the data. This pair is not unique, as indicated by Figure 7-27, which shows a plot of $g(r_o)$ vs. r_o such that all points on the curve represent potential parameters adequate to fit the data. As expected, for smaller r_o the corresponding peak height must be increased to maintain the collision frequency ($\sim r_o^2\, g(r_o)$).

7.6 The Isothermal Pressure Derivative of $S(Q,\omega)$

The relationship between the triplet time correlation function, $G_3(\vec{r}',o;\vec{r}'',o;\vec{r},t)$, and the isothermal pressure derivative, $\frac{\partial S(Q,\omega)}{\partial P}$, has been discussed in Section 3.4. Here, we present experimental measurements of $\frac{\partial S(Q,\omega)}{\partial P}$ for low density xenon gas. Since our theoretical understanding of $S(Q,\omega)$ is still incomplete, no comparison between the experimental data for $\frac{\partial S(Q,\omega)}{\partial P}$ and the kinetic theory analysis of the previous section will be made. Rather, we present the experimental values as an indication of the degree to which this quantity can

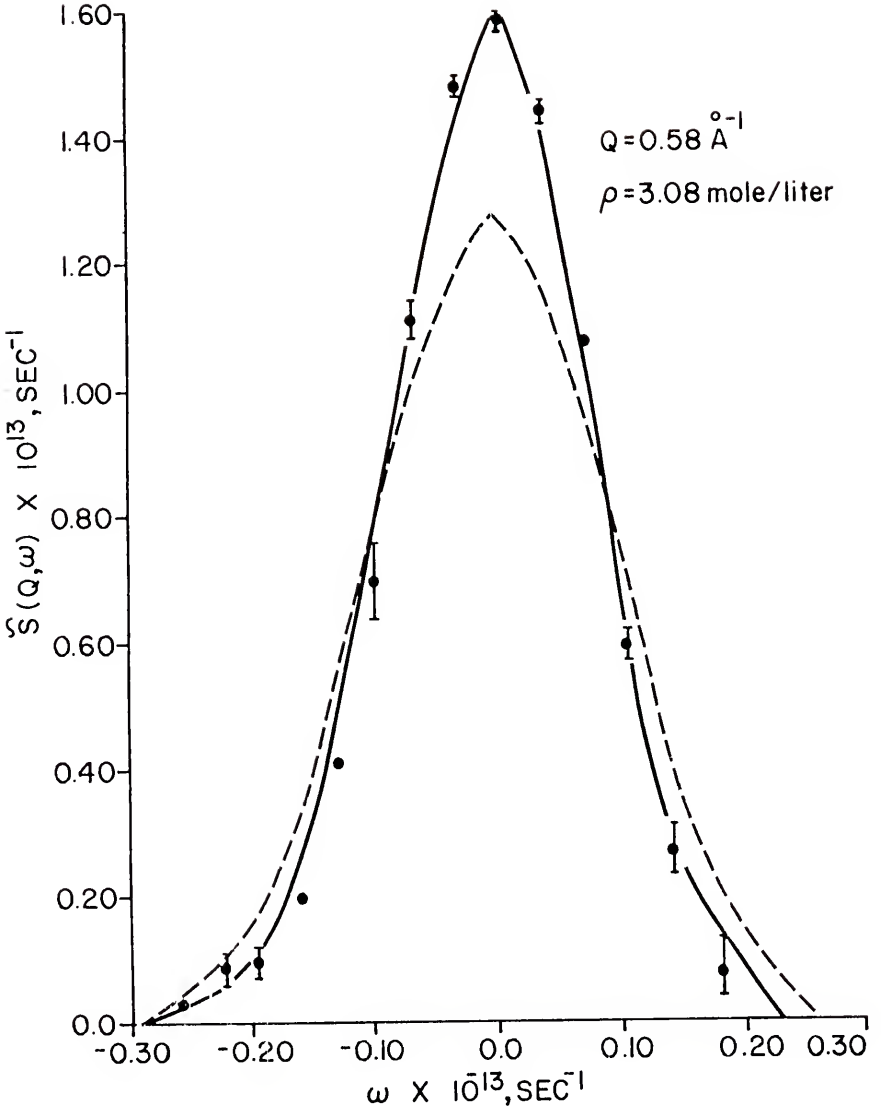

Figure 7-26. The structure factor $\tilde{S}_c(Q,\omega)$ as calculated from the Enskog kinetic equation (——, $r_o = r_m$) for a hard core fluid having attractive forces. Also included is the Enskog calculation for hard spheres (---, $r_o = r_m$), and the experimental results (•).

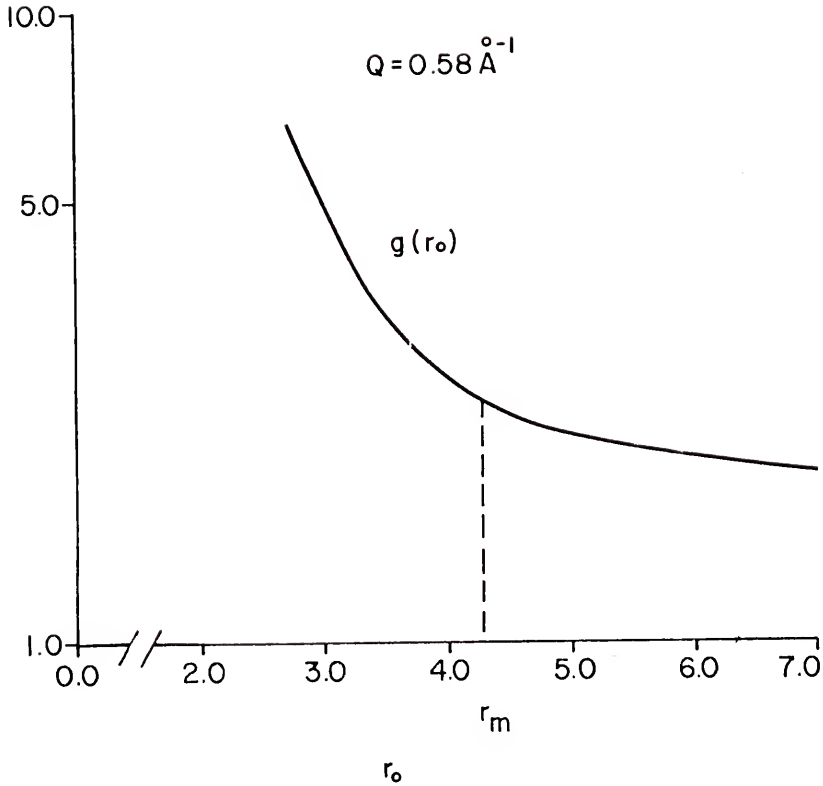

Figure 7-27. Behavior of $g(r_o)$ as determined by fitting the attractive hard core $\tilde{S}_c(Q,\omega)$ to experiment.

be probed experimentally. Measurements of $\frac{\partial S(Q,\omega)}{\partial P}$ for two Q-values (e.g., $Q = 0.58\ \mathring{A}^{-1}$ and $Q = 1.10\ \mathring{A}^{-1}$) are presented. Although additional data on the isothermal pressure derivative could be generated, the two Q-values chosen are representative of the behavior exhibited by $\frac{\partial S(Q,\omega)}{\partial P}$ and the extension to other regions of Q-space would provide no additional information at this time.

The pressure derivative is obtained by differencing between two pressures,

$$\frac{\partial S(Q,\omega)}{\partial P} = \frac{S(Q,\omega;P_2) - S(Q,\omega;P_1)}{P_2 - P_1} \quad . \tag{7-15}$$

Based on the results found for $\frac{\partial S(Q)}{\partial P}$, the differencing of $S(Q,\omega)$ was between widely spaced pressures (e.g., $P_1 = 62.7$ atm, $P_2 = 72.9$ atm). In Figures 7-28 and 7-29, the reduced pressure derivative, $\rho kT\ \frac{\partial S(Q,\omega)}{\partial P}$, is shown as a function of ω at fixed Q-values of $0.58\ \mathring{A}^{-1}$ and $1.10\ \mathring{A}^{-1}$, respectively. We see from these figures that there is a great deal of structure contained in $\frac{\partial S(Q,\omega)}{\partial P}$. However, because of the large amount of scatter in the data, these results are only qualitative.

It was shown in Section 3.4 that a comparison between $\frac{\partial \ln S(Q)}{\partial P}$ and $\frac{\partial \ln S(Q,\omega)}{\partial P}$ provides information on the collision operator appearing in the formal kinetic theory for $S(Q,\omega)$. In particular,

$$\frac{\partial \ln S(Q,\omega)}{\partial P} = \frac{\partial \ln S(Q)}{\partial P} + \frac{1}{\rho kTS(Q,\omega)} \int dx_1 dx_2\ e^{i\vec{Q}\cdot\vec{q}_1}$$

$$\times\ P^{(2)}(x_1,x_2;\omega|\psi^{(1)}) \ , \tag{3-114}$$

so that it is of considerable interest to determine the degree to which $\frac{\partial \ln S(Q,\omega)}{\partial P}$ can be measured experimentally. Figures 7-30

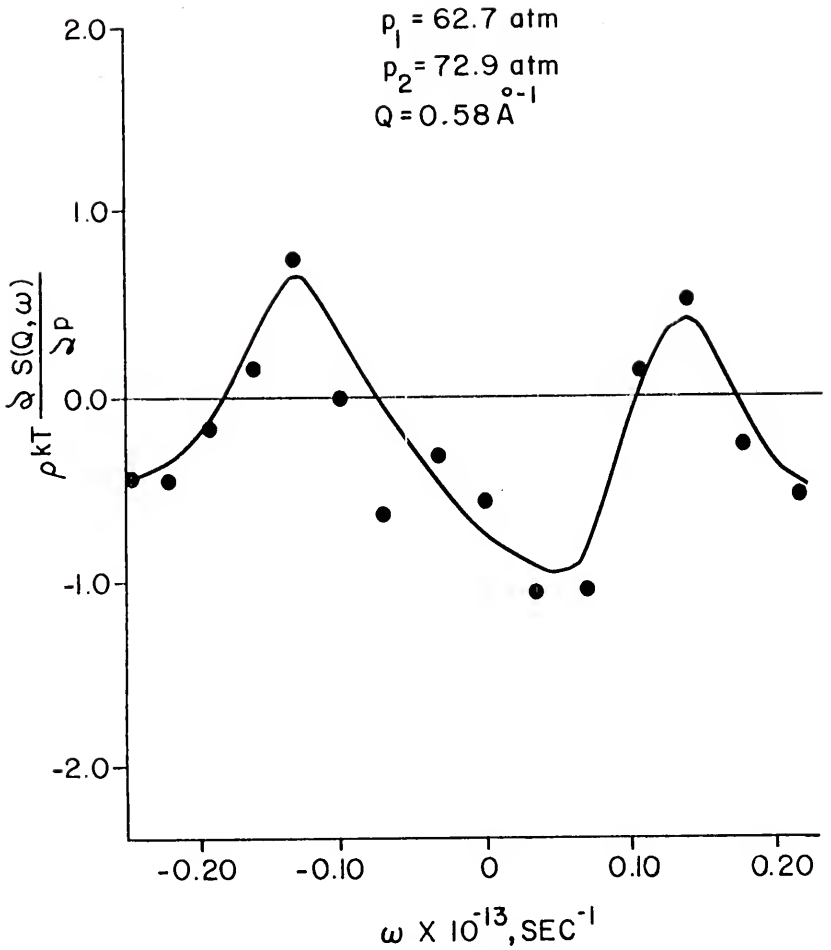

Figure 7-28. The isothermal pressure derivative of $S(Q,\omega)$ at a fixed $Q = 0.58$ Å^{-1}. The solid line is drawn as a visual aid.

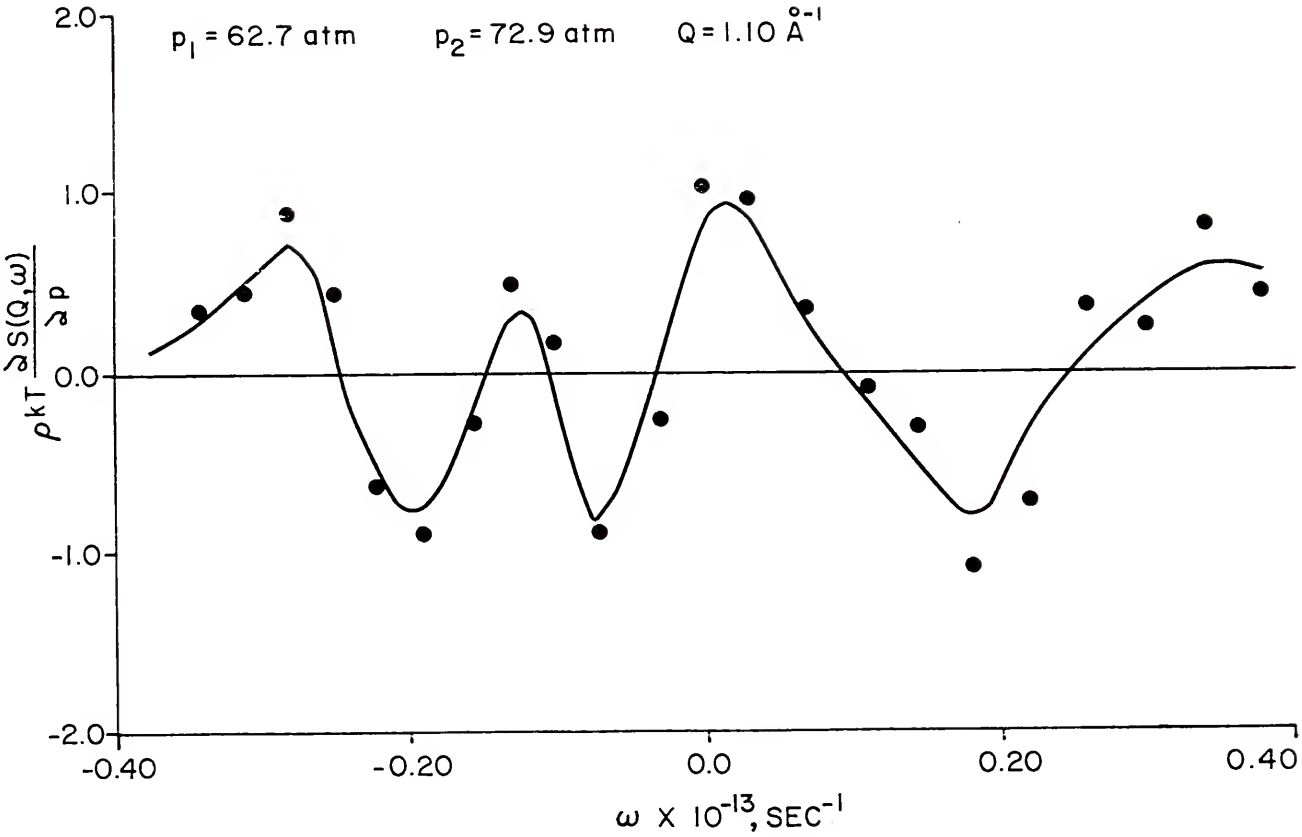

Figure 7-29. Same as Figure 7-28 except: Q = 1.10 Å^{-1}.

and 7-31 illustrate the behavior of $\frac{\partial \ln S(Q,\omega)}{\partial P}$ as a function of ω at fixed Q ($Q = 0.58\ \mathring{A}^{-1}$ and $Q = 1.10\ \mathring{A}^{-1}$, respectively). This function was determined experimentally by

$$\frac{\partial \ln S(Q,\omega)}{\partial P} = \frac{1}{S(Q,\omega;P)} \frac{\partial S(Q,\omega)}{\partial P} , \tag{7-16}$$

where $S(Q,\omega;P)$ is given by equation (7-17):

$$S(Q,\omega;P) = \frac{S(Q,\omega;P_2) + S(Q,\omega;P_1)}{2} \tag{7-17}$$

Evaluating $\frac{\partial \ln S(Q,\omega)}{\partial P}$ in this way results in a ratio which eliminates any random error in a given detector, thus reducing the scatter in the data. The results of Figures 7-30 and 7-31 are somewhat smoother than the corresponding plots of $\frac{\partial S(Q,\omega)}{\partial P}$ (i.e., Figures 7-28 and 7-29, respectively), although the observed difference is not significant. The erratic behavior of $\frac{\partial \ln S(Q,\omega)}{\partial P}$ for large $|\omega|$ is presumably due to the uncertainty in $S(Q,\omega)$ for large $|\omega|$, since

$$\lim_{|\omega|\to\infty} S(Q,\omega) \to 0 .$$

The results of this section suggest that information concerning G_3, and the collision operator appearing in the linear kinetic theory for the time-dependent correlation functions G_2 and G_3, can be obtained from experimental measurements of $\frac{\partial S(Q,\omega)}{\partial P}$ for a low density gas. The stability of the spectrometer has been demonstrated to be poor, so that the uncertainty in the data is rather large. However, the structure exhibited by $\frac{\partial S(Q,\omega)}{\partial P}$ is quite clear, and further experimental analysis of this quantity should prove valuable in analyzing models for $\hat{M}(Q,\omega)$ and G_3.

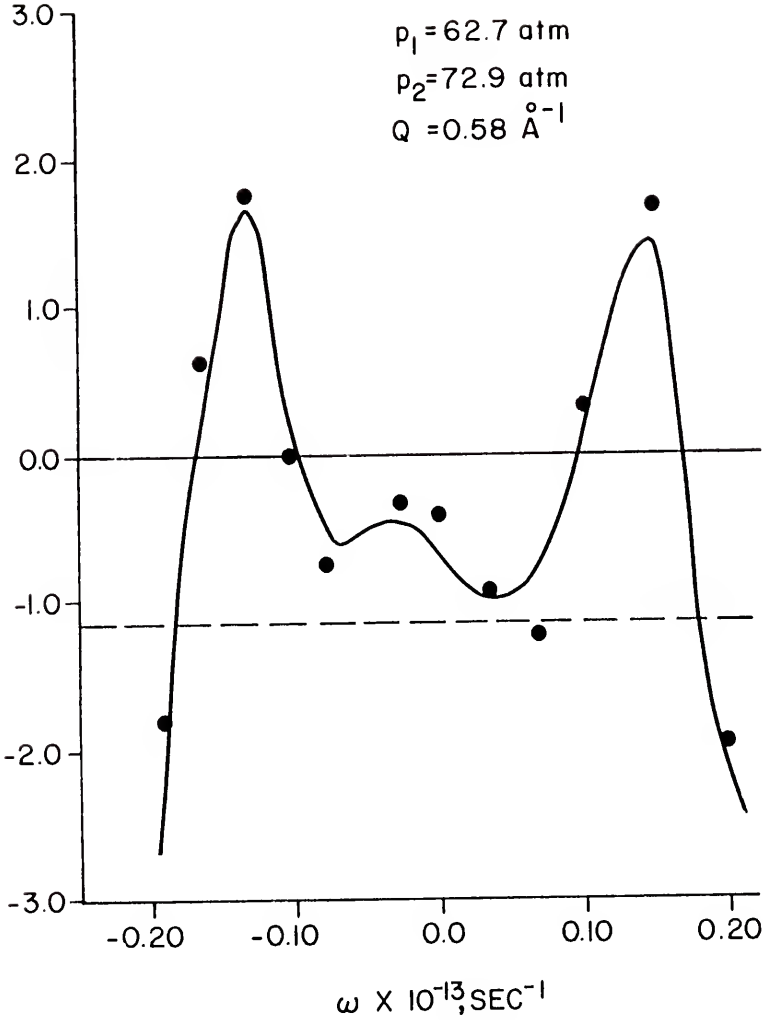

Figure 7-30. The isothermal pressure derivative of $\ln S(Q,\omega)$ at a fixed $Q = 0.58$ Å^{-1}. The solid line is drawn as a visual aid, and (---) denotes the quantity $\partial \ln S(Q)/\partial P$.

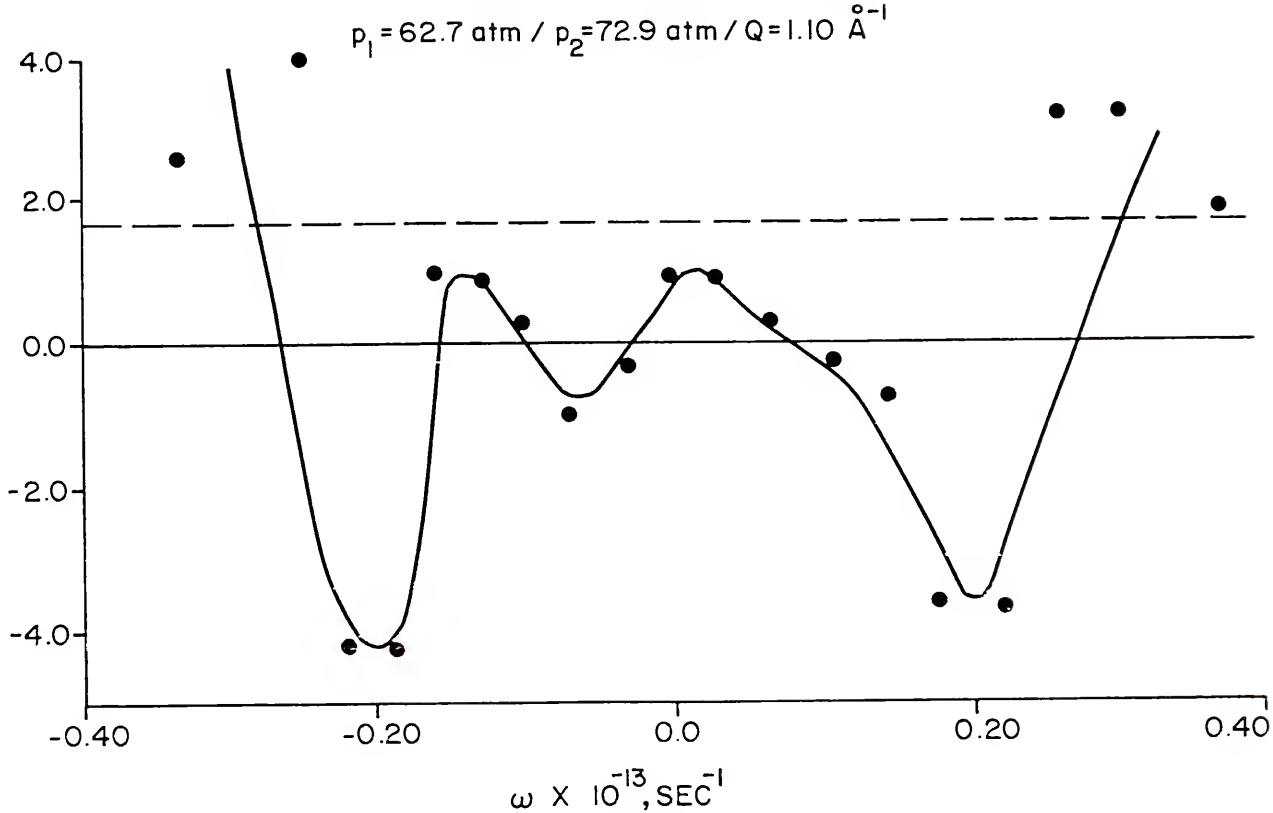

Figure 7-31. Same as Figure 7-30 except: Q = 1.10 $\mathring{A}^{-1}$.

7.7 Concluding Remarks

In this section the results of the comparison between theory and experiment are summarized. A detailed analysis of the experimental results, and the subsequent extraction of information concerning the microscopic behavior of the fluid (in this case, dilute xenon gas), requires precise measurements of both the dynamic and static structure factors. Unfortunately, the uncertainty in the experimental data is quite large. It is for this reason that no definite conclusions concerning the isothermal pressure derivatives, $\frac{\partial S(Q)}{\partial P}$ and $\frac{\partial S(Q,\omega)}{\partial P}$, can be made. However, definite trends in the experimental data for $S(Q)$ and $S(Q,\omega)$ are observed with changes in density, indicating the applicability of neutron scattering techniques for studying the structure and dynamical behavior of dilute gases.

Despite the scatter in the data, several conclusions concerning the theories for $S(Q)$ and $S(Q,\omega)$ have been established, and are summarized below.

7.7.1 Summary of the Results for the Static Structure Factor.

In Chapter 2 we found the static structure factor for xenon to be relatively insensitive to $S_2(Q)$ and $S_3(Q)$ beyond the first peak in $S(Q)$ ($Q \sim 1.5$ Å^{-1}) in the density range

$$3.08 \text{ mole/liter} \leq \rho \leq 7.60 \text{ mole/liter}.$$

This observation was based on the truncated virial equation

$$S(Q) = 1 + \rho S_1(Q) + \rho^2 S_2(Q) + \rho^3 S_3(Q) \ , \qquad (7\text{-}4)$$

where S_1, S_2, and S_3 were calculated assuming pairwise additivity of the interatomic potential, and Barker's pair potential for xenon. Including three-body effects (e.g., the Axilrod-Teller dispersion model) revealed $S_2(Q)$ to be sensitive to non-additive three-body contributions to the potential energy in the region $Q \sim 1.0$ Å^{-1}.

The comparison of equation (7-4) (assuming pairwise additivity and the Barker pair potential for xenon) with the experimental measurements of S(Q) for low density xenon tentatively suggests that Barker's pair potential may be somewhat erroneous. However, the addition of the non-additive three-body contribution (as modeled by the Axilrod-Teller dispersion potential) reduced the discrepancy between theory and experiment, particularly at the lower densities. In view of these results, it seems likely that a combination of uncertainty in both the pair and three-body potentials contributes to the difference between the theoretical calculations and experimental measurements of S(Q). Because of the uncertainty in the data, additional measurements on S(Q) in the low density range (perhaps for $\rho < 3$ mole/liter) are necessary to distinguish between two- and three-body contributions to the interatomic potential. Based on the results found in this study, three-body effects on S(Q) can best be studied in the region

$$0.5 \text{ Å}^{-1} < Q < 1.0 \text{ Å}^{-1} .$$

7.7.2 Summary of the Results for the Dynamic Structure Factor. It was found in Section 7.5.2 that neither free-particles nor collisionless particles can adequately represent the time-of-flight measurements of $\tilde{S}(Q,\omega)$, where

$$\tilde{S}(Q,\omega) \equiv b^2_{coh}\, S(Q,\omega) + b^2_{incoh}\, S_s(Q,\omega) \ , \qquad (6\text{-}30)$$

for xenon at a density of 3.08 mole/liter and a Q-value of 0.58 $\mathring{A}^{-1}$. These results suggest that the neutrons are sampling $\tilde{S}(Q,\omega)$ in a (Q,ω) region sensitive to the details of the collision dynamics. An analysis of the collisionless models for hard spheres and for a hard core fluid having attractive forces revealed a qualitative difference between the mean field operators for the two fluids. In particular, the hard sphere mean field operator broadened (somewhat) the kinetic model calculations over its free-particle value, whereas the corresponding calculation for the attractive hard core fluid results in a significant narrowing of the line shape, thereby reducing the discrepancy between theory and experiment.

The results for the collisionless and free-particle kinetic models suggest that collisional effects are necessary to adequately interpret the data. It was found that increasing the collision frequency (by increasing the hard sphere diameter, r_o) tended to narrow the line shape over its free-particle value and hence provide better agreement between theory and experiment. However, the Enskog theory for hard spheres was found to be rather insensitive[5] to changes in r_o so that, even for artificially large hard sphere diameters, the data apparently cannot be fit assuming a hard sphere fluid.

---

[5] Presumably due to the competition between the collisional narrowing and the broadening effect due to the mean field operator.

The only difference between the generalized Enskog equation for attractive spheres and that for hard spheres is in the replacement of the hard sphere $C(Q)$ and $g(r_o)$ by the corresponding values for the attracting hard sphere fluid. The analysis of the hard core fluid was limited to the special case of the Sutherland potential; the parameters (r_o, ε/k) in the Sutherland potential were chosen to give a good representation of the actual pair correlation function (as calculated for Barker's potential from the virial expansion for terms up to and including $g_2(r)$) for xenon. Choosing $C(Q)$ the experimental value, and $g(r_o)$ as that predicted from the Sutherland potential (e.g., $g(r_o) = e^{\varepsilon/kT}$), the agreement between experiment and the kinetic theory for attractive hard spheres was quite good. Based on these results we conclude that the effect of the attractive part of the xenon potential is significant in representing the collisional narrowing, particularly at the experimental temperature ($T^* = kT/\varepsilon = 1.08$ for the Barker pair potential for xenon) studied. It would be useful to repeat the experiment at a much higher temperature (say $T^* > 2$). Here, the fluid structure and dynamic behavior is determined by the repulsive wall of the potential, and it is expected that Enskog's hard system theory would do better under these conditions. There remains a great deal more to be done with the present data to firm up these conclusions. For example, a thorough analysis of the Q dependence for $S(Q,\omega)$ has not been completed. Additionally, the comparison between theory and experiment has not been carried out at higher densities, along with the determination of the theoretical pressure derivatives.

APPENDIX A

PROPERTIES OF THE COMPLEX SUSCEPTIBILITY

In this appendix, properties of the complex susceptibility, $\tilde{\chi}(Q,\omega)$, are presented. In particular, the imaginary part of this function, denoted $\tilde{\chi}''(Q,\omega)$, is related to the dynamic structure factor, $S(Q,\omega)$ (equation (3-7)), and the sum rule expression (equation (3-9)) is derived.

A.1 Derivation of Equation (3-7)

The first step is to relate $\tilde{\chi}(Q,\omega)$ to $\tilde{\chi}''(Q,\omega)$. Write $\tilde{\chi}(Q,\omega)$ as

$$\tilde{\chi}(Q,\omega) = \frac{-1}{kT} \int_{-\infty}^{+\infty} dt e^{i\omega t} \langle n_{-Q}(0)\ \dot{n}_Q(t) \rangle \theta(t), \tag{A-1}$$

where $\theta(t)$ is the Heaviside step function

$$\theta(t) = \begin{cases} 0 \ , & t < 0 \\ 1 \ , & t > 0 \end{cases} , \tag{A-2}$$

and may be represented by

$$\theta(t) \equiv \lim_{\varepsilon \to 0^+} \int_{-\infty}^{+\infty} \frac{d\omega}{2\pi i} \frac{e^{i\omega t}}{\omega - i\varepsilon} . \tag{A-3}$$

Substituting equation (A-3) for $\theta(t)$ into equation (A-1) yields

$$\tilde{\chi}(Q,\omega) = - \lim_{\varepsilon \to 0^+} \int_{-\infty}^{+\infty} \frac{dz}{\pi i} \frac{Z(Q,z)}{z-\omega-i\varepsilon} , \tag{A-4}$$

where

$$Z(Q,z) \equiv \frac{1}{2kT} \int_{-\infty}^{+\infty} dt e^{izt} \langle n_{-Q}(0)\ \dot{n}_Q(t) \rangle . \tag{A-5}$$

But,

$$\frac{1}{z-\omega-i\varepsilon} = \frac{z-\omega}{(z-\omega)^2 + \varepsilon^2} + i \frac{\varepsilon}{(z-\omega)^2 + \varepsilon^2} , \tag{A-6}$$

and, from the definition of the δ-function,

$$\delta(x) \equiv \frac{1}{\pi} \lim_{\varepsilon \to 0^+} \left[\frac{\varepsilon}{x^2 + \varepsilon^2} \right] , \tag{A-7}$$

equation (A-4) becomes

$$\tilde{\chi}(Q,\omega) = i \int_{-\infty}^{+\infty} \frac{dz}{\pi} \frac{Z(Q,z)}{z-\omega} - Z(Q,\omega) . \tag{A-8}$$

If we write $\tilde{\chi}(Q,\omega)$ explicitly as

$$\tilde{\chi}(Q,\omega) = \tilde{\chi}'(Q,\omega) + i\, \tilde{\chi}''(Q,\omega) , \tag{A-9}$$

and identify the real and imaginary parts of equation (A-8), we see that

$$\tilde{\chi}'(Q,\omega) = \int_{-\infty}^{+\infty} \frac{dw'}{\pi} \frac{\tilde{\chi}''(Q,\omega')}{\omega'-\omega} , \tag{A-10}$$

and

$$\tilde{\chi}''(Q,\omega) = \frac{i}{2kT} \int_{-\infty}^{+\infty} dt e^{i\omega t} \langle n_{-Q}(0)\ \dot{n}_Q(t)\rangle . \tag{A-11}$$

The time derivative in equation (A-11) may be eliminated on integrating by parts to give

$$\tilde{\chi}''(Q,\omega) = \frac{\omega}{2kT} \int_{-\infty}^{+\infty} dt e^{i\omega t} \langle n_{-Q}(0)\ n_Q(t)\rangle . \tag{A-12}$$

By definition,

$$G(\vec{r};t) \equiv \frac{1}{\rho} \langle n(\vec{0},0) n(\vec{r},t)\rangle , \tag{A-13}$$

so that

$$S(Q,\omega) = \frac{1}{\rho} \int_{-\infty}^{+\infty} dt e^{i\omega t} \langle n_{-Q}(0)\ n_Q(t)\rangle \ . \tag{A-14}$$

Comparison of equation (A-14) with equation (A-12) then yields the desired result:

$$S(Q,\omega) = \frac{2kT}{\rho\omega}\ \tilde{\chi}''(Q,\omega) \ . \tag{A-15}$$

A.2 Sum Rule Relations

Define the moments, $M_n(Q)$, by

$$M_n(Q) \equiv \int_{-\infty}^{+\infty} \frac{d\omega}{\pi}\ \omega^n\ \tilde{\chi}''(Q,\omega) . \tag{A-16}$$

A rearrangement of equation (A-15) gives

$$\tilde{\chi}''(Q,\omega) = \frac{\rho}{2kT}\ [\omega S(Q,\omega)] \ , \tag{A-17}$$

so that

$$M_n(Q) = \frac{\rho}{kT} \int_{-\infty}^{+\infty} \frac{d\omega}{2\pi}\ \omega^{n+1}\ S(Q,\omega) \ , \tag{A-18}$$

which is equation (3-12) in the text. However,

$$\tilde{\chi}(Q,\omega) = \int_{-\infty}^{+\infty} \frac{d\omega'}{\pi}\ \frac{\tilde{\chi}''(Q,\omega')}{\omega'-\omega}$$

$$= \frac{-1}{\omega} \int_{-\infty}^{+\infty} \frac{d\omega'}{\pi}\ \frac{\tilde{\chi}''(Q,\omega')}{1 - \frac{\omega'}{\omega}} \ , \tag{A-19}$$

and an expansion of $(1 - \frac{\omega'}{\omega})^{-1}$ yields

$$\tilde{\chi}(Q,\omega) = -\sum_{n\geq 0}^{\infty} \left(\frac{1}{\omega}\right)^{n+1} M_n(Q) \quad , \tag{A-20}$$

which is the desired result.

APPENDIX B

DETERMINATION OF $\Psi^{(2)}(x_1,x_2;t=o|\cdot)$ and $B[\cdot]$

In this appendix equations (3-58) and (3-64) are established. We begin by writing

$$\psi^{(1)}(x_1;t) = \hat{U}(x_1;t)\ y(x_1)\ , \tag{B-1}$$

$$\psi^{(2)}(x_1,x_2;t) = \hat{U}(x_1,x_2;t)y(x_2)\ . \tag{B-2}$$

Here, $y(x_1) = \delta(\vec{r}-\vec{q}_1)$ for the special case of the density-density time correlation function,

$$\hat{U}(x_1;t) \equiv \frac{1}{\rho} \sum_{N\geq 2} N \int dx_2 \ldots dx_N\ e^{iL_N t}\ f_N[1 + \sum_{i=2}^{N} P_{i1}]$$

and

$$\hat{U}(x_1,x_2;t) \equiv \frac{1}{\rho^2} \sum_{N\geq 3} N(N-1) \int dx_3 \ldots dx_N\ e^{iL_N t}\ f_N[1 + \sum_{i=2}^{N} P_{i1}]\ , \tag{B-3}$$

where f_N is defined in equation (3-45) and the permutation operator, P_{ij}, is given by equation (3-46). To identify the functional $\Psi^{(2)}(x_1,x_2;t=o|\cdot)$, we consider equations (B-1) and (B-2) at t=o:

$$\psi^{(1)}(x_1;t=o) = \hat{U}(x_1;t=o)\ y(x_1)\ , \tag{B-4}$$

$$\psi^{(2)}(x_1,x_2;t=o) = \hat{U}(x_1,x_2;t=o)\ y(x_1)\ . \tag{B-5}$$

The left side of these equations may be evaluated directly from the definitions, equation (3-27), with the results

$$\psi^{(1)}(x_1;t=o) = f_o(x_1)\ y(x_1) + \rho \int dx_2\ f_o(x_1)\ f_o(x_2)\ h(\vec{q}_{12})\ y(x_2)\ , \tag{B-6}$$

$$\psi^{(2)}(x_1,x_2;t=o) = f_o(x_1)\ f_o(x_2)\ g^{(2)}(\vec{q}_{12})\ [y(x_1) + y(x_2)]$$
$$+ \rho \int dx_3\ f_o(x_1)\ f_o(x_2)\ f_o(x_3)\ [g^{(3)}(\vec{q}_1,\vec{q}_2,\vec{q}_3)$$
$$- g^{(2)}(\vec{q}_{12})]\ y(x_3)\ . \tag{B-7}$$

Here, $h(\vec{q}_{12}) \equiv g^{(2)}(\vec{q}_{12}) - 1$, and $g^{(2)}$ and $g^{(3)}$ are, respectively, the two- and three-particle equilibrium correlation functions. Comparison of equation (B-4) with (B-6) (and (B-5) with (B-7)) identifies the operators $\hat{U}(x_1;t=o)$ and $\hat{U}(x_1,x_2;t=o)$:

$$\hat{U}(x_1;t=o) = f_o(x_1)\ [1 + \rho \int dx_2\ f_o(x_2)\ h(\vec{q}_{12})\ P_{12}] \tag{B-8}$$

and

$$\hat{U}(x_1,x_2;t=o) = f_o(x_1)\ f_o(x_2)\ \{g^{(2)}(\vec{q}_{12})\ [1 + P_{12}]$$
$$+ \rho \int dx_3\ f_o(x_3)\ [g^{(3)}(\vec{q}_1,\vec{q}_2,\vec{q}_3) - g^{(2)}(\vec{q}_{12})]P_{13}\}\ . \tag{B-9}$$

The inverse of $\hat{U}(x_1;t=o)$, denoted $\hat{U}^{-1}(x_1;t=o)$, is readily found (using the Orstein-Zernicke equation for $h(\vec{q}_{12})$ and the method discussed in Appendix C),

$$\hat{U}^{-1}(x_1;t=o) = [1 - \rho \int dx_2\ f_o(x_2)\ C(\vec{q}_{12})P_{12}]\ f_o^{-1}(x_1)\ , \tag{B-10}$$

or, more compactly,

$$\hat{U}^{-1}(x_1;t=o) = [1 - \rho\hat{\Delta}]\ f_o^{-1}(x_1)\ , \tag{B-11}$$

where the operator $\hat{\Delta}$ is defined by

$$\hat{\Delta} \equiv \int dx_2\ f_o(x_2)\ C(\vec{q}_{12})\ P_{12}\ . \tag{B-12}$$

Substitution of equations (B-9) and (B-11) into

$$\Psi^{(2)}(x_1,x_2;t=o|\psi^{(1)}(t)) = \hat{U}(x_1,x_2;t=o)\ \hat{U}^{-1}(x_1;t=o)\ \psi^{(1)}(x_1;t) \tag{B-13}$$

yields equation (3-58), the final result for $\Psi^{(2)}(x_1,x_2;t=o|\psi^{(1)}(t))$.

To determine the operator $B[\psi^{(1)}]$ from its definition, equation (3-34), it is convenient to use an alternative form of equation (3-58),

$$\begin{aligned}\Psi^{(2)}(x_1,x_2;t=o|\psi^{(1)}(t)) &= f_o(x_1)\ f_o(x_2)\ g^{(2)}(\vec{q}_{12})\ [y(x_1) + y(x_2)] \\ &+ \rho \int dx_3\ f_o(x_1)\ f_o(x_2)\ f_o(x_3)\ [g^{(3)}(\vec{q}_1,\vec{q}_2,\vec{q}_3) \\ &\qquad - g^{(2)}(\vec{q}_{12})]\ y(x_2)\ ,\end{aligned} \tag{B-14}$$

which is simply equation (B-7) with $y(x_1)$ considered as a functional of $\psi^{(1)}$ through

$$\begin{aligned}y(x_1) &= \hat{U}^{-1}(x_1;t=o)\ \psi^{(1)}(x_1;t=o) \\ &= [1 - \rho\hat{\Delta}]\ f_o^{-1}(x_1)\ \psi^{(1)}(x_1;t=o)\ .\end{aligned} \tag{B-15}$$

Using equation (B-14), the operator $B[\psi^{(1)}]$ is given by

$$B[\psi^{(1)}] = \rho \int dx_2\ \theta_{12}\ \Psi^{(2)}(x_1,x_2;t=o|\psi^{(1)}(t))$$

$$= \rho \int dx_2\ \theta_{12}\ f_o(x_1)\ f_o(x_2)\ g^{(2)}(\vec{q}_{12})\ [y(x_1) + y(x_2)]$$

$$+ \rho^2 \int dx_2\ dx_3\ \theta_{12}\ f_o(x_1)\ f_o(x_2)\ f_o(x_3)$$

$$\times\ [g^{(3)}(\vec{q}_1,\vec{q}_2,\vec{q}_3) - g^{(2)}(\vec{q}_{12})]\ y(x_3)$$

$$= \rho \int dx_2 [\theta_{12}\ f_o(x_1)\ g^{(2)}(\vec{q}_{12})$$

$$+ \rho \int dx_3\ \theta_{13}\ g^{(3)}(\vec{q}_1,\vec{q}_2,\vec{q}_3)]\ f_o(x_2)\ y(x_2)$$

or

$$B[\psi^{(1)}] = \rho \int dx_2\ (\frac{\vec{p}_1}{m} \cdot \vec{\nabla}_1)\ f_o(x_1)\ g^{(2)}(\vec{q}_{12})\ f_o(x_2)\ y(x_2). \quad \text{(B-16)}$$

This last equality follows from the second equation of the equilibrium BBGKY hierarchy. Finally, introducing equation (B-15) for $y(x_2)$ into equation (B-16) yields the desired result, equation (3-64).

APPENDIX C

DETERMINATION OF $G_2^{-1}(\vec{r}',0;\vec{r}'',0)$

From the definition

$$G(\vec{r}',0;\vec{r}'',0) \equiv \frac{1}{\rho} \langle n(\vec{r}',0)n(\vec{r}'',0)\rangle \quad , \tag{C-1}$$

it is easy to show that

$$G(\vec{r}',0;\vec{r}'',0) = \delta(\vec{r}'-\vec{r}'') + \rho h(\vec{r}'-\vec{r}'') \ , \tag{C-2}$$

where $h(\vec{r}'-\vec{r}'') \equiv g^{(2)}(\vec{r}'-\vec{r}'') - 1$. To find the function $G_2^{-1}(\vec{r}',0;\vec{r}'',0)$, begin by assuming it to be of the form

$$G_2^{-1}(\vec{r}',0;\vec{r}'',0) = \delta(\vec{r}'-\vec{r}'') - \rho\ K(\vec{r}''-\vec{r}') \ , \tag{C-3}$$

where the variable $K(\vec{r}''-\vec{r}')$ has not yet been identified.

By definition, equation (3-102) must be satisfied:

$$\int d\vec{r}''[\delta(\vec{r}'-\vec{r}'') + \rho h(\vec{r}'-\vec{r}'')][\delta(\vec{r}''-\vec{r}) - \rho K(\vec{r}-\vec{r}'')] = \delta(\vec{r}'-\vec{r}), \tag{C-4}$$

or

$$\int d\vec{r}''\ \delta(\vec{r}'-\vec{r}'')\delta(\vec{r}''-\vec{r}) + \rho \int d\vec{r}''h(\vec{r}'-\vec{r}'')\delta(\vec{r}''-\vec{r})$$

$$-\rho \int d\vec{r}''\ K(\vec{r}-\vec{r}'')\delta(\vec{r}'-\vec{r}'') - \rho^2 \int d\vec{r}''h(\vec{r}'-\vec{r}'')K(\vec{r}-\vec{r}'') = \delta(\vec{r}'-\vec{r}). \tag{C-5}$$

Making use of the property of the δ-function,

$$\int dx\ f(x)\delta(x-a) = f(a),$$

we find that equation (C-5) reduces to

$$h(\vec{r}'-\vec{r}) = K(\vec{r}'-\vec{r}) + \rho \int d\vec{r}''\ h(\vec{r}'-\vec{r}'')K(\vec{r}-\vec{r}''). \tag{C-6}$$

Comparing equation (C-6) with the Ornstein-Zernike equation,

$$h(\vec{r}'-\vec{r}) = C(\vec{r}'-\vec{r}) + \rho \int d\vec{r}'' \; h(\vec{r}'-\vec{r}'')C(\vec{r}-\vec{r}'') \quad , \tag{C-7}$$

we see that

$$G_2^{-1} \; (\vec{r}',0;\vec{r}'',0) = \delta(\vec{r}'-\vec{r}'') - \rho C(\vec{r}''-\vec{r}') \quad , \tag{C-8}$$

where $C(\vec{r}''-\vec{r}')$ is the direct correlation function.

APPENDIX D

DETAILS OF MODEL CALCULATIONS (SECTION 3.5)

In this appendix the details of the model calculations for Section 3.5 are presented. Specifically, $A(Q)$ is chosen to satisfy the fourth frequency moment of $S(Q,\omega)$, and $\tau(Q)$ is related to $S(Q,\omega=o)$, as suggested by Kugler (40).

D.1 Expression for A(Q)

To develop and expression for $A(Q)$, we begin with (see equations (3-107) and (3-112))

$$M(Q,\omega) = -\frac{A(Q)\tau(Q)}{1-i\omega\tau(Q)}\,[1-P] \;, \tag{D-1}$$

where the projection operator P is defined by equation (3-109). By expanding the collision operator in ω, we find

$$M(Q,\omega) = M^{(o)}(Q,\omega) + \left(\frac{1}{\omega}\right) M^{(1)}(Q,\omega) + \ldots \;, \tag{D-2}$$

or, since $M(Q,\omega)$ vanishes in the limit as $\omega\to\infty$ (48), $M^{(o)}(Q,\omega) = 0$ and

$$M(Q,\omega) \sim \left(\frac{1}{\omega}\right) M^{(1)}(Q,\omega) \;. \tag{D-3}$$

The large ω limit of equation (D-1),

$$\lim_{\omega\to\infty} M(Q,\omega) = \frac{1}{\omega}\,(-i\,A(Q))\,[1-P] \;,$$

identifies $M^{(1)}(Q,\omega)$:

$$M^{(1)}(Q,\omega) = -i\ A(Q)\ [1-P]\ . \tag{D-4}$$

The parameter A(Q) is determined by considering the frequency moments of the complex susceptibility, $\tilde{\chi}(q,\omega)$. We begin by expanding the denominator of equation (3-85):

$$\tilde{\chi}(Q,\omega) = I(Q,\omega)\ [1 + kT\ C(Q)\ I(Q,\omega) + \ldots]\ . \tag{D-5}$$

Next we note that expanding $I(Q,\omega)$ as ω^{-1} yields

$$I(Q,\omega) = -\sum_{n=o}^{\infty} \left(\frac{1}{\omega}\right)^{n+1} \alpha_n(Q)\ , \tag{D-6}$$

with the first four moments of $I(Q,\omega)$ given below:

$$\alpha_o(Q) = o$$

$$\alpha_1(Q) = \frac{\rho}{kT} \int d\vec{p}\ f_o(p)\ \left(\frac{\vec{Q}\cdot\vec{p}}{m}\right)^2$$

$$\alpha_2(Q) = o$$

$$\alpha_3(Q) = \frac{\rho}{kT}\ [\ \int d\vec{p}\ f_o(p)\ \left(\frac{\vec{Q}\cdot\vec{p}}{m}\right)^4$$

$$+\ i \int d\vec{p}\ f_o(p)\ \left(\frac{\vec{Q}\cdot\vec{p}}{m}\right) M^{(1)}\ \left(\frac{\vec{Q}\cdot\vec{p}}{m}\right)]\ . \tag{D-7}$$

In evaluating the moments, $\alpha_n(Q)$, equation (D-3) was used for $M(Q,\omega)$. Returning to equation (D-5), we see that, to lowest order in ω^{-1},

$$\tilde{\chi}(Q,\omega) = -\left(\frac{1}{\omega}\right)^2 [\alpha_1(Q)]$$

$$-\left(\frac{1}{\omega}\right)^4 [\alpha_3(Q) - kT\ C(Q)\ \alpha_1^2(Q)]$$

$$-\ \ldots\ . \tag{D-8}$$

A comparison of equation (D-8) with equation (A-20) then relates $A(Q)$ to $M_3(Q)$:

$$M_3(Q) = \frac{\rho}{kT} \left[\int d\vec{p}\, f_o(p) \left(\frac{\vec{Q}\cdot\vec{p}}{m}\right)^4 \right.$$

$$\left. + A(Q) \int d\vec{p}\, f_o(p) \left(\frac{\vec{Q}\cdot\vec{p}}{m}\right) [1-P] \left(\frac{\vec{Q}\cdot\vec{p}}{m}\right) \right] . \qquad \text{(D-9)}$$

Replacing $M_3(Q)$ with equation (3-13), and solving for $A(Q)$, results in equation (3-113). For numerical evaluation, the integral appearing in equation (3-113) was placed in the form

$$\int d\vec{r}\, g(r)\, [1-\cos \vec{Q}\cdot\vec{r}]\, (\hat{Q}\cdot\vec{\nabla})^2\, \phi(r)$$

$$= 4\pi \int_0^\infty dr\, r\, g(r)\, \{\phi'(r)\, [1 - \frac{\sin(Qr)}{Qr}]$$

$$- f(Qr)\, [\phi'(r) - r\, \phi''(r)] \quad , \qquad \text{(D-10)}$$

where $\phi'(r)$ and $\phi''(r)$ denote the first and second derivations (with respect to r) of $\phi(r)$, respectively, and $f(x)$ is defined as

$$f(x) \equiv \frac{1}{3} - \frac{\sin x}{x} + \frac{2(\sin x - x \cos x)}{x^3} . \qquad \text{(D-11)}$$

D.2 Expression for $\tau(Q)$

We being by considering the relaxation parameter, $\tau_K(Q)$, as determined by Kugler (40):

$$\tau_K(Q) = \frac{\lim_{\omega\to\infty} [\frac{\phi''(Q,\omega)}{\omega}]}{\phi_o(Q)-\phi_\infty(Q)} . \qquad \text{(D-12)}$$

Here, $\phi''(Q,\omega)$ is the imaginary part of $\phi(Q,\omega)$, the difference, $\phi_o(Q)-\phi_\infty(Q)$, is given by (40)

$$\phi_o(Q) - \phi_\infty(Q) = -\left(\frac{m}{\rho Q^2}\right) A(Q) \quad , \tag{D-13}$$

and $\phi(Q,\omega)$ is related to $I(Q,\omega)$ through equation (D-14):

$$\phi(Q,\omega) = -kT\ C(Q) + \frac{I_o - I}{I\ I_o} \quad . \tag{D-14}$$

The integrals I and I_o are defined by equations (3-37) and (3-73), respectively, and, for the simple single relaxation time operator (equation (3-107)) reduces to

$$I(Q,\omega) = \left(\frac{\rho}{kT}\right) \left[\frac{1 + (i\omega - \lambda)\ F(Q,\omega)}{1 - \lambda F(Q,\omega)}\right] \tag{D-15}$$

and

$$I_o(Q,\omega) = \left(\frac{\rho}{kT}\right) [1 + i\omega\ F_o(Q,\omega)] \quad , \tag{D-16}$$

where $F(Q,\omega)$ and $F_o(Q,\omega)$ are defined below:

$$F(Q,\omega) \equiv \int d\vec{p}\ f_o(p)\ \left[-i\omega + \frac{i\vec{Q}\cdot\vec{p}}{m} + \lambda\right]^{-1} \tag{D-17}$$

$$F_o(Q,\omega) \equiv \int d\vec{p}\ f_o(p)\ \left[-i\omega + \frac{i\vec{Q}\cdot\vec{p}}{m}\right]^{-1} \quad . \tag{D-18}$$

It is a simple matter to show

$$I_o - I = i\omega \left(\frac{\rho}{kT}\right) \left[F_o - \frac{F}{1-\lambda F}\right] \tag{D-19}$$

and

$$\lim_{\omega\to o} I\ I_o = \left(\frac{\rho}{kT}\right)^2 \quad , \tag{D-20}$$

so that

$$\lim_{\omega\to o} \left[\frac{\phi(Q,\omega)}{\omega}\right] = \lim_{\omega\to o} \left[-\frac{kT\ C(Q)}{\omega}\right] + i\left(\frac{kT}{\rho}\right) \lim_{\omega\to o} \left[F_o - \frac{F}{1-\lambda F}\right] \quad . \tag{D-21}$$

Since we are concerned with $\phi''(Q,\omega)$, we need only consider

$$\lim_{\omega\to o} \left[\frac{\phi''(Q,\omega)}{\omega}\right] = \left(\frac{kT}{\rho}\right) \lim_{\omega\to o} \left[F_o - \frac{F}{1-\lambda F}\right] . \tag{D-22}$$

Equation (D-22) can be evaluated by writing

$$\omega = z + i\varepsilon$$

and making use of equations (A-6) and (A-7), with the result:

$$\lim_{\omega\to o} F_o(Q,\omega) = \left(\frac{\pi}{2}\right)^{\frac{1}{2}} \left(\frac{1}{Qv_o}\right) \tag{D-23}$$

$$\lim_{\omega\to o} F(Q,\omega) = \lambda(Q,\omega=o) \int d\vec{p}\ f_o(p) \left[\frac{(\vec{Q}\cdot\vec{p})^2}{m} + \lambda^2(Q,\omega=o)\right]^{-1} . \tag{D-24}$$

Substituting equations (D-23) and (D-24) into equation (D-22), and noting that (see equation (3-112))

$$\lambda(Q,\omega=o) = A(Q)\ \tau(Q) , \tag{D-25}$$

relates our relaxation parameter, $\tau(Q)$, to that of Kugler (40):

$$\tau(Q) = -\frac{2z}{\sqrt{\pi}} \left[1 - \frac{H(z)}{1 - \sqrt{\pi}\ zH(z)}\right] \tau_K(Q) , \tag{D-26}$$

where

$$z \equiv \frac{A(Q)\ \tau(Q)}{\sqrt{2}\ Q\ v_o} \tag{D-27}$$

and

$$H(z) \equiv \frac{2z}{\pi} \int_{-\infty}^{+\infty} dx\ \frac{e^{-x^2}}{x^2 + z^2} . \tag{D-28}$$

To simplify the calculation of $\tau(Q)$, $H(z)$ is expanded in z,

$$H(z) = \frac{1}{\sqrt{\pi}} \left[\frac{1}{z} - \frac{1}{2z^3} + \ldots\right] ,$$

and equation (D-26) becomes, in the limit of large z,

$$\tau(Q) = \frac{\tau_K(Q)}{1 - \frac{\sqrt{\pi}}{2z}} \quad . \tag{D-29}$$

Equation (D-29) is the expression for $\tau(Q)$ used in the calculations of Section 3.5; $\tau_K(Q)$ is evaluated from experimental data on $S(Q,\omega=o)$ for liquid argon near its triple point in reference (40).

APPENDIX E

THE N = 6 GROSS-JACKSON KINETIC MODEL

In this Appendix the steps leading to $S(Q,\omega)$ as calculated using the N = 6 kinetic model for a dilute, hard sphere gas, discussed in Section 4.2, are presented.

We begin by noting that an alternative to equation (4-1) for $S(Q,\omega)$ is

$$S(Q,\omega) = 2 \text{ Real } \left\{ \frac{S(Q)\ (1,\bar{Y})}{1 - \rho[(Q)-g(r_o)C_o(Q)](1,\frac{i\vec{Q}\cdot\vec{p}}{m}\bar{Y}) + \lambda_6(1,\bar{Y})} \right\} . \tag{E-1}$$

Here, $\bar{Y}$ satisfies the equation

$$\bar{Y}(p) = R_{oo}1 + R_{oo} \sum_{\alpha=2}^{6} \sum_{\beta=2}^{6} \mu_{\alpha\beta}\ \psi_\alpha(p)\ (\psi_\beta,\bar{Y}) , \tag{E-2}$$

with

$$R_{oo} \equiv [-i\omega + \frac{i\vec{Q}\cdot\vec{p}}{m} - {}_6(Q,\omega)]^{-1} \tag{4-15}$$

and

$$\mu_{\alpha\beta} \equiv (\psi_\alpha,\ M\ \psi_\beta) - \lambda_6\ \ \delta_{\alpha\beta}. \tag{4-12}$$

The calculation of $S(Q,\omega)$ was performed for the following set, :

$$\psi_1 = 1,$$

$$\{\psi_2,\psi_3,\psi_4\} = \{(\frac{\beta}{m})^{\frac{1}{2}}\ p_x,\ (\frac{\beta}{m})^{\frac{1}{2}}\ p_y,\ (\frac{\beta}{m})^{\frac{1}{2}}\ p_z\} ,$$

$$\psi_5 = (\frac{2}{3})^{\frac{1}{2}}\ [\frac{\beta p^2}{2m} - \frac{3}{2}] ,$$

$$\psi_6 = (\frac{\beta}{10m})^{\frac{1}{2}}\ p_z\ [\frac{\beta p^2}{m} - 5] ,$$

and the eigenvalue λ_6 is given by

$$\lambda_6 = (\frac{\beta}{m})^2\ (p_y p_z,\ M\ p_y p_z).$$

Equation (4-13) can be simplified by using a vector notation, yielding

$$\bar{Y}(P) = R_{oo} + R_{oo} \{\vec{U}\cdot\vec{Q}\ [I_{um5}\ I_{5y} + \mu_{uu}\ I_{uy} + I_{um6}\ I_{6y}]$$

$$+ \psi_5\ [Q^2 I_{5mu}\ I_{uy} + I_{5m6}\ I_{6y} + \mu_{55}\ I_{5y}] \qquad \text{(E-3)}$$

$$+ \psi_6\ [Q^2\ I_{6mu}\ I_{uy} + I_{6m5}\ I_{5y} + \mu_{66}\ I_{6y}]\} \ ,$$

where the following notation has been introduced[1]:

$$\vec{U} \equiv \{(\tfrac{\beta}{m})^{\frac{1}{2}}\ p_x,\ (\tfrac{\beta}{m})^{\frac{1}{2}}\ p_y,\ (\tfrac{\beta}{m})^{\frac{1}{2}}\ p_z\ \} \ ,$$

$$\vec{I}_{umj} \equiv (\vec{U}, M\psi_j)$$

$$\vec{I}_{uy} \equiv (\vec{U}, \bar{Y}) \qquad \text{(E-4)}$$

$$I_{5y} \equiv (\psi_5, \bar{Y})$$

$$I_{6y} \equiv (\psi_6, \bar{Y})$$

Since the momentum dependence of $\vec{I}_{uy}$ has been integrated out, all the vectorial properties of $\vec{I}_{uy}$ (and $\vec{I}_{umj}$) are due to $\vec{Q}$ only. Hence, use has been made of the following property in arriving at equation (E-3):

$$\vec{I}_{uy} = I_{uy}\ \vec{Q} \ , \qquad \text{(E-5)}$$

which then implies

$$I_{uy} = \frac{\vec{Q}\cdot\vec{I}_{uy}}{Q^2} \ . \qquad \text{(E-6)}$$

---

[1]Recall the scalar product notation, equation (4-3).

In equation (E-3) there are three unknowns (I_{5y}, I_{6y}, and I_{uy}), requiring three independent equations for solution. These three equations are obtained by (1) multiplying equation (E-3) by ψ_5 and integrating over the momentum, (2) multiplying equation (E-3) by ψ_6 and integrating over the momentum, and (3) multiplying equation (E-3) by $\vec{Q}\cdot\vec{U}$ and integrating over the momentum. This procedure results in the following set of three linearly independent equations:

$$I_{5y} = I_o + J_1 I_1 + J_2 I_2 + J_3 I_5 \ , \tag{E-7}$$

$$I_{6y} = I_6 + J_1 I_7 + J_2 I_5 + J_3 I_8 \ , \tag{E-8}$$

$$I_{uy} = I_3 + J_1 I_4 + J_2 I_1 + J_3 I_7 \ , \tag{E-9}$$

with

$$J_1 \equiv Q^2 [I_{um5} I_{5y} + \mu_{uu} I_{uy} + I_{um6} I_{6y}] \ , \tag{E-10}$$

$$J_2 \equiv Q^2 \ I_{5mu} I_{uy} + I_{5m6} I_{6y} + \mu_{55} I_{5y} \ , \tag{E-11}$$

and

$$J_3 \equiv Q^2 \ I_{uy} I_{6mu} + I_{6m5} I_{5y} + \mu_{66} I_{6y} \ . \tag{E-12}$$

Here, the following integrals have been introduced:

$$I_o \equiv (\psi_5, \ R_{oo} \ 1)$$

$$I_1 \equiv Q^{-2} (\vec{U}\cdot\vec{Q}, \ R_{oo} \ \psi_5)$$

$$I_2 \equiv (\psi_5, \ R_{oo} \ \psi_5)$$

$$I_3 \equiv Q^{-2} (\vec{U}\cdot\vec{Q}, \ R_{oo} \ 1)$$

$$I_4 \equiv Q^{-2} (\vec{U}\cdot\vec{Q}, \ R_{oo} \ \vec{U}\cdot\vec{Q})$$

$$I_5 \equiv (\psi_5, \ R_{oo} \ \psi_6)$$

$$I_6 \equiv (\psi_6, R_{oo}\, 1)$$

$$I_7 \equiv Q^{-2}(\vec{U}\cdot\vec{Q}, R_{oo}\, \psi_6)$$

$$I_8 \equiv (\psi_6, R_{oo}\, \psi_6) \quad . \tag{E-13}$$

The integral, (1,Y), is also required

$$I_y = I_{oo} + J_1 I_3 + J_2 I_o + J_3 I_6 \ , \tag{E-14}$$

with

$$I_y \equiv (1,\bar{Y}) \tag{E-15}$$

and

$$I_{oo} \equiv (1, R_{oo}\, 1) \ . \tag{E-16}$$

Solution of equations (E-7), (E-8) and (E-9), For I_{5y}, I_{6y}, and I_{uy}, was accomplished using Cramer's Rule, and the expression for $S(Q,\omega)$ in terms of the above integrals is readily found from equation (4-1):

$$S(Q,\omega) = 2 \text{ Real } \left\{ \frac{S(Q)\ I_y}{1-i\rho[C(Q)-g(r_o)C_o(Q)]I_{uy}+\lambda_6 I_y} \right\} \ , \tag{E-17}$$

or, in dimensionless form,

$$R(x,y) \quad \frac{\sqrt{2}}{\pi}\ Qv_o\ S(Q,\omega) \ ,$$

with

$$x \equiv \frac{\omega}{\sqrt{2}\ Qv_o} \tag{4-15}$$

and

$$y \equiv \frac{4r_o^3\rho}{Qr_o} \quad .$$

For a dilute gas of hard spheres, the static correlations, S(Q) and C(Q), may be expressed in terms of the spherical Bessel function,

$j_1(k_o)$:

$$S(Q) \to 1 - 4\pi \left(\frac{n}{x_o}\right) j_1(x_o) \ ,$$

$$\rho\, C(Q) \to -4\pi \left(\frac{n}{x_o}\right) j_1(x_o) \ , \qquad \text{(E-18)}$$

$$g(r_o) \to 1 \ ,$$

with

$$n \equiv \rho r_o^3$$

$$x_o \equiv Q r_o \ . \qquad \text{(E-19)}$$

Equation (E-17) reduces, in the low density limit, to

$$S(Q,\omega) \to 2S(Q) \text{ Real } \left\{\frac{I_y}{1+\lambda_1 I_{6y}}\right\} \ . \qquad \text{(E-20)}$$

The integrals I_y, I_{5y}, I_{6y} and I_{uy} were found to be:

$$I_y = I_{oo} + Z_{10} I_3 + Z_{11} I_o + Z_{12} I_6 \ , \qquad \text{(E-21)}$$

$$I_{uy} = \{I_3(1-Z_1)(1-Z_5) + I_o Z_4 Z_8 + I_o Z_7 (1-Z_5) - I_3 Z_2 Z_4\}\Delta^{-1}, \qquad \text{(E-22)}$$

$$I_{5y} = \{I_o(1-Z_5)(1-Z_9) + \left(\frac{1}{x_o}\right) I_3 Z_2 Z_6 + \left(\frac{1}{x_o}\right) I_3 Z_3 (1-Z_5)$$

$$- \left(\frac{1}{x_o}\right) I_o Z_6 Z_8\}\Delta^{-1}, \qquad \text{(E-23)}$$

$$I_{6y} = \{\left(\frac{1}{x_o}\right) I_o Z_6 Z_7 + \left(\frac{1}{x_0}\right) I_3 Z_3 Z_4 + I_o Z_4 (1-Z_9)$$

$$- \left(\frac{1}{x_o}\right) I_3 Z_6 (1-Z_1)\}\Delta^{-1} \ , \qquad \text{(E-24)}$$

with Δ and the Z-functions defined by:

$$\Delta \equiv (1-Z_1)(1-Z_5)(1-Z_9) - (\frac{1}{x_o})Z_2Z_6Z_7 - (\frac{1}{x_o})Z_3Z_4Z_8$$

$$- (\frac{1}{x_o})Z_3Z_7(1-Z_5) - Z_2Z_4(1-Z_9) - (\frac{1}{x_o})Z_6Z_8(1-Z_1) \ , \qquad \text{(E-25)}$$

$$Z_1 \equiv (\frac{n}{x_o}) \ [I_1 \ I_{um5} + I_2\mu_{55} + I_5I_{5m6}] \ ,$$

$$Z_2 \equiv (\frac{n}{x_o}) \ [I_1 \ I_{um6} + I_2I_{5m6} + I_5\mu_{66}] \ ,$$

$$Z_3 \equiv n[I_1\mu_{uu} + I_2I_{5mu} + I_5I_{6mu}] \ ,$$

$$Z_4 \equiv (\frac{n}{x_o}) \ [I_7I_{um5} + I_5\mu_{55} + I_8\mu_{66}] \ ,$$

$$Z_5 \equiv (\frac{n}{x_o}) \ [I_7I_{um6} + I_5I_{5m6} + I_8\mu_{66}] \ ,$$

$$Z_6 \equiv n[I_7\mu_{uu} + I_5I_{5mu} + I_8I_{6mu}] \ ,$$

$$Z_7 \equiv (\frac{n}{x_o}) \ [I_4I_{um5} + I_1\mu_{55} + I_7I_{6m5}] \ ,$$

$$Z_8 \equiv (\frac{n}{x_o}) \ [I_4I_{um6} + I_1I_{5m6} + I_7\mu_{66}] \ ,$$

$$Z_9 \equiv (\frac{n}{x_o}) \ [I_4\mu_{uu} + I_1I_{5mu} + I_7I_{6mu}] \ ,$$

$$Z_{10} \equiv (\frac{n}{x_o}) \ [I_{um5}I_{5y} + \mu_{uu}I_{uy} + I_{um6}I_{6y}] \ ,$$

$$Z_{11} \equiv (\frac{n}{x_o}) \ [I_{5mu}I_{uy} + I_{5m6}I_{6y} + \mu_{55}I_{5y}] \ ,$$

$$Z_{12} \equiv (\frac{n}{x_o}) \ [I_{uy}I_{6mu} + I_{6m5}I_{5y} + \mu_{66}I_{6y}] \ . \qquad \text{(E-26)}$$

The integrals I_{oo}, I_1, ..., I_8 may be expressed in terms of the plasma dispersion function[2], $\Phi(z)$, defined in equation (4-50):

$$I_{oo} = -i \frac{\sqrt{2}}{2} \Phi(z) ,$$

$$I_o = -i \frac{\sqrt{3}}{3} [z(1+z\Phi(z)) - \frac{1}{2}\Phi(z)] ,$$

$$I_1 = \sqrt{2}\, z\, I_o$$

$$I_2 = - \frac{\sqrt{2}}{3} [\frac{5}{4} \Phi(z) - z(1 + z\Phi(z))$$

$$+ z(\frac{1}{2} + z^2 [1 + z\Phi(z)])] ,$$

$$I_3 = -i[1 + z\Phi(z)] ,$$

$$I_4 = \sqrt{2}\, z\, I_3 ,$$

$$I_5 = -i \frac{\sqrt{60}}{60} [(7-8z^2+4z^4) (1+z\Phi(z)) + 2z^2-1] ,$$

$$I_6 = -i \frac{\sqrt{10}}{10} [1 + (2z^2-3) (1+z\Phi(z))] ,$$

$$I_7 = \frac{\sqrt{2}}{2} z\, I_6 ,$$

$$I_8 = -i \frac{\sqrt{2}}{10} z[2z^2-3+(13-12z^2+4z^4) (1+z\Phi(z))] . \qquad \text{(E-27)}$$

The matrix elements, $(\psi_\alpha, M\, \psi_\beta)$, have been calculated by Furtado *et al.* (91) and are given below for completeness:

---

[2]The plasma dispersion function, $\Phi(z)$, was evaluated numerically using the Harwell subroutine FC21A.

$$\mu_{uu} = -8\sqrt{\pi}\ g(r_o)\ [\frac{1}{3} + \frac{d^2}{dx_o^2}\ j_o(x_o)] - \lambda_6\ ,$$

$$\mu_{55} = -\frac{8}{3}\sqrt{\pi}\ g(r_o)\ [1 - j_o(x_o)] - \lambda_6\ ,$$

$$\mu_{66} = -\frac{\sqrt{\pi}}{15}\ g(r_o)\ [59 + 81\ \frac{d^2}{dx_o^2}\ j_o(x_o)] - \lambda_6\ ,$$

$$I_{5mu} = \frac{2\sqrt{6}}{3}\ \pi\ g(r_o)\ j_1(x_o)\ ,$$

$$I_{um5} = I_{5mu}\ ,$$

$$I_{um6} = -\frac{\sqrt{10\pi}}{5}\ g(r_o)\ [\frac{1}{3} + \frac{d^2}{dx_o^2}\ j_o(x_o)]\ ,$$

$$I_{6mu} = I_{um6}\ ,$$

$$I_{5m6} = -\frac{2\sqrt{15\pi}}{5}\ g(r_o)\ j_1(x_o)\ ,$$

$$I_{6m5} = I_{5m6}\ ,$$

$$\lambda_6 = -16\sqrt{\pi}\ g(r_o)\ [\frac{4}{15} + \frac{d^2}{dx_o^2}\ (\frac{1}{x_o}\ j_1(x_o))]\ .$$

Use of the results in equation (E-17) or (E-20) gives $S(Q,\omega)$ for our N=6 kinetic model.

APPENDIX F

THE OPTIMIZED KINETIC MODEL FOR THE FOKKER-PLANCK COLLISION OPERATOR

In this appendix the derivation of the optimized kinetic model equation for $\lambda(Q,\omega)$, equation (4-53), is given. For the Fokker-Planck collision operator (see equation (4-41)),

$$(1,\ R_{oo}\ M_s\ R_{oo}) = \gamma_o[I_1 - \beta m I_2]\ , \tag{F-1}$$

where[1]

$$I_1 \equiv \int d\vec{v}\ f_o(v)\ R_{oo}(v)\ \vec{\nabla}_v \cdot \vec{\nabla}_v\ R_{oo}(v)\ , \tag{F-2}$$

$$I_2 \equiv \int d\vec{v}\ f_o(v)\ R_{oo}(v)\ \vec{v} \cdot \vec{\nabla}_v\ R_{oo}(v)\ , \tag{F-3}$$

and

$$R_{oo}(v) \equiv [-i\omega + i\vec{Q}\cdot\vec{v} - \lambda(Q,\omega)]^{-1}\ . \tag{F-4}$$

Here, use will be made of the recurrence relation

$$(1,\ R_{oo}^{\ N}\ 1) = \left(\frac{1}{N-1}\right)\left(\frac{\beta m}{Q^2}\right)\ [(1,\ R_{oo}^{\ N-2}\ 1) + (i\omega+\lambda)(1,\ R_{oo}^{\ N-1}\ 1)]. \tag{F-5}$$

The integral I_1 is readily evaluated by integration by parts,

$$I_1 = f_o(v)\ R_{oo}(v)\ \vec{A}(v)\ \Bigg|_{v=-\infty}^{v=+\infty} - \int d\vec{v}\ \vec{A}(v)\cdot\vec{\nabla}_v\ f_o(v)\ R_{oo}(v)\ , \tag{F-6}$$

---

[1] Note: $f_o(v) \equiv \left(\frac{m}{2\pi kT}\right)^{3/2} e^{-\frac{mv^2}{2kT}}$.

where $\vec{A}(v)$ has been defined as

$$\vec{A}(v) \equiv \vec{\nabla}_v R_{oo}(v) \ . \tag{F-7}$$

Since the surface integral vanishes, I_1 reduces to

$$I_1 = - \int d\vec{v} \ \vec{A}(v) \cdot \vec{\nabla}_v f_o(v) R_{oo}(v) \ . \tag{F-8}$$

However,

$$\vec{\nabla}_v f_o(v) R_{oo}(v) = R_{oo} \vec{\nabla}_v f_o(v) + f_o(v) \vec{\nabla}_v R_{oo}(v)$$

$$= -\beta m f_o(v) R_{oo}(v) \vec{v} + f_o(v) \vec{\nabla}_v R_{oo}(v) \ , \tag{F-9}$$

so that I_1 becomes

$$I_1 = \beta m I_2 - \int dv f_o(v) (\vec{\nabla}_v R_{oo}(v)) \cdot (\vec{\nabla}_v R_{oo}(v)) \ , \tag{F-10}$$

where the definition for I_2, equation (F-3), has been introduced. Then,

$$(1, R_{oo} M_s R_{oo}) = - \gamma_o \int d\vec{v} f_o(v) (\vec{\nabla}_v R_{oo}(v)) \cdot (\vec{\nabla}_v R_{oo}(v)) \ ,$$

or

$$(1, R_{oo} M_s R_{oo}) = \gamma_o Q^2 (1, R_{oo}^4 1) \ . \tag{F-11}$$

Successive application of equation (F-5) yields the desired result:

$$(1, R_{oo} M_s R_{oo}) = \frac{\gamma_o}{3} \left(\frac{\beta m}{Q}\right)^2 [1 - z^2 + (\frac{3}{2} - z^2) z \Phi(z)]. \tag{F-12}$$

The denominator is readily evaluated by writing

$$(1, R_{oo}[1 - P_1] R_{oo} 1) = (1, R_{oo}^2 1) - (1, R_{oo} 1)^2 \ . \tag{F-13}$$

Use of equation (F-5) yields

$$(1,\ R_{oo}{}^{2}\ 1) = \left(\frac{\beta m}{Q^2}\right)\ [1 + z\ \Phi\ (z)] \tag{F-14}$$

and

$$(1,\ R_{oo}\ 1)^2 = -\ \left(\frac{\beta m}{Q^2}\right)\ \frac{\Phi(z)}{z}\ , \tag{F-15}$$

so that

$$(1,\ R_{oo}[1-P_1]\ R_{oo}\ 1) = \left(\frac{\beta m}{Q^2}\right)\ [1 + z\ \Phi\ (z) + \frac{1}{2}\ \Phi^2(z)]. \tag{F-16}$$

Substituting equation (F-12) for $(1,\ R_{oo}\ M_s\ R_{oo})$ and equation (F-16) for $(1,\ R_{oo}[1-P_1]\ R_{oo}\ 1)$ into equation (4-52) yields equation (4-53) for $\lambda(Q,\omega)$.

APPENDIX G

THE OPTIMIZED KINETIC MODEL FOR THE BOLTZMANN-LORENTZ COLLISION OPERATOR

G.1 Evaluation of $(1, R_{oo} M_s R_{oo} 1)$

For convenience, the expressions for R_{oo} and M_s are written below:

$$R_{oo} = [-i\omega + \frac{\vec{Q}\cdot\vec{p}}{m} - \lambda(Q,\omega)]^{-1} , \tag{G-1}$$

$$M_s\, b(p) \equiv \rho \int d\vec{p}_2\, f_o(p_1)\, f_o(p_2) \int d\Omega \left|\frac{\vec{p}_1-\vec{p}_2}{m}\right| \cdot \hat{r}_o$$

$$\times\, [b(p_1) - b(p_1')] , \tag{G-2}$$

and the integral $I(Q,\omega)$ is defined[1] as

$$I(Q,\omega) \equiv (1, R_{oo} M_s R_{oo}) . \tag{G-3}$$

Making the change in variables

$$\vec{g} \equiv \vec{v}_1 - \vec{v}_2 ,$$
$$\vec{G} \equiv \frac{\vec{v}_1 + \vec{v}_2}{2} , \tag{G-4}$$

leads to the following expression for $I(Q,\omega)$:

$$I(Q,\omega) = I_1(Q,\omega) + I_2(Q,\omega) , \tag{G-5}$$

---

[1]Note: Equation (6-3) is not to be confused with equation (3-37).

with

$$I_1(Q,\omega) \equiv -\frac{2\rho}{\pi^3} \int d\vec{G}\, e^{-G^2} \int d\vec{g}\, |\vec{g}|\, e^{-g^2} \int_0^{r_o} dbb \int_0^{2\pi} d\varepsilon \left[\frac{1}{z+\vec{Q}\cdot\vec{G}}\right]^2 , \tag{G-6}$$

and

$$I_2(Q,\omega) \equiv \frac{2\rho}{\pi^3} \int d\vec{G}\, e^{-G^2} \int d\vec{g}\, |\vec{g}|\, e^{-g^2} \int_0^{r_o} dbb \int_0^{2\pi} d\varepsilon$$

$$\times \left[\frac{1}{z+\vec{Q}\cdot\vec{G}}\right] \left[\frac{1}{z+\vec{Q}\cdot\vec{G}}\right] . \tag{G-7}$$

The variable z is defined as

$$z \equiv -z + \vec{Q}\cdot\vec{g} \tag{G-8}$$

with

$$z \equiv \omega - i\lambda \quad . \tag{G-9}$$

Begin by considering $I_1(Q,\omega)$. The integrations over b and ε can be performed immediately, and the change to polar coordinates reduces $I_1(Q,\omega)$ to

$$I_1(Q,\omega) = -\frac{2\rho\, r_o^2}{\pi^2} \int_0^{\infty} dg\, g^3\, e^{-g^2} \int_0^{2\pi} d\phi_g \int_{-1}^{+1} dx_g$$

$$\int_0^{\infty} dG\, G^2\, e^{-G^2} \int_0^{\infty} d\phi_G \int_{-1}^{+1} dx_G \left[\frac{1}{z + QGx_G}\right]^2 , \tag{G-10}$$

where

$$\vec{Q}\cdot\vec{G} = QG \cos\theta_G ,$$

$$\vec{Q}\cdot\vec{g} = Qg \cos\theta_g , \tag{G-11}$$

and $x_i \equiv \cos\theta_i$ for i=g,G. The integrations over ϕ_g and ϕ_G are trivial, and

$$\int_{-1}^{+1} dx \left[\frac{1}{z + QG\, x}\right]^2 = -\frac{1}{QG}\left[\frac{1}{z + QG} - \frac{1}{z - QG}\right] , \tag{G-12}$$

so that

$$I_1(Q,\omega) = \frac{8\rho\ r_\Omega^2}{Q} \int_0^\infty dg\ g^3\ e^{-g^2} \int_{-1}^{+1} dx_g \int_0^\infty dGG\ e^{-G^2} [\frac{1}{z+QG} - \frac{1}{z-QG}] . \tag{G-13}$$

Next, note that

$$\int_{-1}^{+1} dx_g\ [\frac{1}{z+QG}] = \frac{1}{Qg}\ \ln[\frac{-z + QG + Qg}{-z - QG - Qg}] \tag{G-14}$$

and integration by parts yields

$$\int_0^\infty dGG\ e^{-G^2}\ \ln[z + QG] = \frac{Q}{2} \int_0^\infty dG\ \frac{e^{-G^2}}{z+QG} \quad , \tag{G-15}$$

so that $I_1(Q,\omega)$ takes on the desired form:

$$I_1(Q,\omega) = \frac{4\rho\ r_\Omega^2}{Q^2 v_o} \int_0^\infty dg\ g^2\ e^{-g^2} \int_0^\infty dG\ e^{-G^2}$$

$$\times\ [\frac{1}{G-z_-} + \frac{1}{G+z_+} - \frac{1}{G-z_+} - \frac{1}{G+z_-}] \ , \tag{G-16}$$

where

$$z_+ \equiv \frac{z+Qg}{Q}$$

and (G-17)

$$z_- \equiv \frac{z-Qg}{Q} \quad .$$

Further rearrangement of $I_1(Q,\omega)$ is possible, but equation (G-16) is best suited for numerical evaluation.

The reduction of $I_2(Q,\omega)$ is somewhat more involved. Begin by noting

$$[\frac{1}{z+\vec{Q}\cdot\vec{G}}]\ [\frac{1}{z'+\vec{Q}\cdot\vec{G}}] = (z'-z)^{-1}[\frac{1}{z+\vec{Q}\cdot\vec{G}} - \frac{1}{z'+\vec{Q}\cdot\vec{G}}] \quad , \tag{G-18}$$

and hence

$$I_2(Q,\omega) = \frac{2\rho}{\pi^3 v_o} \int_0^{r_o} dbb \int_0^{2\pi} d\varepsilon \int d\vec{g}\ |\vec{g}|\ e^{-g^2} \int d\vec{G}\ e^{-G^2}$$

$$\times\ (z'-z)^{-1} \left[\frac{1}{z+\vec{Q}\cdot\vec{G}} - \frac{1}{z'+\vec{Q}\cdot\vec{G}}\right] . \qquad \text{(G-19)}$$

The integration over $\vec{G}$ is done in the same manner as before, with the result

$$I_2(Q,\omega) = \frac{2\rho}{\pi^2 v_o} \int_{-\infty}^{+\infty} dG\ e^{-G^2} \int_0^{r_o} dbb \int_0^{2\pi} d\varepsilon \int d\vec{g}\vec{g}\ e^{-g^2} \left[\frac{1}{y+\vec{Q}\cdot\vec{g}}\right] \left[\frac{1}{y+\vec{Q}\cdot\vec{g}'}\right] , \qquad \text{(G-20)}$$

where the variable y has been defined as

$$y \equiv -z + QG . \qquad \text{(G-21)}$$

Expanding $(y+\vec{Q}\cdot\vec{g}')^{-1}$ in terms of Legendre polynomials,

$$\frac{1}{y+\vec{Q}\cdot\vec{g}'} = \sum_{\ell=o}^{\infty} A_\ell\ P_\ell\ (\hat{Q}\cdot\hat{g}') , \qquad \text{(G-22)}$$

with

$$A_\ell \equiv -\frac{(2\ell+1)}{Qg}\ \bar{Q}_\ell\ \left(\frac{-y}{Qg}\right) , \qquad \text{(G-23)}$$

leads to the following expression for $I_2(Q,\omega)$:

$$I_2(Q,\omega) = \frac{2\rho}{\pi^2 v_o} \sum_{\ell=o}^{\infty} \int_{-\infty}^{+\infty} dG\ e^{-G^2} \int d\vec{g}\vec{g}\ e^{-g^2} \left[\frac{1}{y+\vec{Q}\cdot\vec{g}}\right]$$

$$A_\ell(g,G)\ P_\ell(\hat{Q}\cdot\hat{g}) \int_0^{r_o} dbb \int_0^{2\pi} d\varepsilon\ P_\ell(\hat{g}\cdot\hat{g}') . \qquad \text{(G-24)}$$

Use has been made of the addition theorem:

$$P_\ell(\hat{Q}\cdot\hat{g}') = P_\ell(\hat{Q}\cdot\hat{g})\ P_\ell(\hat{g}\cdot\hat{g}') + O(e^{im\varepsilon}) , \qquad \text{(G-25)}$$

with $O(e^{im\varepsilon})$ vanishing for $\ell=o$.

From Figure G-1,

$$\hat{g}\cdot\hat{g}' = \cos(180-2\theta g) \ , \tag{G-26}$$

$$\sin\theta g = \frac{b}{r_o}$$

and

$$\cos\theta g = \left(1 - \frac{b^2}{r_o^2}\right)^{\frac{1}{2}} \ ,$$

so that equation (G-24) for $I_2(Q,\omega)$ becomes, after integrating over ε,

$$I_2(Q,\omega) = \frac{4\rho}{\pi^2 v_o} \sum_{\ell=o}^{\infty} \int_{-\infty}^{+\infty} dG\ e^{-G^2} \int d\vec{g}\vec{g}\ e^{-g^2}$$

$$\times \left[\frac{1}{y+\vec{Q}\cdot\vec{g}}\right] A_\ell(g,G)\ P_\ell(\hat{Q}\cdot\hat{g}) \int_0^{r_o} dbb\ P_\ell(\hat{g}\cdot\hat{g}') \ . \tag{G-28}$$

But,

$$P_\ell(\hat{g}\cdot\hat{g}') = P_\ell\left(\frac{2b^2}{r_o^2} - 1\right) \ , \tag{G-29}$$

so that, making the change of variables

$$x \equiv \left(1 - \frac{2b^2}{r_o^2}\right)$$

gives

$$\int_0^{r_o} dbb\ P_\ell(\hat{g}\cdot\hat{g}') = \frac{r_o^2}{4} \int_{-1}^{+1} dx\ P_\ell(x) \ , \tag{G-30}$$

or, from the orthogonality condition on $P_\ell(x)$,

$$\int_0^{r_o} dbb\ P_\ell(\hat{g}\cdot\hat{g}') = \frac{r_o^2}{2}\ \delta_{o\ell} \ . \tag{G-31}$$

Substituting for $\bar{Q}_o(x)$

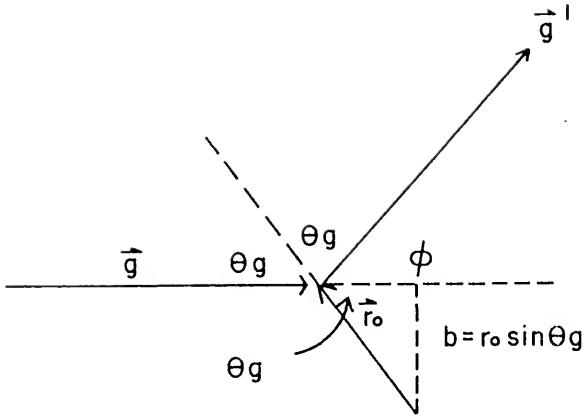

Figure G-1. Binary collision geometry.

$$A_o\left(\frac{-y}{Qg}\right) = \frac{1}{2Qg}\,\ell n\left(\frac{y + Qg}{y - Qg}\right) , \tag{G-32}$$

and substitution of equation (G-32) into equation (G-29) gives the final result for $I_2(Q,\omega)$:

$$I_2(Q,\omega) = \frac{2\rho\, r_o^2}{Q^2\, v_o} \int_0^\infty dG\; e^{-G^2} \int_0^\infty dgg\; e^{-g^2}\; [F_1^2(Q,\omega) + F_2^2(Q,\omega)] , \tag{G-33}$$

with

$$F_1(Q,\omega) \equiv \ell n\left(\frac{G + z_-}{G + z_+}\right) ,$$

$$F_2(Q,\omega) \equiv \ell n\left(\frac{G - z_-}{G - z_+}\right) ,$$

$$z_+ \equiv z + g \quad ,$$

$$z_- \equiv z - g \quad ,$$

and

$$z \equiv \frac{\omega - i\lambda}{Q\, v_o} \quad . \tag{G-34}$$

Note the absence of the factor of $\sqrt{2}$ in the expression for z.

The denominator,

$$(1,\; R_{oo}\; [1-P_1]\; R_{oo}\; 1) ,$$

is the same as for the Fokker-Planck collision operator and is given by equation (F-16).

G.2 Large Z expansion of $\lambda(Q,\omega)$

Begin by considering $I_1^*(Q,\omega)$ in the form

$$I_1^* \equiv -4 \int_0^\infty dgg^2\; e^{-g^2} \int_{-\infty}^{+\infty} dG\; e^{-G^2}\; \left[\frac{1}{G-z_+} - \frac{1}{G-z_-}\right] \quad . \tag{G-35}$$

A direct expansion of $(G-z_+)^{-1}$ and $(G-z_-)^{-1}$ in z leads to

$$I_1^*(Q,\omega) = -\frac{4}{z} \sum_{i=1}^{\infty} \left(\frac{1}{z}\right)^i \int_0^{\infty} dg g^2 e^{-g^2} \int_{-\infty}^{+\infty} dG\, e^{-G^2} (x_+^i - x_-^i) \ , \tag{G-36}$$

where x_+ and x_- are defined as

$$x_+^i \equiv (G+g)^i$$

and

$$x_-^i \equiv (G-g)^i \ . \tag{G-37}$$

Using the binomial theorem, it is easy to show

$$x_+^i - x_-^i = 2 \sum_{\substack{j=1 \\ j \text{ odd}}}^{i} \binom{i}{j} g^j G^{i-j} \ , \tag{G-38}$$

so that $I_1^*(Q,\omega)$ becomes

$$I_1^*(Q,\omega) = -\frac{8}{z} \sum_{i=1}^{\infty} \left(\frac{1}{z}\right)^i \sum_{\substack{j=1 \\ j \text{ odd}}}^{i} \binom{i}{j} \left[\int_0^{\infty} dg\, e^{-g^2} g^{j+2} \right] \times \left[\int_{-\infty}^{+\infty} dG\, e^{-G^2} G^{i-j} \right] \ . \tag{G-39}$$

Note that

$$\int_0^{\infty} dx\, e^{-x^2} x^N = \begin{cases} \dfrac{(N-1,2)!}{2^{\frac{N+2}{2}}} \sqrt{\pi} & N \text{ even} \\[2ex] \dfrac{(N-1,2)!}{2^{\frac{N+1}{2}}} & N \text{ odd} \ , \end{cases} \tag{G-40}$$

where $(N,2)! \equiv N(N-2)\ (N-4)\ \ldots\ 1$. The final form for $I_1^*(Q,\omega)$ is:

$$I_1^*(Q,\omega) = -4\sqrt{\pi} \sum_{\substack{i=1 \\ i \text{ odd}}}^{\infty} \left(\frac{1}{\sqrt{2}\, z}\right)^{i+1} \sum_{\substack{j=1 \\ j \text{ odd}}}^{i} \binom{i}{j} (j+1,2)!\ (i-j-1,2)! \tag{G-41}$$

The analysis of $I_2^*(Q,\omega)$ proceeds in a similar fashion. Begin with

$$I_2^*(Q,\omega) = 2\int_0^\infty dgg\ e^{-g^2}\int_{-\infty}^{+\infty} dG\ e^{-G^2}\ [\ell n\ (\frac{G+z_-}{G+z_+})]^2 \tag{G-42}$$

and expand $\ell n(x)$ as

$$\ell n[\frac{G+z_-}{G+z_+}] = \sum_{k=1}^{\infty} \frac{(-1)^{k-1}}{k} (\frac{1}{z})^k\ [x_-^k - x_+^k] \quad . \tag{G-43}$$

Following the same procedure as before leads to the desired expression for $I_2^*(Q,\omega)$:

$$\begin{aligned} I_2^*(Q,\omega) = 4\sqrt{\pi} \sum_{\substack{i=1 \\ i+\ell=\text{even}}}^{\infty} \sum_{\ell=1}^{\infty} (\frac{1}{i\ell}) (\frac{1}{\sqrt{2}\ z})^{i+\ell} \sum_{\substack{j=1 \\ j\ \text{odd}}}^{i} \binom{i}{j} \\ \times \sum_{k=1}^{\ell} \binom{\ell}{k} (j+k,2)!\ (i+\ell-j-k-1,2)! \end{aligned} \tag{G-44}$$

The first few terms of $I_1^*(Q,\omega)$ and $I_2^*(Q,\omega)$ are

$$\begin{aligned} I_1^*(Q,\omega) &= -4\sqrt{\pi}\ (\frac{1}{z})^2 - 14\sqrt{\pi}\ (\frac{1}{z})^4 - \ldots , \\ I_2^*(Q,\omega) &= 4\sqrt{\pi}\ (\frac{1}{z})^2 + \frac{34}{3}\sqrt{\pi}\ (\frac{1}{z})^4 + \ldots , \end{aligned} \tag{G-45}$$

and the leading term in the donominator is $(\frac{1}{z})^4$, so that

$$\lim_{z\to\infty} \lambda(Q,\omega) \to -\frac{8}{3}\sqrt{\pi}\ \rho r_o^2\ v_o\ , \tag{G-46}$$

which is the Boltzmann-Lorentz expression for the self diffusion coefficient:

$$D_s = -\frac{1}{\beta m \lambda}$$

$$= \frac{3}{8}\left(\frac{kT}{\pi m}\right)^{\frac{1}{2}} \frac{1}{\rho r_o^2} \quad . \qquad \text{(G-47)}$$

APPENDIX H

DETAILED DRAWINGS OF THE HIGH PRESSURE XENON SAMPLE VESSEL

This appendix contains detailed drawings of the high pressure xenon sample vessel used in the time-of-flight experiment discussed in Chapters 5 and 6. All dimensions given are in inches.

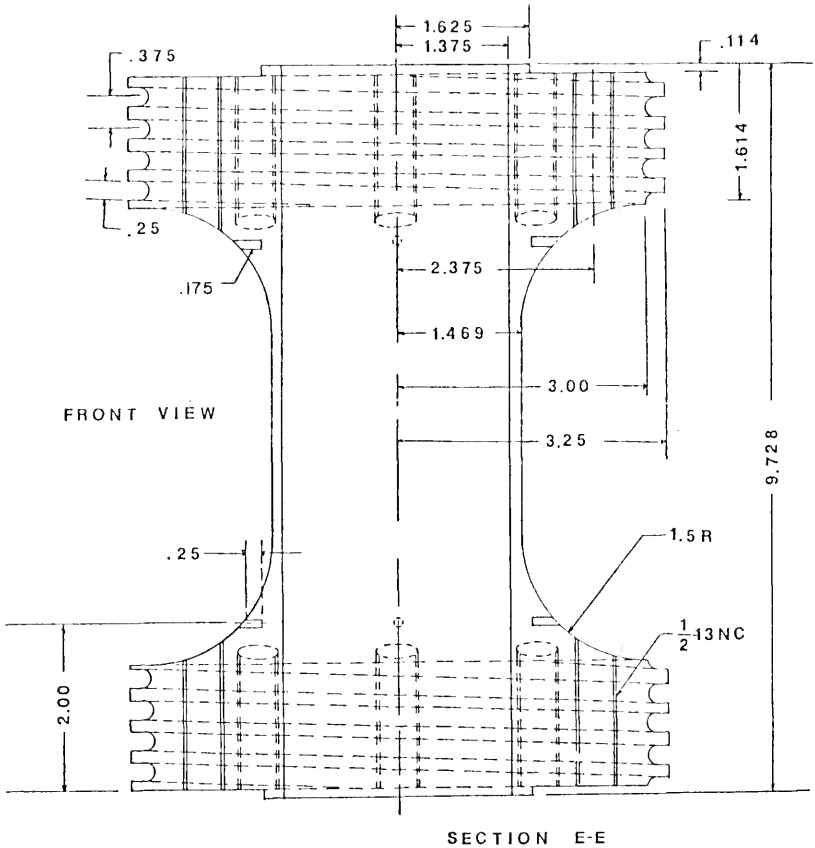

Figure H-1. Front view of sample vessel.

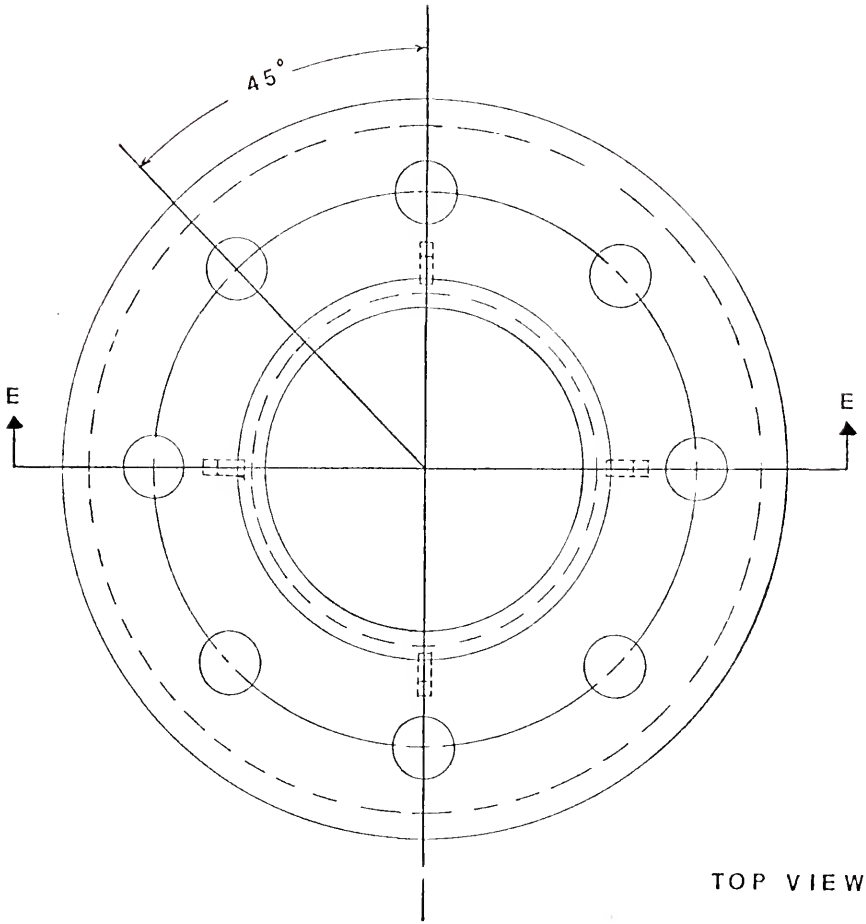

Figure H-2. Top view of sample vessel.

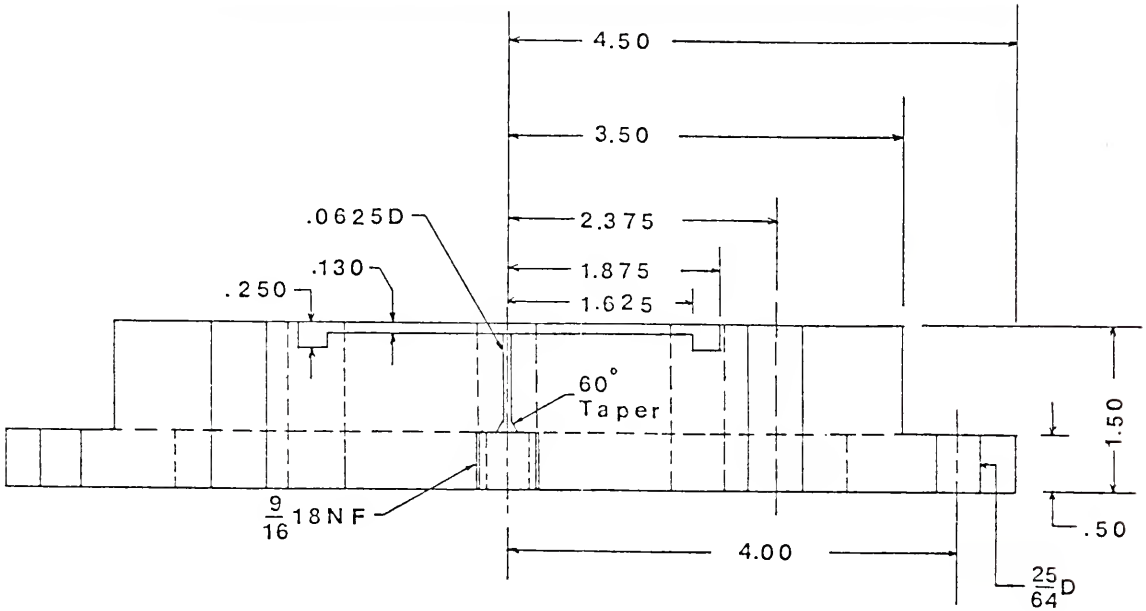

SECTION A-A

END CAP

Figure H-3. Side view of end cap.

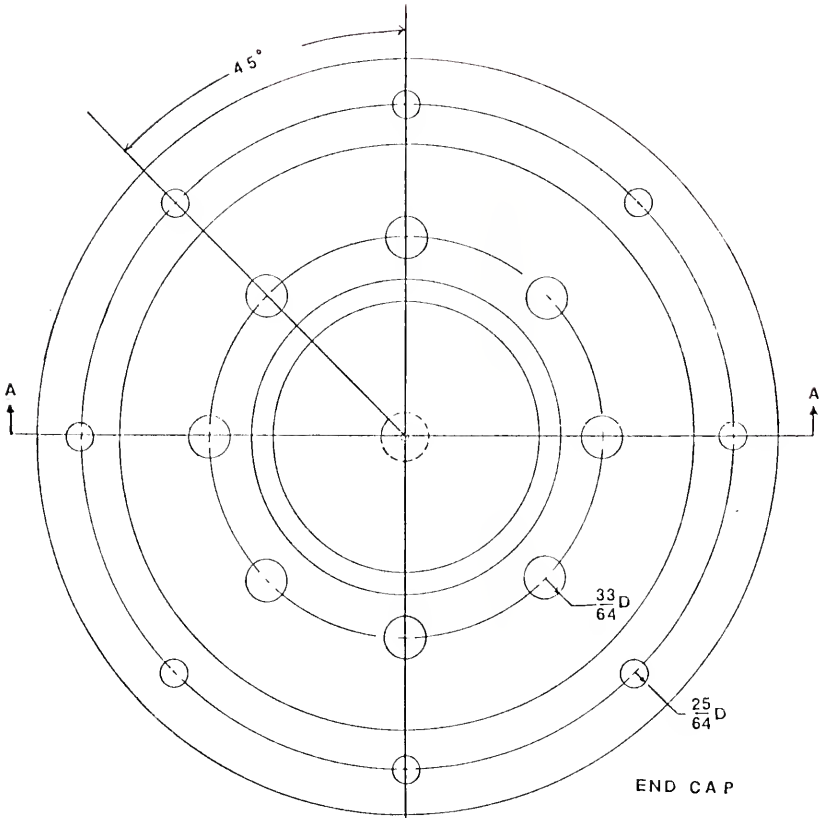

Figure H-4. Top view of end cap.

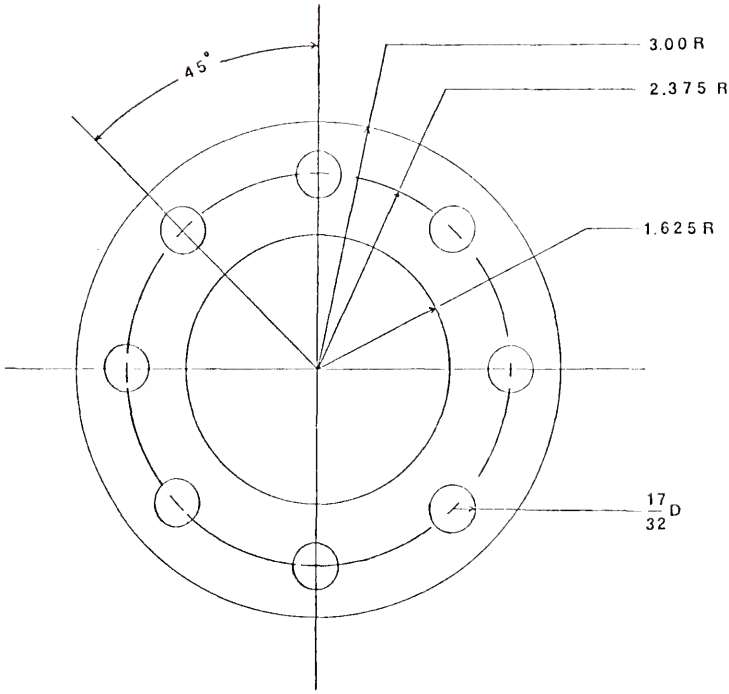

1/8 TOOL STEEL WASHER

Figure H-5. Top view of 1/8 tool steel washer.

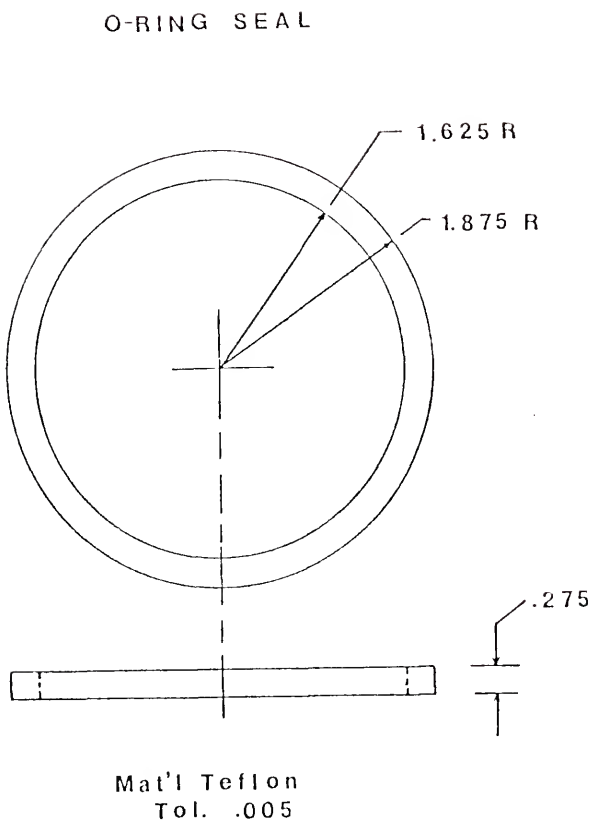

Figure H-6. Top view of Teflon O-ring seal.

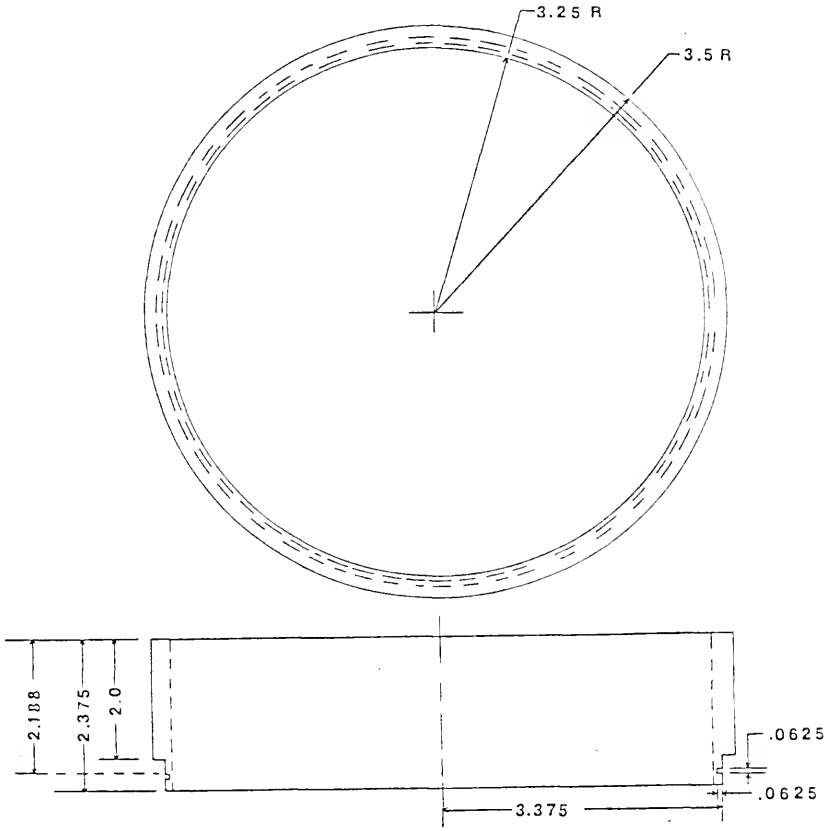

END COVER

Figure H-7. Plastic end cover.

APPENDIX I

SAMPLE HOMOGENIZATION

In this appendix the concept of sample homogenization is discussed. It was assumed in the calculations of Chapter 6 that the sample can be homogenized by determining the total number of atoms present in the total sample volume. For example, the vanadium sample was made by rolling several 0.025 cm thick sheets of vanadium into a spiral of total length 81.3 cm and diameter 6.0 cm. The total number of vanadium atoms in the sample (beam height: 3.5 cm) is then

$$N = \rho \times v$$

$$= 0.705 \times 10^{23} \frac{\text{atoms}}{\text{cm}^3} \times 81.3 \text{ cm} \times 3.5 \text{ cm} \times 0.025 \text{ cm}$$

$$= 5.01 \times 10^{23} \text{ atoms} \quad .$$

The sample is then homogenized, i.e., we assume the sample to be a cylinder with a volume

$$v = \pi R^2 H$$

$$= \pi \times 3.5 \text{ cm} \times (3.0 \text{ cm})^2$$

$$= 98.8 \text{ cm}^3 \quad ,$$

and the effective number density, ρ_{eff}, becomes

$$\rho_{eff} = \frac{N}{V}$$

$$= 0.51 \times 10^{22} \text{ atoms/cm}^3 .$$

The effective number density is used in the evaluation of the absorption correction, $A(\theta,\tau)$. Because of the uncertainty in determining the number of atoms in the sample which actually "see" the neutron beam, a more reliable technique for estimating ρ_{eff}, and thus $A(\theta,\tau)$, is by fitting the experimental transmissions with the theoretical calculation (equation (6-14)), as shown in Figure 6-10. The effective number density for xenon is summarized in Table I-1, and a plot of ρ_{eff} versus the xenon number density appears in Figure I-1. The linear relationship is expected, since the effective number density is found from the relation

$$\rho_{eff} = K_1\rho_{xe} + K_2\rho_{a\ell} , \qquad \text{(I-1)}$$

where K_1 and K_2 are constants. We note that the ρ=o limit (---) in Figure I-1 yields the effective number density for the sample vessel, i.e.,

$$\rho_{eff}^{a\ell} = 0.18 \times 10^{22} \text{ atoms/cc.}$$

TABLE I-1

EFFECTIVE XENON NUMBER DENSITIES.
ALL RUNS AT T = 303 K.

P, atm	$\rho \times 10^{-22}$, atoms/cc	$\rho^*_{eff} \times 10^{-22}$, atoms/cc
51.7	0.184	0.263
57.1	0.226	0.283
62.9	0.279	0.308
66.5	0.330	0.331
72.7	0.450	0.380

*Determined by fitting experimental transmission with the theoretical calculation (equation (6-14)) as shown in Figure 6-10.

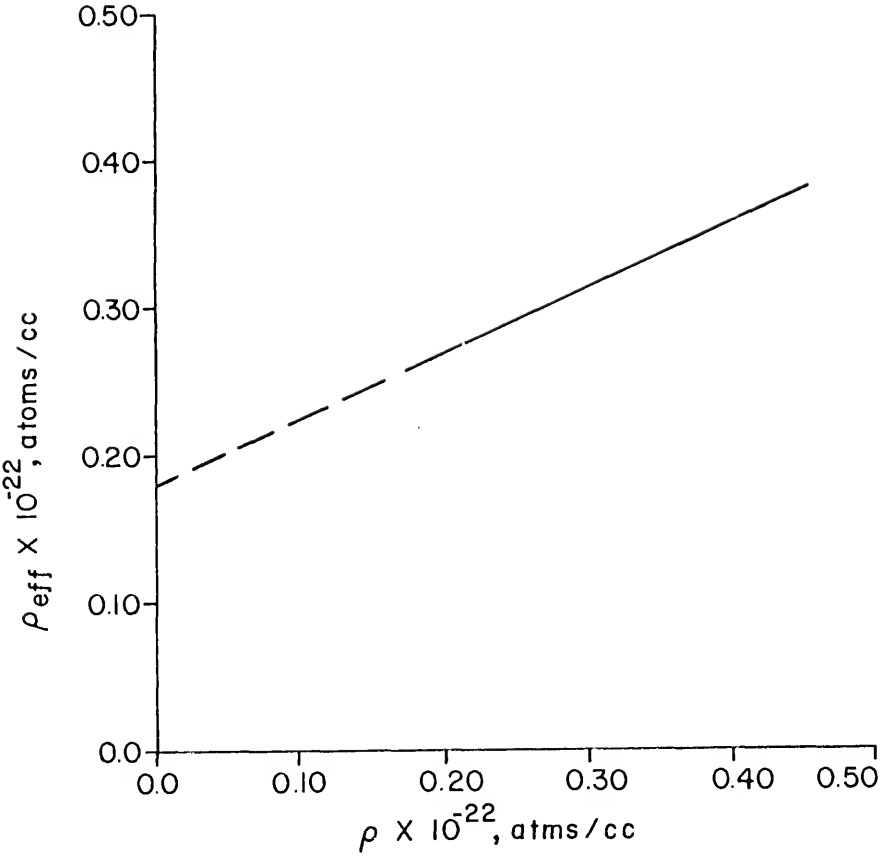

Figure I-1. Xenon effective number density, ρ_{eff}, as a function of the xenon number density, ρ. The extrapolation (---) to $\rho = 0$ yields ρ^{al}_{eff}, the aluminum effective number density.

APPENDIX J

DATA TABLES

In this appendix the experimental measurement of the static structure factor, $S(Q)$, and the dynamic structure factor, $S(Q,\omega)$, where

$$\tilde{S}(Q,\omega) \equiv b^2_{coh}\, S(Q,\omega) + b^2_{incoh}\, S_s(Q,\omega) \ , \qquad (6\text{-}30)$$

are presented in tabular form. Here, $S(Q)$ is normalized to the second node (as discussed in Section 7.2) and $\tilde{S}(Q,\omega)$ satisfies equation (7-8):

$$\int_{-\infty}^{+\infty} d\omega\, \tilde{S}(Q,\omega) = b^2_{coh}\, S_a(Q) + b^2_{incoh} \ , \qquad (7\text{-}8)$$

where

$$S_a(Q) = 1 + \rho * F(Q) \qquad (7\text{-}7)$$

and $F(Q)$ is given in Table 7-2. For xenon,

$$b^2_{coh} = 0.237$$

$$b^2_{incoh} = 0.110.$$

TABLE J-1

THE STATIC STRUCTURE FACTOR, S(Q)

Q, $Å^{-1}$	P=51.7 atm	P=57.1 atm	P=62.9 atm	P=66.5 atm	P=72.7 atm
0.58	0.90	0.83	0.86	0.89	0.79
0.66	0.83	0.89	0.86	0.86	0.82
0.74	0.86	0.85	0.90	0.86	0.84
0.81	0.87	0.90	0.90	0.78	0.86
0.89	0.85	0.93	0.87	0.89	0.76
1.04	0.93	0.94	0.98	0.97	0.99
1.11	0.96	1.04	0.98	1.03	0.96
1.18	0.97	1.08	1.03	1.03	1.05
1.26	0.98	1.05	1.16	1.07	1.02
1.33	1.04	1.11	1.00	1.13	1.11
1.48	1.07	1.14	1.14	1.17	1.26
1.55	1.24	1.30	1.18	1.27	1.26
1.62	1.14	1.17	1.20	1.22	1.27
1.70	1.04	1.09	1.06	1.17	1.24
1.77	1.08	0.99	1.01	1.03	1.11
1.91	1.06	1.04	0.96	0.98	1.13
1.98	1.04	0.97	0.97	1.05	1.01
2.05	1.00	1.05	0.96	0.98	0.91
2.33	1.00	1.06	0.97	0.91	0.96
2.40	0.99	0.95	1.00	0.91	1.03
2.47	0.92	0.94	0.86	0.86	0.88
2.54	0.99	1.00	0.98	1.02	0.97
2.60	0.94	0.97	0.93	0.93	0.90
2.74	0.97	0.99	0.98	1.00	0.93
2.80	0.94	0.99	1.02	0.92	0.92
2.87	0.99	1.04	0.94	0.92	0.91
2.94	1.03	1.03	0.91	0.87	0.95

TABLE J-2

$\tilde{S}(Q,\omega)$: P = 51.7 atm, ρ = 3.08 mole/liter, T = 303 K (Run 1)

Q	0.58	0.66	0.74	0.81	0.89	1.04
S(Q)	0.877	0.871	0.872	0.878	0.902	0.949
w*10**-13			S(Q,w)*10**13			
0.851	0.020	-0.015	0.023	0.026	0.004	0.013
0.805	0.041	0.018	0.019	0.012	0.020	0.026
0.557	0.029	0.053	0.029	-0.007	0.026	0.039
0.511	0.026	0.036	0.032	0.008	0.038	0.055
0.467	0.030	-0.012	0.033	0.025	0.023	0.053
0.425	0.003	0.012	0.049	0.031	0.015	0.062
0.380	0.007	0.004	0.027	0.029	-0.016	0.062
0.339	0.006	-0.020	-0.007	0.030	-0.005	0.013
0.298	0.003	0.021	0.028	0.030	0.043	0.014
0.258	-0.018	0.025	0.067	0.107	0.067	0.077
0.219	0.023	0.073	0.085	0.104	0.096	0.143
0.180	0.127	0.172	0.187	0.186	0.185	0.300
0.143	0.313	0.372	0.399	0.415	0.438	0.512
0.106	0.623	0.711	0.651	0.679	0.792	0.737
0.070	1.064	1.094	1.027	0.961	1.175	0.972
0.035	1.460	1.379	1.324	1.269	1.435	1.175
0.0	1.596	1.523	1.404	1.435	1.459	1.296
-0.034	1.497	1.487	1.293	1.342	1.374	1.234
-0.067	1.078	1.159	0.973	1.050	1.098	0.980
-0.100	0.645	0.686	0.678	0.632	0.713	0.776
-0.132	0.469	0.320	0.470	0.391	0.469	0.511
-0.165	0.265	0.121	0.257	0.233	0.250	0.358
-0.194	0.075	0.066	0.051	0.153	0.081	0.190
-0.224	0.087	0.067	-0.027	0.085	0.106	0.099
-0.254	0.060	0.053	-0.051	0.027	0.117	0.070
-0.283	0.016	0.058	-0.058	0.011	0.030	-0.043
-0.311	-0.028	-0.003	0.017	0.015	-0.035	-0.078
-0.339	-0.051	-0.079	0.016	-0.044	-0.015	0.019
-0.367	-0.055	-0.013	-0.022	-0.002	-0.041	0.012
-0.394	-0.028	0.035	-0.040	-0.004	-0.062	0.001
-0.420	0.044	0.046	-0.032	-0.003	0.018	0.052

TABLE J-2 (continued)

G	1.11	1.18	1.25	1.35	1.48	1.55
S(G)	0.995	1.016	1.037	1.069	1.094	1.125
w*10**-13			S(G,w)*10**13			
0.651	-0.037	0.052	-0.021	0.020	0.035	0.036
0.603	0.049	-0.028	-0.003	0.028	0.014	0.040
0.557	0.048	-0.050	0.017	0.022	0.041	0.019
0.511	0.050	-0.015	0.045	0.055	0.054	0.006
0.467	0.041	-0.020	0.037	0.039	-0.033	0.037
0.425	0.019	0.001	0.047	-0.012	-0.045	0.036
0.380	-0.026	0.033	-0.004	-0.016	0.008	-0.010
0.339	-0.042	-0.010	-0.052	0.031	0.025	0.032
0.298	0.000	-0.042	-0.008	0.076	0.033	0.114
0.258	0.109	0.059	0.119	0.136	0.147	0.186
0.219	0.213	0.117	0.263	0.208	0.218	0.213
0.180	0.274	0.262	0.392	0.323	0.347	0.291
0.145	0.500	0.503	0.596	0.569	0.586	0.514
0.106	0.628	0.808	0.821	0.875	0.648	0.785
0.070	1.137	1.093	1.073	1.146	1.100	1.019
0.035	1.365	1.294	1.375	1.321	1.215	1.091
0.0	1.400	1.434	1.469	1.367	1.298	1.066
-0.034	1.255	1.363	1.310	1.322	1.226	1.049
-0.067	0.990	1.104	1.104	1.117	1.060	0.932
-0.100	0.744	0.867	0.850	0.802	0.808	0.687
-0.132	0.574	0.609	0.565	0.520	0.540	0.520
-0.165	0.334	0.372	0.376	0.291	0.417	0.410
-0.194	0.164	0.160	0.235	0.211	0.293	0.312
-0.224	0.147	0.059	0.117	0.185	0.200	0.249
-0.254	0.116	-0.025	0.056	0.115	0.116	0.189
-0.285	-0.001	-0.004	0.014	0.059	0.079	0.114
-0.311	-0.060	0.115	-0.122	-0.005	0.089	0.064
-0.339	-0.069	0.131	-0.160	0.001	0.034	0.125
-0.367	-0.053	0.005	-0.056	-0.072	0.015	0.060
-0.394	-0.060	0.005	-0.051	-0.110	0.041	0.041
-0.420	0.013	0.060	0.038	-0.025	0.039	0.150

TABLE J-2 (continued)

G	1.62	1.70	1.77	1.91	1.98	2.05
S(G)	1.129	1.098	1.082	1.041	1.012	1.008
w*10**-13			S(G,w)*10**13			
0.651	0.036	0.009	-0.001	-0.051	0.017	-0.018
0.605	0.080	0.016	-0.021	-0.016	0.035	-0.053
0.557	0.056	-0.012	0.021	-0.016	0.015	-0.037
0.511	0.052	-0.027	0.009	-0.005	-0.026	-0.016
0.467	0.053	-0.043	-0.006	0.035	-0.025	0.003
0.425	0.022	-0.014	-0.014	0.056	0.011	0.010
0.386	-0.001	0.001	-0.003	0.058	0.050	0.046
0.339	0.036	0.009	0.022	0.055	0.049	0.093
0.298	0.112	0.072	0.060	0.105	-0.019	0.072
0.258	0.220	0.127	0.123	0.157	0.146	0.081
0.219	0.317	0.235	0.254	0.204	0.256	0.242
0.180	0.415	0.394	0.455	0.352	0.277	0.403
0.145	0.593	0.623	0.597	0.517	0.524	0.485
0.106	0.657	0.667	0.790	0.726	0.739	0.618
0.070	1.145	1.092	1.021	0.843	0.868	0.825
0.035	1.325	1.219	1.108	0.857	0.924	0.923
0.0	1.274	1.302	1.151	0.991	1.003	0.944
-0.034	1.231	1.286	1.158	0.998	1.067	1.007
-0.067	1.043	1.104	0.998	0.897	0.924	0.962
-0.100	0.722	0.908	0.799	0.813	0.710	0.795
-0.132	0.622	0.725	0.608	0.676	0.575	0.641
-0.165	0.485	0.498	0.431	0.538	0.505	0.502
-0.194	0.253	0.354	0.266	0.379	0.417	0.402
-0.224	0.115	0.220	0.113	0.245	0.360	0.308
-0.254	0.096	0.094	0.073	0.214	0.222	0.187
-0.283	0.142	0.007	0.102	0.175	0.119	0.155
-0.311	0.020	0.012	0.048	0.070	0.130	0.152
-0.339	-0.053	0.086	0.022	0.066	0.237	0.170
-0.367	-0.055	0.059	0.098	0.051	0.300	0.132
-0.394	-0.131	0.045	0.120	0.029	0.092	0.091
-0.420	-0.061	0.071	0.024	0.068	0.068	0.140

TABLE J-2 (continued)

Q	2.35	2.40	2.47	2.54	2.60	2.74
S(Q)	0.989	0.984	0.981	0.980	0.980	0.978
w*10**-13			S(Q,w)*10**13			
0.051	-0.001	0.017	0.002	-0.003	-0.009	-0.018
0.085	-0.042	-0.018	0.040	0.005	-0.045	0.022
0.357	-0.006	0.019	0.061	-0.014	0.054	0.036
0.311	-0.023	0.043	0.026	-0.035	0.017	0.012
0.407	0.011	0.014	0.017	0.027	-0.006	-0.025
0.423	0.056	0.027	0.034	0.053	-0.001	-0.016
0.380	0.055	0.019	0.071	0.046	0.045	0.070
0.339	0.078	0.080	0.180	0.100	0.156	0.088
0.298	0.165	0.235	0.231	0.122	0.173	0.141
0.258	0.221	0.306	0.195	0.190	0.320	0.250
0.219	0.249	0.276	0.246	0.356	0.473	0.325
0.180	0.330	0.321	0.376	0.420	0.482	0.500
0.145	0.475	0.478	0.468	0.571	0.504	0.571
0.106	0.622	0.667	0.595	0.749	0.621	0.689
0.070	0.737	0.701	0.635	0.742	0.788	0.738
0.035	0.865	0.676	0.713	0.718	0.881	0.692
0.0	0.840	0.771	0.775	0.805	0.855	0.699
-0.034	0.814	0.805	0.794	0.791	0.786	0.682
-0.067	0.813	0.769	0.840	0.709	0.787	0.660
-0.100	0.639	0.713	0.738	0.666	0.825	0.604
-0.132	0.556	0.608	0.658	0.639	0.682	0.593
-0.165	0.494	0.556	0.566	0.567	0.488	0.613
-0.194	0.424	0.449	0.467	0.450	0.359	0.522
-0.224	0.352	0.293	0.330	0.394	0.359	0.439
-0.254	0.195	0.256	0.165	0.346	0.311	0.366
-0.283	0.143	0.296	0.149	0.314	0.231	0.252
-0.311	0.230	0.227	0.171	0.186	0.243	0.214
-0.339	0.239	0.175	0.153	0.031	0.191	0.222
-0.367	0.165	0.194	0.069	0.176	0.145	0.187
-0.394	0.138	0.179	0.121	0.209	0.076	0.209
-0.420	0.064	0.169	0.182	0.017	0.043	0.222

TABLE J-2 (continued)

G	2.80	2.87	2.94
S(G)	0.977	0.978	0.980
*10**-15		S(G,*)*10**13	
0.651	-0.019	-0.048	-0.002
0.605	0.008	0.026	-0.006
0.557	-0.004	0.064	-0.009
0.511	-0.003	0.023	-0.017
0.467	-0.004	-0.003	-0.002
0.425	0.058	0.020	0.012
0.380	0.078	0.055	0.048
0.339	0.117	0.133	0.132
0.298	0.166	0.190	0.156
0.258	0.192	0.248	0.220
0.219	0.267	0.361	0.309
0.180	0.440	0.442	0.377
0.143	0.533	0.470	0.448
0.106	0.680	0.607	0.519
0.070	0.822	0.697	0.624
0.035	0.803	0.742	0.706
0.0	0.773	0.734	0.705
-0.034	0.786	0.678	0.669
-0.067	0.749	0.646	0.684
-0.100	0.716	0.650	0.652
-0.132	0.652	0.626	0.562
-0.165	0.551	0.498	0.412
-0.194	0.502	0.393	0.361
-0.224	0.381	0.324	0.394
-0.254	0.286	0.277	0.301
-0.283	0.244	0.198	0.228
-0.311	0.199	0.147	0.218
-0.339	0.254	0.220	0.251
-0.367	0.304	0.250	0.209
-0.394	0.277	0.232	0.131
-0.420	0.142	0.079	0.138

TABLE J-3

$\tilde{S}(Q,\omega)$: P = 51.7 atm, ρ = 3.08 mole/liter, T = 303 K (Run 2)

Q	0.58	0.66	0.74	0.81	0.89	1.04
S(Q)	0.877	0.871	0.872	0.878	0.902	0.949
*10**-13			S(Q,ω)*10**13			
0.651	0.013	-0.022	0.022	0.010	0.004	0.020
0.603	0.017	0.046	-0.001	-0.005	0.010	0.029
0.557	0.018	0.051	-0.015	0.007	0.018	0.018
0.511	0.000	0.036	0.000	0.020	0.020	0.029
0.467	0.030	0.009	0.020	0.014	0.022	0.030
0.423	0.033	0.021	0.022	0.010	0.023	0.039
0.380	-0.013	0.025	0.052	0.005	0.023	0.053
0.339	0.016	-0.017	0.058	-0.010	0.030	0.036
0.298	0.015	-0.034	-0.003	-0.001	0.028	0.025
0.258	-0.033	-0.027	0.028	-0.005	0.003	0.038
0.219	-0.052	0.021	0.061	0.023	-0.015	0.076
0.180	0.040	0.083	0.119	0.126	0.083	0.199
0.143	0.229	0.202	0.323	0.325	0.323	0.449
0.105	0.566	0.605	0.658	0.591	0.710	0.756
0.070	1.067	1.026	1.080	1.052	1.118	1.047
0.035	1.423	1.371	1.436	1.530	1.378	1.303
0.0	1.563	1.542	1.551	1.485	1.488	1.413
-0.034	1.470	1.435	1.381	1.397	1.417	1.289
-0.067	1.144	1.168	1.047	1.023	1.057	1.014
-0.100	0.756	0.753	0.734	0.640	0.665	0.737
-0.132	0.415	0.442	0.462	0.428	0.408	0.531
-0.163	0.198	0.192	0.240	0.316	0.237	0.371
-0.194	0.126	0.039	0.140	0.169	0.180	0.178
-0.224	0.107	0.020	0.109	0.084	0.165	0.052
-0.254	0.048	0.061	0.035	0.040	0.169	0.071
-0.283	0.050	0.043	0.052	0.033	0.102	0.038
-0.311	0.004	0.032	0.025	0.082	0.019	-0.002
-0.339	-0.007	0.072	-0.047	0.073	0.050	0.032
-0.367	-0.067	0.013	-0.074	0.053	0.000	0.026
-0.394	-0.075	0.000	-0.095	0.080	-0.068	0.024
-0.420	0.051	0.003	0.014	0.103	-0.030	0.049

TABLE J-3 (continued)

Q	1.11	1.18	1.25	1.33	1.48	1.55
S(Q)	0.995	1.016	1.037	1.069	1.094	1.125
*#10**-13			S(Q,*)#10**13			
0.651	0.004	-0.022	0.050	-0.007	-0.014	0.045
0.603	0.040	-0.001	0.057	0.004	-0.005	0.004
0.557	0.027	-0.000	-0.004	0.004	0.023	-0.019
0.511	-0.026	-0.012	-0.013	0.033	-0.005	-0.010
0.467	-0.021	0.017	0.043	0.087	-0.003	0.016
0.423	0.022	0.051	0.077	0.058	0.055	0.079
0.380	-0.010	0.018	0.014	-0.027	0.057	0.077
0.339	-0.023	-0.016	-0.036	0.026	0.034	0.047
0.298	0.002	-0.009	-0.007	0.065	0.031	0.085
0.258	0.051	0.008	0.074	0.057	0.077	0.161
0.219	0.135	0.110	0.176	0.105	0.144	0.155
0.180	0.257	0.270	0.307	0.258	0.287	0.254
0.143	0.500	0.483	0.532	0.523	0.520	0.465
0.105	0.800	0.802	0.880	0.829	0.811	0.732
0.070	1.131	1.104	1.159	1.162	1.069	1.069
0.035	1.387	1.362	1.349	1.388	1.273	1.292
0.0	1.381	1.453	1.489	1.446	1.381	1.353
-0.034	1.287	1.332	1.400	1.319	1.247	1.233
-0.067	1.109	1.072	1.165	1.104	1.059	0.964
-0.100	0.817	0.811	0.907	0.873	0.852	0.724
-0.132	0.547	0.588	0.595	0.578	0.627	0.603
-0.163	0.332	0.381	0.363	0.307	0.500	0.499
-0.194	0.205	0.213	0.219	0.202	0.322	0.363
-0.224	0.154	0.127	0.120	0.186	0.142	0.250
-0.254	0.109	0.063	0.103	0.131	0.077	0.171
-0.283	0.044	0.099	0.082	0.087	0.108	0.123
-0.311	0.019	0.140	0.005	0.037	0.091	0.124
-0.339	0.074	0.053	-0.050	0.041	0.068	0.162
-0.367	0.087	-0.052	-0.041	-0.044	0.013	0.090
-0.394	0.092	-0.028	-0.068	-0.090	0.043	-0.001
-0.420	0.100	0.025	0.024	-0.001	0.062	-0.002

TABLE J-3 (continued)

Q	1.62	1.70	1.77	1.91	1.98	2.05
S(Q)	1.129	1.098	1.062	1.041	1.012	1.008
W*10**-13			S(Q,W)*10**13			
0.651	-0.003	-0.005	0.010	-0.021	0.029	-0.009
0.603	-0.016	0.033	0.007	0.002	0.024	-0.026
0.557	0.015	-0.000	0.020	0.009	-0.004	-0.024
0.511	0.015	-0.022	-0.007	0.013	-0.015	-0.022
0.467	0.018	-0.008	0.006	0.009	-0.007	-0.028
0.423	0.069	0.010	0.002	0.001	0.020	0.016
0.380	0.080	0.009	-0.032	0.036	0.074	0.039
0.339	0.042	0.015	-0.016	0.062	0.110	0.020
0.298	0.043	0.065	0.038	0.092	0.095	0.033
0.258	0.107	0.102	0.114	0.152	0.145	0.151
0.219	0.180	0.177	0.201	0.251	0.225	0.290
0.180	0.348	0.295	0.370	0.396	0.329	0.401
0.143	0.567	0.515	0.533	0.509	0.522	0.553
0.106	0.851	0.805	0.711	0.697	0.673	0.697
0.070	1.163	1.043	0.952	0.895	0.791	0.889
0.035	1.321	1.141	1.101	0.991	0.914	1.043
0.0	1.279	1.158	1.170	1.039	1.002	1.062
-0.034	1.144	1.124	1.183	1.061	0.996	1.049
-0.067	0.973	1.024	1.054	0.990	0.916	1.054
-0.100	0.788	0.923	0.804	0.859	0.776	0.919
-0.132	0.643	0.713	0.566	0.720	0.621	0.702
-0.163	0.499	0.521	0.452	0.551	0.524	0.549
-0.194	0.326	0.433	0.360	0.379	0.390	0.367
-0.224	0.197	0.351	0.236	0.226	0.259	0.241
-0.254	0.137	0.153	0.131	0.133	0.126	0.234
-0.283	0.079	0.043	0.128	0.061	0.043	0.163
-0.311	0.058	0.066	0.052	0.034	0.078	0.076
-0.339	0.057	0.011	0.014	0.022	0.088	0.052
-0.367	0.009	0.035	0.097	0.042	0.067	0.020
-0.394	-0.098	0.059	0.072	0.054	0.016	0.069
-0.420	-0.113	0.042	0.043	0.055	-0.001	0.080

TABLE J-3 (continued)

Q	2.33	2.40	2.47	2.54	2.60	2.74
S(Q)	0.989	0.984	0.981	0.980	0.980	0.978
w*10**-13			S(Q,w)*10**13			
0.651	-0.013	0.005	-0.021	-0.014	0.005	0.003
0.603	-0.036	-0.015	0.004	0.016	-0.015	0.024
0.557	0.005	0.005	0.051	0.013	0.033	0.009
0.511	0.027	-0.011	0.019	-0.008	0.019	0.002
0.467	0.025	0.014	0.005	0.043	0.032	0.020
0.423	0.047	0.029	0.052	0.059	0.055	0.040
0.380	0.040	0.037	0.054	0.064	0.082	0.057
0.339	0.091	0.083	0.109	0.117	0.094	0.092
0.298	0.131	0.173	0.186	0.169	0.156	0.154
0.258	0.210	0.279	0.244	0.213	0.293	0.241
0.219	0.314	0.337	0.329	0.274	0.341	0.320
0.180	0.357	0.417	0.448	0.346	0.427	0.465
0.143	0.502	0.558	0.544	0.513	0.551	0.553
0.106	0.693	0.684	0.655	0.740	0.633	0.625
0.070	0.830	0.737	0.733	0.781	0.711	0.684
0.035	0.886	0.817	0.776	0.707	0.730	0.704
0.0	0.901	0.897	0.862	0.756	0.776	0.731
-0.034	0.908	0.892	0.924	0.795	0.810	0.694
-0.067	0.856	0.817	0.852	0.751	0.763	0.701
-0.100	0.767	0.723	0.738	0.675	0.736	0.677
-0.132	0.592	0.648	0.541	0.600	0.676	0.550
-0.163	0.447	0.583	0.542	0.517	0.522	0.472
-0.194	0.388	0.476	0.462	0.470	0.348	0.400
-0.224	0.308	0.325	0.356	0.392	0.201	0.333
-0.254	0.262	0.267	0.245	0.279	0.163	0.278
-0.283	0.195	0.198	0.132	0.199	0.198	0.198
-0.311	0.127	0.060	0.165	0.136	0.134	0.169
-0.339	0.099	0.112	0.140	0.049	0.062	0.174
-0.367	0.063	0.092	-0.019	0.070	0.078	0.129
-0.394	0.062	0.040	-0.043	0.069	0.125	0.106
-0.420	0.092	0.051	0.015	-0.038	0.062	0.104

TABLE J-3 (continued)

Q	2.80	2.87	2.94
S(Q)	0.977	0.978	0.980

w*10**-13	S(Q,w)*10**13		
0.651	0.038	0.017	-0.028
0.603	0.041	0.025	-0.041
0.557	0.005	0.034	-0.029
0.511	-0.022	0.007	-0.012
0.467	-0.027	0.007	0.018
0.423	0.040	0.024	0.051
0.380	0.095	0.044	0.105
0.339	0.115	0.109	0.152
0.298	0.158	0.192	0.209
0.258	0.239	0.283	0.275
0.219	0.358	0.358	0.348
0.180	0.479	0.457	0.442
0.143	0.578	0.592	0.508
0.106	0.659	0.655	0.616
0.070	0.715	0.655	0.700
0.035	0.721	0.682	0.724
0.0	0.759	0.737	0.744
-0.034	0.844	0.768	0.758
-0.067	0.773	0.728	0.734
-0.100	0.717	0.682	0.681
-0.132	0.676	0.654	0.651
-0.163	0.538	0.553	0.514
-0.194	0.403	0.412	0.332
-0.224	0.358	0.318	0.389
-0.254	0.318	0.307	0.382
-0.283	0.193	0.216	0.244
-0.311	0.123	0.150	0.156
-0.339	0.111	0.145	0.083
-0.367	0.098	0.035	0.039
-0.394	0.109	0.046	0.004
-0.420	0.053	0.064	0.136

TABLE J-4

$\tilde{S}(Q,\omega)$: P = 57.1 atm, ρ = 3.80 mole/liter, T = 303 K

Q	0.58	0.66	0.74	0.81	0.89	1.04
S(Q)	0.851	0.844	0.846	0.853	0.882	0.938
W*10**-13			S(Q,W)*10**13			
0.651	0.013	-0.025	0.022	0.008	0.020	0.015
0.603	0.014	0.030	-0.007	0.024	0.012	0.023
0.557	0.000	0.023	-0.004	0.019	0.017	0.035
0.511	-0.028	-0.029	0.038	-0.002	0.031	0.020
0.467	0.008	-0.010	0.057	0.027	0.011	-0.020
0.423	0.017	0.025	0.045	0.038	0.026	-0.003
0.380	-0.023	0.018	0.059	0.018	-0.004	0.024
0.339	-0.008	0.016	0.043	0.020	-0.020	-0.003
0.298	0.002	0.037	0.027	0.033	0.002	-0.013
0.258	-0.027	0.036	0.017	0.058	-0.017	0.019
0.219	-0.022	0.054	0.042	0.070	0.047	0.075
0.180	0.099	0.073	0.132	0.144	0.178	0.227
0.143	0.298	0.228	0.330	0.340	0.369	0.477
0.106	0.613	0.609	0.587	0.657	0.687	0.737
0.070	1.103	1.014	1.096	1.011	1.008	1.041
0.035	1.479	1.335	1.378	1.315	1.245	1.279
0.0	1.662	1.517	1.530	1.433	1.376	1.377
-0.034	1.584	1.427	1.437	1.294	1.318	1.319
-0.067	1.189	1.103	1.052	1.007	1.038	1.066
-0.100	0.752	0.712	0.678	0.672	0.727	0.768
-0.132	0.414	0.372	0.378	0.451	0.476	0.601
-0.163	0.193	0.153	0.195	0.313	0.283	0.432
-0.194	0.140	0.096	0.188	0.197	0.216	0.200
-0.224	0.109	0.078	0.112	0.107	0.162	0.097
-0.254	0.032	0.072	-0.016	0.056	0.105	0.052
-0.283	0.035	0.031	0.016	0.031	0.083	-0.062
-0.311	-0.010	-0.032	0.037	-0.038	0.074	-0.069
-0.339	-0.006	-0.010	0.066	-0.058	0.088	0.099
-0.367	-0.074	-0.020	0.010	0.016	0.024	0.094
-0.394	-0.020	0.007	-0.093	0.059	-0.034	0.016
-0.420	0.097	0.050	-0.008	0.044	0.030	0.018

TABLE J-4 (continued)

Q	1.11	1.18	1.26	1.33	1.48	1.55
S(Q)	0.994	1.019	1.045	1.083	1.113	1.150
w*10**-13			S(Q,w)*10**13			
0.651	0.021	0.016	0.027	0.023	0.034	0.029
0.503	0.052	-0.030	0.026	0.022	0.065	0.005
0.557	0.033	-0.035	-0.020	-0.012	0.035	0.002
0.511	-0.025	-0.009	-0.050	0.022	0.015	-0.010
0.467	-0.025	0.013	-0.030	0.009	0.022	-0.006
0.423	0.019	0.050	-0.000	0.017	0.021	0.101
0.380	-0.014	0.032	0.000	0.038	0.049	0.130
0.339	-0.001	0.012	-0.008	0.026	0.064	0.052
0.298	0.044	0.005	0.011	0.048	0.008	0.039
0.258	0.049	0.030	0.069	0.053	0.067	0.126
0.219	0.150	0.125	0.149	0.107	0.170	0.210
0.180	0.280	0.222	0.323	0.284	0.274	0.317
0.143	0.465	0.412	0.570	0.535	0.500	0.545
0.106	0.779	0.742	0.858	0.810	0.821	0.799
0.070	1.049	1.041	1.133	1.142	1.114	1.033
0.035	1.250	1.262	1.361	1.394	1.337	1.242
0.0	1.287	1.361	1.440	1.473	1.407	1.313
-0.034	1.170	1.243	1.341	1.336	1.269	1.168
-0.067	1.007	1.086	1.177	1.137	1.102	0.951
-0.100	0.809	0.843	0.905	0.930	0.881	0.752
-0.132	0.605	0.594	0.609	0.600	0.604	0.615
-0.163	0.376	0.422	0.400	0.354	0.402	0.532
-0.194	0.246	0.220	0.265	0.268	0.272	0.371
-0.224	0.163	0.095	0.117	0.133	0.184	0.202
-0.254	0.132	0.059	0.080	0.009	0.091	0.130
-0.283	0.123	0.061	0.057	0.031	0.055	0.069
-0.311	0.072	0.095	-0.009	0.049	0.069	0.035
-0.339	0.055	0.059	0.009	0.072	0.039	0.132
-0.367	-0.038	-0.045	-0.068	0.004	0.016	0.069
-0.394	-0.046	-0.009	-0.114	-0.049	0.024	-0.031
-0.420	0.038	-0.003	-0.009	-0.026	0.002	0.059

TABLE J-4 (continued)

Q	1.62	1.70	1.77	1.91	1.98	2.05
S(Q)	1.156	1.118	1.075	1.049	1.015	1.009
W*10**-13			S(Q,W)*10**13			
0.651	0.005	-0.034	0.004	-0.024	-0.005	-0.008
0.603	0.030	-0.001	0.003	-0.028	0.024	-0.025
0.557	0.041	0.019	0.032	0.010	0.001	-0.016
0.511	0.029	0.002	0.021	0.045	-0.044	0.024
0.467	0.033	0.003	-0.019	0.047	-0.050	0.014
0.423	0.029	0.023	-0.014	0.041	-0.016	0.023
0.380	0.038	0.019	0.016	0.034	0.051	0.071
0.339	0.008	0.034	0.011	0.015	0.077	0.086
0.298	0.013	0.119	0.022	0.058	0.125	0.093
0.258	0.100	0.188	0.119	0.138	0.209	0.145
0.219	0.209	0.228	0.266	0.242	0.227	0.237
0.180	0.385	0.349	0.420	0.409	0.312	0.356
0.143	0.626	0.601	0.549	0.564	0.544	0.515
0.106	0.968	0.871	0.803	0.721	0.749	0.679
0.070	1.255	1.073	1.074	0.917	0.874	0.828
0.035	1.336	1.193	1.202	1.019	0.988	0.965
0.0	1.322	1.277	1.296	1.037	1.092	1.020
-0.034	1.243	1.261	1.269	1.056	1.068	0.987
-0.067	1.030	1.148	1.086	0.997	0.993	0.935
-0.100	0.837	0.955	0.872	0.857	0.876	0.842
-0.132	0.623	0.698	0.654	0.691	0.692	0.716
-0.163	0.447	0.523	0.508	0.584	0.550	0.538
-0.194	0.361	0.363	0.403	0.471	0.415	0.357
-0.224	0.203	0.210	0.204	0.295	0.311	0.292
-0.254	0.084	0.098	0.127	0.197	0.220	0.229
-0.283	0.045	0.061	0.102	0.179	0.122	0.145
-0.311	0.057	0.068	0.047	0.148	0.093	0.126
-0.339	0.008	0.028	0.059	0.130	0.137	0.076
-0.367	-0.087	0.012	0.030	0.040	0.152	0.050
-0.394	-0.132	0.017	-0.053	-0.017	0.083	0.101
-0.420	-0.057	0.025	-0.070	0.033	0.034	0.106

TABLE J-4 (continued)

Q	2.33	2.40	2.47	2.54	2.60	2.74
S(Q)	0.987	0.981	0.977	0.976	0.976	0.974
W*10**-13			S(Q,W)*10**13			
0.651	-0.039	-0.012	-0.015	0.004	-0.030	-0.019
0.603	-0.042	-0.025	0.006	-0.003	-0.022	-0.003
0.557	-0.015	-0.004	0.019	0.005	0.012	-0.004
0.511	0.025	-0.005	-0.001	0.034	0.026	-0.004
0.467	0.032	-0.008	0.035	0.054	0.041	0.023
0.423	0.004	0.023	0.053	0.021	0.045	0.026
0.380	0.040	0.041	0.036	0.048	0.066	0.088
0.339	0.105	0.068	0.077	0.100	0.097	0.147
0.298	0.153	0.131	0.149	0.155	0.143	0.160
0.258	0.193	0.241	0.244	0.196	0.226	0.239
0.219	0.259	0.284	0.316	0.273	0.312	0.321
0.180	0.361	0.373	0.423	0.428	0.426	0.435
0.143	0.514	0.582	0.539	0.532	0.581	0.562
0.106	0.543	0.702	0.647	0.653	0.667	0.642
0.070	0.700	0.759	0.758	0.723	0.705	0.670
0.035	0.824	0.813	0.814	0.745	0.748	0.690
0.0	0.876	0.888	0.909	0.818	0.817	0.707
-0.034	0.805	0.862	0.897	0.769	0.812	0.701
-0.067	0.785	0.814	0.787	0.686	0.721	0.655
-0.100	0.745	0.761	0.717	0.703	0.673	0.638
-0.132	0.623	0.667	0.659	0.660	0.644	0.633
-0.163	0.502	0.590	0.542	0.602	0.603	0.549
-0.194	0.428	0.476	0.445	0.412	0.439	0.461
-0.224	0.351	0.362	0.385	0.365	0.297	0.362
-0.254	0.260	0.287	0.279	0.249	0.244	0.294
-0.283	0.215	0.241	0.234	0.241	0.262	0.282
-0.311	0.248	0.216	0.211	0.230	0.279	0.258
-0.339	0.248	0.189	0.167	0.131	0.183	0.212
-0.367	0.160	0.154	0.179	0.137	0.142	0.188
-0.394	0.118	0.124	0.148	0.185	0.124	0.163
-0.420	0.116	0.080	0.107	0.085	0.079	0.100

TABLE J-4 (continued)

Q	2.80	2.87	2.94
S(Q)	0.972	0.974	0.976
w*10**-13		S(Q,w)*10**13	
0.651	-0.013	-0.033	-0.033
0.603	-0.010	-0.017	-0.006
0.557	0.004	0.004	-0.008
0.511	0.002	0.011	-0.022
0.467	-0.001	0.030	0.037
0.423	0.022	0.052	0.064
0.380	0.055	0.088	0.081
0.339	0.137	0.124	0.125
0.298	0.190	0.173	0.162
0.258	0.214	0.272	0.227
0.219	0.324	0.356	0.307
0.180	0.475	0.415	0.406
0.143	0.571	0.508	0.551
0.106	0.639	0.630	0.662
0.070	0.721	0.673	0.735
0.035	0.779	0.699	0.789
0.0	0.775	0.738	0.833
-0.034	0.719	0.756	0.799
-0.067	0.712	0.736	0.740
-0.100	0.680	0.674	0.704
-0.132	0.580	0.640	0.616
-0.163	0.489	0.527	0.495
-0.194	0.444	0.375	0.386
-0.224	0.410	0.238	0.401
-0.254	0.261	0.266	0.362
-0.283	0.225	0.253	0.287
-0.311	0.198	0.200	0.275
-0.339	0.113	0.238	0.244
-0.367	0.155	0.228	0.209
-0.394	0.135	0.136	0.141
-0.420	0.087	0.132	0.103

TABLE J-5

$\tilde{S}(Q,\omega)$: P = 62.9 atm, ρ = 4.67 mole/liter, T = 303 K

Q	0.58	0.66	0.74	0.81	0.89	1.04
S(Q)	0.881	0.879	0.879	0.879	0.881	0.923
W*10**-13			S(Q,W)*10**13			
0.651	-0.021	-0.027	0.011	0.016	0.006	0.010
0.603	0.015	0.006	0.001	0.014	0.014	0.038
0.557	0.054	0.012	-0.004	0.008	0.036	0.027
0.511	0.020	0.015	0.042	0.029	0.039	0.041
0.467	0.030	0.017	0.045	0.046	0.040	0.057
0.423	0.042	0.004	0.040	-0.011	0.045	0.024
0.380	0.016	0.002	0.039	-0.012	0.029	0.019
0.339	-0.006	-0.013	0.038	0.037	0.020	0.007
0.298	-0.014	-0.025	0.038	0.060	0.048	0.011
0.258	0.017	0.025	0.051	0.084	0.071	0.085
0.219	0.075	0.076	0.101	0.108	0.114	0.163
0.180	0.146	0.132	0.209	0.188	0.220	0.274
0.143	0.277	0.316	0.396	0.382	0.400	0.452
0.106	0.598	0.652	0.630	0.645	0.684	0.693
0.070	1.044	1.025	0.944	0.919	1.037	0.936
0.035	1.355	1.332	1.250	1.186	1.270	1.103
0.0	1.471	1.445	1.359	1.298	1.327	1.198
-0.034	1.371	1.369	1.236	1.194	1.231	1.148
-0.067	1.094	1.118	0.991	0.969	0.999	0.933
-0.100	0.733	0.745	0.657	0.701	0.728	0.689
-0.132	0.432	0.419	0.397	0.470	0.462	0.482
-0.163	0.230	0.269	0.218	0.316	0.245	0.303
-0.194	0.123	0.175	0.126	0.175	0.155	0.205
-0.224	0.080	0.090	0.056	0.066	0.087	0.123
-0.254	0.065	0.043	-0.023	0.017	0.025	0.067
-0.283	0.097	0.016	0.011	0.023	0.062	0.028
-0.311	0.101	0.018	0.017	0.058	0.008	0.004
-0.339	0.031	0.002	0.032	0.053	-0.028	0.055
-0.367	-0.060	0.025	0.022	0.051	0.023	0.058
-0.394	-0.048	0.033	-0.042	0.047	0.026	0.107
-0.420	0.003	0.031	-0.027	0.067	0.062	0.140

TABLE J-5 (continued)

Q	1.11	1.18	1.26	1.33	1.48	1.55
S(Q)	0.993	1.023	1.056	1.103	1.140	1.186
W*10**-13			S(Q,W)*10**13			
0.651	0.003	0.024	-0.017	-0.002	0.026	0.047
0.603	0.045	0.009	0.002	0.034	0.048	0.023
0.557	0.054	0.012	0.033	0.046	0.033	0.024
0.511	0.033	-0.000	0.060	0.042	0.023	0.020
0.467	0.030	-0.017	0.034	0.047	0.034	0.028
0.423	0.011	0.004	-0.004	0.020	0.020	0.066
0.380	-0.011	0.020	-0.007	0.009	-0.011	0.040
0.339	0.014	0.007	0.012	0.012	0.020	0.020
0.298	0.060	0.015	0.032	0.046	0.084	0.047
0.258	0.113	0.063	0.097	0.093	0.114	0.159
0.219	0.230	0.179	0.202	0.177	0.177	0.276
0.180	0.347	0.315	0.333	0.352	0.334	0.369
0.143	0.521	0.498	0.549	0.582	0.517	0.602
0.106	0.778	0.773	0.814	0.884	0.771	0.931
0.070	1.013	1.021	1.066	1.209	1.098	1.205
0.035	1.202	1.226	1.247	1.455	1.351	1.334
0.0	1.270	1.345	1.328	1.554	1.400	1.327
-0.034	1.230	1.252	1.253	1.440	1.277	1.235
-0.067	1.052	1.061	1.047	1.200	1.073	1.071
-0.100	0.762	0.813	0.782	0.915	0.816	0.795
-0.132	0.533	0.553	0.558	0.621	0.581	0.598
-0.163	0.362	0.376	0.360	0.353	0.428	0.490
-0.194	0.246	0.209	0.193	0.251	0.267	0.358
-0.224	0.160	0.126	0.087	0.169	0.141	0.238
-0.254	0.094	0.081	0.071	0.042	0.107	0.125
-0.283	0.072	0.036	0.098	0.070	0.060	0.061
-0.311	0.036	0.073	0.025	0.055	0.012	0.047
-0.339	0.007	0.066	-0.032	0.008	0.021	0.094
-0.367	0.018	0.051	0.046	0.011	-0.006	0.066
-0.394	0.008	0.043	0.113	-0.041	-0.023	0.023
-0.420	0.044	0.024	0.085	-0.030	0.035	0.066

TABLE J-5 (continued)

Q	1.62	1.70	1.77	1.91	1.98	2.05
S(Q)	1.193	1.147	1.093	1.061	1.019	1.012
w*10**-13			S(Q,w)*10**13			
0.651	0.005	-0.003	-0.001	-0.015	0.012	0.005
0.603	0.036	-0.001	0.004	-0.004	-0.005	-0.008
0.557	0.062	-0.021	0.012	-0.000	-0.007	0.023
0.511	0.047	-0.008	0.002	0.001	0.018	0.042
0.467	0.023	0.003	0.003	-0.007	0.022	0.019
0.423	0.013	-0.009	0.007	0.028	0.033	0.012
0.380	0.014	0.007	0.007	0.050	0.041	0.053
0.339	0.022	0.057	0.015	0.038	0.054	0.052
0.298	0.049	0.089	0.066	0.070	0.103	0.056
0.258	0.158	0.124	0.127	0.137	0.173	0.152
0.219	0.262	0.232	0.218	0.251	0.266	0.251
0.180	0.415	0.380	0.396	0.380	0.393	0.349
0.143	0.638	0.590	0.574	0.549	0.544	0.489
0.106	0.895	0.838	0.813	0.762	0.715	0.650
0.070	1.148	1.101	1.068	0.942	0.882	0.845
0.035	1.296	1.257	1.199	1.077	0.956	0.968
0.0	1.334	1.272	1.277	1.169	1.014	0.983
-0.034	1.247	1.195	1.225	1.139	0.999	1.031
-0.067	1.045	1.090	1.072	1.017	0.901	0.969
-0.100	0.801	0.905	0.865	0.903	0.816	0.818
-0.132	0.628	0.664	0.623	0.739	0.700	0.714
-0.163	0.445	0.498	0.444	0.622	0.574	0.598
-0.194	0.259	0.384	0.330	0.484	0.429	0.416
-0.224	0.182	0.238	0.198	0.300	0.299	0.242
-0.254	0.128	0.142	0.091	0.175	0.202	0.168
-0.283	0.058	0.081	0.117	0.169	0.145	0.158
-0.311	0.050	0.085	0.103	0.163	0.148	0.163
-0.339	0.131	0.126	0.021	0.094	0.167	0.170
-0.367	0.126	0.034	0.026	0.039	0.170	0.123
-0.394	0.031	-0.013	0.080	0.071	0.047	0.049
-0.420	0.016	-0.005	0.092	0.045	-0.033	0.052

TABLE J-5 (continued)

Q	2.33	2.40	2.47	2.54	2.60	2.74
S(Q)	0.984	0.977	0.972	0.970	0.970	0.967
10-13			S(Q,W)*10**13			
0.651	-0.002	0.013	-0.050	-0.026	-0.027	0.011
0.603	-0.012	0.015	-0.013	-0.008	-0.007	0.012
0.557	0.023	0.014	0.016	0.024	0.029	-0.013
0.511	0.041	0.008	0.010	0.023	0.026	-0.017
0.467	0.051	0.016	0.009	0.030	0.026	0.031
0.423	0.051	0.039	0.024	0.051	0.018	0.072
0.380	0.055	0.039	0.054	0.053	0.097	0.095
0.339	0.097	0.064	0.084	0.091	0.157	0.102
0.298	0.170	0.142	0.114	0.180	0.140	0.156
0.258	0.230	0.195	0.223	0.229	0.212	0.272
0.219	0.277	0.265	0.329	0.289	0.324	0.361
0.180	0.377	0.365	0.412	0.397	0.410	0.439
0.143	0.486	0.487	0.549	0.528	0.524	0.525
0.106	0.614	0.623	0.667	0.644	0.631	0.637
0.070	0.738	0.739	0.756	0.717	0.736	0.696
0.035	0.804	0.781	0.814	0.735	0.822	0.697
0.0	0.857	0.784	0.843	0.787	0.837	0.727
-0.034	0.905	0.798	0.841	0.818	0.807	0.703
-0.067	0.828	0.746	0.804	0.739	0.728	0.611
-0.100	0.707	0.703	0.753	0.656	0.594	0.557
-0.132	0.639	0.620	0.649	0.615	0.649	0.568
-0.163	0.550	0.534	0.558	0.554	0.518	0.547
-0.194	0.436	0.440	0.463	0.460	0.398	0.440
-0.224	0.351	0.308	0.328	0.339	0.311	0.326
-0.254	0.250	0.281	0.257	0.234	0.206	0.245
-0.283	0.190	0.270	0.244	0.213	0.200	0.254
-0.311	0.189	0.185	0.216	0.189	0.171	0.244
-0.339	0.149	0.159	0.186	0.149	0.105	0.220
-0.367	0.118	0.164	0.141	0.122	0.141	0.213
-0.394	0.107	0.114	0.099	0.107	0.115	0.217
-0.420	0.100	0.065	0.065	0.088	0.106	0.219

TABLE J-5 (continued)

Q	2.80	2.87	2.94
S(Q)	0.965	0.967	0.970
W*10**-13		S(Q,W)*10**13	
0.651	0.021	0.005	0.001
0.603	0.011	-0.004	0.003
0.557	-0.002	0.008	-0.013
0.511	0.001	0.005	-0.009
0.467	0.005	0.012	0.030
0.423	0.040	0.066	0.058
0.380	0.101	0.126	0.073
0.339	0.132	0.143	0.103
0.298	0.177	0.156	0.156
0.258	0.241	0.229	0.235
0.219	0.313	0.361	0.340
0.180	0.424	0.448	0.418
0.143	0.531	0.487	0.507
0.106	0.609	0.596	0.654
0.070	0.683	0.688	0.740
0.035	0.740	0.726	0.767
0.0	0.747	0.728	0.783
-0.034	0.739	0.701	0.738
-0.067	0.664	0.680	0.697
-0.100	0.615	0.664	0.673
-0.132	0.501	0.628	0.629
-0.163	0.471	0.483	0.519
-0.194	0.382	0.345	0.423
-0.224	0.355	0.318	0.354
-0.254	0.306	0.278	0.307
-0.283	0.242	0.219	0.343
-0.311	0.193	0.182	0.332
-0.339	0.180	0.166	0.213
-0.367	0.157	0.206	0.145
-0.394	0.114	0.234	0.144
-0.420	0.111	0.129	0.129

TABLE J-6

$\tilde{S}(Q,\omega)$: P = 66.5 atm, ρ = 5.51 mole/liter, T = 303 K

Q	0.58	0.66	0.74	0.81	0.89	1.04
S(Q)	0.860	0.857	0.857	0.857	0.860	0.909
W*10**-13			S(Q,W)*10**13			
0.051	0.012	-0.027	0.005	-0.004	0.029	0.035
0.085	0.021	0.013	0.010	-0.004	0.035	0.029
0.357	0.015	0.017	0.012	0.004	0.007	0.031
0.511	0.007	0.005	0.029	0.013	0.020	0.028
0.467	0.027	0.010	0.021	0.041	0.027	0.033
0.423	0.018	-0.004	0.016	0.022	0.035	0.018
0.380	-0.001	-0.023	0.027	-0.016	0.014	0.014
0.339	0.010	-0.038	-0.001	-0.042	-0.014	0.011
0.298	0.028	0.018	0.015	0.009	0.033	0.029
0.258	0.030	0.062	0.065	0.084	0.087	0.095
0.219	0.065	0.080	0.079	0.104	0.103	0.146
0.180	0.167	0.171	0.178	0.177	0.203	0.256
0.143	0.304	0.352	0.379	0.378	0.412	0.455
0.106	0.546	0.630	0.640	0.693	0.639	0.687
0.070	0.919	0.981	1.008	1.033	0.932	0.956
0.035	1.203	1.311	1.293	1.339	1.183	1.165
0.0	1.436	1.449	1.408	1.462	1.300	1.250
-0.034	1.358	1.383	1.331	1.377	1.238	1.171
-0.067	1.040	1.113	1.042	1.136	0.986	0.956
-0.100	0.870	0.742	0.705	0.749	0.649	0.712
-0.132	0.370	0.398	0.429	0.466	0.412	0.492
-0.165	0.200	0.200	0.216	0.309	0.232	0.341
-0.194	0.151	0.152	0.111	0.148	0.115	0.228
-0.224	0.079	0.110	0.059	0.079	0.086	0.155
-0.254	0.068	0.081	-0.013	0.046	0.076	0.103
-0.283	0.078	0.043	0.000	0.066	0.071	0.031
-0.311	-0.022	0.010	0.020	0.043	0.048	0.007
-0.339	-0.048	-0.029	0.020	0.016	0.031	0.025
-0.367	-0.026	-0.025	0.036	0.017	-0.011	-0.003
-0.394	-0.001	0.001	0.056	-0.012	-0.060	0.037
-0.420	0.003	0.027	0.039	-0.005	0.004	0.067

TABLE J-6 (continued)

Q	1.11	1.18	1.26	1.33	1.48	1.55
S(Q)	0.992	1.027	1.066	1.121	1.165	1.220
W*10**-13			S(Q,W)*10**13			
0.061	-0.012	0.027	0.010	-0.017	0.027	0.036
0.065	0.020	0.007	0.036	0.013	0.038	0.017
0.557	0.031	0.003	0.021	0.030	0.017	0.024
0.511	-0.010	0.002	0.039	0.035	0.014	0.037
0.467	-0.011	-0.013	0.035	0.046	0.016	0.030
0.423	0.013	-0.003	0.023	0.034	0.007	0.034
0.380	0.005	-0.013	0.004	-0.017	0.019	0.018
0.339	0.017	0.010	-0.012	-0.002	0.025	0.017
0.298	0.040	0.053	0.054	0.054	0.054	0.075
0.258	0.079	0.070	0.155	0.101	0.124	0.182
0.219	0.154	0.154	0.206	0.181	0.195	0.231
0.180	0.292	0.293	0.319	0.341	0.335	0.314
0.143	0.510	0.488	0.552	0.549	0.558	0.553
0.106	0.744	0.768	0.789	0.788	0.850	0.856
0.070	0.999	0.997	1.056	1.122	1.124	1.127
0.035	1.223	1.196	1.324	1.340	1.301	1.328
0.0	1.262	1.317	1.405	1.414	1.400	1.385
-0.034	1.196	1.278	1.350	1.348	1.284	1.262
-0.067	1.069	1.083	1.101	1.115	1.096	1.043
-0.100	0.795	0.803	0.814	0.831	0.891	0.820
-0.132	0.581	0.571	0.602	0.600	0.617	0.625
-0.165	0.347	0.413	0.377	0.390	0.394	0.414
-0.194	0.198	0.295	0.195	0.245	0.236	0.321
-0.224	0.125	0.156	0.141	0.171	0.178	0.221
-0.254	0.103	0.095	0.104	0.112	0.127	0.146
-0.283	0.065	0.136	0.046	0.054	0.100	0.080
-0.311	0.052	0.053	0.010	0.060	0.074	0.041
-0.339	-0.009	0.021	-0.040	0.016	0.011	0.135
-0.367	0.017	0.052	-0.049	-0.050	0.004	0.149
-0.394	0.010	0.029	-0.085	-0.050	0.062	0.059
-0.420	0.010	-0.024	-0.071	0.016	0.116	0.061

TABLE J-6 (continued)

G	1.62	1.70	1.77	1.91	1.98	2.05
S(G)	1.228	1.173	1.110	1.071	1.022	1.014
w*10**-13			S(G,w)*10**13			
0.651	0.008	0.010	-0.022	-0.008	0.016	-0.021
0.603	0.026	0.010	-0.051	-0.010	0.014	-0.023
0.557	0.030	0.007	-0.025	-0.003	0.006	-0.008
0.511	0.032	0.008	0.013	0.026	-0.008	0.013
0.467	0.001	0.006	-0.002	0.041	-0.018	0.023
0.425	-0.008	0.026	-0.002	0.047	0.025	0.045
0.380	0.031	0.029	0.022	0.023	0.075	0.067
0.339	0.057	0.037	0.046	0.025	0.101	0.082
0.298	0.102	0.087	0.066	0.085	0.121	0.122
0.258	0.177	0.155	0.153	0.171	0.160	0.190
0.219	0.267	0.226	0.248	0.260	0.243	0.274
0.180	0.427	0.358	0.442	0.386	0.350	0.395
0.143	0.626	0.606	0.632	0.531	0.484	0.530
0.106	0.883	0.854	0.834	0.759	0.635	0.671
0.070	1.164	1.072	1.006	0.938	0.774	0.852
0.035	1.356	1.249	1.218	1.046	0.924	0.957
0.0	1.397	1.338	1.311	1.140	1.035	0.950
-0.034	1.326	1.301	1.256	1.118	0.994	0.959
-0.067	1.119	1.102	1.097	1.037	0.898	0.949
-0.100	0.838	0.899	0.925	0.861	0.822	0.807
-0.132	0.626	0.692	0.712	0.662	0.748	0.645
-0.165	0.470	0.507	0.500	0.510	0.594	0.509
-0.194	0.311	0.368	0.345	0.393	0.361	0.381
-0.224	0.209	0.225	0.243	0.237	0.223	0.265
-0.254	0.118	0.115	0.136	0.160	0.189	0.177
-0.283	0.071	0.043	0.098	0.150	0.141	0.164
-0.311	0.055	0.075	0.050	0.132	0.094	0.169
-0.339	0.018	0.091	0.053	0.176	0.141	0.095
-0.367	0.000	0.044	0.065	0.166	0.115	0.109
-0.394	-0.007	0.032	0.009	0.120	0.033	0.154
-0.420	-0.017	0.030	0.035	0.088	0.046	0.105

TABLE J-6 (continued)

Q	2.33	2.40	2.47	2.54	2.60	2.74
S(Q)	0.981	0.972	0.967	0.964	0.964	0.961
W*10**-13			S(Q,W)*10**13			
0.651	-0.014	-0.006	0.005	0.013	-0.014	-0.023
0.603	-0.017	0.007	0.005	0.018	0.003	-0.006
0.557	0.007	0.018	0.022	0.001	0.035	0.011
0.511	0.048	0.011	0.018	-0.003	0.036	0.018
0.467	0.019	0.010	0.025	0.022	0.043	0.042
0.423	0.009	0.022	0.059	0.050	0.063	0.083
0.380	0.062	0.068	0.078	0.079	0.106	0.114
0.339	0.089	0.126	0.112	0.109	0.127	0.101
0.298	0.152	0.171	0.155	0.159	0.138	0.146
0.258	0.208	0.232	0.192	0.201	0.213	0.249
0.219	0.305	0.316	0.271	0.271	0.310	0.296
0.180	0.400	0.437	0.394	0.361	0.425	0.383
0.143	0.518	0.546	0.520	0.514	0.533	0.513
0.106	0.629	0.660	0.664	0.653	0.578	0.611
0.070	0.726	0.761	0.746	0.696	0.651	0.674
0.035	0.822	0.812	0.807	0.696	0.705	0.718
0.0	0.864	0.850	0.866	0.740	0.738	0.732
-0.034	0.878	0.822	0.852	0.710	0.760	0.675
-0.067	0.848	0.777	0.781	0.634	0.718	0.649
-0.100	0.757	0.755	0.709	0.627	0.643	0.656
-0.132	0.583	0.683	0.612	0.627	0.561	0.571
-0.165	0.480	0.565	0.525	0.532	0.522	0.508
-0.194	0.453	0.397	0.443	0.421	0.395	0.436
-0.224	0.364	0.318	0.353	0.354	0.259	0.332
-0.254	0.268	0.316	0.225	0.308	0.222	0.271
-0.283	0.259	0.276	0.220	0.244	0.187	0.232
-0.311	0.188	0.170	0.186	0.180	0.177	0.226
-0.339	0.141	0.152	0.124	0.140	0.147	0.200
-0.367	0.125	0.136	0.119	0.124	0.127	0.166
-0.394	0.126	0.127	0.144	0.186	0.118	0.184
-0.420	0.121	0.147	0.151	0.156	0.079	0.171

TABLE J-6 (continued)

Q	2.80	2.87	2.94
S(Q)	0.959	0.951	0.964

w*10**-13	S(Q,w)*10**13		
0.651	-0.000	-0.014	-0.010
0.603	0.000	-0.003	-0.009
0.557	-0.000	-0.002	-0.024
0.511	0.010	0.011	-0.027
0.467	0.018	0.055	0.032
0.423	0.021	0.066	0.073
0.380	0.060	0.098	0.111
0.339	0.123	0.131	0.164
0.298	0.166	0.194	0.160
0.258	0.204	0.252	0.236
0.219	0.294	0.324	0.343
0.180	0.423	0.457	0.425
0.143	0.563	0.516	0.530
0.106	0.650	0.644	0.654
0.070	0.738	0.714	0.765
0.035	0.804	0.743	0.796
0.0	0.766	0.774	0.757
-0.034	0.764	0.770	0.735
-0.067	0.739	0.750	0.728
-0.100	0.666	0.656	0.710
-0.132	0.602	0.654	0.636
-0.163	0.567	0.553	0.526
-0.194	0.474	0.375	0.422
-0.224	0.405	0.293	0.356
-0.254	0.293	0.255	0.334
-0.283	0.213	0.202	0.280
-0.311	0.166	0.235	0.199
-0.339	0.215	0.157	0.145
-0.367	0.160	0.151	0.119
-0.394	0.139	0.152	0.120
-0.420	0.130	0.116	0.155

TABLE J-7

$\hat{S}(Q,\omega)$: P = 72.7 atm, ρ = 7.60 mole/liter, T = 303 K

Q	0.58	0.66	0.74	0.81	0.89	1.04
S(Q)	0.806	0.802	0.802	0.802	0.806	0.375
w*10**-13			S(Q,w)*10**13			
0.651	-0.008	-0.009	0.010	0.019	0.023	0.004
0.603	-0.003	0.013	0.012	0.034	-0.019	0.013
0.557	0.003	0.017	0.021	0.015	-0.010	0.025
0.511	-0.007	-0.010	0.021	0.017	0.005	0.033
0.467	0.002	-0.009	0.017	0.036	0.002	0.021
0.423	-0.012	0.003	0.014	0.023	-0.022	0.017
0.380	0.023	0.040	0.045	0.033	-0.014	0.041
0.339	0.049	0.058	0.063	0.053	0.042	0.047
0.298	0.006	0.054	0.044	0.056	0.035	0.062
0.258	0.001	0.060	0.047	0.086	0.050	0.119
0.219	0.038	0.084	0.099	0.119	0.078	0.179
0.180	0.130	0.162	0.197	0.193	0.168	0.259
0.143	0.308	0.334	0.353	0.359	0.372	0.435
0.106	0.613	0.600	0.630	0.601	0.675	0.674
0.070	0.973	0.949	0.945	0.898	1.009	0.918
0.035	1.276	1.249	1.199	1.162	1.253	1.083
0.0	1.439	1.363	1.311	1.251	1.364	1.149
-0.034	1.350	1.265	1.204	1.144	1.280	1.074
-0.067	1.053	1.000	0.925	0.907	1.017	0.864
-0.100	0.725	0.634	0.630	0.631	0.696	0.653
-0.132	0.475	0.409	0.441	0.419	0.461	0.480
-0.163	0.243	0.204	0.269	0.255	0.269	0.332
-0.194	0.107	0.100	0.134	0.132	0.136	0.214
-0.224	0.049	0.088	0.082	0.087	0.089	0.123
-0.254	0.039	0.079	0.032	0.077	0.078	0.073
-0.283	0.040	0.012	-0.011	0.109	0.017	0.049
-0.311	0.013	0.005	-0.018	0.082	-0.024	0.030
-0.339	0.008	0.015	-0.024	0.016	0.025	0.061
-0.367	0.032	-0.008	-0.043	-0.051	0.071	0.030
-0.394	0.094	0.037	-0.015	-0.043	0.069	-0.021
-0.420	0.023	0.070	0.002	0.042	-0.029	0.010

TABLE J-7 (continued)

Q	1.11	1.18	1.26	1.33	1.48	1.55
S(Q)	0.989	1.038	1.091	1.167	1.228	1.304
W*10**-13			S(Q,W)*10**13			
0.651	-0.029	0.009	-0.005	-0.013	-0.006	0.017
0.603	0.000	0.017	-0.010	0.004	-0.017	0.015
0.557	0.026	0.014	0.011	0.039	-0.006	0.014
0.511	-0.007	-0.005	-0.001	0.045	0.001	0.026
0.467	-0.005	-0.018	0.008	0.033	-0.007	0.049
0.423	0.021	0.005	0.016	0.030	0.008	0.070
0.380	0.027	0.046	0.002	0.043	0.055	0.085
0.339	0.049	0.059	0.028	0.069	0.081	0.092
0.298	0.075	0.067	0.048	0.060	0.053	0.095
0.258	0.135	0.095	0.102	0.073	0.094	0.150
0.219	0.175	0.173	0.181	0.139	0.215	0.218
0.180	0.278	0.306	0.318	0.282	0.366	0.356
0.143	0.501	0.490	0.564	0.554	0.601	0.617
0.106	0.772	0.761	0.865	0.895	0.882	0.885
0.070	1.032	1.030	1.141	1.216	1.146	1.159
0.035	1.266	1.234	1.355	1.432	1.397	1.379
0.0	1.336	1.310	1.464	1.548	1.496	1.437
-0.034	1.209	1.195	1.353	1.432	1.361	1.376
-0.067	0.994	1.016	1.108	1.181	1.153	1.163
-0.100	0.769	0.809	0.851	0.901	0.914	0.857
-0.132	0.562	0.552	0.590	0.582	0.676	0.651
-0.163	0.336	0.331	0.384	0.346	0.417	0.461
-0.194	0.188	0.211	0.233	0.252	0.202	0.250
-0.224	0.120	0.166	0.149	0.201	0.167	0.148
-0.254	0.116	0.110	0.148	0.127	0.148	0.137
-0.283	0.128	0.074	0.056	0.098	0.112	0.133
-0.311	0.067	0.079	-0.017	0.087	0.090	0.067
-0.339	0.021	0.018	-0.017	0.105	0.017	0.061
-0.367	0.014	0.004	-0.030	0.027	0.023	0.064
-0.394	-0.001	0.059	0.033	-0.002	0.054	0.031
-0.420	-0.030	0.050	0.074	0.018	0.029	0.059

TABLE J-7 (continued)

Q	1.62	1.70	1.77	1.91	1.98	2.05
S(Q)	1.315	1.239	1.152	1.099	1.030	1.019
w*10**-13			S(Q,w)*10**13			
0.651	0.010	0.013	-0.014	0.007	0.016	-0.015
0.603	0.023	0.002	0.004	0.023	0.033	-0.018
0.557	0.018	-0.010	0.027	0.019	-0.030	-0.022
0.511	0.013	0.006	0.016	0.048	-0.005	0.004
0.467	-0.004	0.015	0.002	0.046	0.049	0.041
0.423	-0.002	0.038	0.006	0.034	0.049	0.058
0.380	0.058	0.052	0.020	0.023	0.041	0.094
0.339	0.087	0.063	0.047	0.080	0.095	0.092
0.298	0.076	0.122	0.113	0.147	0.180	0.095
0.258	0.150	0.179	0.149	0.180	0.234	0.150
0.219	0.243	0.237	0.227	0.266	0.289	0.245
0.180	0.394	0.366	0.378	0.385	0.345	0.368
0.143	0.620	0.602	0.552	0.561	0.502	0.513
0.106	0.960	0.870	0.810	0.757	0.719	0.662
0.070	1.317	1.131	1.077	0.902	0.901	0.766
0.035	1.503	1.305	1.254	1.022	1.067	0.842
0.0	1.551	1.362	1.314	1.120	1.144	0.901
-0.034	1.448	1.341	1.244	1.118	1.116	0.961
-0.067	1.208	1.194	1.113	1.033	1.007	0.936
-0.100	0.967	0.937	0.883	0.862	0.873	0.781
-0.132	0.739	0.676	0.617	0.686	0.789	0.640
-0.163	0.471	0.472	0.417	0.565	0.615	0.487
-0.194	0.262	0.299	0.287	0.382	0.402	0.311
-0.224	0.163	0.223	0.186	0.200	0.237	0.247
-0.254	0.138	0.160	0.091	0.137	0.120	0.234
-0.283	0.132	0.099	0.088	0.101	0.123	0.199
-0.311	0.081	0.080	0.069	0.105	0.143	0.197
-0.339	0.040	0.048	0.020	0.130	0.049	0.173
-0.367	-0.024	0.019	0.047	0.072	0.053	0.021
-0.394	-0.074	0.026	0.062	0.051	0.120	0.043
-0.420	-0.004	0.011	0.043	0.055	0.128	-0.025

TABLE J-7 (continued)

Q	2.33	2.40	2.47	2.54	2.60	2.74
S(Q)	0.973	0.962	0.954	0.951	0.951	0.947
w*10**-13			S(Q,w)*10**13			
0.651	0.009	0.044	-0.037	0.012	-0.022	-0.012
0.603	0.011	0.053	-0.025	0.019	-0.008	0.032
0.557	-0.002	0.017	-0.009	0.023	0.033	-0.001
0.511	0.026	-0.005	0.014	0.057	0.060	-0.018
0.467	0.049	0.028	0.031	0.044	0.063	0.051
0.423	0.039	0.067	0.060	0.021	0.065	0.069
0.380	0.030	0.078	0.115	0.069	0.071	0.094
0.339	0.091	0.115	0.139	0.115	0.092	0.096
0.298	0.190	0.153	0.222	0.172	0.152	0.142
0.258	0.212	0.220	0.257	0.242	0.199	0.287
0.219	0.274	0.298	0.346	0.307	0.301	0.325
0.180	0.424	0.342	0.458	0.390	0.440	0.395
0.143	0.608	0.465	0.528	0.501	0.540	0.551
0.106	0.714	0.628	0.632	0.613	0.671	0.617
0.070	0.730	0.747	0.721	0.721	0.788	0.701
0.035	0.832	0.745	0.825	0.771	0.792	0.760
0.0	0.888	0.752	0.890	0.815	0.840	0.776
-0.034	0.798	0.777	0.869	0.801	0.925	0.787
-0.067	0.730	0.733	0.800	0.729	0.732	0.719
-0.100	0.705	0.638	0.747	0.642	0.710	0.594
-0.132	0.568	0.529	0.722	0.572	0.615	0.502
-0.163	0.482	0.473	0.642	0.522	0.547	0.475
-0.194	0.451	0.417	0.455	0.416	0.429	0.419
-0.224	0.370	0.298	0.256	0.268	0.284	0.355
-0.254	0.305	0.254	0.211	0.184	0.212	0.318
-0.283	0.181	0.233	0.182	0.204	0.213	0.219
-0.311	0.154	0.174	0.142	0.168	0.213	0.140
-0.339	0.169	0.144	0.130	0.105	0.163	0.176
-0.367	0.180	0.115	0.046	0.122	0.107	0.200
-0.394	0.118	0.160	0.041	0.159	0.037	0.092
-0.420	-0.002	0.259	0.035	0.185	0.055	0.058

TABLE J-7 (continued)

0	2.80	2.87	2.94
S(0)	0.943	0.947	0.951

W*10**-13	S(Q,W)*10**13		
0.651	-0.025	-0.038	0.005
0.603	-0.007	-0.018	-0.003
0.557	-0.014	0.017	0.014
0.511	0.003	-0.002	0.024
0.467	0.033	0.010	0.044
0.423	0.061	0.039	0.049
0.380	0.105	0.085	0.064
0.339	0.159	0.117	0.120
0.298	0.190	0.212	0.211
0.258	0.244	0.346	0.268
0.219	0.315	0.403	0.299
0.180	0.392	0.439	0.399
0.143	0.569	0.517	0.556
0.106	0.694	0.666	0.692
0.070	0.753	0.748	0.751
0.035	0.795	0.791	0.778
0.0	0.851	0.851	0.756
-0.034	0.880	0.827	0.672
-0.067	0.775	0.755	0.658
-0.100	0.692	0.690	0.620
-0.132	0.615	0.642	0.586
-0.163	0.504	0.579	0.494
-0.194	0.382	0.449	0.357
-0.224	0.295	0.291	0.351
-0.254	0.259	0.253	0.350
-0.283	0.227	0.230	0.325
-0.311	0.171	0.177	0.221
-0.339	0.173	0.190	0.133
-0.367	0.250	0.253	0.108
-0.394	0.229	0.205	0.103
-0.420	0.102	0.047	0.058

BIBLIOGRAPHY

1. JANAF Thermochemical Tables, Second Ed., Dow Chemical Co., Thermal Laboratory, Midland, Mich., 1965.

2. F. D. Rossini, Selected Values of Chemical Thermodynamic Properties, Natl. Bur. Std., Circ. 500, 1952.

3. E. A. Mason and T. H. Spurling, The Virial Equation of State, Pergamon Press, N. Y., 1969.

4. R. C. Reid, J. M. Prausnitz, and T. K. Sherwood, The Properties of Liquids and Gases, McGraw-Hill, N. Y., 1977.

5. K. E. Gubbins, A. I. Ch. E. J., 19, 684 (1973).

6. W. R. Smith, Specialist Reports: Statistical Mechanics, 1, Chem. Soc., London, 1973.

7. M. S. Green, J. Chem. Phys., 20, 1281 (1952); R. Kubo, M. Yokota, and S. Nakajima, J. Phys. Soc. Jap., 12, 1203 (1957).

8. R. L. Peterson, Rev. Mod. Phys., 39, 69 (1967); K. Kawasaki and J. Gunton, Phys. Rev., A8, 2048 (1973).

9. S. Harris, Mol. Phys., 21, 933 (1971).

10. P. A. Egelstaff, D. I. Page, and C. R. Heard, J. Phys., C4, 1435 (1971).

11. P. A. Egelstaff, C. Gray and K. E. Gubbins, Phys. Lett., 37A, 321 (1971).

12. J. A. Barker, R. O. Watts, J. K. Lee, T. P. Schafer, and Y. T. Lee, J. Chem. Phys., 61, 3081 (1974).

13. B. M. Axilrod and E. Teller, J. Chem. Phys., 11, 299 (1943).

14. P. A. Egelstaff, D. I. Page, and C. R. Heard, Phys. Lett., 30A, 376 (1969).

15. L. Van Hove, Phys. Rev., 95, 249 (1954).

16. T. L. Hill, Statistical Thermodynamics, Addisson-Wesley, Reading, Mass., 1960.

17. P. A. Egelstaff, An Introduction to the Liquid State, Academic Press, N. Y., 1967.

18. K. Gottfried, Quantum Mechanics, W. A. Benjamin, Inc., London, 1966.

19. E. Fermi, Ricerca Sci., 7, 13 (1936).

20. J. A. Barker, R. A. Fisher, and R. O. Watts, Mol. Phys., 21, 657 (1971).

21. P. A. Egelstaff, Ann. Rev. Phys. Chem., 24, 159 (1973).

22. S. A. Rice and P. Gray, The Statistical Mechanics of Simple Liquids, Interscience, N. Y., 1965.

23. T. M. Reed and K. E. Gubbins, Applied Statistical Mechanics, McGraw-Hill, N. Y., 1973.

24. A. E. Sherwood, A. G. DeRocco, and E. A. Mason, J. Chem. Phys., 44, 2993 (1966).

25. P. A. Egelstaff, private communication.

26. For the method used here, see: D. Henderson and L. Oden, J. Chem. Phys., 43, 4172 (1965).

27. P. Schofield, Proc. Phys. Soc., 88, 149 (1966); see reference (11), also.

28. L. Verlet, Phys. Rev., 165, 201 (1968).

29. S. H. Chen, Y. Leferre, G. Mazenko, and P. A. Egelstaff, in Molecular Motions in Liquids, ed. J. Lascombe, Reidel, Dordrect, Holland, 1974.

30. See for example: P. C. Martin, in Many Body Physics, ed. DeWitt and Bolian, Gordon and Breach, N. Y., 1968.

31. P. Schofield, Specialist Reports: Statistical Mechanics, 2, Chem. Soc., London, 1977.

32. L. Onsager, Phys. Rev., 37, 405 (1931); ibid., 38, 2265 (1931).

33. L. D. Landau and E. M. Lifshitz, Fluid Mechanics, Addison Wesley, N. Y., 1959.

34. R. D. Mountain, Rev. Mod. Phys., 38, 205 (1966).

35. E. H. Hara, A. D. May, and H. F. P. Knapp, Can J. Phys., 49, 420 (1971).

36. C. D. Boley, R. C. Desai, and G. Tenti, Can. J. Phys., 50, 2158 (1972).

37. E. Gulari, R. J. Brown, and C. J. Pings, A. I. Ch. E. J., 19, 1196 (1973).

38. C-H Chung and S. Yip, Phys. Rev., 182, 323 (1969).

39. N. K. Ailawadi, R. Zwanzig, and A. Rahman, Phys. Rev., A4, 1616 (1971).

40. A. A. Kugler, J. Stat. Phys., 8, 107 (1973).

41. J. Lebowitz, J. Percus, and J. Sykes, Phys. Rev., 188, 487 (1969).

42. The literature on this subject is large. For references, see: G. Mazenko, Phys. Rev., 9, 360 (1974).

43. L. J. Groome, K. E. Gubbins, and J. W. Dufty, Phys. Rev., A13, 437 (1976).

44. G. S. Rushbrooke, in Physics of Simple Liquids, ed. H. N. V. Temperly, J. S. Rowlinson, and G. S. Rushbrooke, North Holland, Amsterdam, 1968.

45. B. D. Fried and S. D. Conte, The Plasma Dispersion Function, Academic Press, N. Y., 1961.

46. S. Chapman and T. Cowling, The Mathematical Theory of Non-Uniform Gases, Cambridge University Press, N. Y., 1960.

47. For references, see: B. J. Berne and D. Forster, Ann. Rev. Phys. Chem., 22, 563 (1971).

48. D. Forster, Phys. Rev., A9, 943 (1974).

49. P. A. Egelstaff, C. Gray, and K. E. Gubbins, to appear.

50. L. Blum and J. L. Lebowitz, Phys. Rev. 185, 273 (1969); D. Forster and P. C. Martin, Phys. Rev., A2, 1575 (1970). For difficulties associated with the density expansions, see: M. H. Ernst, L. K. Haines, and J. R. Dorfman, Rev. Mod. Phys., 41, 296 (1969).

51. E. G. D. Cohen, Physica, 28, 1025 (1962).

52. E. P. Gross, in Lectures in Theoretical Physics-Kinetic Theory, ed. W. Brittin, A. Barut, and M. Guenin, Gordon and Breach, N. Y., 1957.

53. R. Zwanzig and R. D. Mountain, J. Chem. Phys., 43, 4464 (1965).

54. K. Sköld, J. M. Rowe, G. Ostrowski, and P. D. Randolph, Phys. Rev., A6, 1107 (1972).

55. Such measurements on the temperature derivative have not yet been performed. See reference (40) for the theoretical development.

56. E. P. Gross and E. A. Jackson, Phys. Fluids, 2, 432 (1959).

57. A. Sugawara, S. Yip, and L. Sirovich, Phys. Rev., 168, 121 (1969); ibid., Phys. Fluids, 11, 925 (1968).

58. G. F. Mazenko, T. Y. C. Wei, and S. Yip, Phys. Rev. A6, 1981 (1972).

59. S. Yip, private communication.

60. S-H Chen and A. Rahman (preprint); J. W. Dufty, L. J. Groome, K. J. Gubbins, and P. A. Egelstaff, Proceedings of the Conference on Neutron Scattering, Gatlinburg, Tenn., 1976.

61. B. P. Schoenborn, C. EN., 25, 31 (1977).

62. P. A. Egelstaff, C. Gray, K. E. Gubbins, and K. C. Mo, J. Stat. Phys., 13, 315 (1975).

63. F. Gompf, W. Gläser, G. Ehret, G. Wilhelmi, W. Reichardt, and K. H. Beckurts, Proceedings of the Panel Conference on Instrumentation for Neutron Inelastic Scattering Research, Vienna, 1969.

64. L. B. Koppel, Introduction to Control Theory with Applications to Process Control, Prentice-Hall, Englewood Cliffs, N. J., 1968.

65. F. Hoßfeld and R. Amadori, and R. Scherm, Instrumentation for Neutron Inelastic Scattering Research, Vienna, 1970.

66. F. Hoßfeld and R. Amadori, Report Jül-684-FF, KFA Jülich, (1970).

67. R. Von Jan and R. Scherm, Nucl. Instrum. Methods, 63, 351 (1968).

68. H. A. Mook and M. K. Wilkinson, Instrumentation for Neutron Inelastic Scattering Research, Vienna, 1970.

69. C. G. Shull, E. O. Wollan, and W. A. Strauser, Phys. Rev., 81, 483 (1951).

70. J. H. Dymond and E. B. Smith, The Virial Coefficients of Gases, Oxford Science Research Papers, Clarendon Press, Oxford, 1969.

71. R. D. McCarty, A. L. Gosman, and J. G. Hust, Natl. Bur. Stds., NSRDS-NBS 27, 1969.

72. J. A. Beattie, R. J. Barriault, and J. S. Brierly, J. Chem. Phys., 19, 1219 (1951).

73. P. A. Egelstaff, personal communication.

74. I. Kaplan, Nuclear Physics, Addison-Wesley, Reading, Mass., 1962.

75. E. P. Popov, Introduction to Mechanics of Solids, Prentice-Hall, Englewood Cliffs, N. J., 1968.

76. G. H. Vineyard, Phys. Rev., 96, 93 (1954).

77. R. K. Hawkins and P. A. Egelstaff, Mol. Phys., 29, 1639 (1975).

78. V. F. Sears (preprint).

79. For example, see: F. G. Bischoff, M. L. Yeater, and W. E. Moore, Nucl. Sci. Eng., 48, 266 (1972); J. R. D. Copley and J. M. Rowe, Phys. Rev. Lett., 32, 49 (1974); A. Tiitta and E. Tunkelo, Nucl. Instr. Meth., 103, 575 (1972).

80. I. A. Blech and B. L. Averbach, Phys. Rev., A137, 1113 (1965).

81. F. C. Blake, Rev. Mod. Phys., 54, 169 (1933).

82. H. L. Ritter, J. Appl. Phys., 22, 169 (1951).

83. H. H. Paalman and C. J. Pings, J. Appl. Phys., 33, 2635 (1962).

84. A. P. Kendig and C. J. Pings, J. Appl. Phys., 36, 1692 (1965).

85. P. A. Egelstaff and D. H. C. Harris, Disc. Fard. Soc., No. 49, 193 (1970).

86. P. A. Egelstaff, W. G. Graham, L. Hahn, K. Suzuki, and D. J. Winfield, Can. J. Phys., 52, 2093 (1974).

87. P. A. Egelstaff, private communication.

88. D. J. Winfield and P. A. Egelstaff, Can. J. Phys., 51, 1965 (1973). See reference (77) also.

89. J. A. Barker, R. A. Fisher, and R. O. Watts, Mol. Phys., 21, 657 (1971).

90. D. Henderson, private communication.

91. P. M. Furtado, G. F. Mazenko, and S. Yip, Phys. Rev., A13, 1641 (1976); ibid., A12, 1653 (1975).

BIOGRAPHICAL SKETCH

Lynn James Groome was born in Brantford, Ontario, Canada, on August 12, 1950. He is the son of Mr. and Mrs. Arthur R. Groome, now of Vero Beach, Florida. At age two he and his family moved from Brantford to Miami, Florida, where Lynn attended public school. He graduated from Miami Carol City Senior High School in June of 1968, and in August of that same year entered Clemson University.

At Clemson Lynn was a member of the student chapter of the American Institute of Chemical Engineers, Phi Kappa Phi, and Tau Beta Pi. He received his Bachelor of Science degree in Chemical Engineering, graduating with high honors in May, 1972, and began graduate studies there in the fall of that year. He received his Master of Science in Chemical Engineering in May, 1975. Lynn continued his graduate education at the University of Florida, entering graduate school in Chemical Engineering in March, 1974.

Lynn is married to the former Chadi Ree Daum, daughter of Mr. and Mrs. Joel Daum, of Miami, Florida.

I certify that I have read this study and that in my opinion it conforms to acceptable standards of scholarly presentation and is fully adequate, in scope and quality, as a dissertation for the degree of Doctor of Philosophy.

K. E. Gubbins

K. E. Gubbins, Chairman
Professor of Chemical Engineering

I certify that I have read this study and that in my opinion it conforms to acceptable standards of scholarly presentation and is fully adequate, in scope and quality, as a dissertation for the degree of Doctor of Philosophy.

J. W. Dufty

J. W. Dufty, Co-chairman
Professor of Physics

I certify that I have read this study and that in my opinion it conforms to acceptable standards of scholarly presentation and is fully adequate, in scope and quality, as a dissertation for the degree of Doctor of Philosophy.

J. P. O'Connell

J. P. O'Connell
Professor of Chemical Engineering

This dissertation was submitted to the Graduate Faculty of the College of Engineering and to the Graduate Council, and was accepted as partial fulfillment of the requirements for the degree of Doctor of Philosophy.

August, 1977

Dean, College of Engineering

Dean, Graduate School

UNIVERSITY OF FLORIDA
3 1262 08666 287 0